# Mechanophotonics: Pseudo-Plastic Organic Crystal-based Photonic Components and Circuits

A Thesis Submitted in Partial Fulfillment for the Degree of DOCTOR OF PHILOSOPHY



 $\mathbf{B}\mathbf{y}$ 

### **AVULU VINOD KUMAR**

School of Chemistry
University of Hyderabad
(An Institution of Eminence)
Hyderabad-500046
INDIA
DEC-2023

# **CONTENTS**

Declaration		Ι
Certificate		II
Acknowledgr	ments	III
List of Acron	yms	$\mathbf{V}$
List of Symbo	ols	VII
Chapter-1	An Introduction to Inorganic and Organic Materials-based Photonic Components	1-53
1.1	and Circuits Photonic integrated circuits	2
		4
1.4	Nature of light	•
13	1.2.1 Light-matter interaction  Principles of light propagation in materials	8
1.5		Ü
1 /	1.3.1 Optical losses in waveguides Optical micro resentant	13
1.4	Optical micro-resonators	13
	1.4.1 FP resonators	
	1.4.1.1 Quality ( $Q$ ) factor	
	1.4.1.2 Axial FP resonators	
	1.4.1.3 Lateral FP resonators	
	1.4.2 Whispering gallery mode resonators	
1.5	Silicon-based optical components	23
	1.5.1 Interferometers	
	1.5.2 Fiber loop mirror	
	1.5.3 Directional Couplers	
	1.5.4 Wavelength division multiplexer	
	1.5.5 Spiral waveguides	
1.6	Organic crystals for photonics	31
	1.6.1 Mechanical properties	
	1.6.1.1 Plastically bendable organic crystals	
	1.6.1.2 Elastically bendable organic crystals	
	1.6.1.3 Pseudo-plastically bendable organic crystals	

	1.6.2 Mechanophotonics	
	1.6.3 Organic flexible waveguides	
	1.6.4 Bending-induced fluorescence changes	
	1.6.5 Organic photonic components and circuits	
	1.6.5.1 Organic crystal-based 2×2 directional couplers	
	1.6.5.2 Organic interferometers	
	1.6.5.3 Organic add-on-drop filter	
	1.6.5.4 Organic photonic integrated circuits	
1.7	Overview of thesis	47
Chapter-2	A Mechanophotonic Approach Towards	54-68
	an Organic, Flexible Crystal-based Optical	
	Interferometer	
2.1	Abstract	55
2.2	Introduction	55
2.3	Results and discussion	56
	2.3.1 Synthesis of BPyIN	
	2.3.2 Solid-state optical characteristics of BPyIN	
	2.3.3 X-Ray diffraction and mechanical studies of BPyIN	
	crystals	
	2.3.4 Mechanophotonic studies of BPyIN crystals	
	2.3.4.1 Self-assembly of BPyIN crystals	
	2.3.4.2 Optical waveguiding properties of BPyIN crystal	
	2.3.4.3 Pseudo-plastic behaviour of BPyIN microcrystal	
	2.3.5 Fabrication of compact organic interferometer	
2.4	Summary	68
<b>Chapter-3</b>	Mechanophotonics: Fabrication of a 2×2	69-82
	hybrid directional coupler from flexible	
	organic crystals	
3.1	Abstract	70
3.2	Introduction	70
3.3	Results and discussion	71
	3.3.1 Synthesis of CF <sub>3</sub> OMe	

	3.3.2 Solid-state optical characteristics CF <sub>3</sub> OMe	
	3.3.3 Structural basis for mechanical flexibility in	
	CF <sub>3</sub> OMe crystals	
	3.3.4 Self-assembly of CF <sub>3</sub> OMe	
	3.3.5 Mechanophotonic studies of CF <sub>3</sub> OMe and BPyIN	
	crystals	
	3.3.6 Fabrication of a hybrid directional coupler	
	3.3.7 Optical performance of hybrid directional coupler	
3.4	Summary	82
<b>Chapter-4</b>	A Broadband, Multiplexed-Visible-Light-	83-98
	<b>Transport in Composite Flexible-Organic-</b>	
	Crystal Waveguide	
4.1	Abstract	84
4.2	Introduction	84
4.3	Results and discussion	85
	4.3.1 Synthesis of BTD2CF <sub>3</sub>	
	4.3.2 Synthesis of BPP	
	4.3.3 Solid-state optical characteristics of materials	
	employed for WDM	
	4.3.4 Single crystal X-Ray and mechanical studies of	
	BTD2CF <sub>3</sub> crystals	
	4.3.5 Mechanophotonic studies	
	4.3.5.1 Preparation of microcrystals	
	4.3.5.2 Optical waveguiding studies of microcrystals	
	4.3.6 Fabrication of organic photonic component (PC-1)	
	4.3.7 Micromechanical fabrication of organic WDM	
	4.3.8 Optical functioning of organic WDM	
4.4	Summary	98
Chapter-5	A Pick-and-Place Technology Enabled,	99-119
_	Mechanically Programmable, Spiral	
	Optical Waveguides Integrated Hybrid	
	Circuits from Four Extremely Pseudo-	

<b>Plastic</b>	<b>Organic</b>	<b>Crystals</b>	for	Visible
Spectral	<b>Band Tur</b>	nability		

5.1	Abstract	100
5.2	Introduction	100
5.3	Results and discussion	103
	5.3.1 Synthesis of Cz-2CF <sub>3</sub>	
	5.3.2 Synthesis of BTD	
	5.3.3 Optical characteristics of Cz-2CF <sub>3</sub> , BPyIN, DBA,	
	and BTD	
	5.3.4 Single crystal X-Ray analysis and nanoindentation	
	studies of Cz-2CF <sub>3</sub>	
	5.3.5 Preparation of microcrystals	
	5.3.6 Fabrication of strained spiral crystal architectures	
	5.3.7 Fabrication of spiral waveguide-based	
	reconfigurable OPICs	
5.4	Summary	119
Chapter-6	<b>Conclusions and Future Scope</b>	120
	6.1 Conclusion	120
	6.2 Future scope	122
	References	124
	Appendix A (Methods)	132
	Appendix B (Instrumentation)	133
	Research publications and presentations	138
	Curriculum vitae	142

#### **DECLARATION**

I hereby declare that the matter embodied in the thesis entitled "Mechanophotonics: Pseudo-Plastic Organic Crystal-based Photonic Components and Circuits" is the result of investigations carried out by me in the School of Chemistry, University of Hyderabad, Hyderabad, India, under the supervision of Prof. Rajadurai Chandrasekar.

In keeping with the general practice of reporting scientific observations, due acknowledgments have been made on the basis of the findings of other investigators. Any omission that might have occurred by oversight or error is regretted. This research work is free from Plagiarism. I hereby agree that my thesis can be deposited in Shodhganga/INFLIBNET. A report on plagiarism statistics from the University Librarian is enclosed.

**Avulu Vinod Kumar** 

PC-V.M

(17CHPH44)



This is to certify that the thesis entitled "Mechanophotonics: Pseudo-Plastic Organic Crystal-based Photonic Components and Circuits" submitted by Avulu Vinod Kumar bearing registration number 17CHPH44 in partial fulfillment of the requirements for the award of Doctor of Philosophy in the School of Chemistry is a bonafide work carried out by him under my supervision and guidance.

This thesis is free from plagiarism and has not been submitted previously in part or in full to this or any other University or Institution for the award of any degree or diploma.

#### Parts of the thesis have been published in the following publications:

- A. V. Kumar and R. Chandrasekar. Adv. Opt. Mater. 2023, 11, 2201009.
- A. V. Kumar and R. Chandrasekar. J. Mater. Chem. C 2023, 11, 7995.
- 3. A. V. Kumar, M. Godumala, J. Ravi and R. Chandrasekar. Angew. Chem. Int. Ed. 2022, 61, e202212382.
- A. V. Kumar, M. Godumala, J. Ravi and R. Chandrasekar. Adv. Opt. Mater. 2023, DOI: 10.1002/adom.202302807.

#### B. Presented in the following conferences:

- 1. Poster presentation, ICOBIN-2023, at IIT-Roorkee, Roorkee, India. (Best poster award)
- 2. Oral presentation, Rasayanam Research Award-2023, Dr. K. V. Rao Scientific Society, Hyderabad. (Winner of Rasayanam Research Award)
- 3. Poster presentation, CHEMFEST-2023 at SoC, UoH, Hyderabad, India. (Best poster award)
- 4. Poster presentation, BSCI MEETING-2022 at Banaras Hindu University, Varanasi. (National conference, Best poster award)
- 5. Oral presentation, CHEMFEST-2022 at SoC, UoH, Hyderabad, India. (Best Question and Answer award)

Further the student has passed the following courses towards fulfilment of course work requirement for Ph.D.

Course. No	Title	Credits	Grade
CY801	Research Proposal	4	B+
CY802	Chemical Pedagogy	4	B+
CY805	Instrumental Methods A	4	В
CY806	Instrumental Methods B	4	В

Rajadurai Chandrasekar

(Thesis Supervisor)

Dr. R. CHANDIVASEKAR Professor School of Chemistry University of Hydershad Hyderabad-500046, India

29. Dec. 200

School of Chemistry

Dean SCHOOL OF CHEMISTRY UNIVERSITY OF HYDERARAD HYDERABAD-500 046

II

in Mengie

#### **ACKNOWLEDGEMENTS**

This thesis embodies the results of the last few years' work whereby I have been accompanied and supported by many people. It is an honour and a very pleasant opportunity to express my gratitude to all of them.

First of all, I would like to thank my teachers at every level from the school to university, without them I would not have reached this position. I invariably fall short of words to express my heartfelt gratitude to my supervisor **Prof. Rajadurai Chandrasekar**. His unerring support, uncompromised patience, coherence of scientific thoughts, and insightful discussions along with great support and enthusiasm for research navigated me during the finest moments and the darkest hours of scholarly tenure.

I would like to express my sincere thanks to my doctoral committee members, Prof. K. Muralidharan and Prof. K. V. Jovan Jose for their timely support.

Words are inadequate to express my heartiest obligation to Dr. Evgeniy Mamonov, and Prof. Tatiana Murzina for their help in FTDT calculations, Dr. Rajulapati V. Koteshwarrao for the nanoindentation studies. I would like to thank several other collaborations from the groups of Prof. Panče Naumov, Prof. Satoshi Takamizawa, Prof. Chilla Malla Reddy, Dr. Soumyajith Ghosh, Dr. Sivakumar Vaidyanath, Prof. Pradipta Purkayasta, Dr. Manas. K. Panda, and Prof. Pilar Prieto.

I wish to express my deep sense of indebtedness to Prof. Ashwini Nangia, Dean, School of Chemistry, and former Deans of the School of Chemistry.

I wish to express my deep sense of appreciation to the technical staff operating NMR, Single crystal X-ray Diffraction, PXRD, TEM, FTIR, HRMS, and FESEM facilities of the school, especially SC-XRD and FESEM operators Mr. Mahesh and Mr. Sunil, respectively, for their timely help whenever required. I express my heartfelt thanks to my friend, Ms. Govu Radha, for helping me with photoluminescence quantum yield studies.

With utmost sincerity, I thank my seniors Dr. Naisa Chandrasekhar, Dr. Supratim Basak, Dr. Dasari Venkatakrishnarao, Dr. Uppara Venkataramudu, Dr. Vattikunta Radhika, Dr. Jada Ravi and my batchmate Dr. Vuppu Vinay Pradeep and my juniors Mr. Rohullah, Mr. Melchi, Mr. Ankur Khapre, Ms. Sindhuja, Ms. Vinaya and Kapil for their generous help, critical suggestions and able guidance and creating a cordial environment during my stay in Lab. I would like to remember the fruitful discussions and suggestions embraced by senior post-doctoral fellows Dr. Mari Annadhasan and Dr. Mallesham Godumala. Their assistance during the tenure of my work is gratefully acknowledged. I also like to thank Dr. Biswajit Barman for his help during the thesis.

My special thanks to my friends: Navaneetha, Hemanth, Ravindar, Sashikanth, Sneha Banerjee, Hema, Sumantha Pal, Ali, and Vamsi. Seniors: Dr. Anil, Dr. Suryanayana Allu, Dr. Vikranth, Bala Raju, Dr. Tanmay, Dr. Subham Dutta, Dr. Sugato, Dr. Chandrahas, Dr. Sateesh Pon, Dr. Ashok, Dr. Ranguprasad. Juniors: Ranadeep, Santhosh, Ramanaidu, Debu Jana, Sandeep, Arun, Sneha, Koneti Kondalrao, Dheeraj, Praveen Yash, Manohar for their camaraderie, constant support and helping me whenever necessary. I would like to remember my childhood friends Devendar, Sai Kumar, T Vinod, Pantham Shiva, Ch Vikky and others for their constant encouragement.

A special mention about my college seniors Mahender Anna, Pavan, Naresh Chary, Krishna Akka, Laxmi Narayana, Srinivas, Y. Rakesh, Sudheer, Subani, Bhavani, Golla Mahesh, and many others is necessary.

My sincere gratitude to the teams', **TAB** (*The Almighty Brigade*), Two Hundred not out (200\*), Super Strikers, CrickGuns, and Run for Beer, for constantly shaping me into a better person not only in terms of gentlemen's game but for the overall development as well.

I will not be sincere in my acknowledgments if I do not extend them to my relatives. Firstly, I would like to remember my grandmother Late Ch. Lakshmamma who kept full faith in my abilities and encouraged me unconditionally since my childhood. I would like to thank my other relatives Ch. Venkatesh (uncle), Ch. Kalavathi (aunt), cousins: Ch Sai, Rajeshwari, Mounika, Parvathal, Ch. Praveen, Bala Shankar, Naveen, Bharath, Bhikshapathi, Manjula, Naresh, and Madhuri for their love and appreciation.

I have no words to express my heartfelt gratitude and respect towards my mother Anuradha and father Devender for their blessings, and their endless love for teaching me the essence of education and integrity.

I heartily thank my beloved brothers Bhanu Prakash and Divakar whose unconditional love and affection have always been my strength.

Finally, I would like to thank my wife Mrs. Maheshwari for her constant support in all the ups and downs in my life since our marriage. If it was not for my daughter, Dhaksha, this immense burden and pressure would have consumed me long back.

I gratefully acknowledge SERB, UoH-IoE, and HEFA for providing me partial financial support during my Ph. D tenure and the School of Chemistry, University of Hyderabad for providing instrumental facilities and a peaceful environment to accomplish my Ph. D. degree.

**Avulu Vinod Kumar** 

University of Hyderabad.

# LIST OF ACRONYMS

ASW	Archimedean spiral waveguide
aMZI	asymmetric Mach Zehnder interferometer
AFM	atomic force microscopy
СВ	conduction band
CSSI	crystal surface and substrate's adhesive interactions
DC	directional coupler
EBL	electron beam lithography
EP	exciton-polariton
FP	Fabry-Pérot resonator
FLM	fiber loop mirror
FESEM	field emission scanning electron microscopy
FDTD	finite difference time domain numerical calculation
FL	fluorescence
FIB	focused ion beam
FTIR	fourier transform infrared spectroscopy
FSR	free spectral range
FWHM	full width half maxima
HRMS	high-resolution mass spectrometry
HDC	hybrid directional coupler
IM	interferometer
LiFi	light fidelity
MFOC	mechanically flexible organic crystal
μ-SAs	micro-spiral architectures
NIR	near infrared
NLO	nonlinear optics
RR	ring resonators
NMR	nuclear magnetic resonance
BW	optical bandwidth
OPIC	organic photonic integrated circuit
OSW	organic spiral waveguide
PR	phosphorescence

PLQY	photoluminescence quantum yield
PIC	photonic integrated circuit
PSW	polygonal spiral waveguide
rSC	reconfigured spiral circuit
SAED	selected area electron diffraction
SOI	silica-on-insulator
SC	spiral circuit
SW	spiral waveguide
TADF	thermally activated delayed fluorescence
TLC	thin layer chromatography
TIR	total internal reflection
TEM	transmission electron microscopy
VB	valance band
VLC	visible light communication
WDM	wavelength division multiplexer
WGM	whispering gallery mode

# LIST OF SYMBOLS

A	acceptor
θ	angle
ω	angular frequency
$E_g$	band gap energy
R <sub>c</sub>	bending radius
a	cavity's size
$R_s$	centre point of two spiral branches
e	charge of an electron
d	decay depth
$\varepsilon_r$	dielectric constant
Z	distance from normal
D	donor
n <sub>eff</sub>	effective refractive index
Е	energy
ET	energy transfer
$E_B$	exciton binding energy
$a_B$	exciton Bohr radius
Itip	FL intensity at the collection point
Ibody	FL intensity at the excitation point
f	frequency of light
$\Delta f$	full width at half maxima
G	gap
h	height
n''	imaginary part of refractive index
$P_{in}$	input laser power
q	integer corresponding to angular momentum of photon
m	integer number
L	length
$m_e$	mass of electron
$\lambda_{\mathrm{m}}$	maximum wavelength of resonant mode
α	optical loss

L	optical path length
$\varepsilon_{o}$	permittivity of free space
$P_{out}$	power at the end of waveguide
Q	quality factor
r	radial coordinate
n'	real part of refractive index
$\hbar$	reduced Plank constant
n	refractive index
$\mu_r$	relative permeability
$f_o$	resonant frequency
$S_w$	separation distance
Cm	speed of light in material
ε	strain
σ	stress
Т	transmitted wave
k	wave number
λ	wavelength
W	width

An Introduction to Inorganic and Organic Materials-based Photonic Components and Circuits

#### 1.1 Photonic integrated circuits (PICs)

The globe has witnessed tremendous exploration and exploitation of diverse properties of electron-based technologies in the 20<sup>th</sup> century. A deeper understanding of the properties of electrons and their utility for diverse applications ranging from molecular characterizations to bio-medical applications comprehend the progress made so far.<sup>1</sup> The overwhelming success of electronic circuits for data transfer, processing, and communication technologies will be questioned in the post-Moore era where doubling the number of transistors on a chip every year is no longer possible.<sup>2,3</sup> Electronic circuits become inefficient in dealing with ever-increasing data traffic due to energy wastage on data conversion from electrical to optical regimes. The bosonic photons, which are lighter and faster than electrons with multiple quantum states are potential alternatives to electron-based communication technologies.<sup>4</sup> Therefore, the 21<sup>st</sup> century will be dominated by fascinating revelations of the bosonic photons and related technologies in the areas of quantum computing,<sup>5-7</sup> optical cloaking,<sup>8,9</sup> time crystals,<sup>10,11</sup> and data transfer technologies<sup>12</sup> through the development of advanced photonic circuits.

A PIC is an advanced system-on-a-chip incorporating two or more functional photonic components to perform complex optical functions (Figure 1.1a). <sup>13,14</sup> PICs manipulate optical signals like the way electronic circuits process electrical signals and are effective for data processing and transfer technologies. Recently, Si-based PICs have been extensively studied for space applications; a PIC manufactured by 'effect photonics' is used as 100 Gb/s data transceivers by the National Aeronautics and Space Administration (Figure 1.1b). <sup>15</sup> Apart from data communication technologies, PICs have been considered for applications in various fields from chemical and biological sensing, <sup>16</sup> spectrometers, <sup>17</sup> LIDAR applications, <sup>18</sup> and data processing technologies <sup>19</sup> to advanced quantum computing technologies <sup>5-7</sup> (Figure 1.2). The advantages like high-speed data transmission, compact packing on a chip, the opportunity for miniaturization, and complementary metal oxide

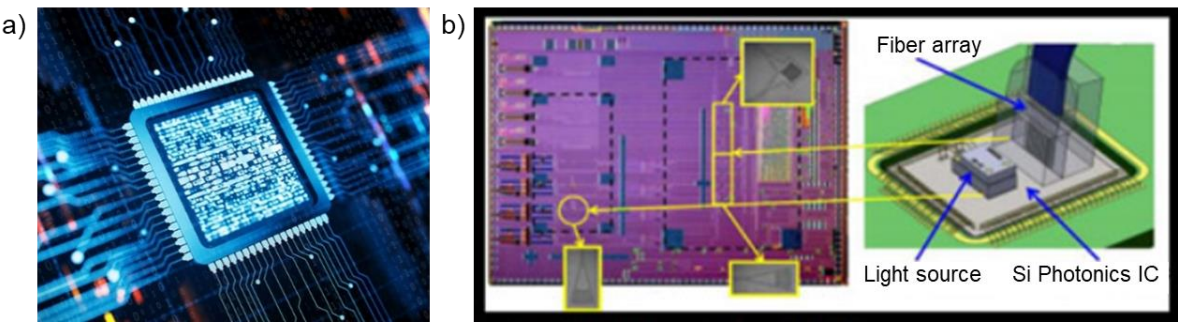


**Figure 1.1.** a) Graphics illustrating the photonic integrated circuit (PIC). b) Silicon PIC 100 Gb/s transceiver manufactured by 'Effect photonics'. Figure adapted from ref. 13 and 15.

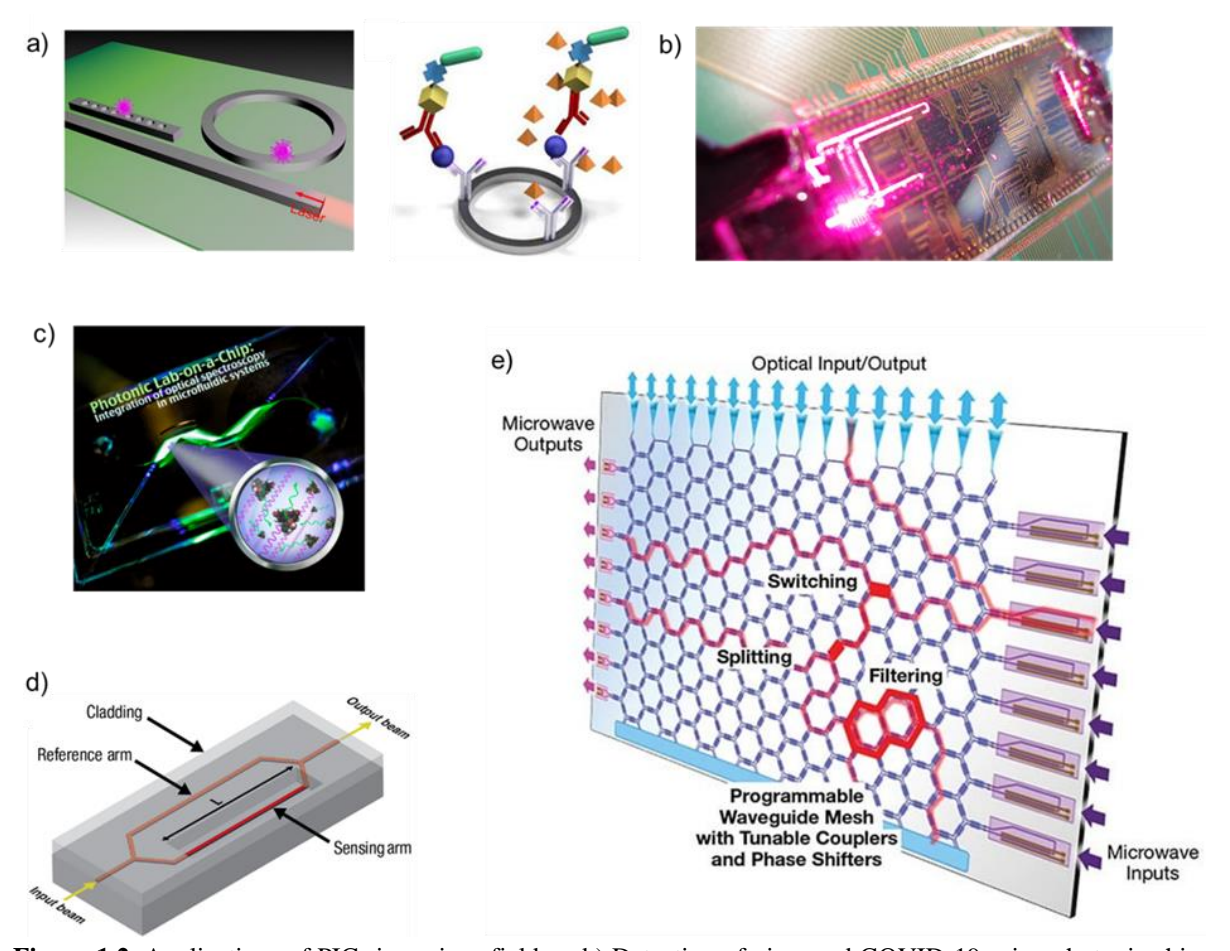


**Figure 1.2.** Applications of PICs in various fields. a,b) Detection of virus and COVID-19 using photonic chips, respectively. c) Optical spectroscopy based-on photonic lab-on-a-chip. d) Interferometric chips for biochemical sensing. e) Programmable photonic circuits. Figures adapted from ref. 5, 16-19.

semiconductors (CMOS) process-compatibility enabled rapid use of PICs for quick detection of SARS-COVID viruses during the COVID-19 oandemic.<sup>20,21</sup>

Typically, the most desired materials for constructing photonic circuits are CMOS-compatible materials like silicon/silica-on-insulator (SOI), silicon nitride (Si<sub>3</sub>N<sub>4</sub>), and indium phosphide (InP) materials.<sup>22,23</sup> These materials, being compatible with the electron beam lithography (EBL) technique, can be easily crafted into desired shapes and geometries with precise dimensional control in x, y, and z directions.<sup>4,14</sup> The well-established complementary metal oxide semiconductor fabrication process employed for manufacturing electronic integrated circuits on a silicon wafer enables the mass production of highly reproducible Sibased structures needed for photonics at lower cost.<sup>4,24-26</sup> However, the issues pertaining to classical optics like interconnects and optical alignment of individual components along with the limited mechanical flexibility and optical transparency in visible regions impede the Si-PICs' progress.<sup>27-29</sup> Therefore, more research into alternative photonics materials platforms is customary for the steadfast progress of PICs.

#### 1.2 Nature of light

Light is an electromagnetic wave comprising an oscillating electric field and magnetic field perpendicular to its propagation direction (Figure 1.3a). It exhibits wave-particle duality. Generally, a photon is defined as the 'quantum of light' and is the energy packet composed of electromagnetic radiation (Figure 1.3b).<sup>30</sup> The energy of a photon can be calculated by  $E = \frac{hc}{\lambda}$ , where h is referred to as Plank's constant, c is the light's speed in vacuum, and  $\lambda$  is the photon's wavelength. Further, Maxwell demonstrated that the photon's properties exclusively depend on the matter with which they interact. Hence, the properties of the photons rely heavily on the  $\lambda$  or frequency (f) of the light and the medium in which they are travelling (Figure 1.3b).<sup>30</sup> The refractive index  $(n)^*$  of a material is given by the following equation,

$$n = \frac{c}{c_m} \tag{1}$$

where  $c_m$  is the speed of light in the medium.

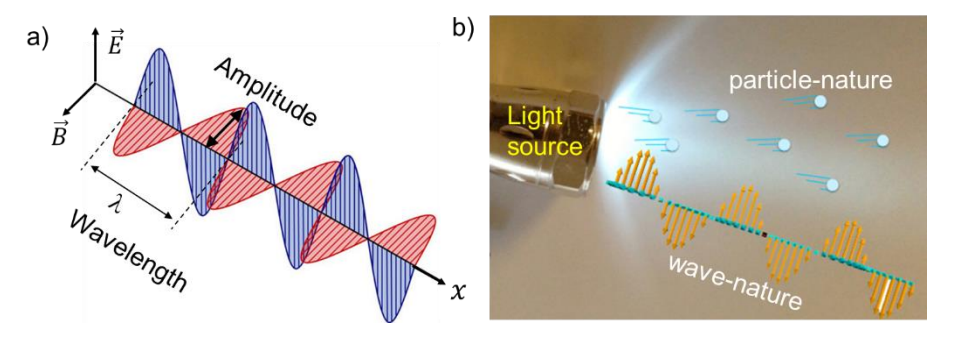


**Figure 1.3.** a) Graphical illustration of wave-particle duality of photons from a light source (torch). b) Wave-description of photons as electromagnetic radiation, where electric field and magnetic field components are mutually perpendicular to each other and the wave propagation direction. Figure adapted from ref. 30.

#### 1.2.1 Light-matter interaction

Light-matter interaction is fundamental to the advancement of science as it is customary to see objects, and characterize molecules or materials when photons interact with matter (Figure 1.4). Most of the materials are semiconductors (inorganic materials like Si, Ge, etc., or small organic molecules) and the band gap energy ( $E_g$ ) is the smallest amount of energy necessary to promote an electron to the conduction band (CB) from valance band

<sup>\*</sup>Refractive index (n) of a material is related to its dielectric constant  $(\varepsilon_r)$  by the equation

 $n = \sqrt{\varepsilon_r \mu_r}$  where  $\mu_r$  = relative permeability and typically,  $\mu_r \approx 1$ , for nonmagnetic materials,

Hence,  $n = \sqrt{\varepsilon_r}$ . Since  $\varepsilon_r$  is represented by a complex expression with both imaginary and real parts,  $\varepsilon_r = \varepsilon'_r + i\varepsilon''_r$  and hence the value of n is also a complex quantity,  $\varepsilon_r = n^2 = (n' + in'')^2$ .

Further, Cauchy's equation describes frequency dependence of refractive index as follows

 $n(\lambda) = A + \frac{B}{\lambda^2}$  where coefficients A and B are specific constants for  $\lambda$ , quoted as vacuum wavelength in micrometres.

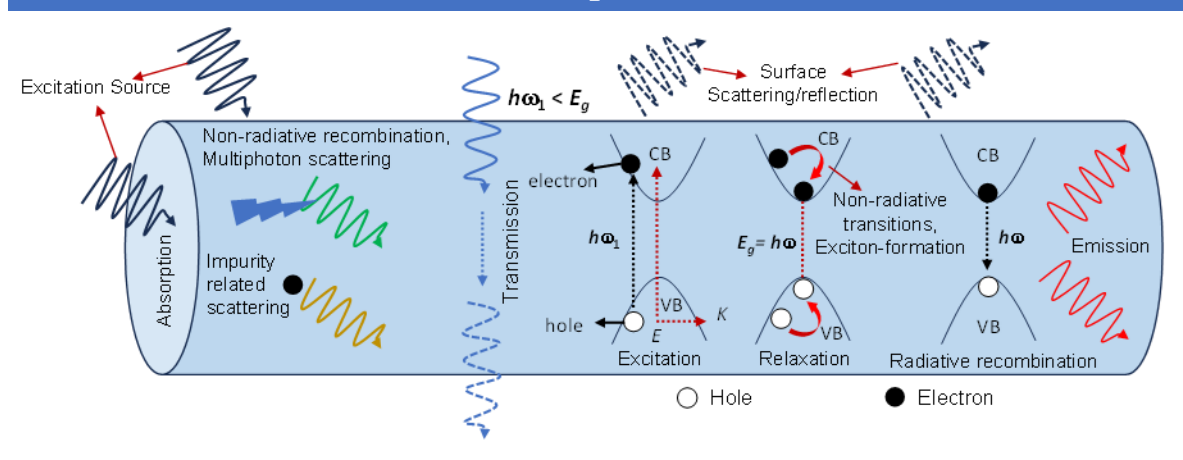


**Figure 1.4.** Schematic illustration of various possible phenomena as light interacts with matter. Figure adapted from ref. 32.

(VB). Usually, for semiconductor materials  $E_g$  lies below 4 eV. An electron may be promoted to the CB by offering energy (greater than  $E_g$ ) in the form of heat, light or other forms of energy, creating a hole in the VB. The electron (negatively charged) in CB and hole (positively charged) in VB act as charge carriers, and the electrostatically bound 'electron-hole pair,' when in its lowest energy state, is called an 'exciton.' When an exciton binds with a photon, it produces a quasi-particle called 'exciton-polariton' (EP).<sup>33</sup> It may be noted that exciton has slightly less energy than unbound electron-hole. The electron can relax back to VB through radiative (fluorescence, FL: no spin inversion; or phosphorescence, PR: spin inversion) or non-radiative (vibrionic or thermal relaxation) pathways.

The concept of interest is how an incident photon interacts with inorganic or organic materials (radiatively or non-radiatively). The excitons can be classified into Frenkel excitons and Wannier-Mott excitons. Typically, organic materials with strong exciton binding energy  $(E_B)$ , of the order of  $\approx 0.1-1$  eV leads to Frenkel excitons whereas inorganic materials (like Si) with low  $E_B$  (0.01 eV) exhibits Wannier-Mott excitons (Figure 1.5a,b).

Most of the commercial PICs employ Si or related material and operate via Wannier-Mott excitons.<sup>34</sup> The solid-state optical and mechanical characteristics of such materials are significantly influenced by the molecular arrangement and the ratio of Si to N in the case of

$$E_B = \frac{e^2}{2\varepsilon_m a_B}$$

where e is the charge of the electron,  $\varepsilon_r$  is connected n of the material and  $a_B$  is the exciton Bohr radius which is described by

$$a_B = \frac{4\pi\varepsilon_0\hbar^2}{m e^2}$$

where  $\hbar$  is the reduced plank's constant,  $\varepsilon_0$  is the free space's permittivity, m is the mass of the electron.

<sup>&</sup>lt;sup>†</sup> Exciton binding energy  $(E_B)$ , and it is associated with the exciton Bohr radius,  $a_B$  can be given as:

silicon nitride (Si<sub>3</sub>N<sub>4</sub>, Figure 1.6a,b).<sup>23,28</sup> Other important material attributes like n, thermo-optic(TO) coefficient, and mechanical properties are listed in Table 1.1.<sup>35-37</sup> The n of a material is strongly dependent on the frequency of the light (discussed earlier in section 1.2) and the n (at 632.8 nm) of Si, SiO<sub>2</sub>, Si<sub>3</sub>N<sub>4</sub>, InP, and organic materials is 3.46, 1.44,

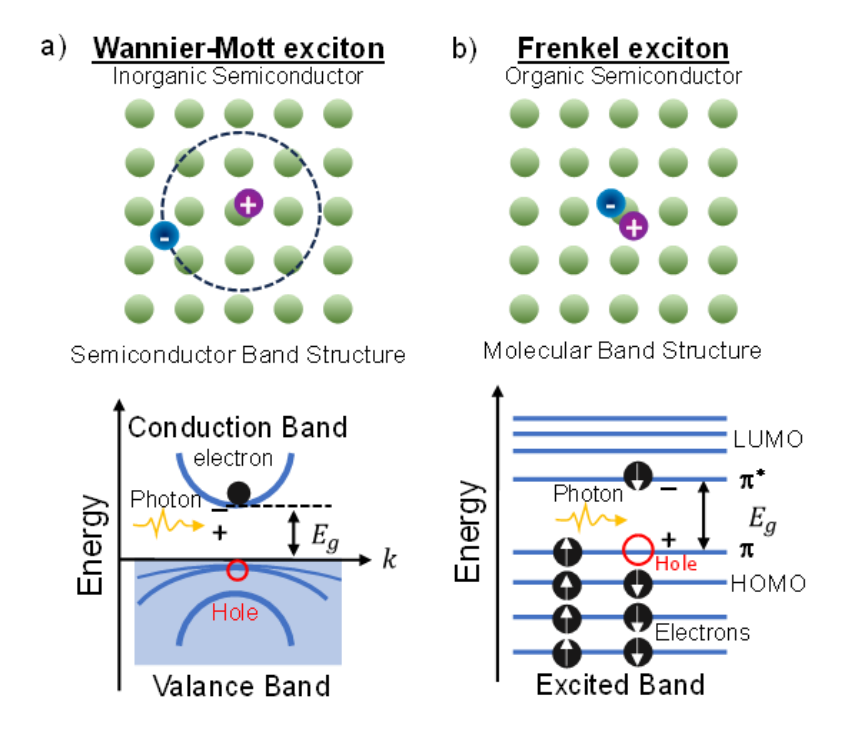


**Figure 1.5.** Graphical representation of a) band structure in inorganic semiconductors responsible for Wannier-Mott excitons and b) HOMO-LUMO gap in organic molecules responsible for Frenkel excitons.

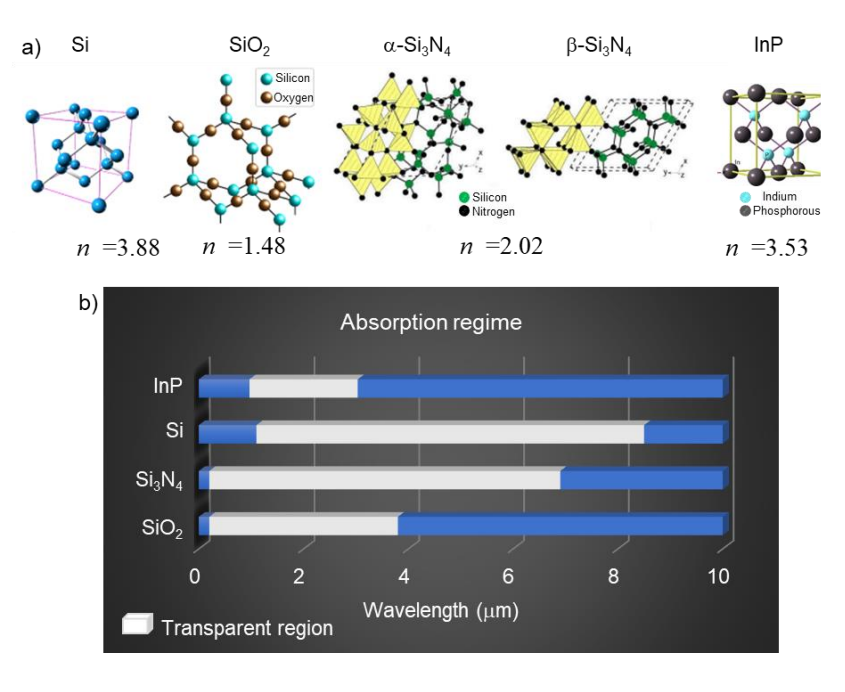


**Figure 1.6.** a) Crystal structures of silicon (Si), silica (SiO<sub>2</sub>), silicon nitride ( $\alpha$  and  $\beta$  forms) and indium phosphide (InP). The refractive index (n) of materials at 632.8 nm are shown below them. b) The absorption properties of different materials. The white portion represents an optically transparent region while the blue band corresponds to absorption loss. Figure adapted from ref. 22-26.

Material	Refractive index (n) at 632.8 nm	TO coefficient (K <sup>-1</sup> ) at 300 K	Hardness ( <i>H</i> ) GPa	Youngs Modulus ( <i>E</i> ) GPa
Silicon (Si)	3.46	1.86 x 10 <sup>-4</sup>	12.5	185
Silica (SiO <sub>2</sub> )	1.44	0.95 x 10 <sup>-5</sup>	9.5	72.8
Silicon nitride (Si <sub>3</sub> N <sub>4</sub> )	≈2	2.45 x 10 <sup>-5</sup>	50.3	≈400
InP	3.53	2.77 x 10 <sup>-5</sup>	7.5	108
Organic materials	≈1.7	1.0 x 10 <sup>-4</sup>	<0.15-0.72	<4-16

**Table 1.1.** Various physical characteristics of silicon, silica, silicon nitride, indium phosphide, and organic materials.

≈2, 3.53, and ≈1.7, respectively. Initially, Si, being a passive transmitter of light with high n became a profoundly used material for PICs. However, as more research paced into PICs, Sibased PICs proved to be costlier compared to InP PICs, while hybrid InP structures on silicon wafers turned out to be a fruitful endeavor in terms of optimal performance and cost-effective fabrication method. The contact hardness (H) and Young's modulus (E) of Si<sub>3</sub>N<sub>4</sub> are greater than silicon and InP (Table 1.1). Compared to Si, SiO<sub>2</sub> has low absorption in visible to NIR region and is employed for mid-IR passive integrated devices. The widely used technique for preparing Si<sub>3</sub>N<sub>4</sub> is by low-pressure chemical vapor deposition technique and the Si to N ratio dictates the material's n and TO properties. The absorption region of Si<sub>3</sub>N<sub>4</sub> is broad and ranges from 2.7 to 5 eV depending on the ratio of Si and N. Hence, these materials cannot be implemented for shorter wavelength applications. Mostly, Si<sub>3</sub>N<sub>4</sub> waveguides are useful for generating frequency combs and supercontinuum.

On the other hand, PICs operating via the Frenkel excitons are scarcely reported due to limited technological facilities. Typically, organic materials exhibit stable Frenkel excitons with a relatively high  $E_B$  (0.1 - 1 eV) compared to inorganic materials, because of the smaller exciton Bohr radius in the earlier, and are advantageous for constructing effective photonic circuit. In 2015, Zhang *et al.* reported solution printing based on organic printed circuits. However, the effects of mechanical bending on individual photonic components were not clear. These polymer-based printed circuits lack the frequency doubling characteristics essential for non-linear photonics technologies.

#### 1.3 Principles of light propagation in materials

The tremendous characteristics (smaller mass and greater speed) of photons outsmart the well-explored electrons for circuit applications. But these photons must be channeled into

specific paths like how electrons are propelled or passed through the wires. To accomplish the same with photons requires materials that can transduce light through them. Such optical components are called optical waveguides, and they transduce or transmit incident photons from one terminal to another.<sup>44-48</sup> The phenomenon of optical waveguiding occurs via the fundamental total internal reflection (TIR) of incident light as photons move from a denser medium to a rarer medium.

According to Snell's law, as incident light moves from a medium of low n ( $n_1 \approx 1$ ) to a higher index medium ( $n_2 > 1$ ), at the boundary, a fraction of the beam is reflected from the medium having low n and the residual portion will be refracted into the medium having high n (Figure 1.7a). The reflected beam angle ( $\theta_1$ ) is equal to the incident beam angle. Most of the light is refracted, and the angle of the incident beam ( $\theta_1$ ) is higher than the angle of the refracted beam ( $\theta_2$ ) at  $n_2 > 1$ . As the light propagates from a medium of higher n to lower n, the light bends away from the normal, abiding the Snell's law (Figure 1.7b). When the angle of incidence is greater than the critical angle ( $\theta_c$ ), then light reverts to the higher refractive index medium ( $n_2 > 1$ ). In this state, the light undergoes TIR within the high-refractive index medium. The TIR is responsible for producing an electromagnetic wave (evanescent wave) on the lower refractive medium side at the normal (Figure 1.7c). The evanescent wave is of

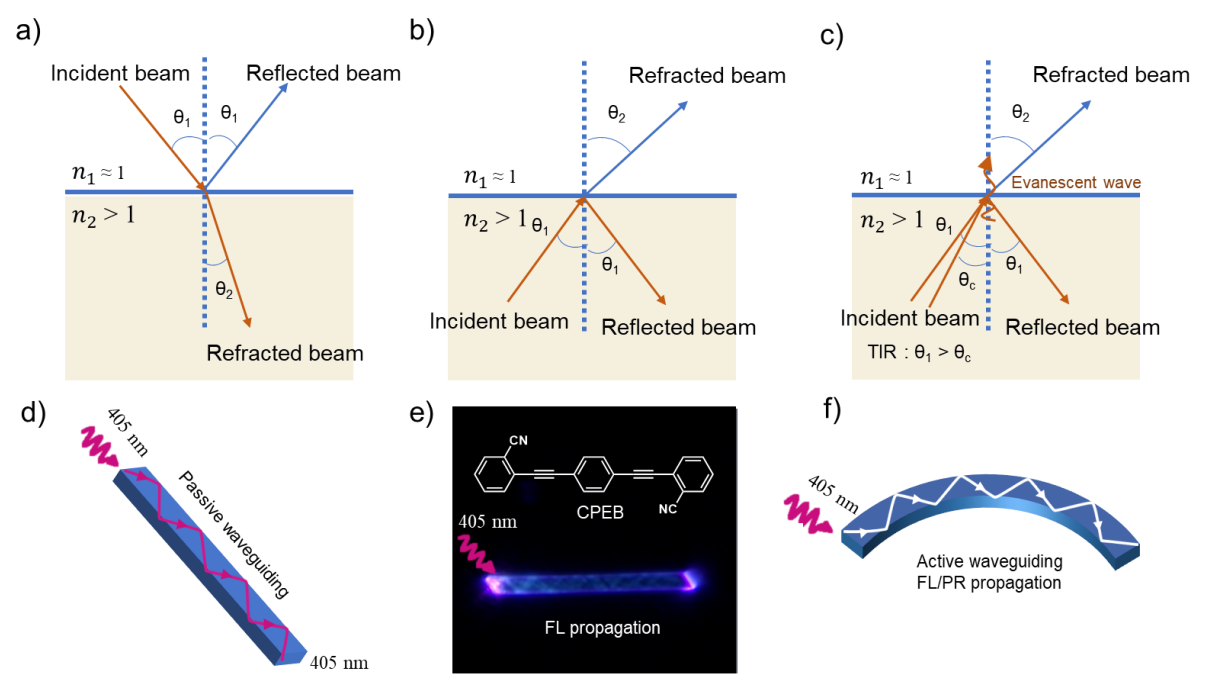


**Figure 1.7.** Light propagation across different n media according to Snell's law when a) light moves from low n to high n, b) high n to low n, and c) total internal reflection condition giving rise to evanescent wave. d) Schematic illustration of passive waveguiding in an optical waveguide. e) Active waveguiding of FL produced in the 1,4-bis(2-cyanophenylethynyl)benzene (CPEB) crystal when illuminated with 405 nm light. f) Schematic illustration of active waveguiding in a bent waveguide. Figure adopted from ref. 49.

the same wavelength as the incident light, but the intensity decreases exponentially as a function of orthogonal propagation distance from the normal as described by eq. 2,<sup>50</sup>

$$I = I_0 e^{-z/d} \tag{2}$$

 $I_0$  is the intensity of incident light, z is the distance from normal, d is the characteristic exponential decay depth.

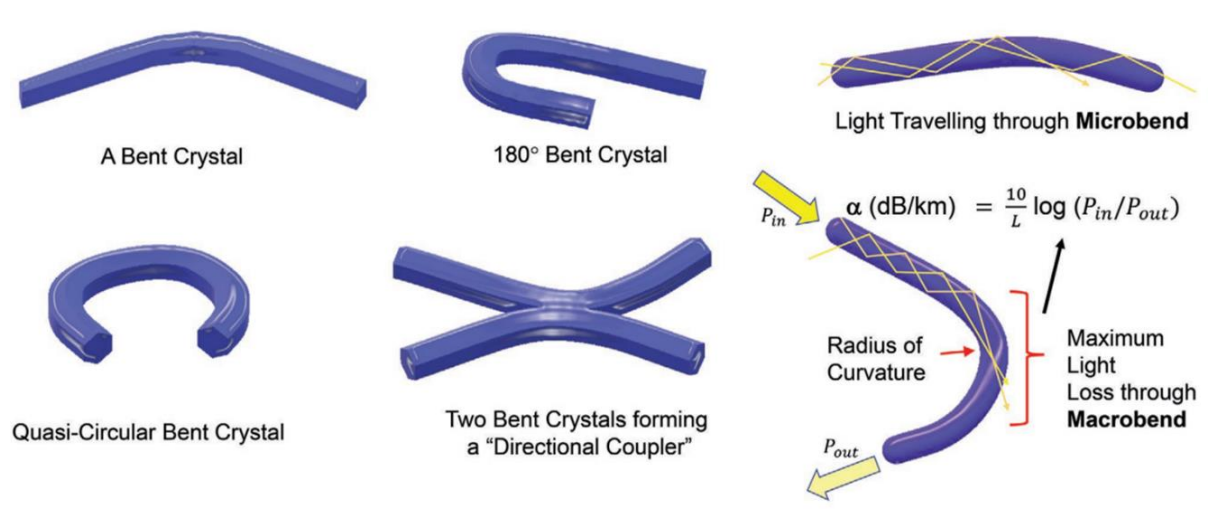
The evanescent field generated through the optical fiber is useful to induce optical coupling between two waveguides, fiber tapping, excite optical cavities, optical splitters production, and wireless photonic devices. <sup>44</sup> Moreover, EP generation enhances the n of the medium, supporting effective coupling, propagation, and more light confinement. <sup>33</sup>

Optical waveguides are classified into two types, passive and active waveguides. A passive waveguide transports the unaltered incident electromagnetic radiation to the other end of the waveguide. Typically, Si or Si-based materials act as passive-only light transporters due to the small  $E_B$  (Figure 1.7d). This property of silicon was vastly exploited for various applications including photonic integrated circuitry. 51-54 However, passive waveguiding organic crystals are scarcely reported. In 2013, Chandrasekar *et al.* reported the first flexible passive organic crystal waveguides using 4,4-bis(2,6-di(1H-pyrazol-1-yl)pyridin-4-yl)-biphenyl (BPP) microtubular waveguides. 55 In contrast to the passive waveguide, an active waveguide propagates modified incident light (upconverted or down-converted signals) through to the other end of the waveguide. 44,45 This includes generated photoluminescence (FL or PR) at the excitation point or NLO waveguides that transport upconverted signals (Figure 1.7e,f). 56-64 In both cases, an incident photon  $h\nu$ , is modified to  $h\nu'$  to alter the frequency of the supplied electromagnetic radiation. Further, the incident radiation can be modified through electro-optical effects, acousto-optical effects or electro-absorption effects, with the easiest being electro-absorption. 30

#### 1.3.1 Optical losses in waveguides

As light transduces along the waveguide, some of it undergoes optical losses. The losses are mainly due to the scattering of light caused by the defects present in the waveguide or the tiny structural differences or material inhomogeneity. It is expected that organic optical waveguides possess smaller losses due to their crystalline nature and smooth surface morphology. Generally, every material is inherently associated with absorption loss which arises from the dispersion of a portion of propagating light into other forms like electrical, thermal, acoustic or electromagnetic radiation. The materials with large variations in band gaps are more susceptible to electromagnetic losses, as observed in semiconductors. The

absorption loss is minimal in a passive waveguide as it functions away from the molecules' absorption region. The radiation loss occurs when the effective n of that particular mode is less than the n of the clad. This is common in waveguides with curved geometries or bends where the phase-matching condition is violated and a portion of light leaks into the surrounding medium. Such losses are termed as bending losses (Scheme 1.1). To guide light through dedicated directions, these curves or bends are mandatory, and often, the loss is proportional to the size (micro or macro) of the waveguide. The decrease in bending radius



**Scheme 1.1.** Schematic illustration of various bent geometries of 1D optical waveguides and light propagation through them with micro- and macrobend. Figure adopted from ref. 59.

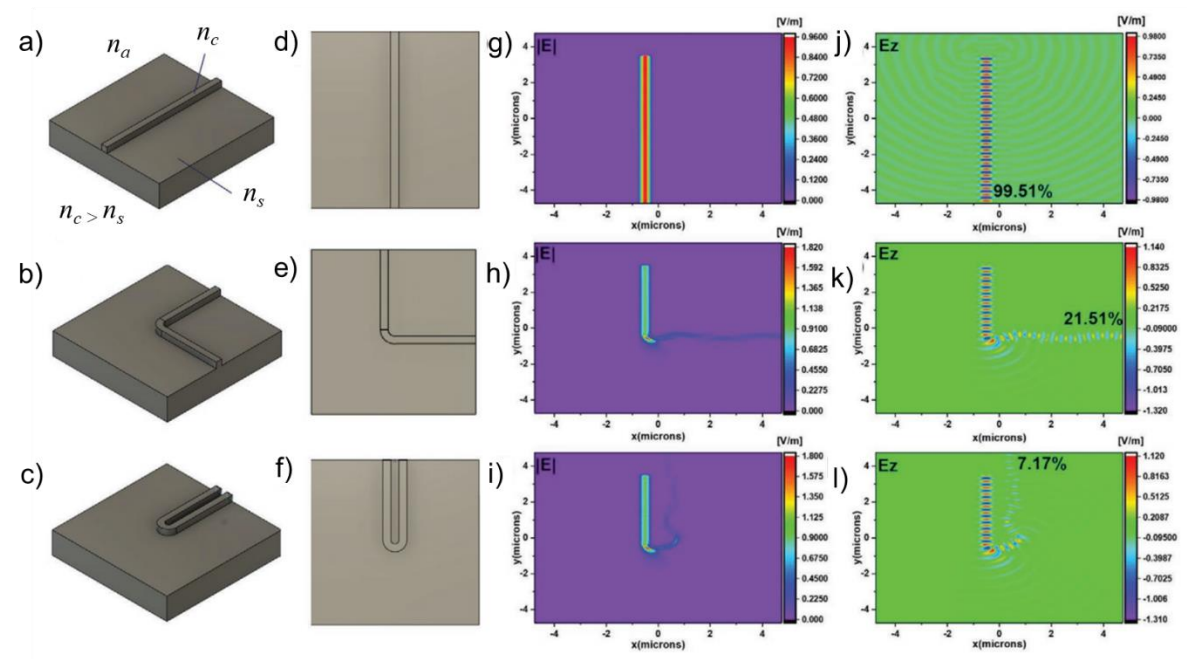


**Figure 1.8.** a–c) 3D and d–f) top view of straight, L- and U-shaped waveguides, respectively, used for the finite difference time domain analysis. g–i) Total electric field distribution of the waveguides through a longitudinal cross-section. j–l) Transverse electric field of the waveguides through a longitudinal cross-section. The transmission efficiencies of straight, L-shaped, and U-shaped waveguides are 99.51%, 21.51%, and 7.17%, respectively.  $n_c$  and  $n_s$  are refractive indices of organic crystal and substrate, respectively. Figure adopted from ref. 59.

results in increased bending-induced optical loss. The finite difference time domain (FDTD) calculation on organic waveguides suggests that the optical loss increases with an increase in the bending angle (Figure 1.8a-d).<sup>59</sup> It is predicted that the transmitted optical efficiency of the straight waveguide was 99.51%, while the waveguide bent over the right angle comprised of transmission efficiency of only 21.51% (Figure g,h,j,k). Further, as the bending angle increased to 180° in a U-shaped waveguide the transmission efficiency reduced to 7.17% only (Figure 1.8i,l). The FDTD calculations of waveguides with bending radius ( $R_c$ ) height (h), width, and [1:1:2, 1:1:1, 1:1:3, respectively] confirm the reduction in transmission efficiency with a decrease in bending radius or increase in bending angle due to more light seepage through the bent portion (Figure 1.9). Usually, under similar conditions (i.e., for a waveguide with the same thickness, clad, and substrate) the transmission efficiency depends on n, polarization, and excitation mode. In the passive waveguide optical signal is vulnerable to attenuation caused by bending-induced loss, photon absorption, and optical scattering phenomenon inside

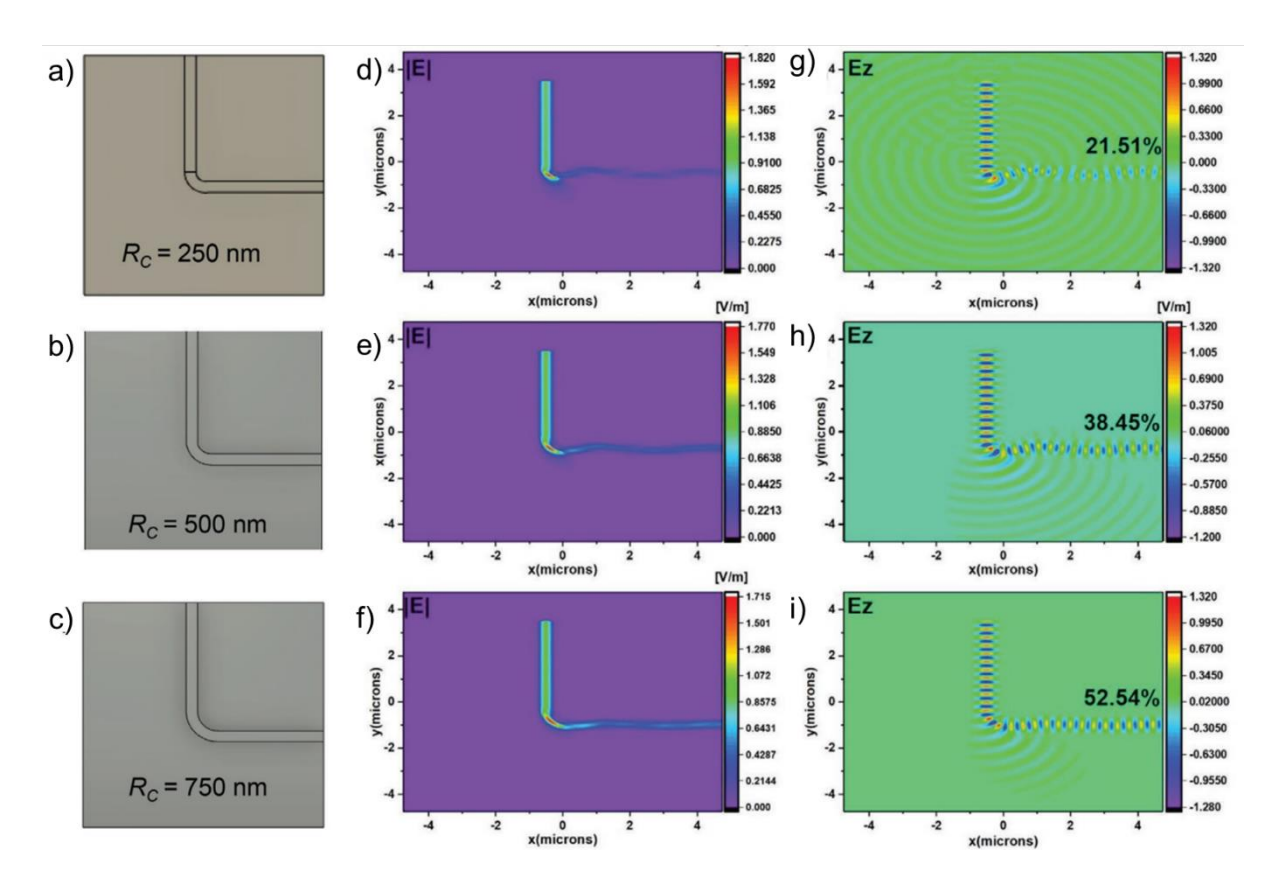


**Figure 1.9.** a–c) Top view of L-shaped waveguides with the Rc:h:d = 1:1:1; 2:1:1; 3:1:1, respectively, used for the FDTD analysis. d–f) Total electric field distribution of the waveguides through a longitudinal cross-section. g–i) Transverse electric field through a longitudinal cross-section for L-shaped waveguide. The transmission efficiencies of L-shaped waveguides with  $R_C$  = 250, 500, 750 are 21.51%, 38.45%, and 52.54%, respectively. Figure adopted from ref. 59.

the waveguide as light travels across them. The amount of power lost during the signal transduction in a waveguide of length (L) can be estimated using the attenuation coefficient or absorption coefficient  $(\alpha)$ ,

$$T = \frac{P_{out}}{P_{in}} = e^{-\alpha L} \tag{3}$$

where  $P_{out}$  and  $P_{in}$  correspond to the output and input laser power, respectively and L is the optical path length. The signal's transmission ratio is given by  $\frac{P_{out}}{P_{in}}$  which varies exponentially with the length of the waveguide. The same transmission efficiency can be calculated in decibel (dB) loss and is given by the following equation

$$\alpha \left(\frac{dB}{mm}\right) = \frac{10}{L} \log_{10} \frac{P_{out}}{P_{in}} \tag{4}$$

The term dB gives a relative power loss value rather than explicitly expressing the power value.

Typically, most organic waveguides perform optical waveguide properties via the active waveguiding mechanism, in which the input optical signal produces a photoluminescence (FL or PR). The generated photoluminescence is transported along the waveguide via 1D/2D optical confinement. The optical loss in such systems can be calculated by a modified equation where power is replaced with photoluminescence (FL/PR) intensity under the presumption that the supplied input energy is completely absorbed with no/minimal reabsorption.

$$I_{tip}/I_{body} = e^{-\alpha L} \tag{5}$$

where  $I_{tip}$  and  $I_{body}$  correspond to photoluminescence (FL/PR) intensities at collection and excitation positions on the waveguide. L is the optical path length traveled by the photons between excitation and collection positions.

Nevertheless, the surface roughness, thickness, and dimensions of the input and output terminals in organic waveguides (in most cases) are non-uniform and lead to differential optical scattering. The optical loss (FL/PR guided in active waveguides) cannot be quantitatively generalized for crystals of one compound, as the dimensions, surface morphology, and defects vary from crystal to crystal. However, a general statistical range of optical loss for a compound may be given depending on the pool size (number of crystals with different aspect ratios) of measurements. Nevertheless, in passive organic waveguides, optical loss primarily arises from the Raman scattering as a portion of input light is driven into molecular vibrations.

#### 1.4 Optical micro-resonators

Optical micro-resonators are crucial components in the field of optics and photonics because of their ability to trap light in a small volume through TIR. They are utilized for numerous applications in NLO, lasers, spectroscopy, sensors, and quantum information processing. In a micro-resonator, as the light bounces back and forth between the two reflective surfaces, an interference pattern is created, thereby effectively trapping the light within the optical cavity. The optical-reflective surfaces may be dielectric layers or mirrors, and the resonator could acquire different shapes, such as disk or spherical particles, ring resonators (RRs) square or rectangular waveguides, etc. 45

Significant progress is made in the field of optical micro-resonators in the past few decades. Advances in nanofabrication techniques have allowed for the creation of resonators with increasingly complex shapes and designs, leading to improvements in their sensitivity and quality factor. As Researchers are also exploring the use of new materials, such as 2D

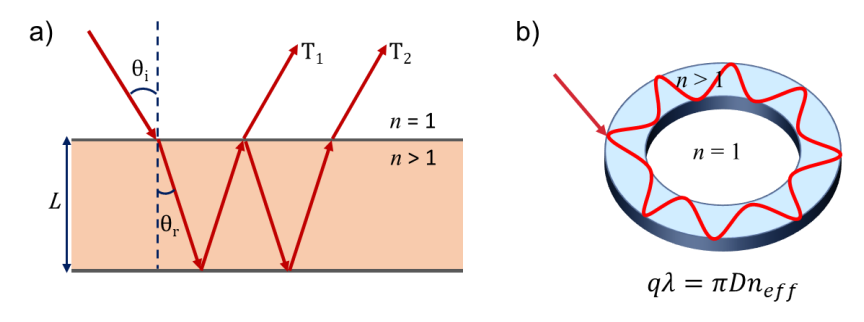


**Figure 1.10.** a) Fabry-Pérot and b) whispering gallery mode type micro-resonators. Symbols L,  $\theta_i$ ,  $\theta_r$ ,  $T_1$ ,  $T_2$ , q,  $\lambda$ , D,  $n_{eff}$  denotes the length of the resonator, incident angle, refracted angle, transmitted waves, , mode number, wavelength of the light, diameter of the resonator, and effective n, respectively.

materials and plasmonic architectures, to create novel micro-resonators with unique properties. There are several types of optical micro-resonators with various geometries. The most common types of optical micro-resonators include Fabry-Pérot (FP) and Whispering gallery mode (WGM) resonators (Figure 1.10). Therefore, a multi-wavelength spectrum (optical modes) can be generated by resonant recombination of the wideband FL light. In the WGM resonator, light that satisfies the resonance condition amplified through constructive interference, and others will be eliminated via destructive interference (for detailed discussion see section 1.4.2).

#### 1.4.1 FP resonators

Fabry-Pérot (FP) resonators are optical components comprising two parallel reflective surfaces kept at a distance from each other at an integral multiple of incident wavelength. The incident light is trapped between the two reflecting surfaces of the resonator (Figure 1.10a).

They were first created during the late  $19^{th}$  century and have been critical in developing high-quality optical spectrometers with improved resolution. A simple illustration of an FP resonator requires two parallelly placed partially transmitting mirrors separated apart by length, L (Figure 1.11). When successively reflected light beams acquire a path difference of 2L, the possibility of interference results from the multiple reflections of optical signals between the reflective surfaces. As a consequence, constructive and destructive interference can occur. Maximum constructive interference takes place when conditions presented in below equation are satisfied.

$$L = (2m+1)\frac{\lambda}{2};\tag{6}$$

where m is an integer and can take the values  $m = 0, 1, 2, 3, 4 \dots$ 

whereas destructive interference occurs for

$$L = m\lambda$$
;  $m = 0, 1, 2, 3, 4 ...$  (7)

FP resonators resemble the described FP cavities, where the emphasis is laid on characteristics of light stored between reflective mirror-like surfaces rather than transmitted

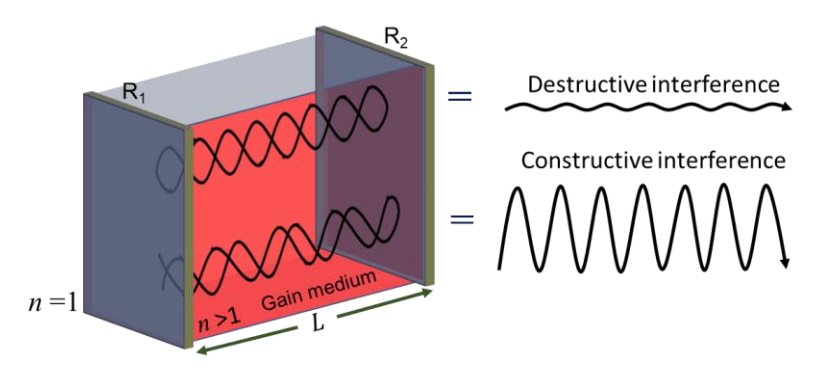


Figure 1.11. The graphical representation of FP resonator depicts the constructive and destructive interferences.

or reflected light's intensity. In the process, the formation of standing waves (stationary waves oscillating with an amplitude at each point) allows the superposition of two waves travelling in opposite directions. Figure 1.12 shows the standing waves of four frequencies. The solid line represents a particular snap of a standing wave at a particular instant of time, and the dashed lines represent snaps at different times. The points without any oscillation are called "nodes" (N, Figure 1.12). Whereas the points that oscillate to maximum amplitudes; are called "anti-nodes" (AN, Figure 1.12). The mathematical representation of the two traveling waves propagating in opposite directions ( $E_R$ : right and  $E_L$ : left) can be written as  $^{86}$ 

$$E_R(x,t) = A\sin(kx - \omega t) \tag{8}$$

$$E_L(x,t) = A\sin(kx + \omega t) \tag{9}$$

The superimposition of these two waves, which is the sum of both the above equations,

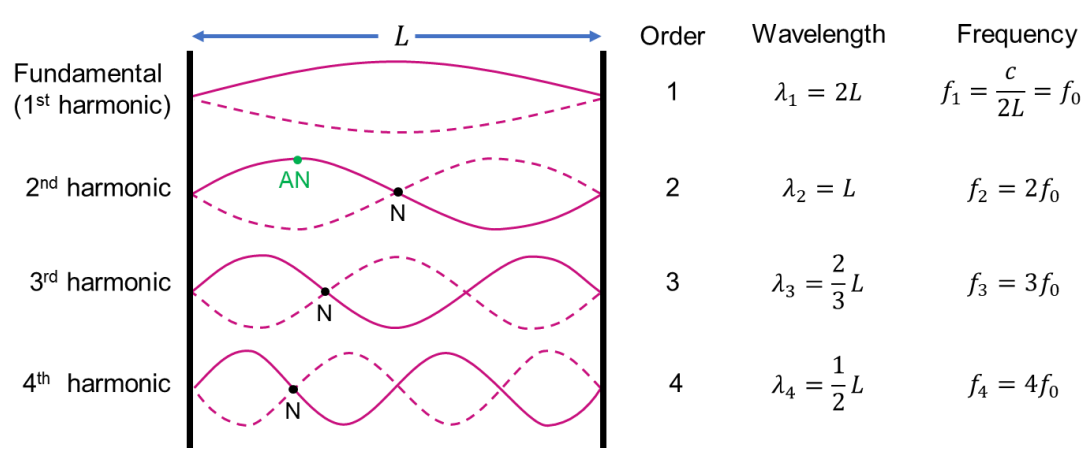


**Figure 1.12.** Standing waves of different frequencies formed in an FP resonator. AN and N represent node and anti-node, respectively.

results in a standing wave and is given by,

$$E(x,t) = E_R(x,t) + E_L(x,t)$$
 (10)

$$= 2A\sin(kx)\cos(\omega t) \tag{11}$$

The amplitude (A) of a particular point at position x on the wave can be given as:

$$A(x) = 2A\sin(kx) \tag{12}$$

Hence, a standing wave with one anti-node is stated to be the first harmonic, two anti-nodes are called the  $2^{nd}$  harmonic, and so on. The order, nodes, and corresponding wavelength of the fourth harmonics correspond to four, three, and 1/2L, respectively (Figure 1.12).

The nodes of the standing wave for the nth harmonic are at,

$$\sin(kx) = 0; where, k = \frac{n\pi}{L}$$

$$\frac{n\pi}{L}x = m\pi; m = 0,1,2,...$$

$$\therefore x = m\frac{L}{n}$$
(13)

The anti-nodes are located at:

$$\frac{n\pi}{L}x = m\frac{\pi}{2}; \qquad m = 1,3,5,...$$

$$\therefore x = m\frac{L}{2n}$$
(14)

Generally, f of the wave can be written as,

$$f = \frac{c}{2L} = \frac{c}{\lambda} = \frac{c}{2\pi} k = \frac{c}{2\pi} \sqrt{k_x^2 + k_y^2 + k_z^2}$$
 (15)

Let the sides of the resonator be a, b, L, and the corresponding allowed resonant frequencies are given by,

$$f_{mno} = \frac{c}{2} \sqrt{\left(\frac{m}{a}\right)^2 + \left(\frac{n}{b}\right)^2 + \left(\frac{o}{L}\right)^2}$$
 (16)

where the speed of the light is denoted by c and the m, n, o are the integer values that correspond to the number of anti-nodes in a, b and L dimensions.

These nodes and anti-nodes are a result of the multiple reflections in the optical resonator. As mentioned above, the superposition of two waves traveling in opposite directions (reflected light waves) results in constructive and destructive interferences. Thereby, enhancing the electromagnetic field inside the resonator. The constructive interference leads to sharp peaks in the FL spectrum, which are also called *optical modes*. The destructive interference of the reflected waves results in nodes that are represented by the vacuum region between optical modes. The mode can also be understood as electromagnetic field distribution that interprets the resonating light's course and *f*.

The free spectra range, FSR  $(\Delta\lambda)$  is the f separation between two consecutive optical modes of a resonator. It is the fundamental property of a resonator and is determined by its dimensions (L, w) or diameter in the case of WGM micro-resonators),  $n_{eff}$ , and surface smoothness or mirror-like reflectivity of the resonator. The electric field distribution of each resonant mode is unique for a particular f and is deterministic for that particular mode number. The FSR  $(\Delta\lambda)$  is identified as the distance between two consecutive resonant modes (m, m+1) and can be represented as,  $^{87}$ 

$$\Delta \lambda = \lambda_m - \lambda_{m+1} \tag{17}$$

FSR is inversely proportional to L of the micro-resonator and can be represented as below.

$$FSR (\Delta \lambda) = \frac{\lambda_m^2}{2L \, n_{eff}} \tag{18}$$

where  $\lambda_m$  is the maximum wavelength of that resonant mode. This equation allows the estimation of the number of possible resonant modes in a resonator of a specific size and can be tuned by varying the resonator's size.

#### **1.4.1.1** Quality (*Q*) factor

The Q-factor is a parameter quantifying the ability of a micro-resonator to confine light inside the cavity or micro-resonator. The larger the Q-factor, the longer the light can be trapped within the micro-resonator, allowing for more efficient photon-matter interactions. The Q-factors of optical micro-resonators can be classified as ultra-high ( $10^8$ ) and high ( $10^3$  to  $10^7$ ) depending on the efficiency of micro-resonator to store light. The development of high-Q optical micro-resonators provides new possibilities for research and innovation, in

strong-coupling quantum electro dynamics, dynamic filters in optical communication, and many other areas.<sup>88</sup> The *Q*-factor may be studied as the number of light oscillations that the optical signal can sustain inside the micro-resonator before losing a significant fraction of photon intensity.

$$Q = \frac{\text{energy stored}}{\text{energy loss}} \tag{19}$$

Q-factor can be estimated using the formula:

$$Q = \frac{f_0}{2\Delta f} \tag{20}$$

where  $f_0$  and  $\Delta f$  are the resonant f of the resonator and the full width at half maxima (FWHM) linewidth of the resonance peak. The FWHM linewidth is a measure of the broadness of the resonance peak and indicates the amount of energy lost by the resonator per cycle.

An ideal micro-resonator would confine light indefinitely. The deviation arises due to various losses in the micro-cavities due to intrinsic and extrinsic factors. For a micro-resonator, the *Q*-value is an inverse of overall losses associated with the optical micro-resonator. It is the result of several intrinsic losses (like scattering, material's absorption, and radiation loss via curvature defects) and extrinsic losses (including coupling induced losses). The external loss arises due to the coupling between any two resonators, which can be used effectively to couple and route the light. The equation associated with all these losses can be written as,

$$\frac{1}{Q} = \frac{1}{Q_{material}} + \frac{1}{Q_{scatering}} + \frac{1}{Q_{radiation}} + \frac{1}{Q_{coupling}}$$
(21)

By optimizing the fabrication/assembly process, the resonator surface roughness and scattering loss can be reduced. The size of the resonator directly affects radiation loss, which can be decreased by controlling the dimension. The micro-resonator which are with high Q values are used as microlasers. The maximum Q-value reported for an FP resonator, to date, is  $10^5$ , whereas it is  $10^{11}$  for WGM resonators.

#### 1.4.1.2 Axial FP resonators

The FP micro-resonators can be classified as axial (optical modes vary with the length of the microcavity) and lateral (optical varies with the width of the microcavity) FP microresonators. Kumar *et al.* reported the microrods of 9,10 dibromo anthracene (DBA) which are

achieved by the self-assembly of DBA molecules in hexane under slow evaporation conditions (Figure 1.13a). The optical illumination of a 175  $\mu$ m long rod at P-3 with a focused laser beam produced a cyan color at the excitation point and the generated FL was transduced to the other end of the microrod to exhibit active waveguiding (Figure 1.13b). The FL spectra collected at P-4 possessed sharp projections on the FL spectrum called *optical modes* with a FSR of 19.4 nm at  $\lambda_{max}$  520 nm (Figure 1.13c). These optical modes arise due to the back- and-forth reflection of generated light inside the microrod because of its smooth reflective surfaces. The optical modes can be varied by changing the length of the rod for a given width and such micro-resonators are called lateral FP micro-resonators. A DBA microrod of length 115  $\mu$ m was cut into microrods of  $L \approx 81$  and  $\approx 53$   $\mu$ m, respectively, and

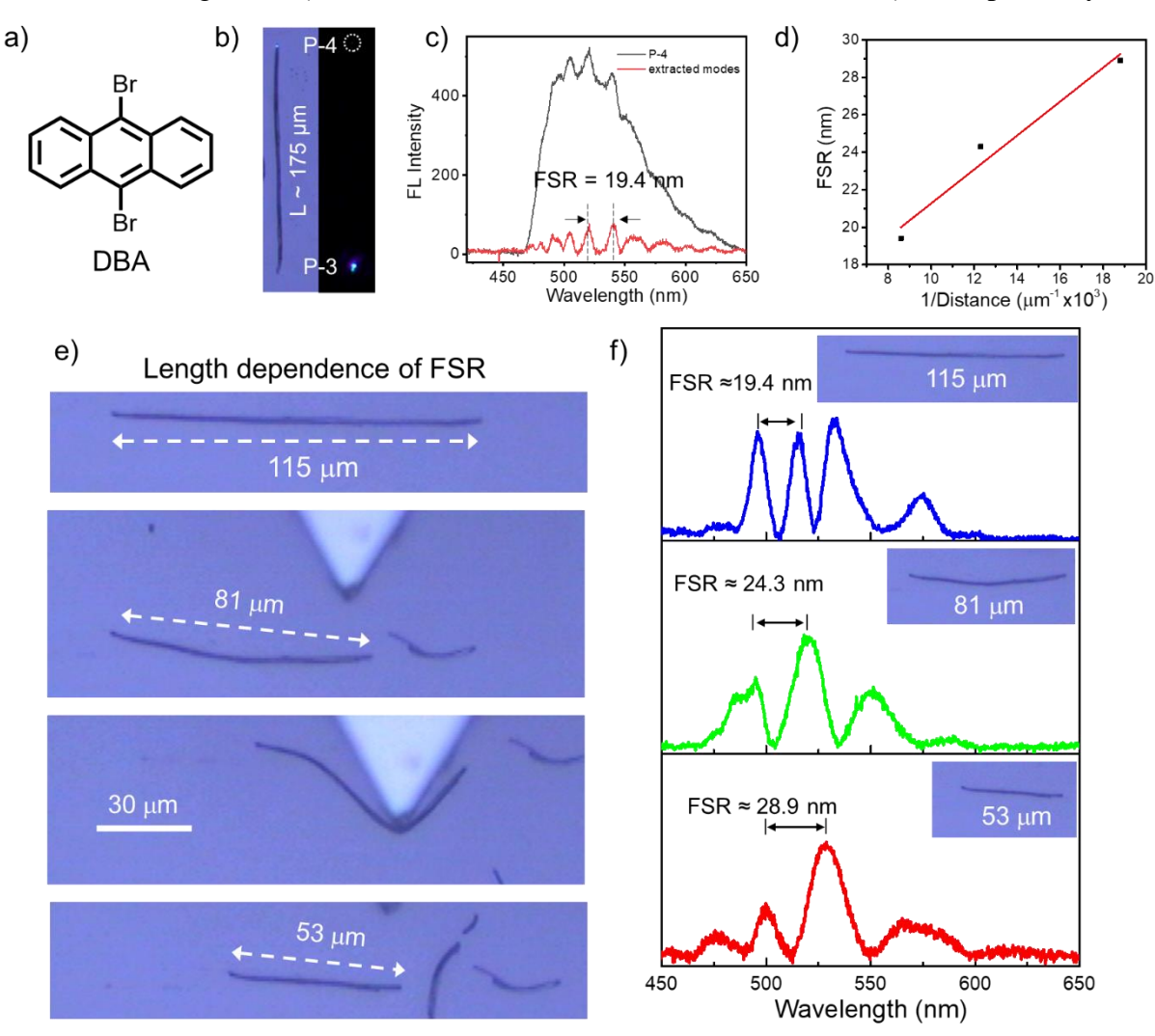


**Figure 1.13.** a) Molecular structure of dibromoanthracene (DBA). b) Confocal optical and FL images of DBA microcrystal when excited at P-3. c) FL spectra collected at P-4 for excitation at P-3 and the corresponding optical modes. FSR is free spectral range. d) The plot of free spectral range, FSR vs 1/Distance. e) Confocal optical microscope images depicting the shaping of DBA microcrystal into three different lengths. f) The optical modes recorded in the DBA microcrystal for different lengths. Figure adopted from ref. 93.

examined the optical modes before and after shortening the DBA microcrystal (Figure 1.13d,e). The FSR changed from 19.4 to 24.3 and 28.9 nm from uncut crystal to gradually shortened crystals suggesting axial-type FP resonances exhibited by DBA microcrystals (Figure 1.13f).

#### 1.4.1.3 Lateral FP resonators

Normally, organic crystals tend to grow along the high-energy axial facets, and most of the reported FP micro-resonators are axial-type FP cavities. However, lateral FP micro-resonators are scarcely reported. Radhika *et al.* reported the near-infrared (NIR) emitting single-crystalline microribbons of (2*E*, 4*E*)-1-(2-hydroxyphenyl)-5-(pyren-1-yl) penta-2,4-dien-1-one (HPPD, Figure 1.14a). The HPPD microribbons were obtained by self-assembly of corresponding molecules from chloroform/ethanol (1:1) solution (Figure 1.14b). The

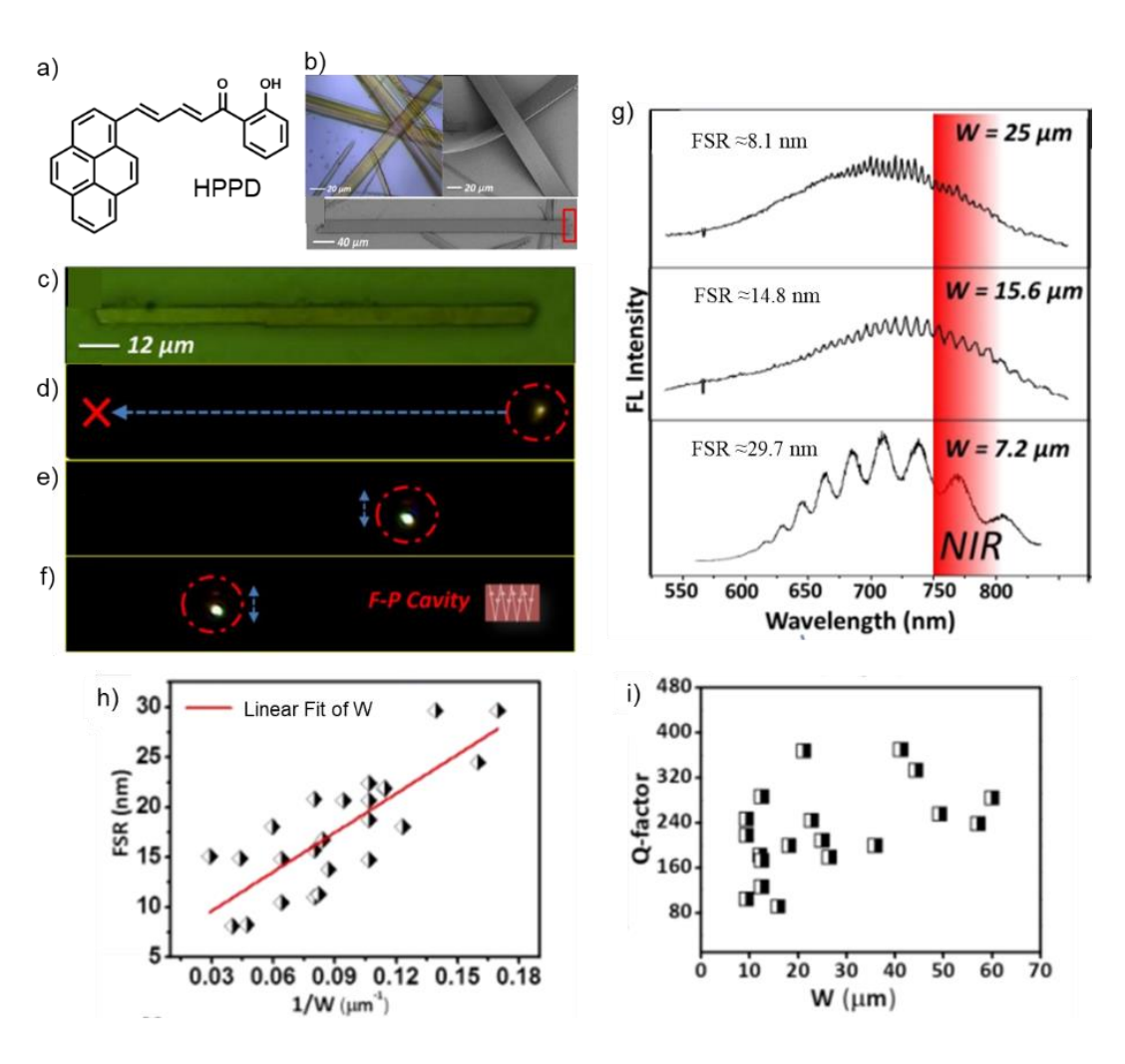


**Figure 1.14.** a) Molecular structure of HPPD. b) Confocal optical microscope and FESEM images of HPPDF microribbons. c-f) Confocal optical and laser FL microscope images when excited at various positions on HPPD FP microribbon. g) FL spectra obtained on the HPPD microribbons of diverse widths (W) depicting the lateral FP-type cavity characteristics. h,i) The plot of free spectral range, FSR vs 1/width (W) and *Q*-factor vs width (W), respectively, constructed from HPPD microribbons. Figure adopted from ref. 94.

FESEM image reveals the presence of bent microribbons suggesting the flexible nature of themicroribbons. The single particle μ-FL studies revealed the lateral optical signal guiding in the HPPD microribbons (Figure 1.14c,f). Surprisingly, no FL was guided along the axial direction of the microribbons (Figure 1.14d). The FL spectrum obtained at the lateral end of a microribbon of width 25 μm constituted several sharp features on the spectrum due to strong optical confinement along the lateral direction between mirror-like facets of the microribbons. The lateral FP micro-resonator attributes were confirmed as FSR decreased with increase in the lateral width of the microribbons (Figure 1.14g). The plot of FSR vs width reaffirms the inverse relation between both (Figure 1.14h). The *Q*-factor (quality factor, a parameter to measure the ability of microcavity to confine photons) varied between 80 and 400 which indicates poor quality of micro-resonators and the occurrence of defects during growth process was attributed to observed low quality (Figure 1.14i).

#### 1.4.2 Whispering gallery mode (WGM) ring resonators (RRs)

WGM optical micro-resonators are optical cavities in which light is trapped and repeatedly circulated multiple times along the circumference of a micro-resonators' surface. The name originated from the acoustic whispering gallery effect first observed by Lord Rayleigh in St. Paul's Cathedral located in London, where sound waves migrate along the curved walls of the gallery due to TIR (Figure 1.15a,b). 96,97 The WGM resonators are today fabricated from a variety of materials (inorganic or organic, crystalline or amorphous) and in numerous shapes (spherical, hemispherical, polygonal, disk, rings, toroids, cylinders, etc) and sizes where diameter of resonator can be nanometer to millimeter and more. 98-107 The microresonator with disk geometry fabricated using silicon nanocrystals exhibits whispering gallery resonances in the visible region with a *Q*-factor of 2800 (Figure 1.15c). The optical signal is captivated in the WGM resonator due to TIR, where light traversing through a

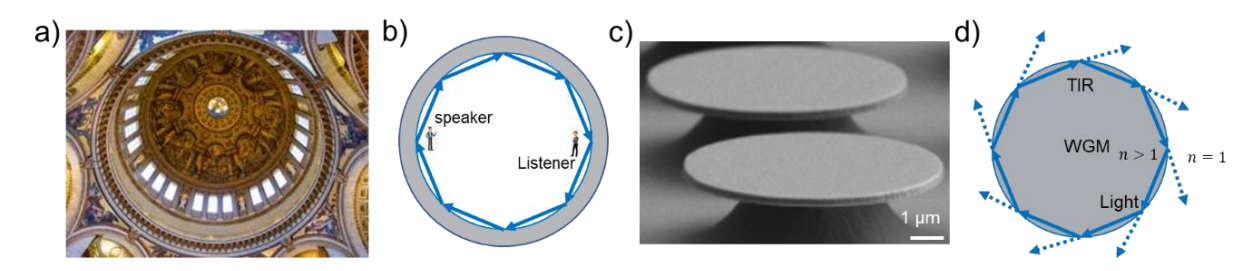


**Figure 1.15.** a) The inner doom view of St. Paul Cathedral, London. b) The graphics illustrating the motion of acoustic WGMs along the walls of the Cathedral's doom. c) Scanning electron microscope image of gallium nitride microdiscs acting as WGM micro-resonators fabricated via EBL. d) Schematic of light confinement in WGM micro-resonator. Figure adopted from ref. 96 and 102.

medium of higher n encounters an interface with a medium of low n, and light is reflected back into the medium with higher n (Figure 1.15d). These WGM resonators can support resonant modes depending on the size,  $n_{eff}$  and thickness of the resonator, where the confined light revolves around the periphery of the micro-resonator with minimal loss. Light can self-reinforce when it meets the resonance criteria as per eq. 22, after traveling one round around the periphery of the resonator. The photons that does not meet the resonance criteria are eliminated due to destructive interference.

$$q\lambda = \pi D n_{eff} \tag{22}$$

where q is an integer corresponding to the angular momentum of the photon revolving inside a micro-resonator. Additionally, different mode numbers (polar, p, azimuthal, m, and radial, q,) are used to describe these WGMs in micro-resonators. The optical mode's azimuthal and radial directions are denoted by the letters m and q, respectively and the spatial structure of WGMs are shown in Figure 1.16.<sup>103</sup> A series of field oscillations produced in the  $\phi$ -direction is represented by the angular mode number, p =  $\ell$ - m =0, 1, 2, 3... The photoluminescence spectra can be used to predict the resonance type (as WGM) and the number of optical modes present in the micro-resonator.

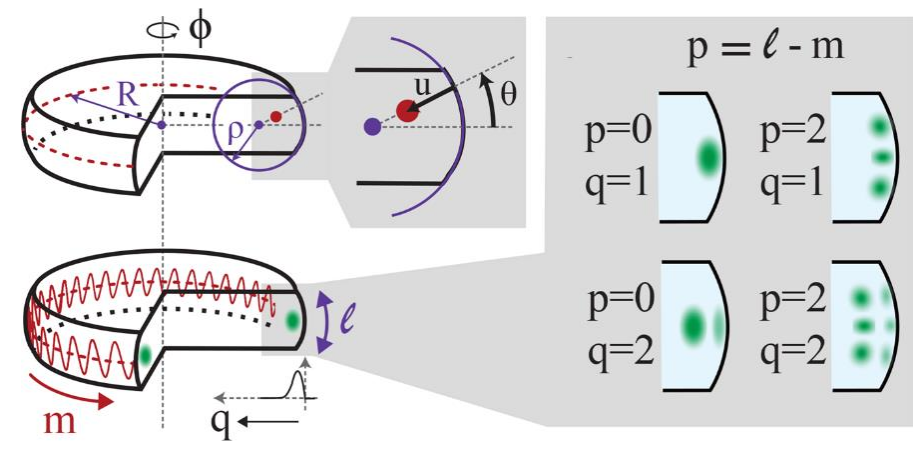
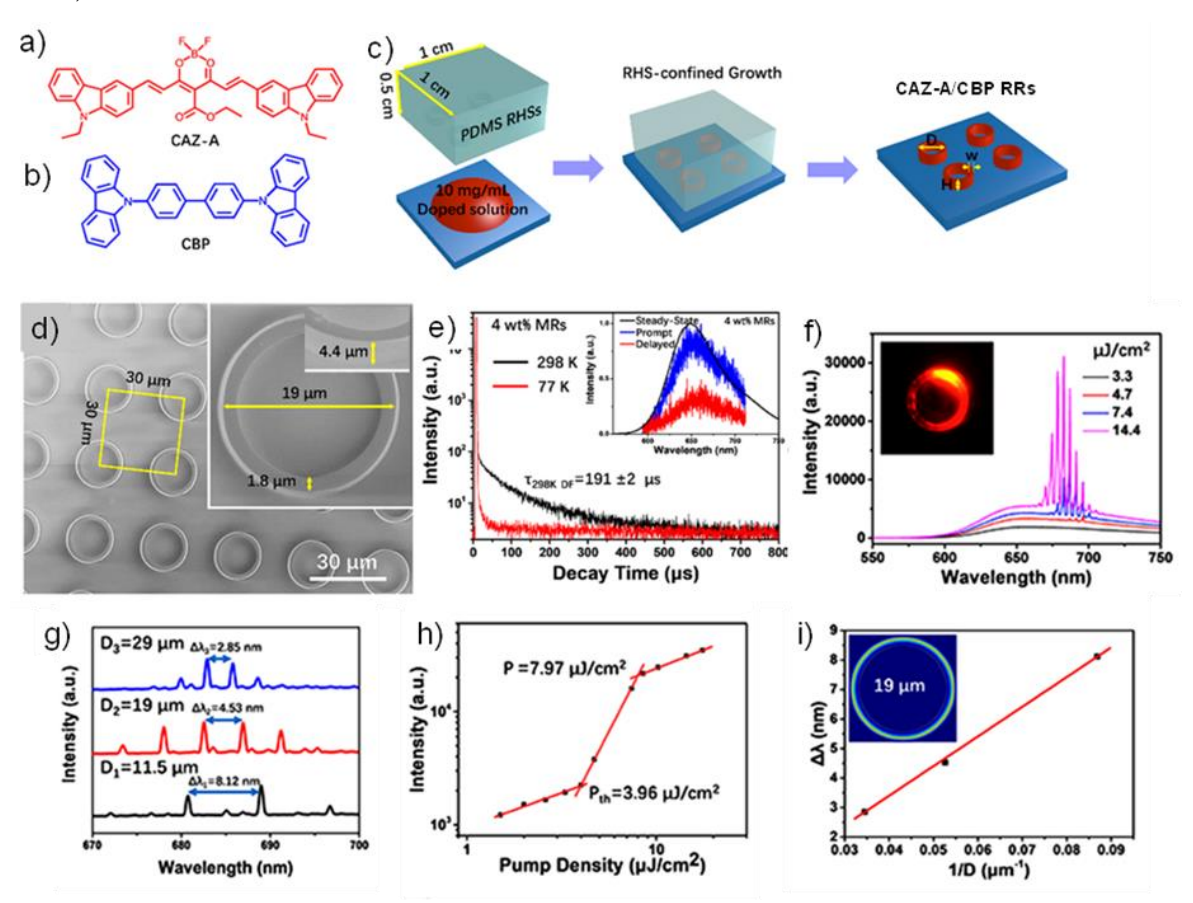


Figure 1.16. Spatial structure of WGMs in a disc resonator. Figure adapted from ref. 103.

RRs are micro-resonators capable of confining light inside the micro/nano rings to effectively amplify the optical signal, acting as superior gain media required for lasing property in microstructures. Huang *et al.* presented the lasing action in RRs obtained from thermally activated delayed fluorescence (TADF) material, namely, borondifluoride curcuminoid derivative, 4,6-bis((*E*)-9-ethyl-3-vinyl-9H-carbazole)-5-(ethoxycarbonyl)-2, 2-difluoro-2H-1,3, 2-ioxaborinin-1-ium-2-uide, (CAZ-A) doped into 4,4'-bis(N-carbazolyl)-1,10-biphenyl (CBP) via polymer ring stamp hole method (Figure 1.17a-c). The RRs obtained by this method yielded homogenously shaped different-sized microcavities with a

thickness of about 4.4  $\mu$ m (Figure 1.17d). The TADF attributes of 4 wt% CAZ-A/CBP RRs array recorded on a streak camera at room temperature,  $\tau_{298K \, DF} = 191 \, \mu$ s, confirms the delayed emission characteristics (Figure 1.17e). The lasing action from a single RR was studied with a 400 nm femtosecond pulsed laser, as the pump power increased gradually from 3.3 to 14.4  $\mu$ J/cm<sup>2</sup> the initially dominant broad spontaneous emission (at low power) giving way to strong harp peaks in the 670-705 nm region (Figure 1.17f). Further, the lasing action in these RRs resulted in the 'S'-shape curve shown in Figure 1.17h. The RRs exhibited WGM resonances, and the same can be reflected from the width dependence of FSR, because as the width of RRs decreases spacing between adjacent lasing modes increases (Figure 1.17g,i). Thus, TADF WGM RRs were illustrated.



**Figure 1.17.** a,b) Molecular structures of CAZ-A and CBP. c) Graphical illustration of fabrication of CAZ-A/CBP ring resonators (RRs). d) FESEM image of the CAZ-A/CBP MRs array. Insets show the close-up view of a single RR's diameter, thickness and height. e) Photoluminescence lifetime profile of CAZ-A/CBP film at 77K and 298K. f) Lasing action from the RRs. g,i) Width dependence of free spectral range observed in the whispering gallery mode resonators fabricated from CAZ-A/CBP RRs. Schematic diagram of the optical field distribution in the RR (D = 19  $\mu$ m). h) Plot of Intensity vs pump density indicating the 'S' shaped curve expected during lasing action beyond the threshold energy. Figure adapted from ref. 109.

#### 1.5 Silicon-based optical components

Silicon-based materials have attracted enormous research interest and emerged as photonic-grade materials, especially after the huge success of the CMOS industry. The high

refractive index of Si or Si-based materials allows efficient light guiding and confinement in the waveguides. The excellent thermal conductivity and optical damage threshold of silicon make them ideal candidates for PICs application. The construction of PICs requires optical components (optical waveguides, optical amplifier, polarization converter and modulator) akin to electronic circuit components (like electrical wire, transistor, capacitor, and resistor). The optical waveguides are building blocks for the construction of photonic circuits or devices. An optical amplifier serves to amplify the input signal. A polarization converter acts as a modulator by changing the speed of light and delaying the time it takes to reach the detector. These fundamental building blocks can be made into other relevant optical components like straight and bent waveguides, spiral waveguides (SWs), RRs, add-on-drop filters, interferometers (IMs), wavelength division multiplexers (WDMs) and many more for their effective use in photonic device applications.

#### 1.5.1 Optical interfeometers

IMs are an important class of optical elements which merge two or more light sources to create an interference, thereby modifying the input light and giving a different output signal. They are one of the crucial components for PICs, having immense importance for the advancement of light-based technologies, which were used for different applications like volatile organic molecular sensors,  $^{112}$  n sensors,  $^{113}$  and single-mode lasers.  $^{114}$  IMs, especially asymmetric Mach-Zehnder (aMZI) type, can be produced by creating a path difference between the distance traveled by photons along two paths. The same can be accomplished by changing the path L or n of one of the arms (Figure 1.18a). They are highly desired for a variety of optical devices like optical switches, sensors, and modulators. Using the EBL technique, Shamy et al. constructed a loop-terminated aMZI (LT-aMZI) on a silicon-oninsulator (SOI) platform. 115 The LT-aMZI were constructed with four different arm lengths  $(\Delta L = 44.7, 89.4, 178.8 \text{ and } 357.6 \text{ } \mu\text{m}, \text{ Figure } 1.18\text{c,d})$ . The optical performance of the constructed modules was tested by studying the device's response for various wavelengths (1500 to 1600 nm) introduced into it using a tunable laser. The device's performance matched the expected optical mode shift as the arm lengths changed which were further confirmed by numerical simulations.<sup>115</sup>

Another way of accomplishing the anticipated interference in an aMZI is by changing the *n* of the sensing arm, as indicated in Figure 1.18b. Jiang and coworkers reported a photochromic molecule-based, bis-(5-chloro-2-methyl- 3-thienyl) cyclopentene (DAECHO)-doped-poly(methylmethacrylate)-co-polystyrene (DAECHO@PMMA-co-PS), polymer-

coated aMZI acting as a *n* sensor (Figure 1.18e). <sup>116</sup> The photochromic molecule DAECHO consists of two forms, open and closed, respectively (Figure 1.18f). The n of the o-DAECH and c-DAECHO-doped polymer films was measured to be 1.5451 and 1.5466, respectively, using the prism coupler @ 1538 nm. Further, the time-dependent *n* changes of the photochromic molecule DAECHO-doped polymer samples revealed a linear change in *n* of the polymer films as the exposure time to 365 nm UV torch light gradually increased. Initially, a symmetric MZI employing the well-known EBL technique on SOI with a core *n* of 1.5730; lower and upper cladding *n* are 1.444 and 1.5595, respectively, was fabricated. Later, the sensing arm was coated with DAECHO@PMMA-co-PS by masking the remaining portion of the MZI. The *n* and absorbance of the sensing arm can be changed by illuminating the modified MZI with UV torch (Figure 1.18g). Thereby, the difference in path length required for the functioning of aMZI is effectively achieved. The interference spectra of the fabricated aMZI gradually changed with the UV exposure time (Figure 1.18h,i). The constructed photochromic-based aMZI acted as a *n* sensor.

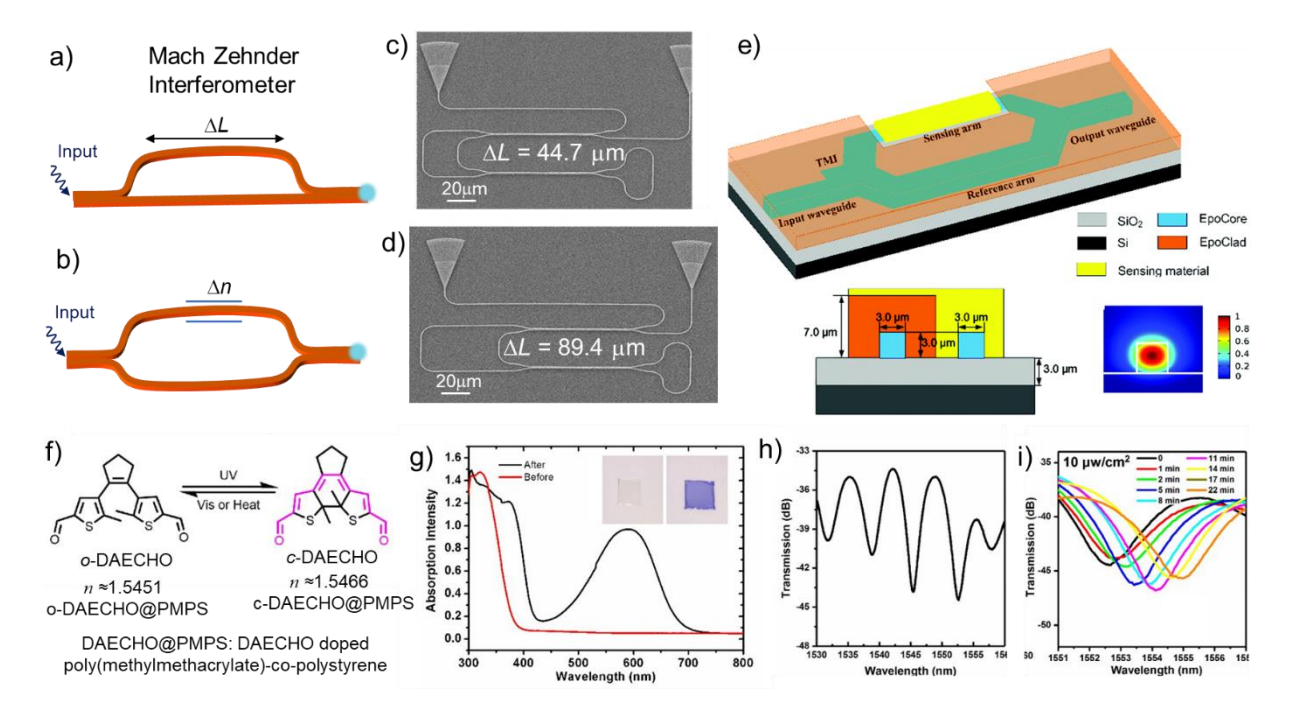


**Figure 1.18.** Graphical representation of functioning of asymmetric Mach-Zehnder IM (aMZI) by changing a) length and b) refractive index, n, respectively. SEM images of the fabricated aMZI with length,  $\Delta L$  c) 44.7 μm and d) 89.4 μm, respectively. e) The designed structure of MZI with a two-mode interfering coupler in the input port (the sensing material on upper cladding was omitted for clarity). Insets show the cross-section of the designed MZI and the simulated power distribution of sensing arm, where the interfaces of waveguide were highlighted in white. f) Molecular structure of open and closed forms of DAECHO. Inset shows the refractive index, n, change in DAECHO-doped polymer film ( $T \approx 6.8 \mu m$ ) upon exposure to UV light. g) The solid-state absorbance changes in the polymer film before and after illuminating with UV torch. Inset shows the photographs of DAECHO-doped polymer films before and after UV exposure. The interference spectra of the aMZI h) before and i) after UV exposure. Figure adapted from ref. 115 and 116.

#### 1.5.2 Fiber loop mirror

Fiber loop mirrors (FLMs), also known as Sagnac IMs, and are interesting optical

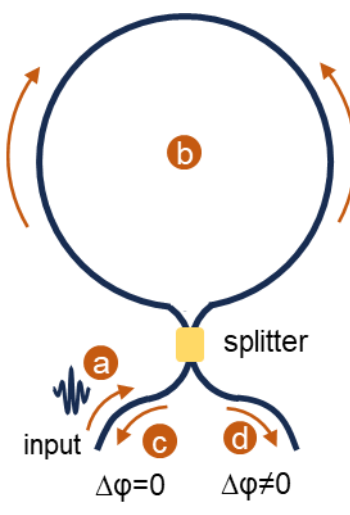


**Figure 1.19.** Schematic representing a fiber loop mirror.

components for use in optical devices and systems. FLMs serve as reflective optical elements in photonic technologies and are widely used for sensing, wavelength division multiplexing and related applications. For an intuitive picture, let a fiber coupler splits an optical signal received at one of its input ports into two equal portions (Figure 1.19, inset a). As the output ports are connected by a fiber loop, the two portions of the optical signal travel in opposite directions and interfere again at the splitter (Figure 1.19, inset b). In the simplest case, this will result in the original pulse reflected back to where it came from the fiber loop acts like a mirror (Figure 1.19, inset c).

The reflectivity of the loop mirror changes if the two counterpropagating optical signals, when optical signals acquire a phase shift relative to each other before intervening. This phase shift will affect the interference conditions such that a certain fraction of the original input pulse will be transmitted into the second input port, rather than being reflected (Figure 1.19, inset d). Now, if the ratio of transmission-to-reflection can be devised to depend on the input pulse's power, the fiber loop can act as fast artificial saturable absorber. However, the utilization of such FLM geometries to demonstrate IMs was not reported. They are utilized in both linear and non-linear optical (NLO) mirror loops. Traditionally, FLMs are fabricated using high-birefringent materials, polarization maintaining materials or photonic crystals-based materials. Concurrently, they are all composed of Si-based materials which require nanometer scale accuracy for fabrication.

#### 1.5.3 Directional coupler

The directional coupler (DC), which splits the incident optical signal into different ratios, comprises two adjacently placed bent waveguides connected through their bends (Figure 1.20d, inset).<sup>44</sup> DCs are essential for the fabrication of advanced optical devices and are pivotal for quantum information processing and neural networking technologies.<sup>122-124</sup> Besides, these DCs are highly necessary for inter-waveguide and inter-component light transfer. Hane *et al.* reported the single and multiple optical switches using ultra-small electrostatic comb-drive actuator.<sup>125</sup> The FESEM image of a 2×6 multiple optical switch employing 2×2 DCs is shown in Figure 1.20a. The functional element of the optical switch is

a DC constructed on a SOI. The height and width of the silicon waveguide correspond to 260 and 400 nm, respectively (Figure 1.20b). They fabricated several optical switches with varying gaps (G) between two waveguides in the DC to study the effect on optical switching. The optical characteristics of the device were tested using a light source of single TE-mode 1.55 μm wavelength. The normalized signal propagation in the DC at through port and drop port as a variable of G between waveguides shows the optical switching behavior at different points, 800 nm, 900 nm, etc. (Figure 1.20c). Importantly, the coupling coefficient, a measure

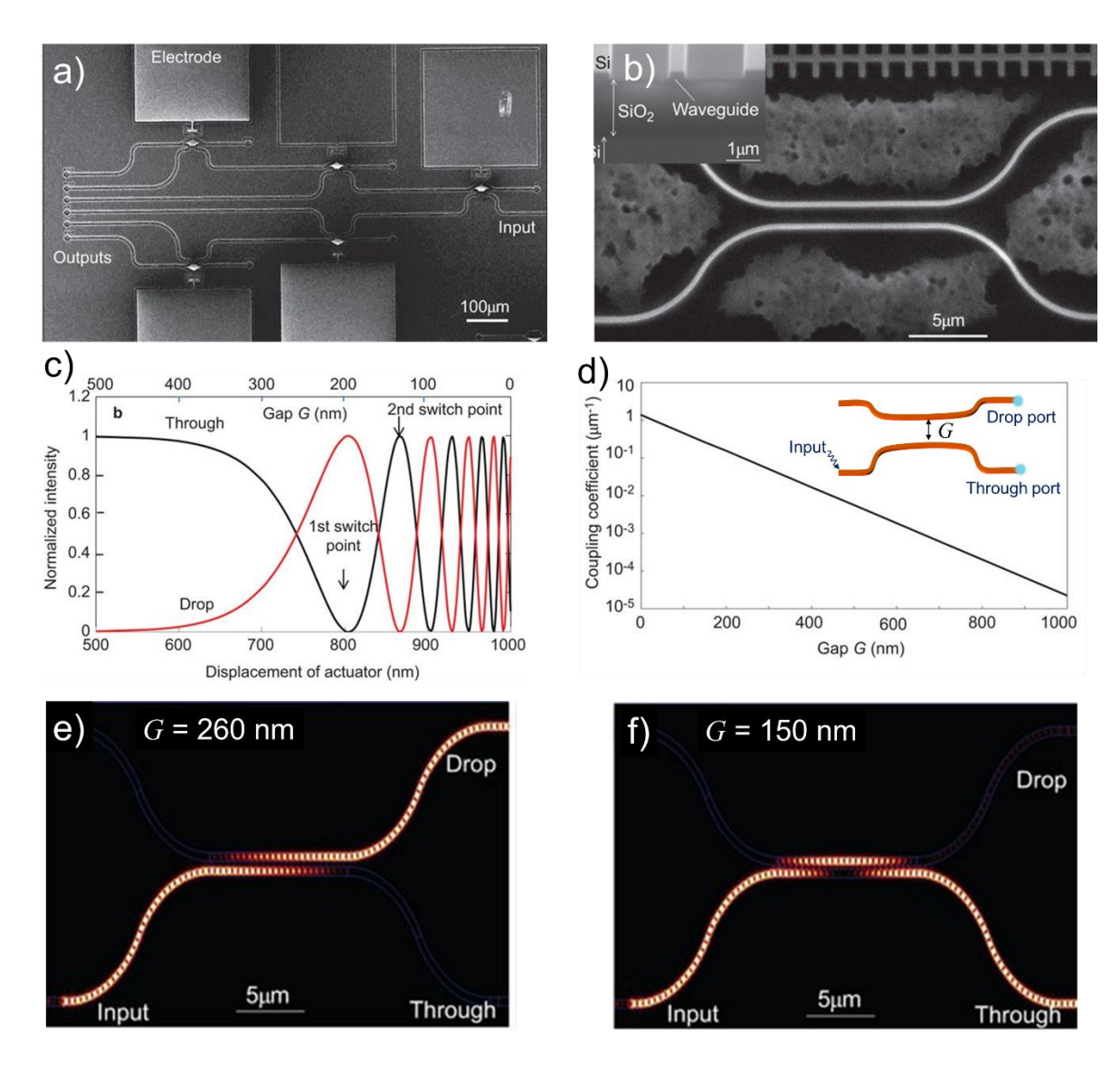


**Figure 1.20.** a) FESEM image of the 2x6 multiple optical switch. b) Close-up view of the directional coupler (DC) region in optical switch. Inset shows the cross-sectional image of the waveguide. c) Normalized light intensities at the through and drop ports calculated as a function of actuator displacement and gap between the waveguides in the coupler. d) Coupling coefficient calculated as a function of gap (*G*) between the waveguides. Inset depicts the functioning of DC. Intensity profile of the propagating light wave calculated using FDTD numerical calculations when the gap between two waveguides is e) 260 nm and f) 150 nm in the optical switch. Figure adopted from ref. 125.

of optical signal communication among the two waveguides in the DC drastically decreased as the gap between the waveguides increased (Figure 1.20d). The FDTD numerical calculations on a DC with a G of 260 nm, clearly depict the intensity distribution as light propagates from one waveguide to another (Figure 1.20e). Interestingly, as the G between the waveguides reduced (G=160 nm) the light transferred from the first waveguide to the second, re-enters the earlier waveguide (Figure 1.20f). Through these studies, the authors could establish silicon optical switches with G-variable couplers using micromechanical combdrive actuators.

#### 1.5.4 Wavelength division multiplexers

A wavelength division multiplexer (WDMs) is an optical component that allows the simultaneous transduction of multiple signals or bandwidths through a single fiber (Figure 1.21a). The multiplexed signals can be demultiplexed later to segregate them. WDM is a core technological component in optical transmission systems to improve spectral efficiency and counter the shortcomings of a single-mode fiber transport capacity. Further, the WDMs are perennial for advancing data transfer and communication technologies. They are also important for constructing next-generation photonic circuits, which find applications in light fidelity (LiFi) and visible light communication technologies.

Melati et al. demonstrated the first PIC capable of executing both multiplexing and demultiplexing in a few-mode fiber transmission constructed using InGaAsP rib-shaped

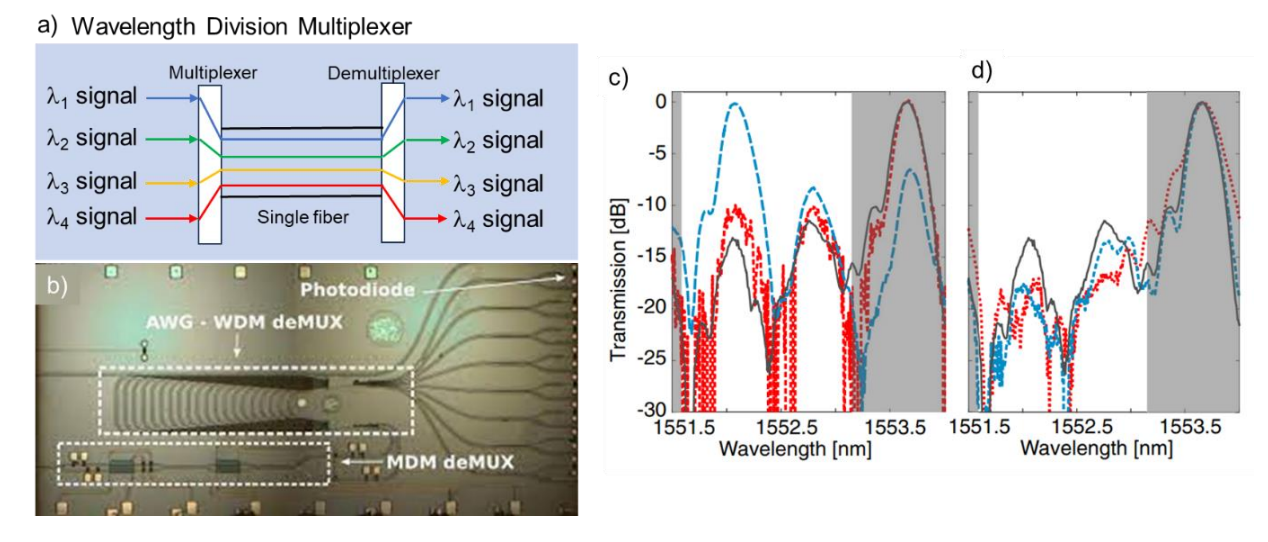


**Figure 1.21.** a) Schematic representation of a wavelength division multiplexer and demultiplexer. b) A InGaAsP rib-waveguide-based photonic integrated circuit module on an InP platform performing wavelength division multiplexing (MDM/WDM) and demultiplexing (deMUX). c) Transmission at output 6 in the reference case (pure LP01 transmission, gray solid curve) and introducing mode mixing (dotted red curve and dashed blue curve). d) Results without multi-input-multi-output processing and exploiting controllers of the mode demultiplexing stage to perform mode unscrambling. Figure adopted from ref. 126 and 130.

waveguides of 1-micron thickness on an InP platform (Figure 1.21b).  $^{130}$  The circuit can allow multiple optical modes through the two-mode waveguide coupled to a 11  $\mu$ m core fiber. The arrayed waveguide grating allowed the introduction of different wavelengths ( $\lambda_1$ -4corresponding to 1551.8, 1553, 1558.1, and 1558.9 nm) which were successfully multiplexed and demultiplexed by the photonic module (Figure 1.21c,d). These multiplexing/demultiplexing capabilities enabled an optical signal transfer rate of 10 GB/s for on/off keying non return-to-zero channels propagating within the wideband multiplexer with minimal crosstalk.

#### 1.5.5 Spiral waveguides

Spiral structures are ubiquitous in nature and spiral patterns are found in marine animal shells, plants, crystals and galaxies. Mathematically, two-dimensional (2D) spiral shapes are described using polar coordinates as  $r = r(\theta)$ , where the radius r is the monotonous continuous function of angle,  $\theta$ . Archimedean, Cornu, Fermat, Fibonacci, hyperbolic, logarithmic, triangular, and square shapes are some well-known 2D spiral configurations. In nanophotonics, the 2D spiral configuration is effectively used to pack long waveguides in a compact area, hence called spiral waveguides (SWs). SWs are utilized in photonic devices as delay line, spectrometer components, high-fidelity sensors, sensors, PICs, and quantum computing. To realize the useful functions of SWs, the quality of optical waveguides must be sufficiently high. The fabrication of SWs from high n materials like Si requires i) compact core with strong light confinement ability, ii) it must allow compact packing of long waveguides with sharp bends and iii) low propagation loss on a chip.

Bogaerts *et al.* fabricated a SW on the SOI surface; its top and cross-sectional images are shown in Figure 1.22a,b.  $^{141}$  The width of the waveguide is 460 nm and its straight losses are measured to be 2.7 dB cm<sup>-1</sup> (Figure 1.22d). The excess bending losses relied on the bend radius, increasing sharply for short bends, while the propagation losses increased with the L of the SW. The bend losses become negligible when the radius of the bend is more than 3  $\mu$ m (Figure 1.22d, inset). Generally, the wider-width waveguides result in higher-order modes, which are controlled by adiabatic tapering. The expanded width (3 microns) also decreases the phase errors through sidewall roughness and non-uniformity. The SW with lower propagation loss has been reported via EBL, but this technique is not suitable for mass fabrication.  $^{142,143}$ 

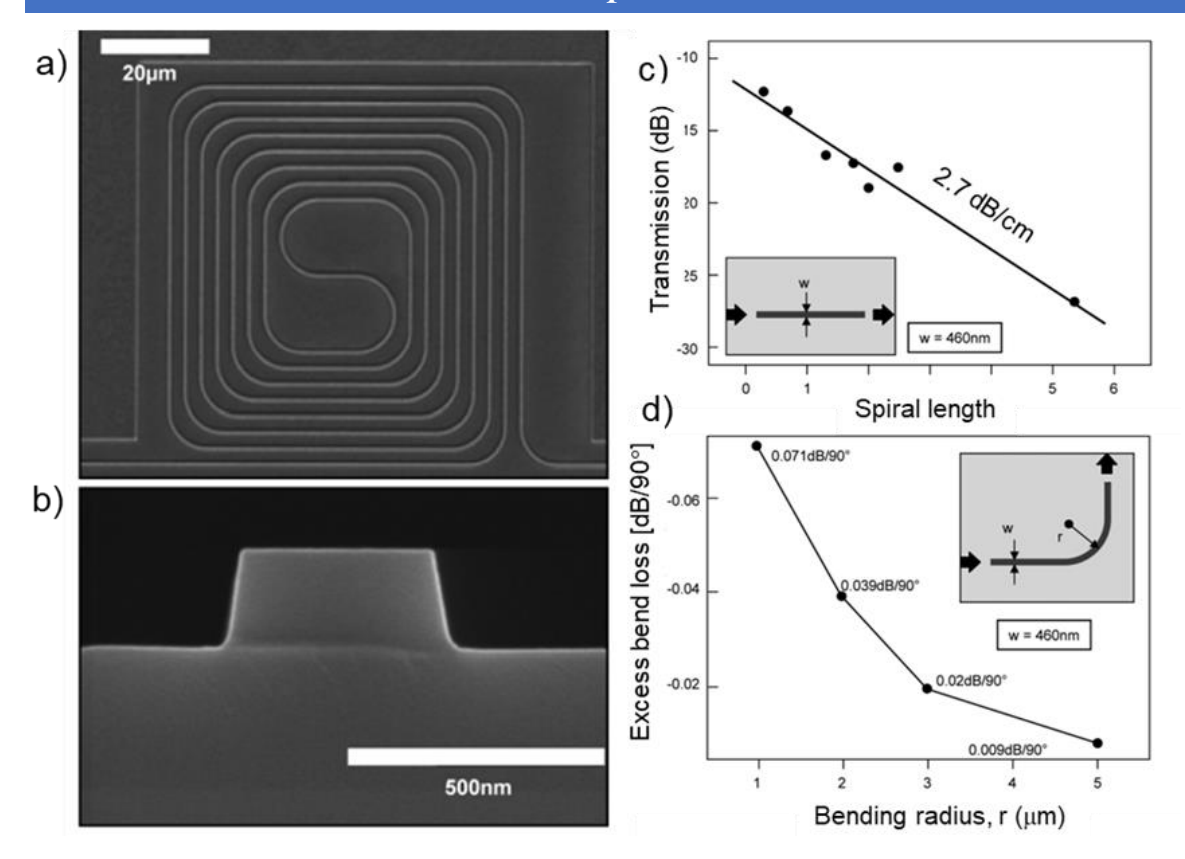


**Figure 1.22.** a) SEM image of spiral waveguide for waveguide loss characterization. b) SEM image depicting the cross-sectional view of SOI photonic wire shown in a. Optical Losses in photonic wires, extracted from spiral waveguides as shown in a, c) Propagation of straight waveguides and d) Excess loss in bends, respectively. Insets show the width and radius of curvature of bends in the SOI photonic wire, respectively. Figure adopted from 141.

An Archimedean SW (ASW) comprises equidistantly spaced successive turns imparting the highest filling ratio among different spiral architectures for a given separation distance between the waveguides. Xu and coworkers reported an ASW constructed on a SOI wafer with a 260 nm thick Si layer buried on a 2 µm SiO<sub>2</sub> template utilizing EBL and plasmaetching techniques. The ASW was exclusively employed for the realization of ultracompact optical comb filters. The final fabricated device consists of two interleaved symmetric SWs attached by two circular arcs at the center (Figure 1.23a,b). The center point of two spiral waveguide branches is expressed using eq. 23

$$R_{s}(\theta) = (S_{w} / \pi)\theta, \qquad \theta > 0$$
 (23)

$$x_{1,2} = \pm R_s \cos(\theta)$$
  $y_{1,2} = \pm R_s \sin(\theta)$  (24)

where  $S_w$  is the waveguide separation distance (Figure 1.23b).

The waveguide loops running towards the inner and outer portions of ASWs are joined externally by two DCs pointed at  $t_1$  and  $t_2$ . An effective add-drop filter (capable of

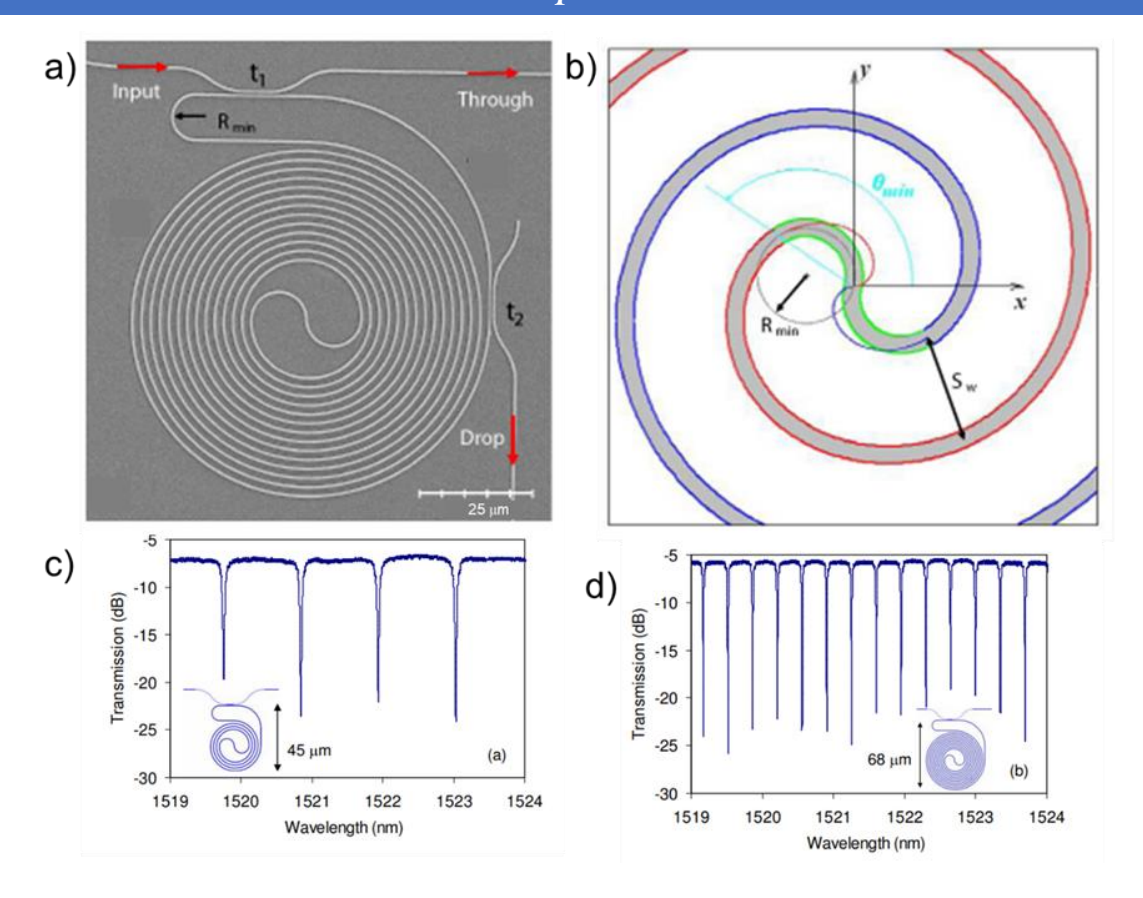


**Figure 1.23.** a) SEM micrograph of an Archimedean spiral waveguide of length 2400  $\mu$ m connected to the adddrop cavity. b) Center portion of the resonator cavity, where the red and blue outlined sections indicate the two interleaved Archimedean spiral waveguides, joined in the center by two arcs of a circle (outlined in green) of radius R<sub>min</sub>. c) Transmission spectra of the fabricated structures c) Ring A with  $L=430~\mu$ m and an FSR of 1.09 nm at  $\lambda=1520$  nm and d) Ring C with  $L=1350~\mu$ m and an FSR of 0.35 nm, respectively. Figure adopted from ref. 144.

routing light selectively at the through port and drop port without disturbing the other channels) was realized, where ASW replaces a RR. The optical performance studied using tuneable laser, scanning wavelengths between 1470 and 1580 nm revealed the change in value from 1.09 to 0.35 nm as the ASW's length varied from 45 to 68  $\mu$ m. Therefore, frequency combing characteristics of the fabricated device as a function of ASW's length and compact packing were illustrated (Figure 1.23c,d).

#### 1.6 Organic crystals for photonics

The utility of organic materials for optoelectronics picked up pace towards the end of 20<sup>th</sup> century as visible from their applications in organic solar cells, light-emitting diodes, displays, etc.<sup>145</sup> Whereas organic materials' usage in photonic applications started recently. The realization of self-assembled organic molecular crystals as optical waveguides, <sup>44,55-62</sup> FP, <sup>93,94</sup> and WGM resonators, <sup>98-102</sup> modulators, <sup>146,147</sup> lasers, <sup>148-150</sup> etc. dominated the early years of 21<sup>st</sup> century. Organic cocrystal-based heterostructures for photonic barcodes, <sup>151,152</sup>

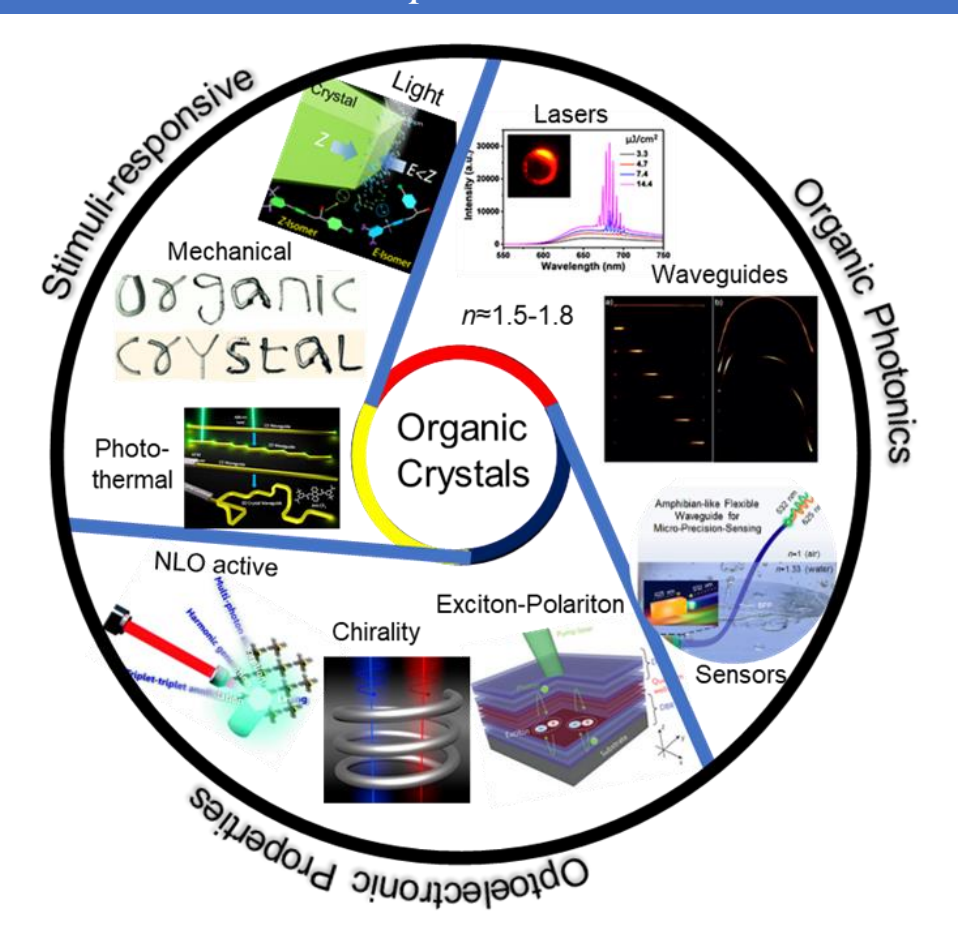


**Figure 1.24.** Schematic illustration of organic crystals' applications for various fields. Figure adapted from ref. 62,159-162,165.

directed sensing,<sup>153</sup> and logic gates,<sup>154,155</sup> were also realized. The unique ability of organic crystals to form room temperature exciton-polaritons,<sup>56,57</sup> efficient optical linear and non-linear properties in the bulk materials (especially crystals),<sup>44,62,156</sup> piezoelectric,<sup>157</sup> ferroelastic properties,<sup>158</sup> stimuli-responsiveness,<sup>159-162</sup> light-weight characteristics and importantly mechanical flexibility,<sup>163-165</sup> marks their sporadic employability for diverse photonic applications (as described in Figure 1.24).

The greatest advantage of organic crystals arises from their facile solution processability to acquire 1D/2D/3D nano/micro structures with ease. The upconverted signals produced due to second harmonic generation and two-photon absorption guided along the organic crystal waveguides are expected to be highly beneficial for NLO photonic circuits. The single-molecular or bulk chirality observed in organic materials is helpful for anti-counterfeiting applications. In the recent past, mechanically flexible organic crystals have sparked a great deal of research attention due to their applications in sensors, actuators, and photonic device applications. However, the serendipitous

employment of organic crystals for photonic device applications, particularly for photonic circuits, remain relatively unexplored. This is largely due to the lack of systematic understanding of mechanical attributes required for the precise shaping and structuring of the organic crystals into desired photonically relevant geometries.

#### 1.6.1 Mechanical properties of organic crystals

The mechanical traits displayed by a wide variety of flora and fauna have long been inspirational for technological advances. To fabricate different photonic structures, it is customary to understand the threshold strain (strain beyond which the material loses its mechanical integrity) of a material. Hence, mechanical properties are essential to investigate how material's retort under different loads. This is crucial for selecting the right crystals with required mechanical characteristics. The important mechanical properties that must be seriously considered are elastic modulus, strength, hardness and fatigue. These characteristics can be obtained from the well-known tensile test, which measures the material's response to forces in tension.

The valuable information obtainable from the test is the load vs elongation curve which can be translated into stress ( $\sigma$ )-strain ( $\epsilon$ ) curve. <sup>59,179</sup> In accordance with Hooke's law, majority of organic crystals possess a linear relation within the proportional limit (till point A depicted in Figure 1.25). The stiffness of an organic crystal can be estimated by the slope of

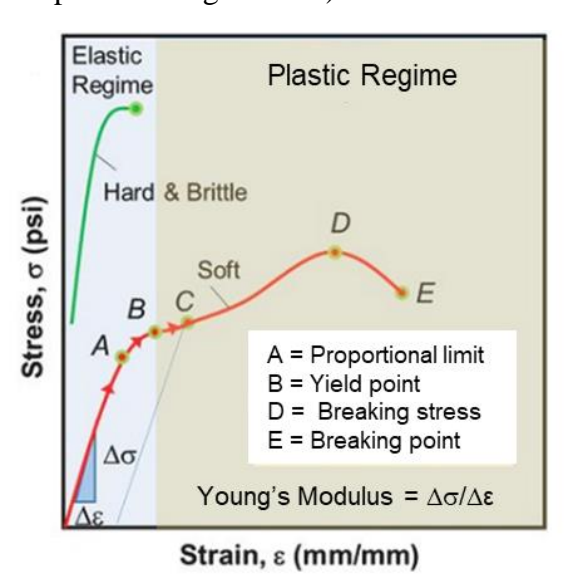


**Figure 1.25.** Stress-strain curve representing various mechanical properties as the material is subjected to constant external stress. Figure adopted from ref. 59.

the curve in linear regime. The elastic region corresponds to the area under stress-strain curve (blue portion, Figure 1.25) where removal of external  $\sigma$  results in the shape regaining of the crystal called yield point (depicted as B at the interface of elastic and plastic regime). It may be noted that Hooke's law may not be satisfied between points A and B on  $\sigma$  -  $\varepsilon$  curve. Beyond the yield point, from point C to point D, the crystal may develop permanent deformation upon subjecting to small external  $\sigma$  leading to plastic behaviour (grey portion in Figure 1.25). At point D, the crystal becomes completely

fragile, and breaks even as the external  $\sigma$  is withdrawn.

Depending on the intended use and environmental conditions, materials with different mechanical properties can be chosen to ensure optimal performance and safety. For a long time, researchers did not acknowledge the mechanical flexibility in organic crystalline materials as they thought most of the organic crystals were brittle. However, recently crystal engineering principles manifested the development of flexible organic crystals with controllable mechanical properties by careful molecular design. Various quantitative techniques like nanoindentation, AFM, etc. are available to study the mechanical properties of flexible organic crystals. <sup>180,181</sup>

The mechanical response of organic crystals can be broadly classified into elastic, plastic, and pseudo-plastic domains. The molecular crystals are termed elastic if they revert to their initial shape after taking away external stimulus, and the crystals are called plastic when they deform under external stress without fracture, but the deformation is irreversible. One of the interesting mechanical phenomena discovered recently is the so-called 'pseudo-plastic deformation/bending' where the crystals adhered on to a surface do not retrieve their initial shape, displaying plastic like characteristics even though they are inherently elastic in nature.

#### 1.6.1.1 Plastically bendable organic crystals

The systematic studies of the mechanism of mechanical flexibility of inorganic crystals started as early as 1978, by Haggery *et al.* They probed the structural basis for the plastic deformation of ZrB<sub>2</sub> crystals.<sup>182</sup> The plastic deformation in the hexagonally packed crystal manifested from the slip planes. However, similar investigations in organic crystals picked up only at the beginning of  $21^{st}$  century. The first structural basis for mechanical deformation in organic crystals was suggested by Reddy *et al.* in 2005.<sup>183</sup> The application of mechanical force perpendicular to the widest (001) face resulted in the permanent deformation of hexachlorobenzene (HCB) crystal and did not come back to its original shape, confirming the plastic mechanical deformation (Figure 1.26a,d). The molecular packing in the crystal growth axis is predominantly dictated by extensive  $\pi \cdots \pi$  ( $\approx 3.5$  Å) stacking leading to a layered arrangement (Figure 1.26b). The adjacent molecular layer is slip-stacked by an angle of 63°. The HCB crystals also possess weak halogen bonding (Cl···Cl) interactions.<sup>‡</sup>

<sup>&</sup>lt;sup>‡</sup> Halogen bonding: When there is an attractive interaction between an electrophilic environment of a halogen atom with the nucleophilic region of another halogen atom in a molecular unit within the same or different molecules, the interaction can be called as halogen bond or X···X bond. Geometrically and chemically, two types of X···X bonds are possible, namely, type I and II. Type-I halogen bonding does not follow the IUPAC definition as it is based only on a geometric contact between halogen entities in a close-packing environment. In contrast, type-II interactions comprise the pairing between the electrophilic area on one halogen atom and the nucleophilic area on the other.

The authors proposed weakening of halogen bonds which may break and reform, leading to the slipping of these stacked corrugated layers during the mechanical bending, was responsible for the observed plastic phenomenon (Figure 1.26c). Further, they investigated ca. 60 molecules with similar molecular arrangement ( $\pi \cdots \pi$  stacking distance is <4) to arrive at the proposed hypothesis, where 15 of them obeyed the deformation criteria as predicted.

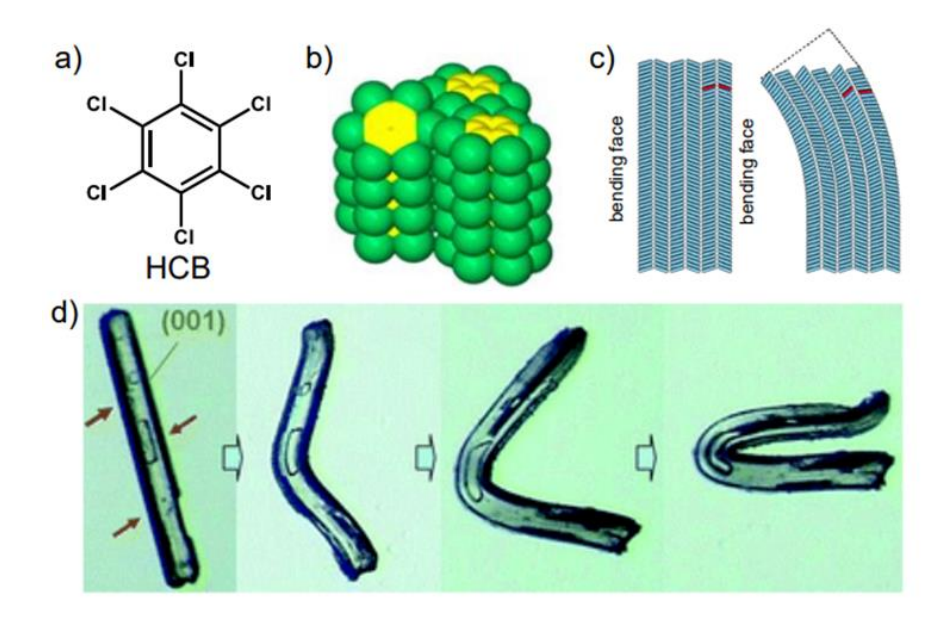


**Figure 1.26.** a) Molecular structure of HCB. b) Molecular packing in the (001) crystal growth axis. c) Graphical illustration of bending mechanism in plastic crystals. d) Optical microscope images showing the plastic deformation in HCB crystals perpendicular to (001) plane. Figure adapted from ref. 183.

#### 1.6.1.2 Elastically bendable organic crystals

The first attempts toward the systematic understanding of the structural basis for the elastic response in mechanically flexible molecular crystals were laid by Ghosh *et al.* in 2012.<sup>184</sup> They reported the elastic bending in methanol solvated cocrystals of 4-chloro-3-nitrobenzoic acid (CNB) and caffeine (CAF) (Figure 1.27a). These mechanically flexible crystals can be folded into previously unreported extremely bent geometries like circular loops using tweezers, however up on releasing of external force they revert to straight geometry (Figure 1.27b,c). The exceptional mechanical quality was attributed to the blockage of slip planes created by van der Waals interactions among the stacked layers between CNB and CAF layers (Figure 1.27d). They believed the presence of methanol also contributed to the smooth mechanical transitions. There was no conclusive evidence of a dissimilar interfacial angle at the bent crystal's end (Figure 1.27e). The de-solvation of the crystal retains the overall molecular packing in the crystal structure with a loss of mechanical elasticity, raising questions about the proposed bending mechanism and the structural basis for elasticity.

# Chapter 1 a) (100)(caffeine) (4-chloro-3-nitrobenzoic acid b) c)

plastic

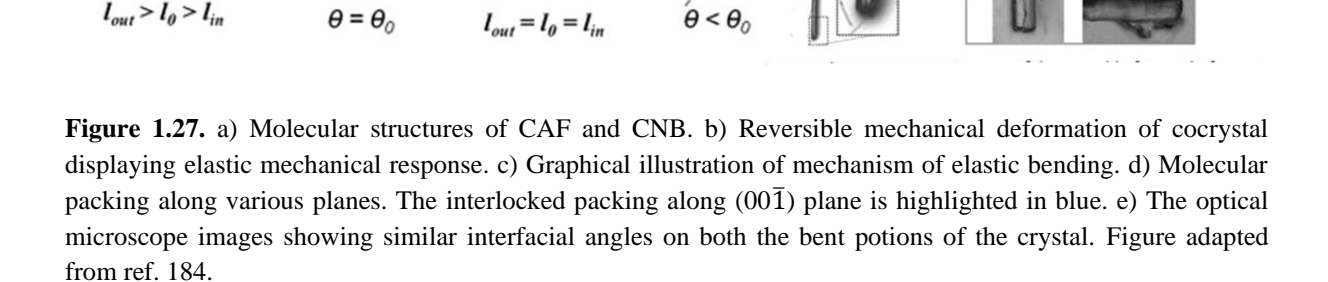
bending

elastic

bending

 $l_{out} > l_0 > l_{in}$ 

e)



In 2018, Huang and coworkers studied the elastic bending in macro-sized (E)-1-(((4-(dimethylamino) phenyl)imino)methyl)naphthalen-2-ol, DPIN crystals (Figure 1.27f-g). 185 DPIN molecule acquired a relatively planar geometry accompanied by intramolecular hydrogen bonding between hydroxyl and imine group (Figure 1.27h). The weak interactions lead to criss-cross packing, which grows into distinct layered structures. These layers contract and expand up on exposure to mechanical force. The molecules on the outer periphery expand while the molecules on the inside contract leading to the mechanical macroscopic response (Figure 1.27i). A similar structural basis for mechanical elasticity in molecular crystals was supported by synchrotron XRD studies performed on copper(II) acetylacetonate complex in 2018 by Worthy et al. 186 The authors proved minute inward movement of atoms on the inside and relative outward movement of atoms on the outer arc, corresponding to the expansion and contraction of molecules.

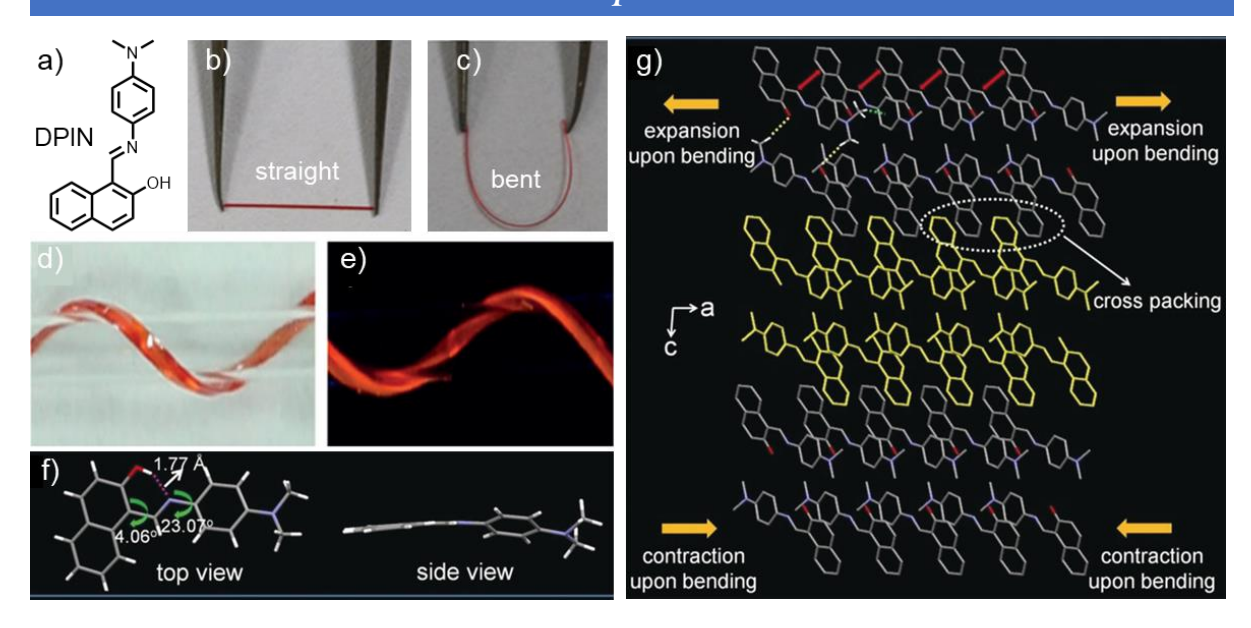


**Figure 1.28.** a) Molecular structure of DPIN molecule. b,c) Photographs of straight and bent DPIN crystals. d,e) Photographs of screwed crystals on a glass tube under normal and UV light, respectively. f) Top and side view of DPIN in the crystal packing. g) Molecular packing along the bending (002) plane. The arrows indicate the expansion and contraction of molecules in the criss-cross layers. Figure adapted from ref. 185.

#### 1.6.1.3 Pseudo-plastically bendable organic crystals

In 2020, Annadhasan *et al.* reported a peculiar observation of irreversible mechanical deformation of elastic microcrystals and termed them as '*pseudo-plastic*' crystals.<sup>174</sup> Even though the phenomenon of curved structures and geometries during self-assembly of organic molecules is not new, <sup>48,94,187,188</sup> the peculiar mechanical response of microcrystals on the substrate is intriguing. The phenomenon is particularly important from a classical physics point of view as it resembles the situation of a man standing on the earth is not thrown into space as the earth revolves around the sun. The reason for pseudo-plastic behaviour can be understood from two important interactions, i. The crystal shape regaining energy: as elastically bent crystal attempts to retain its original geometry, ii. The crystal surface and substrate's adhesive interactions (CSSI) and to what extent the crystal is adhered onto the substrate (Figure 1.29). Therefore, the CSSI plays a major role in the described phenomenon. Therefore, the microcrystal exhibits pseudo-plasticity when CSSI is greater than the crystal's shape regaining energy. Otherwise, it shows normal elastic behaviour.

#### 1.6.2 Mechanophotonics

The construction of PICs using organic materials necessitates the shaping, bending, positioning, and integration of two or more optical waveguides/components. In Si photonics, the same is achieved by EBL or patterning techniques.<sup>24</sup> However, such techniques cannot be employed for organic materials, particularly organic crystals due to their limited chemical

and thermal resistance. Organic crystals are prone to surface and/or bulk damage when exposed to direct high-energy electron/plasma beams. The harsh post-processing conditions employed in EBL or photolithography, during etching of resists with strong acids or solvents (like acetone) for removal of residual debris might damage/dissolve the organic materials. Therefore, a need for alternative methods for fabricating organic photonic components and circuits is necessary. Recently, focused ion beam (FIB) milling has been deployed to carve 2D crystalline materials into desired photonic modules. However, in the FIB technique, the components adhere strongly to the substrate and it is difficult to translocate the modules from one place to another. Thus, restricting its use for hybrid PICs fabrication. An innovative approach to manufacturing organic PICs requires a mechanical manipulation technique where organic crystals can be precisely molded and integrated into desired photonic shapes. Conventional mechanical manipulation techniques like three-point bending are hard to employ for PICs fabrication due to the miniaturization requirement. Hence, a micromanipulation strategy must be devised to construct OPICs from flexible crystals.

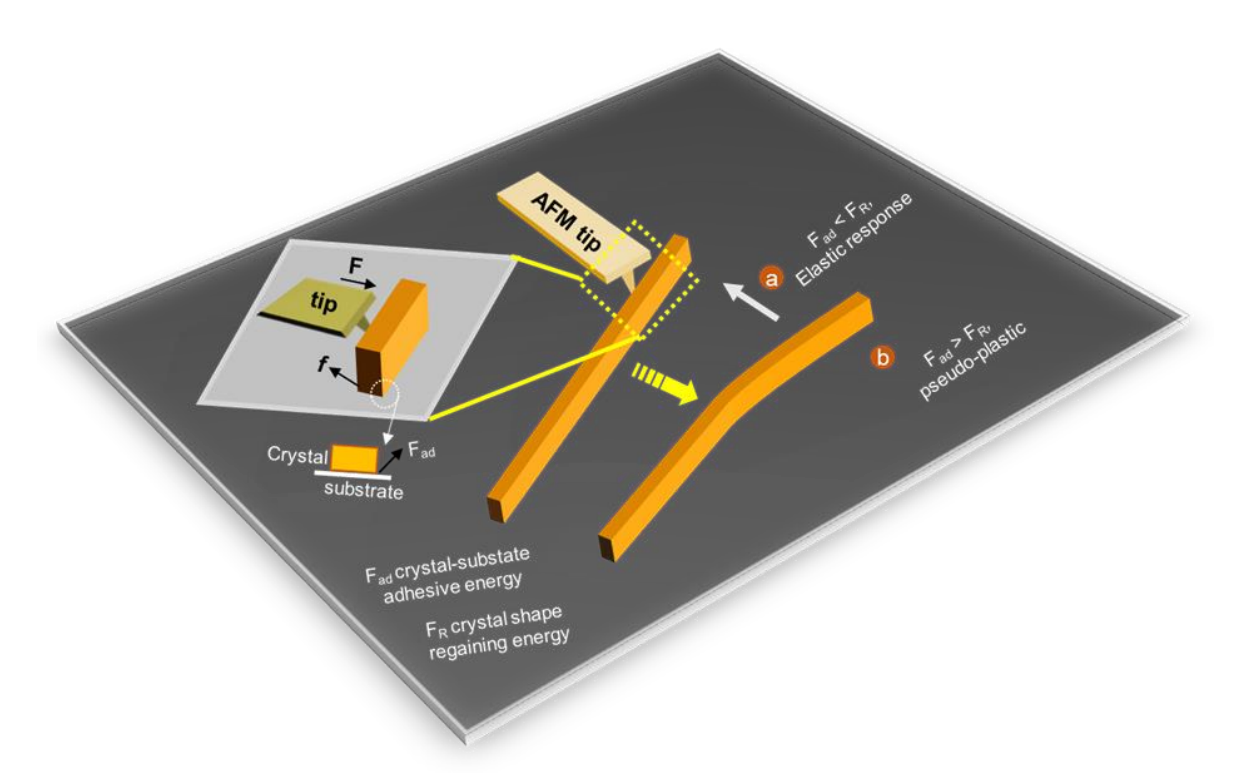


**Figure 1.29.** Graphical illustration of the origin of pseudo-plastic behaviour in organic crystals. F is the force applied by tip on the crystal, f is the frictional force,  $F_{ad}$  and  $F_{R}$  are crystal surface-substrate adhesive and shape regaining energies of elastic crystal, respectively. Case a, represents elastic response ( $F_{R} > F_{ad}$ ) on the substrate whereas case b, represents pseudo-plastic behaviour ( $F_{R} < F_{ad}$ ).

Prof. Chandrasekar's group envisaged the usage of a well-known AFM cantilever tip for manipulating microstructures via different micromechanical operations shown in Figure

1.30.<sup>193</sup> In 2014, they demonstrated *lifting* of 2,2',6,6'- tetra(1H-pyrazol-1-yl)-4,4'-bipyridine, TBP microcrystals using AFM-tip to prove light propagation inside the organic microtubes (Figure 1.30, inset labelled as 1). 194 Thereby, the ambiguity regarding the role of substrate in light propagation through organic microstructures was cleared. Later, in 2016, the same group reported the *cutting* micromechanical operation to illustrate the axial FP modes in 4-(Dicyanomethylene)-2-methyl-6 -(4-dimethylaminostyryl) -4H-pyran, DCM dye microresonators (Figure 1.30, inset labelled as 2). 195 The DCM dye microcrystal was precisely cut into three-crystals of various lengths and their optical modes were studied. The cutting micromechanical operation is useful for shaping the microcrystals into desired shapes and sizes. In the year 2020, they tested the mechanical compliance of elastically flexible dithieno[3,2-a: 2',3'-c]phenazine, DTP crystals on a silica substrate. The microcrystals were subjected to minute mechanical force with the use of AFM-tip. Surprisingly, the elastic crystals on the glass-substrate exhibit pseudo-plastic behavior described in section 1.6.1.3. Further, the pseudo-plastically bent crystals were aligned using aligning/integrating micromechanical tool into a 2×2 DC to fabricate the first organic crystal-based photonic component (Figure 1.30, inset labelled as 3). <sup>174</sup> In 2020, the same group illustrated the

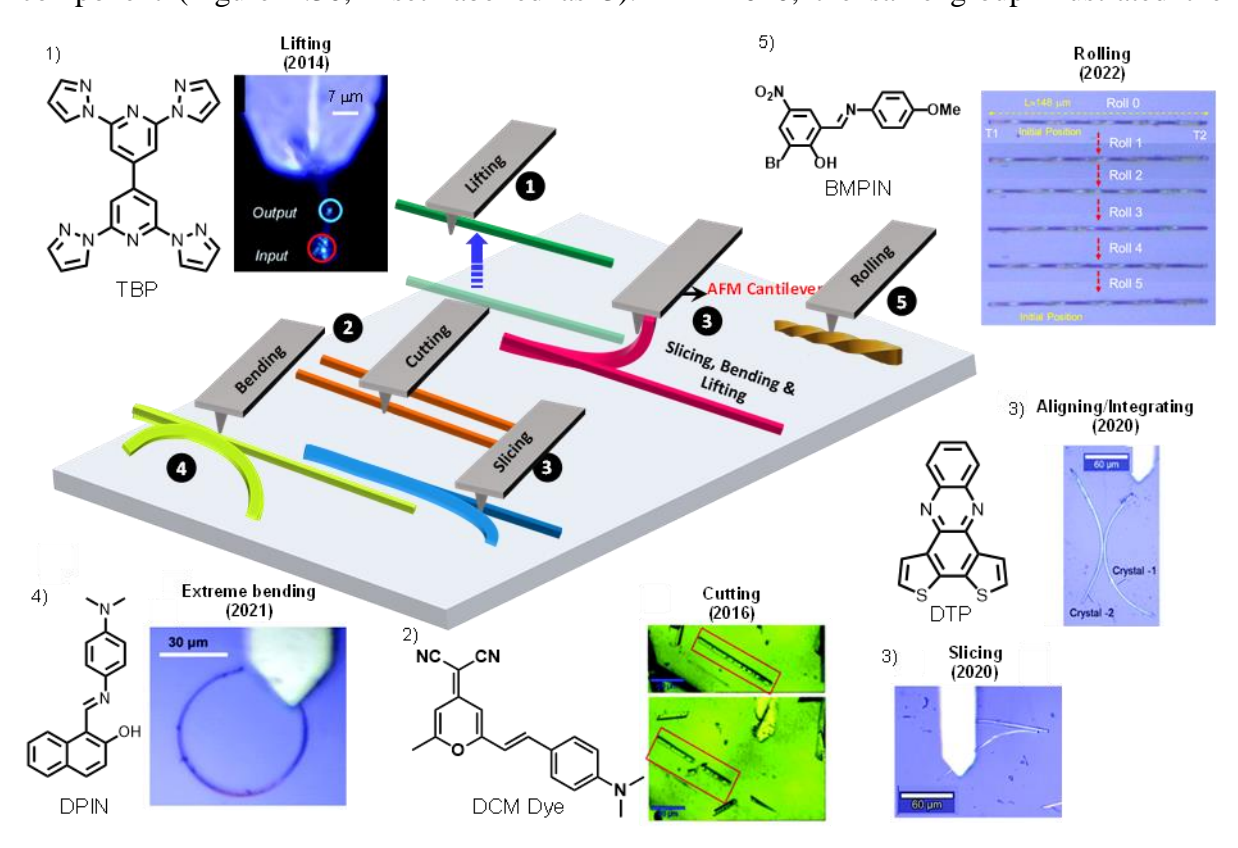


**Figure 1.30.** The schematic illustration of various micromechanical operations used for the mechanophotonics technique, in chronological order 1-5, *lifting*, *cutting*, *slicing/aligning*, *extreme bending and rolling*, respectively. Figure adapted from ref. 174, 193-196.

construction of extremely strained geometries such as circular RRs from (E)-1-(4-(dimethylamino)- phenyl) imino-methyl-2-hydroxyl-naphthalene, DPIN microcrystals using the *extreme bending* micromanipulation operation (Figure 1.30, inset labelled as 4). Later in 2022, the same group demonstrated the rolling of (E)-2-bromo-6-((4-methoxyphenyl)imino)methyl) -4-nitrophenol, BMPIN microcrystals using the *rolling* operation which was supported by the twisted geometries (Figure 1.30, inset labelled as 5).

#### 1.6.3 Organic flexible waveguides

Optical waveguides can be used to build photonic circuits and networks. The waveguides must allow mechanical deformability to guide light in desired pathways to construct complex optical circuitry and hence require flexible waveguides. In 2005, the first organic active waveguide was reported by Takazawa et al. 56 They used 3-ethyl-2-[(3-ethyl-2 (3H)-benzothiazolylidene) methyl]-benzothiazolium iodide (thiacyanine, TC) dye nanofibers, self-assembled from water (0.2 mM TC-dye solution) to obtain fiber-shaped aggregates (Figure 1.31a). These as-grown aggregates (up to 300 µm long and 200 nm to a few microns wide) comprised deformed geometries that were capable of transducing active FL signal when excited optically using laser light (Figure 1.31c,d). The FL intensity decreases as the optical path length increases. The outcoupled light intensity in the waveguide has significant reabsorption of higher frequencies (505 nm) compared to lower frequencies (520 – 540 nm) possibly due to the overlay of TC-dye's absorption with its emission in the solid-state (Figure 1.31e). Along with active waveguides, passive waveguides (analogous to Si-waveguides) are also important for the construction of OPICs. The first flexible passive waveguide was reported by Chandrasekhar et al. in 2013 using the BPP microcrystals obtained via the selfassembly approach (Figure 1.31b).<sup>55</sup> The controlled self-assembly of BPP molecules in dichloromethane yielded microtubular structures of varying diameters from submicron (800 nm) to 1.5 µm and convenient lengths (Figure 1.31h). The molecular growth strategy produced microstructures of linear, curved, cross-shaped and tip-to-tip attached geometries. The photonic studies on a 180° naturally bent crystal-geometry, confirmed guiding of the same 488 nm incident light to the other end of the bent microcrystal to exhibit the passive waveguiding in these microcrystal (Figure 1.31i). The microcrystal transports the same incident light towards both the tips irrespective of the excitation position (Figure 1.31j,k). The transmission electron microscopy images (TEM-images) and selected area diffraction pattern correlates the crystalline nature of BPP microstructures (Figure 1.31f,g).

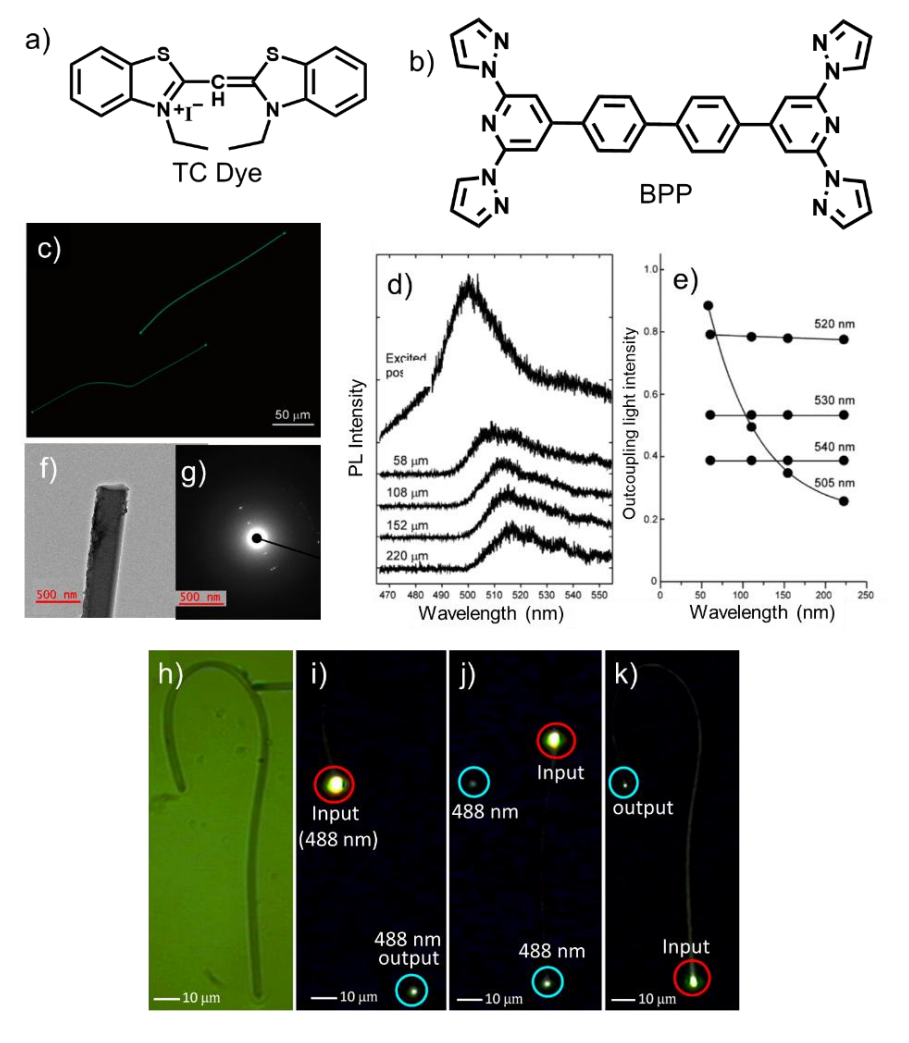


**Figure 1.31.** Chemical structure of a) TC dye and b) BPP molecules, respectively. c) Confocal FL microscope image of TC dye fibres, d) Spatially resolved PL spectra of the excited position and outcoupling light by excitation at a distance of 58-220 µm from the TC dye nano fiber end, and e) PL intensity of the outcoupling light at several wavelengths as a function of the guided distance. f) Confocal optical image of naturally bent BPP microcrystal. f) TEM image and g) selected area diffraction pattern of BPP microcrystal. i-k) Laser confocal microscope images depicting waveguiding in naturally bent BPP crystal excited at different points on the microcrystal. Figure adapted from ref. 55 and 56.

#### 1.6.4 Bending-induced FL changes

The observation of mechanical flexibility in organic crystals itself was fascinating to researchers and little attention was paid to the influence of molecular level changes on electronic properties. The expansion and contraction of the molecules on the outer and inner arc may lead to subtle changes in the electronic structure and orbital contributions. Thus, a non-negligible electronic effect should be observable. In 2020, Hayashi *et al.* reported the relative change in FL emission at the outer arc (506 nm) and inner arc (497 nm) relative to the centre (505 nm) of a mechanically bent DBA crystal. <sup>197</sup> The FL shifts were attributed to the anisotropic Poisson's effect (ratio of relative contraction to relative expansion in a material). In the same year, Bhattacharya and coworkers reported the FL enhancement in the

plastically deformed green fluorescent protein analogue-based crystal relative to unstrained crystal. Similar observations were made by Wang *et al.* recently. They observed a 20 nm shift in fluorescence of the elastically bent dimethyl 2,5-bis((2-bromo-5-(trifluororomethyl)phenyl)amino)terephthalate (DBBTPAT) crystal in comparison to the native straight crystal. These results point at the influence of mechanical bending on photonic properties of organic crystals.

In 2022, Yamamoto *et al.* reported the mechanically tuneable optical micro-resonator. Here they have chosen elastically bendable DPBA crystals (Figure 1.32a).<sup>200</sup> The rectangular microcrystals exhibited decent optical waveguiding properties under optical excitation

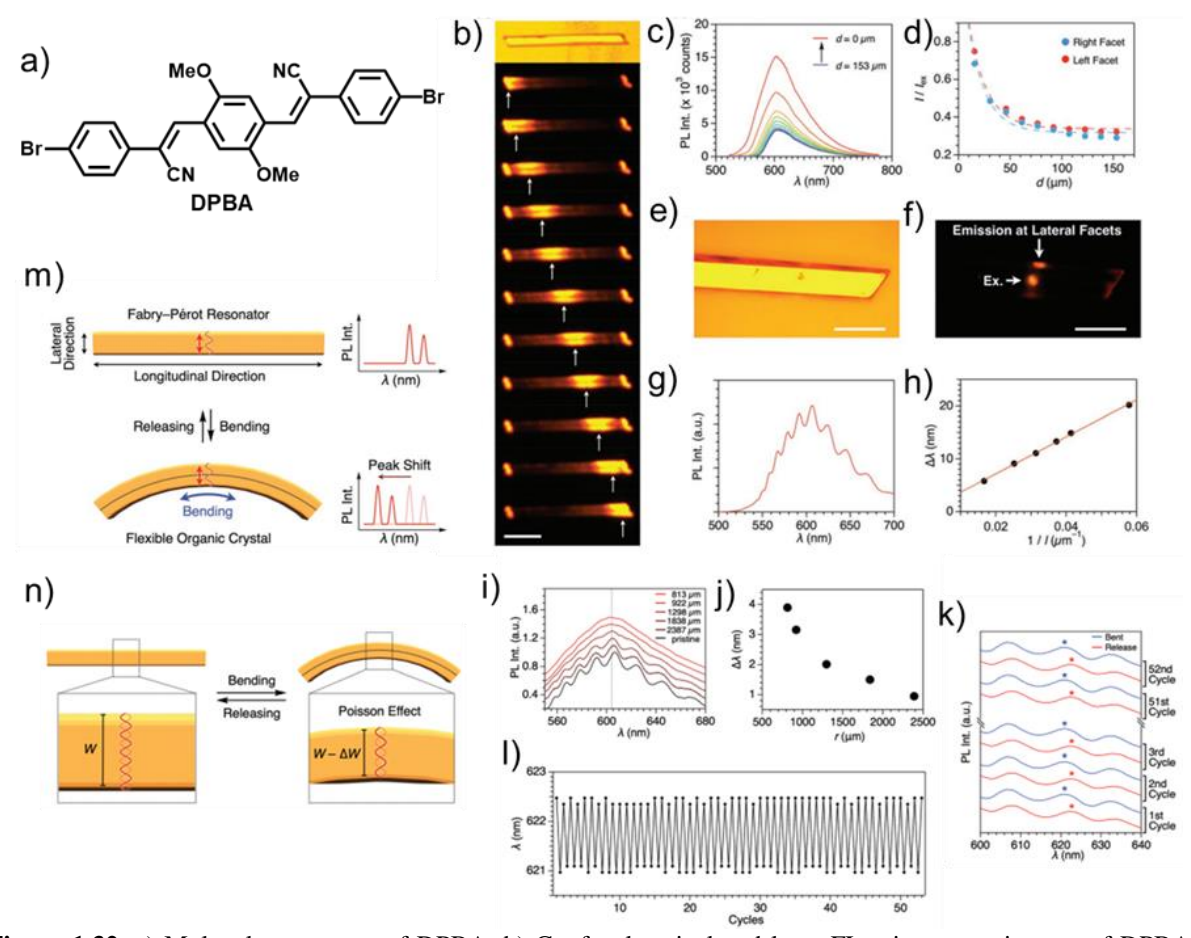


**Figure 1.32.** a) Molecular structure of DPBA. b) Confocal optical and laser FL microscope images of DPBA microcrystals. c) FL spectra obtained at a fixed end for laser excitations at various points on the crystal. d) Comparison of the optical loss variation for FL collection at both the ends of the crystal. e,f) Confocal optical and laser FL images of DPAB microcrystal to show lateral excitation. g) FL spectra collected on the lateral edge of the DPAB microcrystal shown in e. h) Plot of free spectral range, FSR ( $\Delta\lambda$ ) versus 1/optical path length. i) FL spectra collected as a function of bending radius, r, in the mechanically bent DPAB microcavity. j) Plot depicting the relative peak shift vs bending radius. k) PL spectra of single DPAB crystal upon multiple mechanical bending (blue curves) and releasing (red curves). m) Graphics explaining the mechanically flexible organic crystal exhibiting reversible resonance peak shift toward shorter wavelength by the Poisson effect upon mechanical bending. n) Schematic illustration of bent and relaxed DPAB crystal and the Poisson's effect. Figure adapted from ref. 200.

(Figure 1.32b-d). The lateral FP micro-resonator property was confirmed from the optical modes recorded on the lateral end of DPBA microcrystal (Figure 1.32e-g). The lateral-type FP characteristics were confirmed from decreasing FSR of optical modes in DPBA microresonators as the width increased (Figure 1.32h). To understand the influence of mechanical bending on the longitudinal resonator activity, one end of a 1.5 milli meter long crystal was fixed to the substrate. The FL spectra were collected in the straight geometry and mechanically bent geometry at the same position on the crystal. Interestingly, the optical resonances were observed to be blue-shifted in the strained geometry relative to the straight micro-resonator (Figure 1.32i). Importantly, the shift in optical resonances was reversible with mechanical bending and straightening up to 50 cycles (Figure 1.32l,k). The mechanical tuning of optical modes was ascribed to the Poisson's effect during bending. The contributions from minor changes in the n observed during mechanical bending towards the observed optical mode shift cannot be ignored (Figure 1.32m,n). The relative blue-shift upon bending compared to pristine crystal was inversely proportional to the width of the microresonator (Figure 1.32j). A clear understanding of mechanical bending effects on optical properties will be useful in constructing organic crystal-based IMs.

#### 1.6.5 Organic optical components and circuits

The use of organic crystals for photonic circuits was not considered serious until recent past. However, attempts were made as early as 2005 by researchers to construct organic fiber-based optical components like IM, RRs and add-drop filters, etc. which will be discussed in coming sections.

#### 1.6.5.1 Organic crystal-based 2×2 directional couplers

Despite the knowledge of organic flexible active and passive waveguides by the year 2012, the construction of organic crystal-based optical components was long pending due to the dearth of a suitable micro-processing technique that allows precise positioning of these delicate microcrystals on a chip or substrate. In 2020, Annadhasan *et al.* successfully constructed the first organic flexible crystal-based directional coupler by utilizing the 'integrating/aligning' micromechanical operational tool discussed in the earlier section. The authors used elastically flexible DTP crystals displaying pseudoplastic behavior on a glass substrate (Figure 1.33a, the pseudo-plasticity was described in section 1.6.1.3). The waveguiding properties of DTP microcrystals of  $L \approx 206$  and 75  $\mu$ m were established in the straight geometry. Later, the tip-to-tip distance was adjusted to 156 and 67  $\mu$ m in the bigger and smaller microcrystals, respectively.

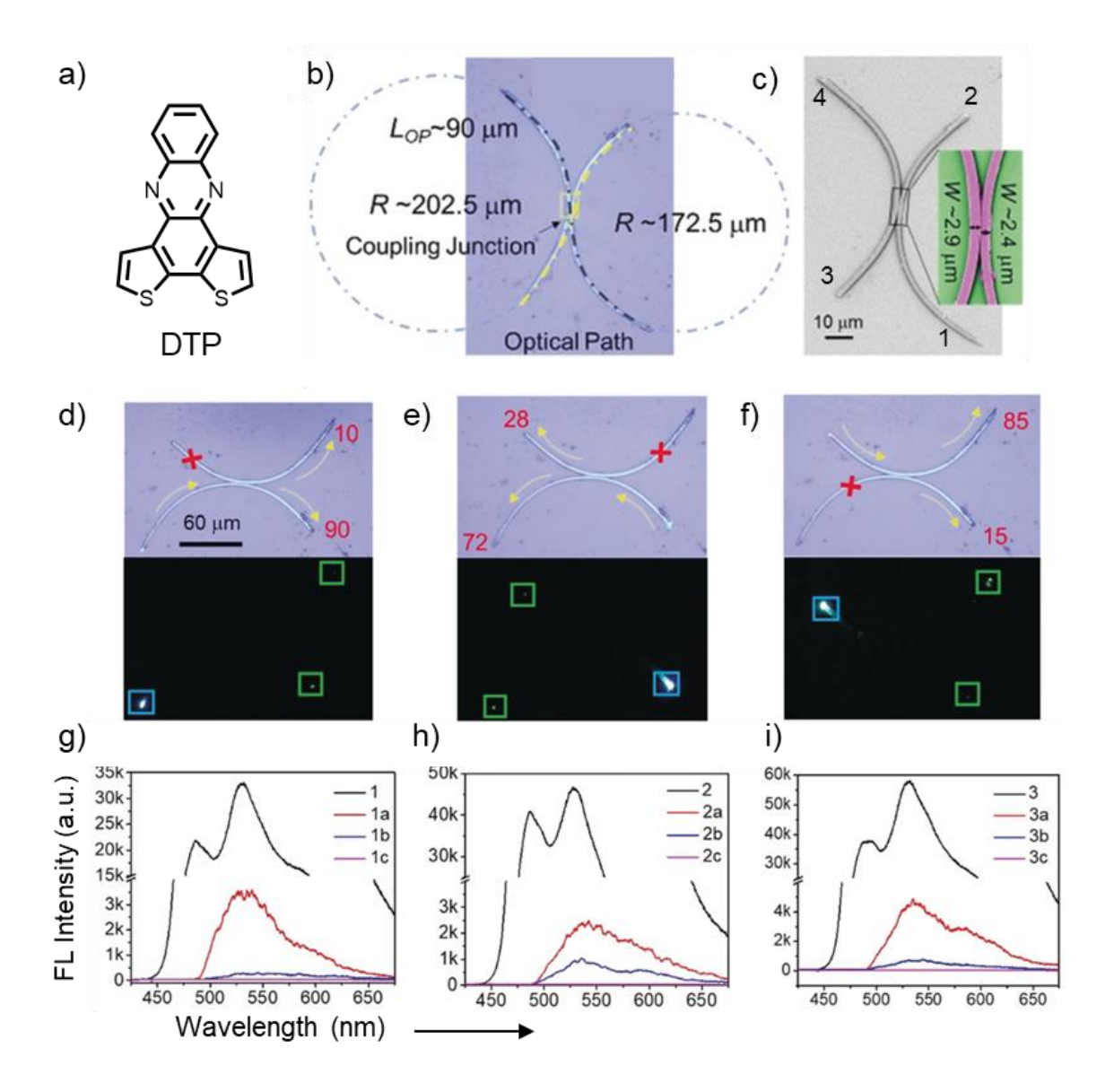


**Figure 1.33.** a) Molecular structure of DTP. b) Optical microscope image of organic directional coupler (DC) fabricated from DTP microcrystals. c) FESEM image of constructed DC. The inset shows false color-coded FESEM image of the junction. d-f) Confocal optical and FL microscope images of DC when excited at 1-3 positions depicted in c, respectively. The yellow arrows indicate the optical signal propagation direction, and the numbers represent the signals' split ratio. Blue and green rectangular boxes correspond to excitation and FL collection points, respectively. g-i) The corresponding FL spectra were recorded at various positions when excited at 1-3, respectively. Figure adapted from ref. 174.

These mechanically deformed microcrystals were brought into optical contact by 'integrating/aligning' micromechanical operation to realizeorganic 2×2 DC (Figure 1.33b). The FESEM image of the DC shows the close contact between the two microcrystals and the four ports are labelled 1-4, respectively (Figure 1.33c). The optical excitation of terminal 1 produces green FL of DTP at the contact point and the same light travels to the other end of the same waveguide at terminal 2 (Figure 1.33d). As the signal crosses the junction, part of

the green light evanescently couples into the smaller waveguide and is reflected at terminal 4. The intensity of the light observed at forward ports varied as the light was split in the ratio 90/10 at terminals 2 and 4, respectively (Figure 1.33g). But no light signal moves towards terminal 3 due to restricted optical path trajectory. The excitation of termini 2 and 3 produced optical signals with split ratios of 72/28 and 85/15, respectively at the forward termini (Figure 1.33e,f,h,i).

#### **1.6.5.2 Organic IM**

IMs are necessary for mode filtering and related applications in PICs. 44 The idea of constructing an asymmetric Mach Zehnder IM (aMZI) using organic fibers first originated in 2013 from Takazawa and coworkers. 201 The aMZI requires light propagating along two different lengths to interact which creates an interference pattern because of the phase difference instigated by the delay in both optical signals. They used TC-dye nanofibers of width 210 nm for this purpose, and the light travels through these nanofibers via the exciton-polariton propagation mechanism (Figure 1.34a,b). Typically, a straight nanofiber dispersed in oil on a glass substrate was brought into evanescent contact with another nanofiber using a micromanipulator (Figure 1.34c). The shape of the longer fiber was such that it created a loop

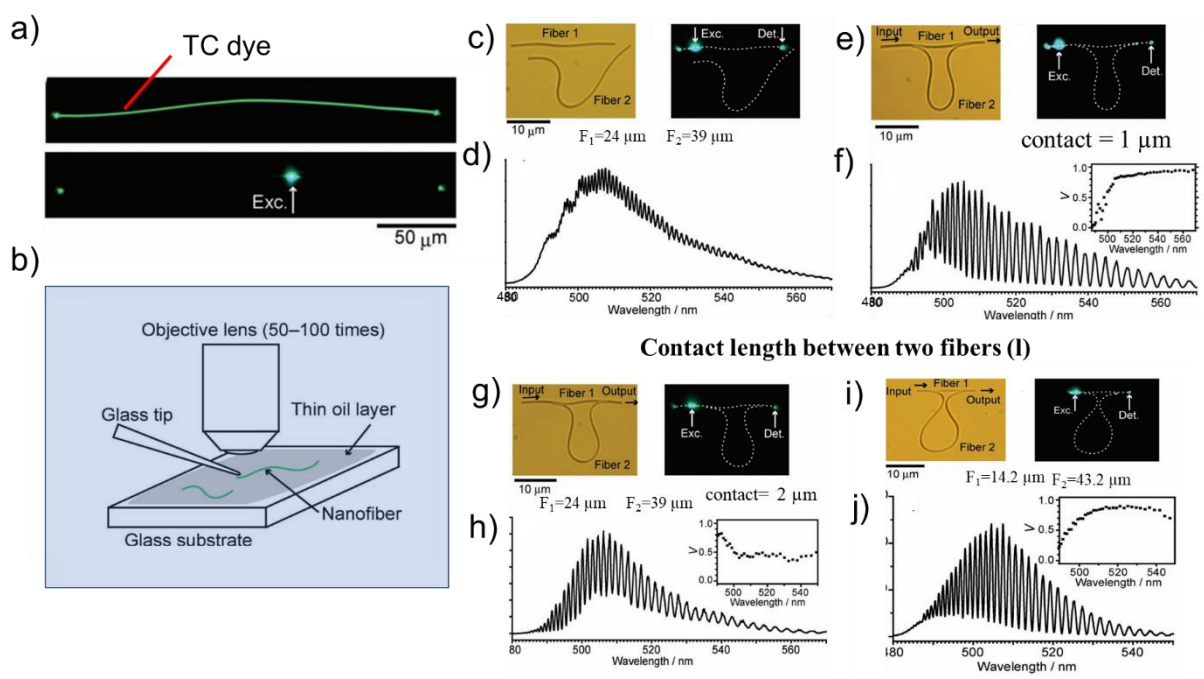


**Figure 1.34.** a) FL microscope and laser FL microscope images of TC dye nano fiber. b) Experimental setup used for the demonstration of organic asymmetric Mach-Zehnder IM (aMZI), glass tip for manipulation and a thin layer of oil as lubricant between substrate and nanofiber. The optical and FL microscope images c) before and e) after integration of two TC dye nano fibers to realize organic aMZI and d,f) their corresponding FL spectra before and after integration, respectively. The optical and FL microscope images of IM when contact length in organic aMZI is g) 2  $\mu$ m and i) 1  $\mu$ m and h, j) their respective FL spectra, respectively. Figure adapted from ref. 201.

structure with the earlier fiber (Figure 1.34d). Thereby creating two light propagation pathways, i) one a shorter straight pathway along the smaller fiber and ii) a longer pathway along the bent nanofiber (Figure 1.34e,f). When one end of the structure was optically illuminated, the generated optical signal propagated in both fibers before interacting at the contact region in the aMZI to produce interference. The interference pattern changes with the variation in the contact length, or the length of the fiber as depicted in Figure 1.34g-j. However, this study ignores the effect of oil (n > 1.5) on the optical modes and the influence of strain on the resonance peaks or interference pattern due to the n perturbation created on the nanofiber because of mechanical bending. Therefore, a clear understanding of the underlying physics to prove the interference phenomenon in the organic crystal-based optical modules is necessary.

#### 1.6.5.3 Add-on-drop filters

Takazawa et al. demonstrated the fabrication of a miniature RR and its applications in wavelength mode filtering desired for sensing devices. 202 The researchers created an add-drop filter using an active type waveguide and a RR with specific dimensions from TC dye nanofibers. The length of the waveguide used in the fabrication of the add-drop filter was 19.3 µm, while the RR had a length of 13.8 µm (Figure 1.35a). The purpose of the ring resonator in this context is to filter wavelength modes in an optical waveguide and to govern the optical signal's trajectory in either clockwise or counterclockwise direction, which is important for various applications including sensors. In this device, the input/output (I/O) bus channel operates by circulating EPs through the straight bus fiber that is coupled to the RR coupling (Figure 1.35c). At the zone, the **EPs** from the ring interfere constructively/destructively with the EPs from the straight bus fiber to alter the course of optical modes. The researchers excited the left terminal of the fiber and collected the resultant spectra at the opposite right terminal. The experimental results showed a sequence of sharp dips in the spectrum at  $\lambda > \approx 530$  nm before and after the coupling of the bus waveguide to RR due to interference (Figure 1.35b,d). These dips corresponded to the RR optical modes, with a small shift in their peak positions. On the other hand, for  $\lambda < \approx 505$  nm, the spectrum exhibited FP modes of the bus waveguide, suggesting that there was a coupling between the fiber and the RR in the device's operational wavelength range.

The first organic flexible crystal-based organic add-drop filter was reported by Ravi *et al.* The DPIN crystals possessed an absorption up to 600 nm and the FL extended till 780 nm with a  $\lambda_{max}$  at 605 nm (Figure 1.35e,g).<sup>203</sup> The elastic DPIN crystals were bent into a circular-

shaped RR of diameter 59  $\mu$ m facilitated by the expansion and contraction of molecules on the outer and inner periphery of the microcrystal (Figure 1.35f). Later, this RR was integrated with two bus waveguides of lengths 285 and 162  $\mu$ m on top (OW3, thickness 4.8  $\mu$ m) and bottom (OW2, thickness 3.4  $\mu$ m) of the RR, respectively, to realize the flexible crystal-based add-drop filter (Figure 1.35h). The excitation of any of the termini labelled Port-1-4 results in an optical output at two ports namely, a straight-through port and a drop the port, while no signal is observed at the other port. The optical illumination of Port-4 produced a red FL of DPIN corresponding to an  $\lambda$ (A)  $\approx$ 525-780 nm and the same propagates to other end of OW3 as a reabsorbed signal with filtered higher wavelengths as  $-\lambda$ (A)  $\approx$ 525-780nm signal at Port-3 (Figure 1.35l,q). As the active signal propagates in OW3 at the contact point of OW3 and RR,

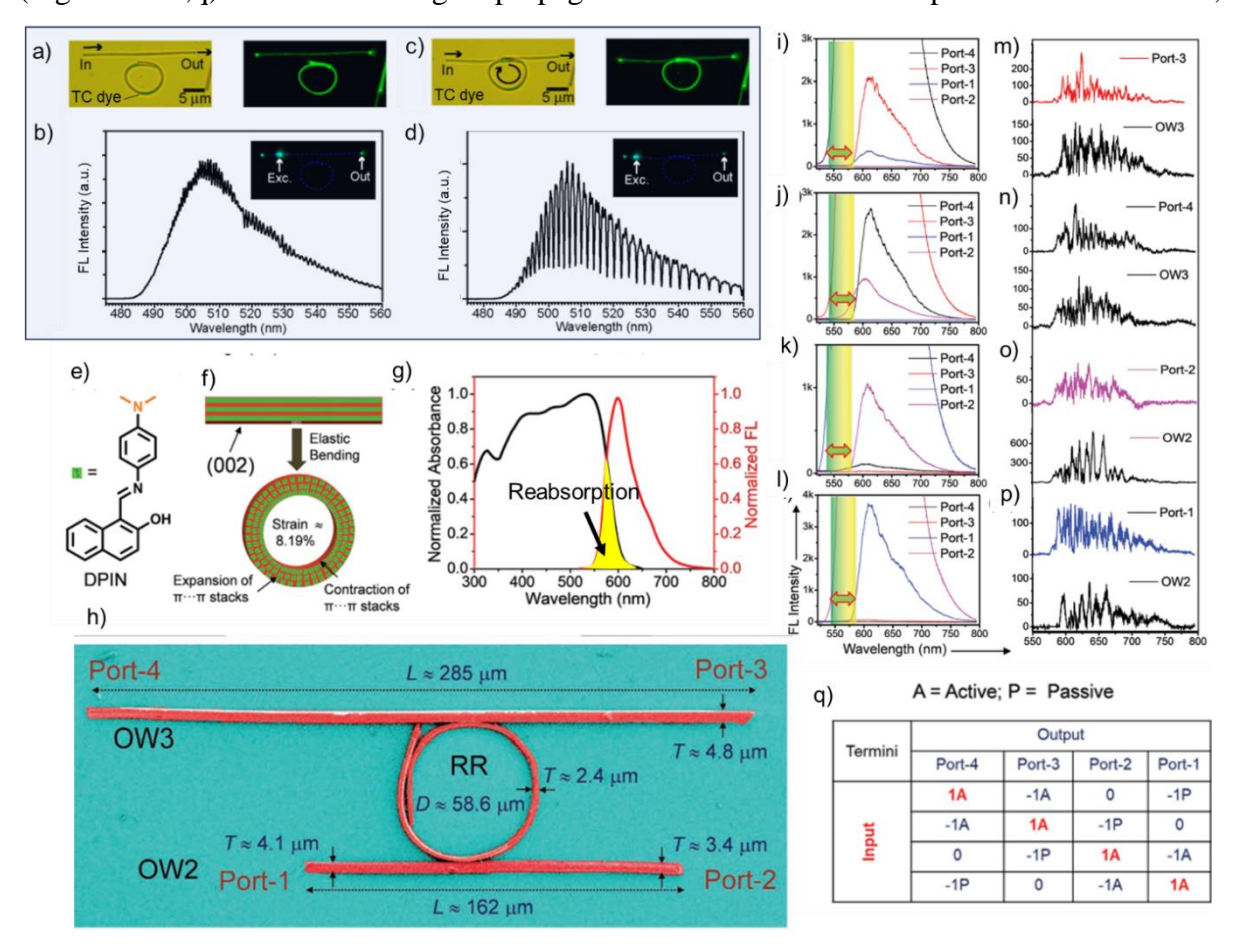


**Figure 1.35.** a,c) Confocal optical and FL microscope images before and after coupling of nanofiber waveguide with ring resonator (RR) for realizing TC dye-based add-drop filter. The FL spectra collected in the waveguide b) before and d) after integration of RR with the waveguide. e) Molecular structure of DPIN. f) Graphical representation of molecular arrangement in the straight and extremely bent DPIN crystal. g) The solid-state absorption and emission spectra depicting the chances of reabsorption (yellow region) in DPIN. h) The color-coded FESEM image of the fabricated add-drop filter using the mechanophotonics approach. i-l) The FL spectra collected at various ports when excited at ports 1-4, respectively and m-p) comparison of optical modes in uncoupled waveguides and add-drop filter, respectively. q) Tabulation of various optical signals at different ports 1-4 for light input at 1-4, respectively. Figures adopted from ref. 202 and 203.

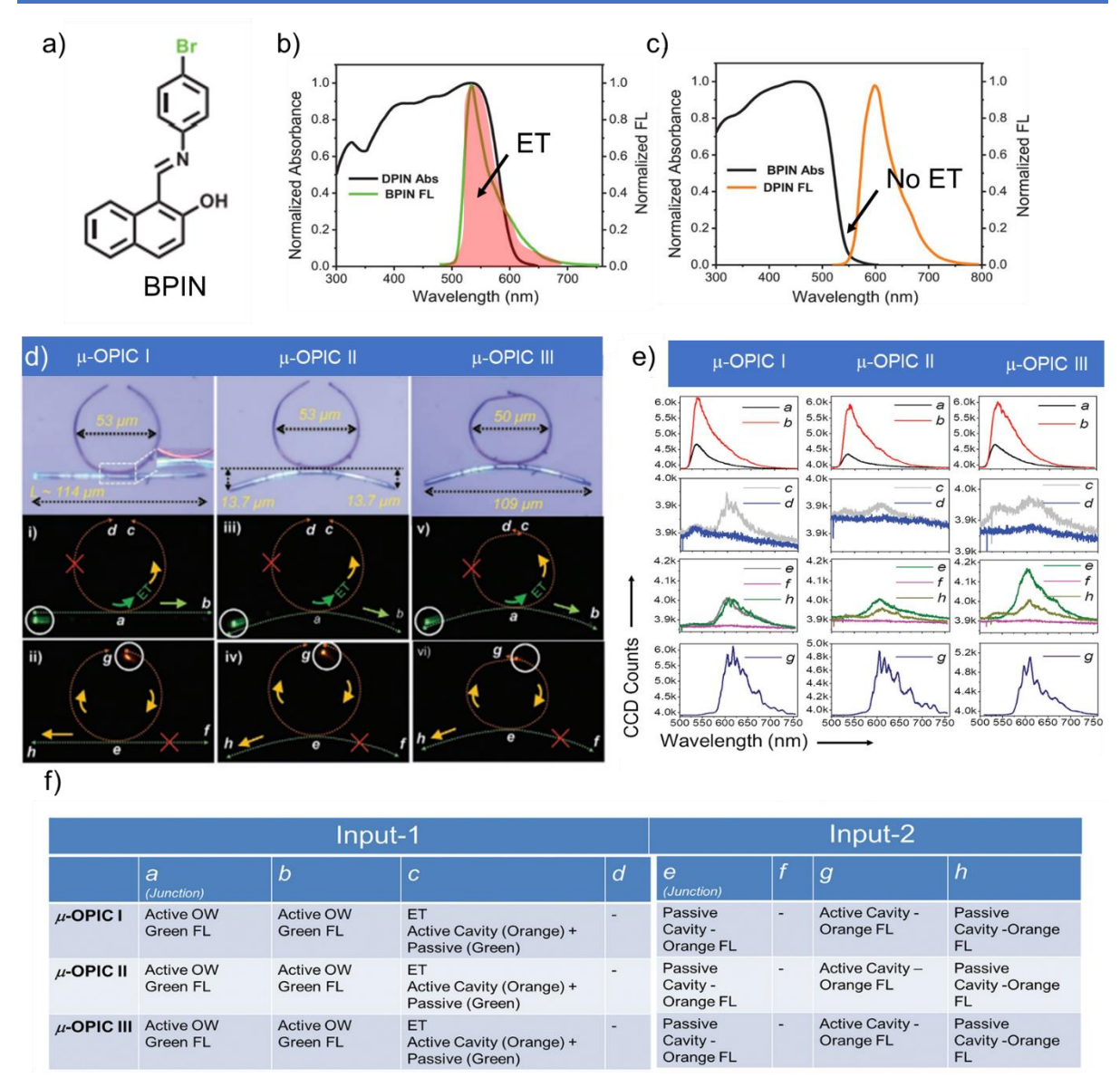


**Figure 1.36.** a) Molecular structure of BPIN. b,c) The solid-state optical characteristics of DPIN and BPIN depicting radiative intermolecular energy transfer (ET) and no ET possibility from BPIN to DPIN crystals. d) The fabricated hybrid micro-organic photonic integrated circuits ( $\mu$ -OPICs) I-III using DPIN and BPIN microcrystals via the mechanophotonics technique. The yellow arrows indicate the light propagation directions. e,f) The optical performance and operational mechanisms in  $\mu$ -OPICs I-III, respectively. Figure adapted from ref. 176.

a portion of the active signal enters the RR evanescently and travels in the clockwise direction. This evanescently coupled light further undergoes one more evanescent coupling at the RR and OW2 junction and enters the OW2 to reflect the same reabsorbed light as a passive signal at Port-1. The clockwise directionality of the RRdoes not allow light to enter the other half of OW2; hence, no optical signal is detected at Port-2. The optical modes observed in the add-drop filter relative to the uncoupled waveguide exhibit a distinctive pattern due to the optical interference possible when the RR circulates the optical signal inside it (Figure 1.35m-p). Similar optical behaviour is observed at all other ports depending

on the clockwise or counterclockwise rotation of light and the light response when excited at other ports is provided in table q (Figure 1.35j-l). Therefore, the authors successfully demonstrated an organic add-drop filter with a long-pass filter effect.

#### 1.6.5.4 Organic photonic integrated circuits (OPICs)

The fabrication of hybrid photonic circuits in silicon-photonics involves numerous fabrication steps and clear design. The implantation of different materials on the chip using multiple patterning techniques with extreme care makes it a tedious and commercially costlier job. On the other hand, easy optical bandwidth tunability in organic compounds with already known plentiful crystals of various optical and physical attributes makes them good candidates for hybrid photonic applications. The availability of mechanophotonics technique allows the transfer of crystals from one substrate to another necessary for hybrid photonic circuit construction. Ravi et al. in 2021, demonstrated the first organic crystal-based hybrid OPIC. The authors employed green emissive BPIN and red emissive DPIN crystals (Figure 1.36a). 176 The apt choice of crystals prompted the energy transfer (ET) from BPIN to DPIN as the emission of earlier intersected with the latter (Figure 1.36b,c). Firstly, the elastic flexibility of DPIN allowed the construction of a circular loop. Then a BPIN crystal from a different substrate was transferred to the circular loop's place using transfer micromechanical operation. Later, both the crystals were integrated by appropriate positioning of the crystals. The photonic studies suggested selective guiding of light inside the OPIC-1 via active, passive and ET mechanisms (Figure 1.36d). The optical illumination of left end of BPIN in OPIC-1 resulted in an active signal (green, active waveguiding) at b, and active signal (due to ET) at c (Figure 1.36e,f). However, no light output is observed at d due to the forbidden light pathway. The mechanical flexibility allowed the reconfiguration of DPIN and BPIN to result in OPIC-II and OPIC-III, which also exhibited similar optical properties as shown by OPIC-1. These results suggest the advantages of organic crystals over inorganic materials for photonic device applications. Moreover, these results inspire the photonic community to work rigorously towards the demonstration of programmable organic photonic circuits, which are highly possible with suitable materials (organic flexible crystals) and techniques (mechanophotonics).

#### 1.7 Overview of the thesis

This thesis outlines the construction of various optical components crucial for organic photonic integrated circuits (OPICs). The recent technological advancements in the burgeoning field of photonics have witnessed tremendous achievements including

programmable photonic circuits, quantum information processing, faster, efficient and safer data transfer technologies utilizing Si or Si-based PICs. 5-7,19 These industrially advantageous materials lack mechanical flexibility (due to high  $E \approx 180$  GPa) and hamper the spontaneous reconfigurability of the fabricated circuits.<sup>29</sup> The isotropic crystal packing in silica or the amorphous nature of Si does not allow frequency doubling characteristics in the Si-based photonic circuits and deter their utility in NLO photonic circuit technologies. 53 The large  $E_B$ of these semiconductor materials mostly allows passive (restricting other possible pathways like active, reabsorption or energy transfer, ET, mechanisms) signal transmission. Therefore, the majority of Si-PICs are monolithic in nature. However, it is difficult for monolithic circuits to meet the stringent needs of advanced quantum technologies.<sup>4</sup> The fabrication of hybrid Si photonic circuits from inorganic semiconductor materials requires the growth of different materials on a chip using lithography or vapor deposition techniques. Such fabrication methods are highly sensitive and become economically saddling.<sup>29</sup> These problems can be addressed using alternative materials platforms like crystalline organic flexible materials. However, the concept of Moore's limit customarily indicates the need for miniaturization and currently there is no relevant analogous technology, like the EBL implemented for Si-PICs, to carry out organic PICs fabrication.

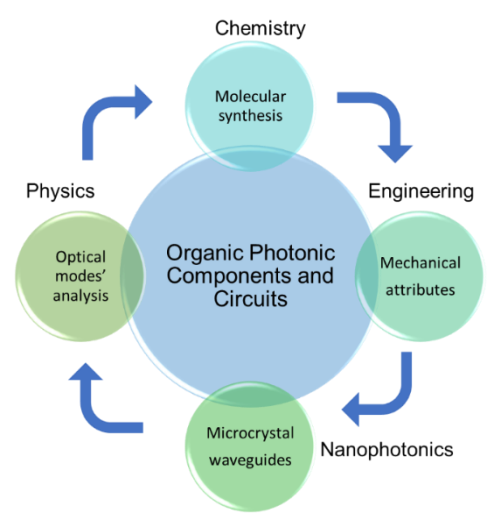


**Figure 1.37.** Schematic representation of the work flow adapted in this thesis.

The recent exploration of *mechanophotonics* technique with the aid of AFM cantilever tip to explore the pseudo-plastic nature of flexible microcrystals serves as a tool to achieve reconfigurable OPICs. 193 The superior material characteristics exhibited by organic crystals in terms of cost-effective synthesis, tunable optical bandwidth, bulk NLO properties, light-weight attributes and mechanical flexibility make them potential alternatives to Si-based materials. 44 The construction of organic optical components requires

the fundamental understanding of the optical and mechanical attributes and how the material responds to external stress. These prerequisites compel a strong background in relevant research areas like chemistry, physics, materials science, and nanoscience engineering. Importantly, the design of mechanically flexible organic single molecular crystals is a

confronting endeavor because the structural basis for the mechanical properties in organic crystals is not clearly established.

The sporadic utility of organic crystal-based circuits for practical applications is mainly diminished by the limited photonic components available with organic crystals. As discussed in the introduction, so far, RRs, add-drop filters, modulators, and monolithic DCs have been constructed using flexible organic crystals. 176,174,203 The construction of practical utility or functional photonic devices needs various photonic components like interferometers (IMs), ring resonators (RRs), directional couplers (DCs), various waveguides (straight, bent, spiral, etc.), wavelength division multiplexers (WDMs), demultiplexers, modulators, etc. The fabrication of IM from organic crystals necessitates a complete understanding of mechanical bending-induced effects on the optical modes (Poisson effect). Therefore, a systematic study of mechanically manipulated fiber loop mirror (FLM) geometry is necessary. Hybrid optical components are crucial to implement multiple tasks with the same circuit geometry. Hence hybrid DCs (HDCs) will be central. The limited transparency of Si in the visible spectral region does not permit their usage in visible light communication devices. An alternative materials platform requires the demonstration of full visible bandwidth transduction through an organic WDM. The need to miniaturize the size of optical components expects compact packing of long waveguides into spiral waveguides (SWs) to ensure dense packing on a chip. The SWs guide light in clockwise or counterclockwise direction and are important to route in controlled paths. In this regard, the construction of organic crystal-based IM, multi-tasking capable HDC, multiple signal transducing composite organic WDM and organic SWs using the mechanophotonic principles are crucial. For that, the ability of organic crystal circuits to perform active, passive, reabsorption, and energy transfer mechanisms, together with mechanical reconfigurability, become vital.

The primary objective of this thesis is to design and develop innovative miniaturized organic optical components necessary for the construction of efficient OPICs from mechanically flexible organic crystals. This task requires a highly interdisciplinary approach showcased in Figure 1.37. The general strategy and work path followed toward the construction of envisioned optical components is presented in Figure 1.38b. The mechanical flexibility in organic crystals is attributed to the weak intermolecular interactions present in the crystal habit. Hence, the design of diverse FL molecules like (*E*)-1-(((5-bromopyridin-2-yl)imino)methyl)naphthalen-2-ol (BPyIN), (*Z*)-3-(3',5'-bis(trifluoromethyl)-[1,1'-biphenyl]-4-yl)-2-(4- methoxyphenyl)acrylonitrile (CF<sub>3</sub>OMe), (*Z*)-2- (3,5-bis(trifluoromethyl)phenyl)-3-

(7-methoxybenzo[c][1,2,5] thiadiazol-4-yl)acrylonitrile (BTD2CF<sub>3</sub>), and (*Z*)-3-(4-(9H-carbazol-9-yl)phenyl)-2-(3,5-bis(trifluoromethyl)phenyl)acrylonitrile (Cz-2CF<sub>3</sub>) with enriched supramolecular interactions governed by the presence of hetero-atoms like N, O, S, and halogen atoms (F, Br) impart weak non-covalent interactions provide the anticipated properties. Apart from these custom-designed molecules flexible waveguiding 4,4-bis(2,6-di(1H-pyrazol-1-yl)pyridin-4-yl)-biphenyl (BPP), 9,10-dibromoanthracene (DBA) and 4,7-bis(4-octylthiophen-2-yl)benzo[c][1,2,5]thiadiazole (BTD) will be used. The crystallization of these molecular crystals is expected to provide desired optical characteristics (absorbance and FL with high PLQY) and mechanical flexibility (with required pseudo-plasticity in micro-regime).

The development of hitherto unknown organic crystal-based IM having FLM geometry requires an extremely flexible crystal waveguide capable of effectively steering optical signals in extremely bent geometries. Therefore, a novel Schiff base type BPyIN molecule will be synthesized, which can provide crystal flexibility. The micromechanical manipulation of BPyIN microcrystal will be used to fabricate IM. The optical modes due to interference can be expected in the crystals' FLM geometry once the delayed and forward moving signals interact with each other. Later, the interference could be elaboratively understood by coupling another waveguide to the FLM in organic IM.

The fabrication of hybrid photonic components or circuits is tedious and very costly in Si photonics due to the complexity involved in the design strategy and the large number of steps involved in the fabrication process. On the other hand, with the aid of mechanophotonics technique both the cost and complexity of hybrid PIC fabrication can be drastically reduced. However, the challenge of micromechanical *transferring* of one microcrystal near the components' construction area persists. This crucial task is accomplished by employing the *lifting* micromechanical operation. The blue emissive CF<sub>3</sub>OMe can be micromechanically integrated to the green emissive BPyIN microcrystal. The input-selective output propagation pathway and variable signal generation via active, passive, reabsorption, and ET mechanisms in the HDC illustrate the multi-tasking capabilities required for reconfigurable and programmable photonic circuits.

Achieving organic crystal-based WDM is highly challenging as it requires the integration of three or more organic flexible microcrystals in one place. Importantly, it necessitates clever choice of crystals such that i) one of the crystals should act as both active and passive waveguide, ii) the emission of three crystals should be different and cover the

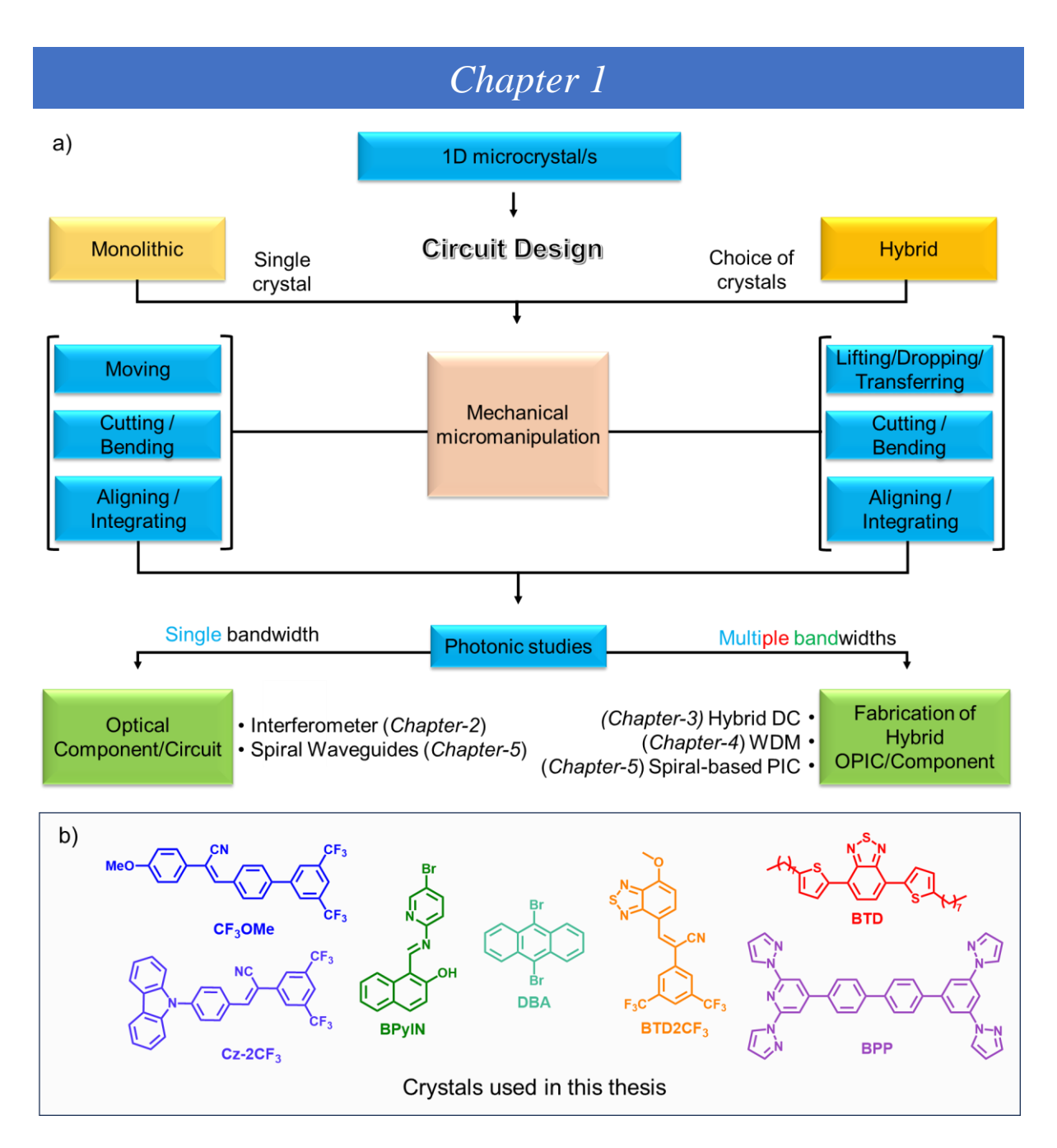


**Figure 1.38.** a) Roadmap to achieve monolithic or hybrid organic photonic components or circuits. b) Molecules used in this thesis.

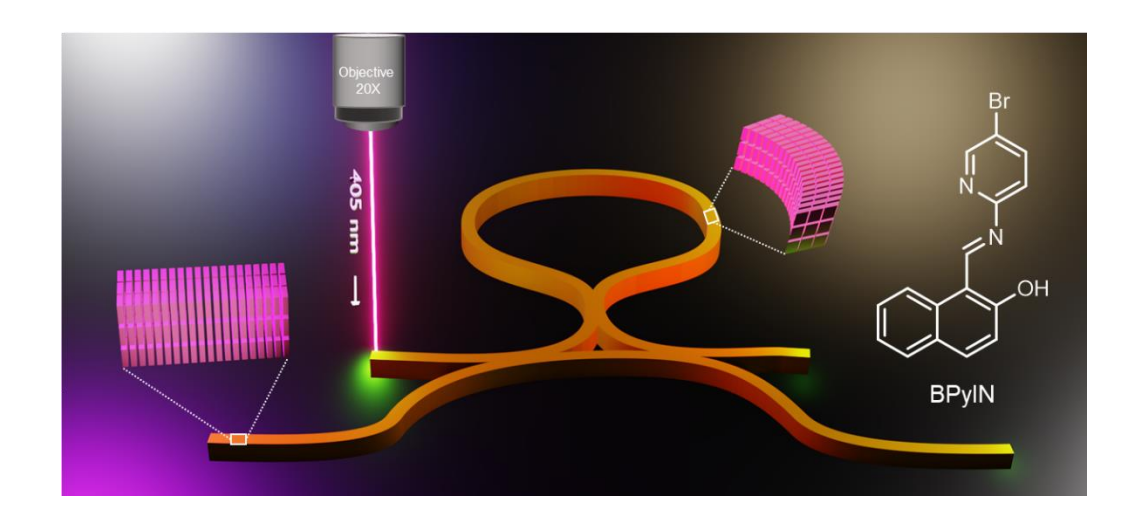
complete visible spectrum, iii) the PLQY of the crystals should be sequentially additive. The desired organic WDM can be constructed from BPP, DBA and BTD2CF<sub>3</sub> crystals and effectively transduce entire visible light from 450-750 nm through the BPP multiplexer.

A major challenge in the field of optics is to regulate the optical signals' pathway in orthogonal directions and control the number of signals generated in the circuit to realize programmable circuits. The construction of SWs comprising right and acute angles from extremely flexible blue emissive Cz-2CF<sub>3</sub> crystal waveguides illustrates the superiority of organic materials for microphotonic applications. Further, the extension of SWs into mechanically reconfigurable circuits by integration of Cz-2CF<sub>3</sub> SW with cyan emissive DBA

and red emissive BTD portrays the light routing capability. Further, the same circuit can be programmed by replacing the cyan emissive DBA crystal with green emissive BPyIN in a tip-to-tip manner to adjust the number of output ports from six to three using the mechanophotonics approach. Thereby demonstrating the strength of organic materials for programmable photonic circuits with the support of mechanophotonics technique.

9

# A Mechanophotonic Approach towards an Organic, Flexible Crystal-based Optical IM



#### 2.1 Abstract:

This chapter demonstrates the design and synthesis of extremely flexible (E)-1-(((5-bromopyridin-2-yl)imino)methyl)naphthalen-2-ol (BPyIN) crystals. The interactions stabilizing the crystal packing and crystal-substrate adhesion dictate the elasticity and pseudo-plasticity, respectively. The extremely flexible BPyIN crystals disclose bending geometry-dependent optical modes in the fluorescence spectra. This understanding is extended for fabricating a fibre loop mirror (FLM)-like geometry using a BPyIN single crystal. The mechanophotonics approach facilitates the integration of FLM-like crystal with a doubly bent waveguide to construct a first-of-its-kind IM. The light propagating path-length dependent optical interference within the IM is established. These proof-of-principle experiments illustrate the usefulness of mechanophotonics to fabricate miniature photonic devices beyond the traditional fabrication approach.

#### 2.2 Introduction

The construction of an organic FLM-like geometry requires a highly flexible photonic quality crystalline material. Importantly, it must transduce optical signals in bent geometries with low optical loss. The optical waveguiding flexible crystals with curved geometries are essential in this vein. It is worth mentioning that mechanically induced strain in a flexible crystal waveguide cavity could significantly influence the intensity and wavelength of the optical modes. However, bending-induced spectral changes in the organic waveguide cavity are seldom studied. Understanding the influence of crystal bending on spectral properties is essential to tracking the optical signals' modulation in IMs. Recently, the alteration of optical modes in flexible crystals while bending them was reported. Earlier in section 1.6.4, the blue shift of optical modes triggered by the mechanical bending of the flexible crystal resonator was discussed. Therefore, more insights into the influence of mechanical strain on optical characteristics are necessary to advance organic crystal for PICs.

This chapter envisions the utilization of hitherto unknown pyridine-based Schiff base compounds to fabricate an organic crystal-based IM using FLMs and bent waveguide via mechanophotonics approach. This work demonstrates the construction of a first-of-its-kind organic IM by employing an extremely flexible crystal waveguide cavity of BPyIN (Figure 2.1). The acicular BPyIN crystals bend when external mechanical stress is applied perpendicular to the (101) plane, indicating minor movement of atoms from the equilibrium position. The BPyIN microcrystal acts as a waveguide-cavity and exhibits bending-induced alteration of optical modes during FLM-like structure fabrication. Mechanophotonic

integration of miniature FLM with a doubly bent BPyIN waveguide provides a compact optical IM.

#### 2.3 Results and Discussion

#### 2.3.1 Synthesis of (E)-1-(((5-bromopyridin-2-yl)imino)methyl)naphthalen-2-ol (BPyIN)

**Scheme 2.1.** Synthesis of BPyIN molecule.

The BPyIN molecule was synthesized by the simple condensation (aldehyde-amine) reaction between 2-hydroxy-1-napthaldehyde and 4-bromo-2-aminopyridine in ethanol at 70 °C to obtain the enol form of BPyIN exclusively (Scheme 2.1). 2-Hydroxy-1-naphthaldehyde (5 mmol, 1eq) and 2-amino-5-bromo pyridine (5 mmol, 1eq) were taken in round bottom (RB) flask and added ethanol (20 mL). The reaction mixture was heated at 70 °C for 4 hours. The formed precipitate was cooled to room temperature and purified by recrystallization in chloroform solvent to obtain green needles of BPyIN (Figure 2.2, 2.3). Yield 70%. <sup>1</sup>H **NMR** (400 MHz, CDCl<sub>3</sub>)  $\delta$  (ppm) 15.36 (s, 1H), 9.95 (d, 1H,  $J_{H,H}$  = 1.8 Hz), 8.52 (d, 1H,  $J_{H,H}$ = 2.5 Hz), 8.15 (d, 1H,  ${}^{3}J_{H,H}$  = 8.5 Hz), 7.85 (dd, 1H,  ${}^{3}J_{H,H}$  = 8.5 Hz,  ${}^{4}J_{H,H}$  = 2.4 Hz), 7.78 (d, 1H,  ${}^{3}J_{H,H} = 9.5 \text{ Hz}$ ), 7.64 (d, 1H,  ${}^{3}J_{H,H} = 8 \text{ Hz}$ ), 7.52 (dt, 1H,  ${}^{3}J_{H,H} = 7.6 \text{ Hz}$ ,  ${}^{4}J_{H,H} = 1 \text{ Hz}$ ), 7.33 (dt, 1H,  ${}^{3}J_{H,H} = 7.6$  Hz,  ${}^{4}J_{H,H} = 1$  Hz), 7.09 (d, 1H,  ${}^{3}J_{H,H} = 8.5$  Hz), 6.94 (d, 1H,  ${}^{3}$ 9.5 Hz); <sup>13</sup>C **NMR** (100 MHz, CDCl<sub>3</sub>):  $\delta$  (ppm) 176.86, 152.25, 151.44, 149.96, 141.12, 139.25, 133.87, 129.40, 128.62, 128.14, 123.92, 119.47, 117.66, 116.92, 109.13.; **FTIR**  $(\bar{v})$ cm<sup>-1</sup>): 2035, 1966, 1616, 1536, 1466, 1320, 1289, 1127, 820, 741; **HR-MS**: m/z Calculated: 326.01, 328.01, Found: 327.01, 329.01; **UV-Vis** (Solid-state):  $\lambda_{abs-max}$  509 nm and  $\lambda_{FL-max}$  $\approx$ 538 nm (green emission); **Melting point**  $\approx$ 234-236 °C.



**Figure 2.1.** Photographs of BPyIN crystals obtained from the recrystallization solution under ambient and UV light illumination.

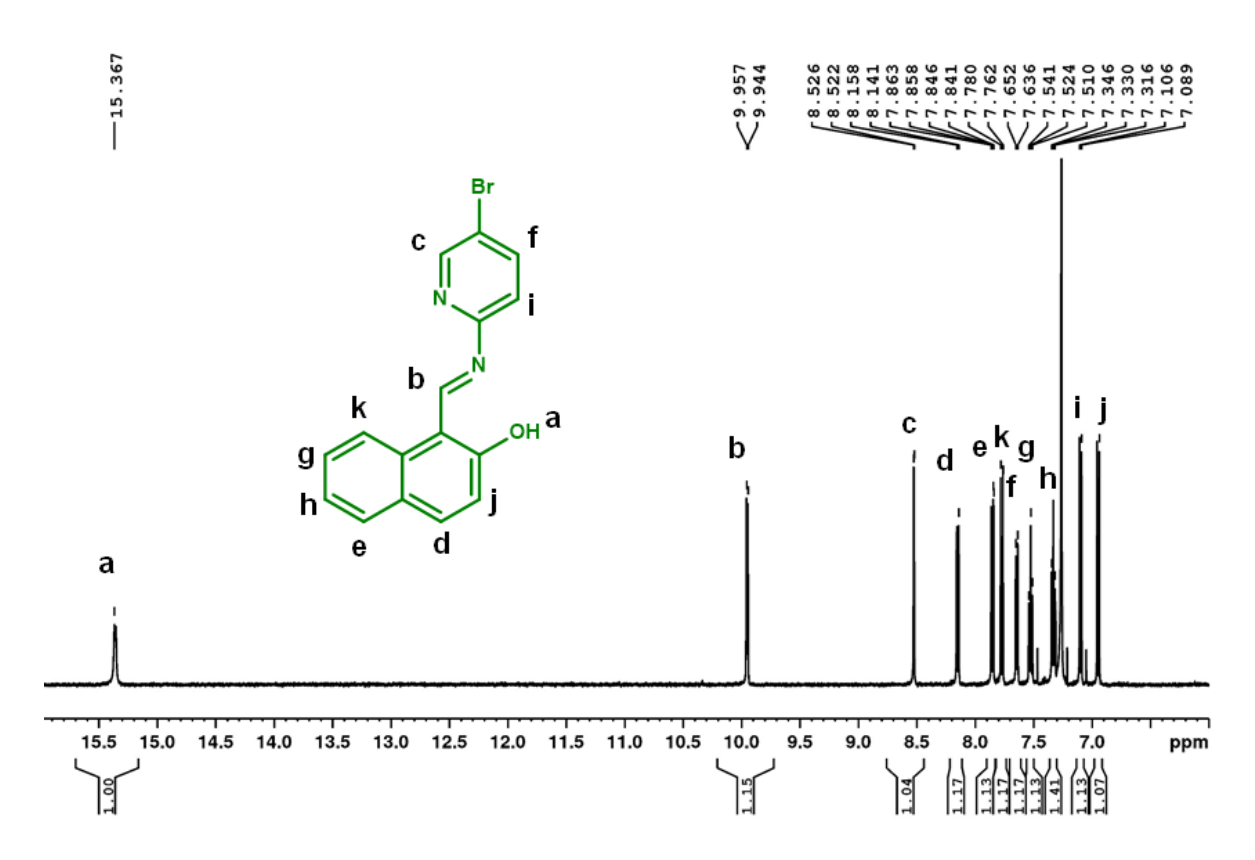


**Figure 2.2.** <sup>1</sup>H-NMR (400 MHz; CDCl<sub>3</sub>) spectrum of BPyIN.

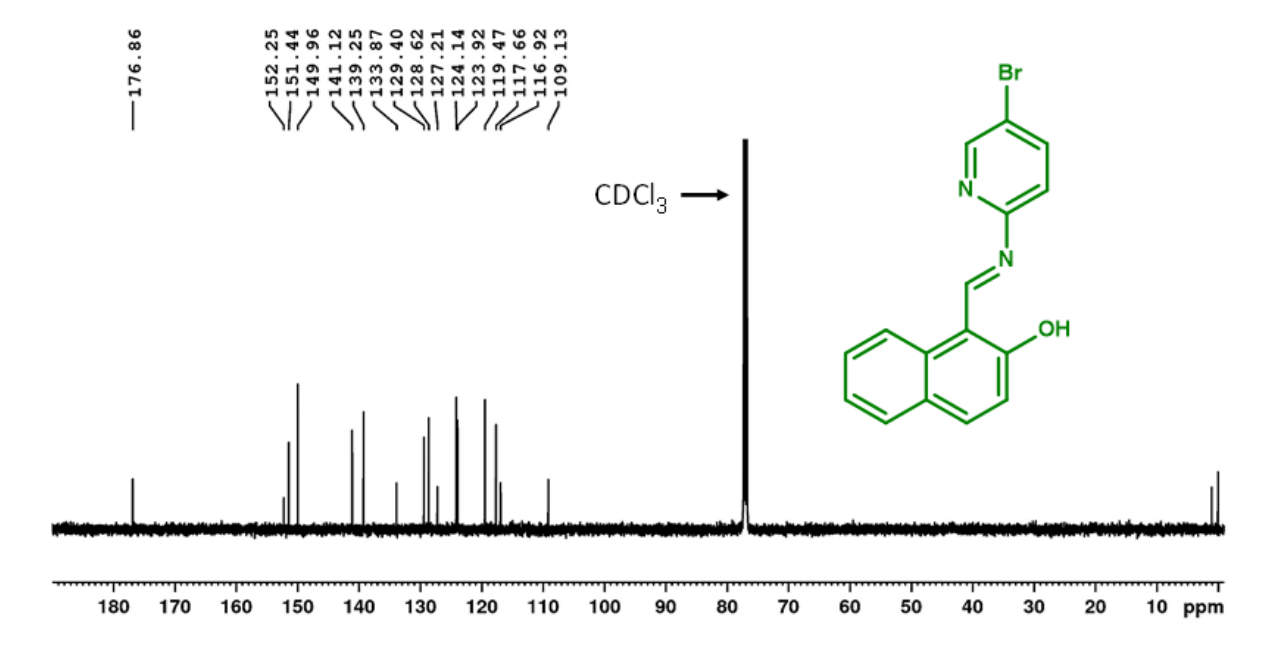
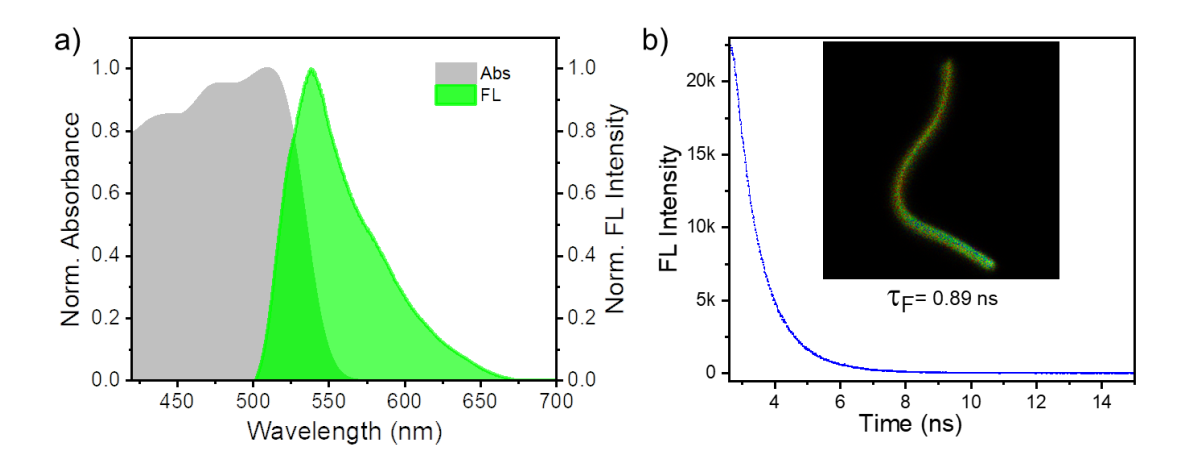


Figure 2.3. <sup>13</sup>C-NMR (100 MHz; CDCl<sub>3</sub>) spectrum of BPyIN.

#### 2.3.2 Solid-state optical characteristics of BPyIN

The solid-state optical properties of BPyIN showed a broad absorption band covering the  $\approx$ 300-550 nm region, while the fluorescence (FL) emission falls in the green part of  $\approx$ 500-650 nm region (Figure 2.4a). The solid-state BPyIN FL consisted  $\lambda_{max}$  of  $\approx$  540 nm is akin to other phenyl Schiff-base derivatives; however, the photoluminescence quantum yield (PLQY  $\approx$ 16.7%) of BPyIN is enhanced. Using the FL lifetime imaging microscopy, the lifetime of the BPyIN crystal was estimated to be 0.89 ns (Figure 2.4b).



**Figure 2.4.** a) Solid-state absorption and FL spectra of BPyIN. b) FL decay profile used to estimate the FL lifetime of BPyIN (Inset shows FL lifetime imaging microscopy image of BPyIN crystal used for lifetime measurement).

#### 2.3.3 Single crystal X-Ray and mechanical studies of BPyIN crystals

Thin needle-like crystals of BPyIN were obtained from a dichloromethane-acetonitrile solution and used for single-crystal X-ray analysis (CCDC: 2169698). The solid-state structure displayed the non-covalent interaction of pyridine's nitrogen atom with the vinylic hydrogen (C-N···H: 2.425 Å) to induce molecular planarity and  $\pi$ -conjugation (Figure 2.5a). The compound stabilized in a near planar conformation due to 172.4° torsional angle between the pyridyl and naphthyl entities (Figure 2.5b). The non-covalent interactions, including hydrogen bonding (C-O···H: 2.576 Å; N-H···O: 1.914 Å; C-H···N: 2.595 Å), C-H···Br (3.006 Å) and  $\pi$ ··· $\pi$  (4.352 Å) interactions stabilize the molecular packing (Figure 2.5c). The extended criss-cross molecular packing along the c-axis constitutes protracted layer packing, enabling mechanical compliance by allowing subtle back-and-forth movements of atoms from their equilibrium positions across these layers. Millimetre sized BPyIN crystals could be mechanically deformed into extremely curved geometries on a coverslip (Figure 2.5f, insets). This exceptional mechanical property is supported by layered molecular packing reinforced through various non-covalent interactions. When the crystals experience external stress

perpendicular to (-101) plane, the weak intermolecular interactions allow the movement of atoms from the equilibrium position (Figure 2.5e). Therefore, the expansion or contraction of molecules along the extended layers on the convex and concave regions of the bent crystals is possible (Figure 2.5f). Hence, these molecular movements avoid crystal breaking by dissipating the external stress. However, when force is exerted along other crystal planes, the lack of stress dissipation channels results in the breaking of the crystals.

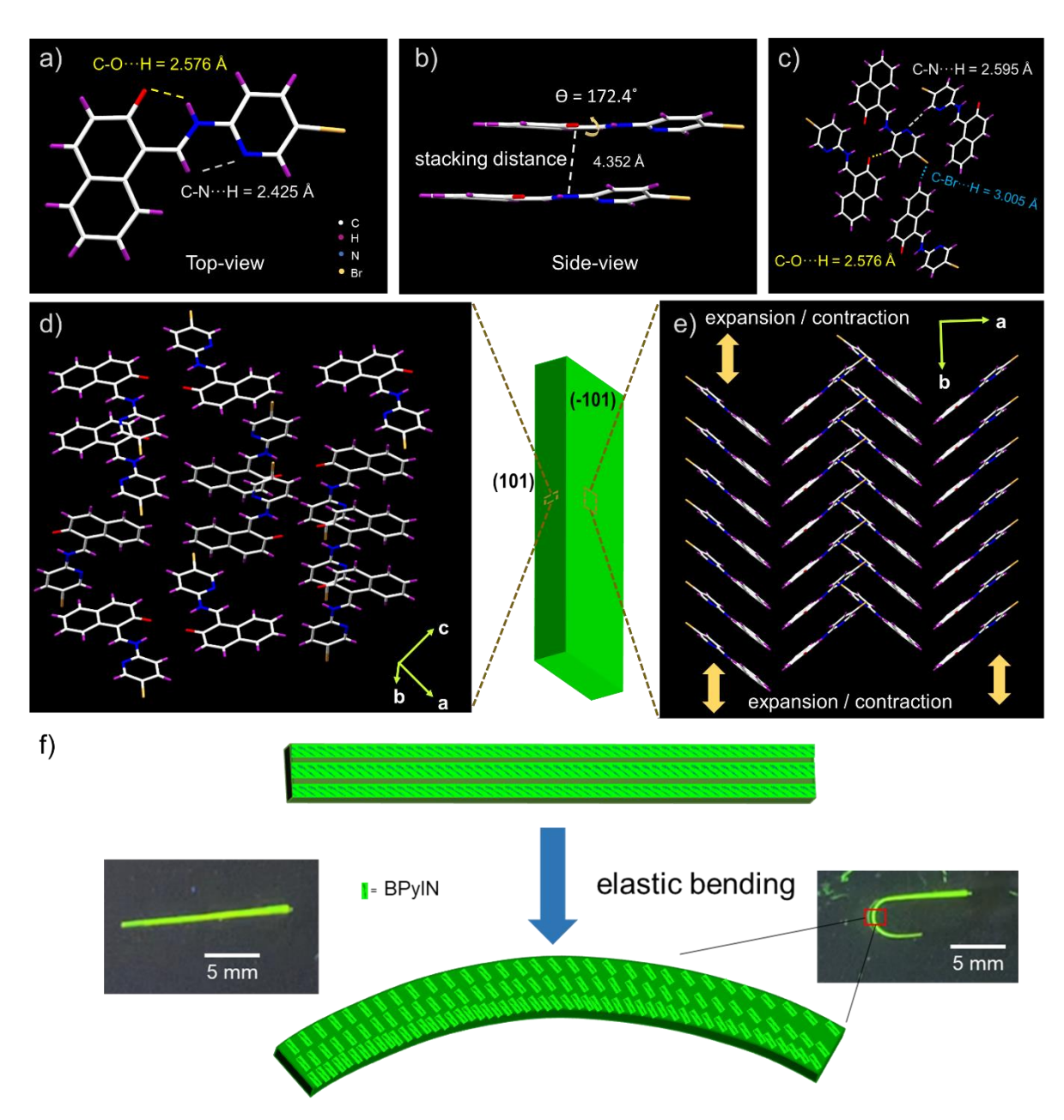


**Figure 2.5.** a) Crystal structure of BPyIN presenting the intramolecular interactions (top-view) and b) dihedral angle between naphthyl and pyridyl moieties (side-view). c) Intermolecular interactions stabilizing the BPyIN crystal structure. Molecular packing along the d) non-bending (101) and e) bending (-101) planes, respectively (double-headed arrows indicate the plausible relative directional movement of atoms supporting mechanical flexibility). f) Schematic representation of molecular packing in straight and bent states. (Insets show the photographs of straight and bent BPyIN crystals under UV light).

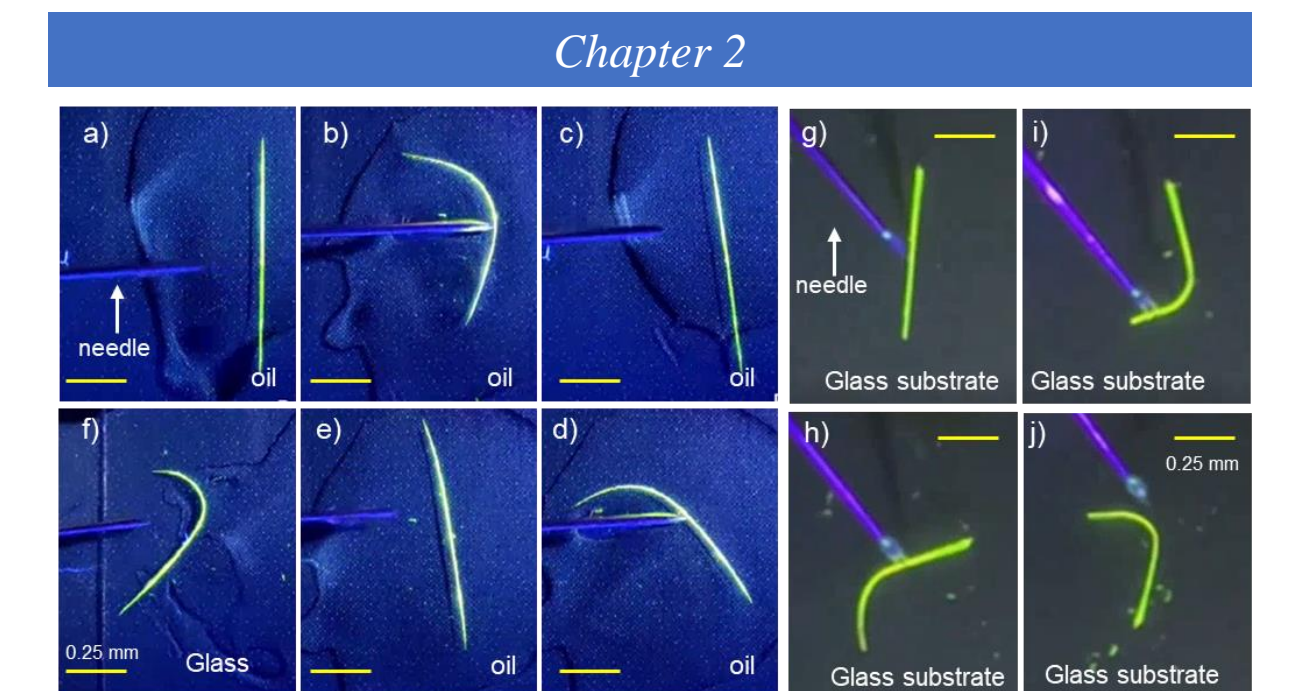


**Figure 2.6.** a-e) Elastic bending of BPyIN microcrystal in oil and f) pseudo-plastic bending on glass substrate under UV light. g-h) Single-point bending of BPyIN microcrystal with a needle on a glass substrate under UV light.

The mechanical properties of the thin needle-like BPyIN crystals were studied using conventional one-point and three-point bending techniques. A long crystal of length,  $L\approx1.2$  cm dispersed in silicone oil, could be reversibly bent several times on a glass substrate by applying force through a metallic needle, illustrating the crystal's elasticity (Figure 2.6a-e). Interestingly, due to the strong substrate-surface (crystal's surface) interaction, i.e. CSSI, the elastic crystal exhibits pseudo-plasticity (the crystal does not regain its initial shape after removing external mechanical stress, Figure 2.6f,g-j). While the same crystal in oil immediately regained its initial geometry defying the pseudo-plastic behaviour as there is no frictional force to hold the crystal against the stored potential energy. Further, when force was applied to the same crystals kept on a paper, the crystals did not bend, affirming the importance of surface adhesion to exhibit mechanical compliance.

#### 2.3.4 Mechanophotonic studies of BPyIN crystals

#### 2.3.4.1 Self-assembly of BPyIN crystal

The microcrystals of BPyIN suitable for miniature photonic device applications were obtained using the well-known self-assembly procedure. Typically, a 20 µL of 2 mM hexane solution of BPyIN was drop-casted onto a coverslip and allowed the solvent to evaporate slowly at room temperature. After complete evaporation of the solvent, the confocal optical microscopy studies revealed the formation of rod-like microstructures (Figure 2.7a). The transmission electron microscopy (TEM) and selected area electron diffraction (SAED) analysis performed along the [010] zone axis exhibited diffraction from different planes,

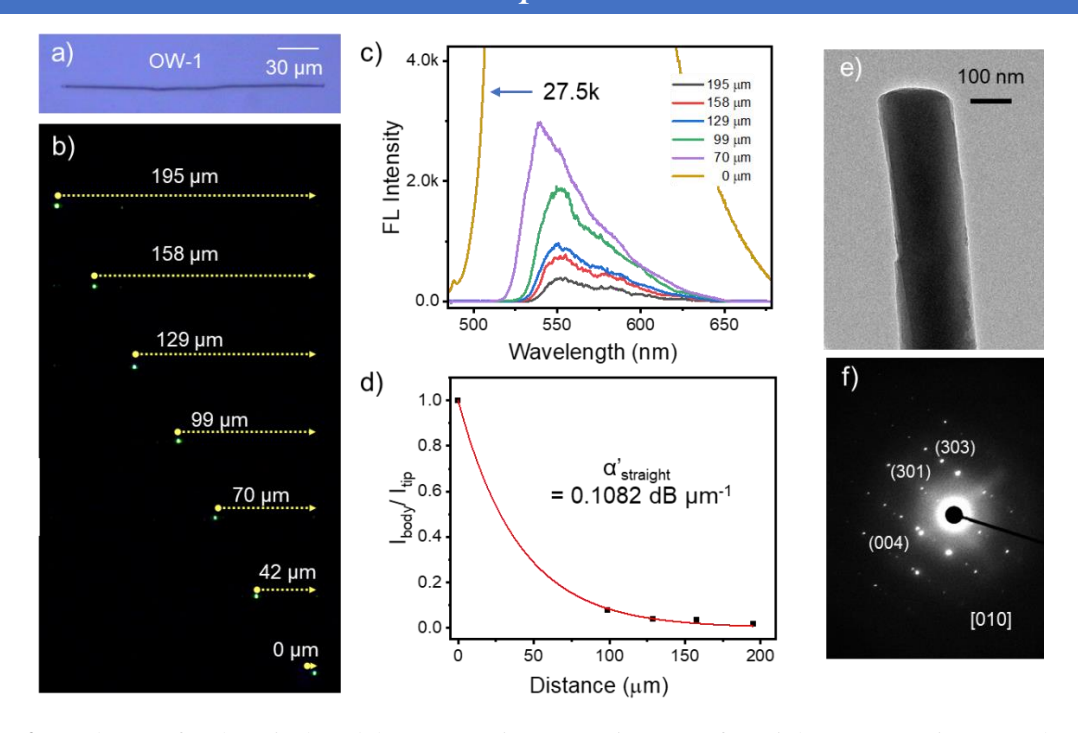


**Figure 2.7.** a,b) Confocal optical and laser FL microscope images of straight BPyIN microcrystals. c) FL spectra collected for various excitation points along the body of OW-1 and d) Plot of  $I_{tip}/I_{body}$  vs distance (red line) used for optical loss calculation, respectively. e,f) Transmission electron microscope image and selected area electron diffraction patterns obtained along [010] zonal axis on BPyIN microstructure, respectively.

including (004), (303) and (304) planes (Figure 2.7e,f). These results confirmed the crystallinity of the observed BPyIN rod-like microstructures.

#### 2.3.4.2 Optical waveguiding properties of BPyIN microcrystals

To study the optical waveguiding properties of BPyIN microcrystals, a microcrystal of length 195  $\mu$ m was selected (OW-1, Figure 2.7a). The FL image of a straight microcrystal displayed bright green emission from the termini, indicating the crystal's active type light-guiding characteristics. Focused optical excitation of the microcrystal at the center with a 405 nm laser produced a bright green FL at the point of excitation, and the same transduced towards both terminals along the body of the microcrystal (Figure 2.7b). The FL spectrum obtained at the tip of the microcrystal possessed several sharp peaks, known as optical modes and the modes were extracted by subtracting the corresponding emission spectrum of the microcrystal (Figure 2.7c). These modes arise due to the multiple reflections of FL between smooth mirror-like facets of the microcrystal cavity. Further, to probe the optical loss coefficient ( $\alpha$ '), excitation position-dependent emission spectra were collected at one of the crystal tips by varying the excitation position along the body of the microcrystal (Figure 2.7b,c). From this data, the  $\alpha$ ' of 0.1082 dB  $\mu$ m<sup>-1</sup> was estimated for the waveguide-cavity (Figure 2.7d). Typical optical loss values for organic active waveguides are reported to be between 0.009 dB  $\mu$ m<sup>-1</sup> to 0.65 dB  $\mu$ m<sup>-1</sup>.

#### 2.3.4.3 Pseudo-plastic behaviour of BPyIN microcrystals

A confocal optical microscope attached with an AFM cantilever tip was used to investigate the mechanophotonic properties of the same straight (OW-1, L=195  $\mu$ m) waveguide-cavity. The microcrystal was slowly manipulated mechanically on either side of OW-1 using an AFM cantilever tip to create a bent microcrystal with a strain ( $\epsilon$ ) of 0.775% (Figure 2.8a-i). During the bending process because of substantial microcrystal's surface-substrate adhesive interactions, they exhibit the *pseudo-plastic* nature. However, the microcrystals are inherently elastically flexible. The measured thickness of bent crystal waveguide-cavity from the field emission scanning electron microscopy (FESEM) images is about 1.24  $\mu$ m (Figure 2.8j). Further, defect-free smooth surface morphology and rectangular geometry support the FP waveguide-cavity (Figure 2.8j, inset).

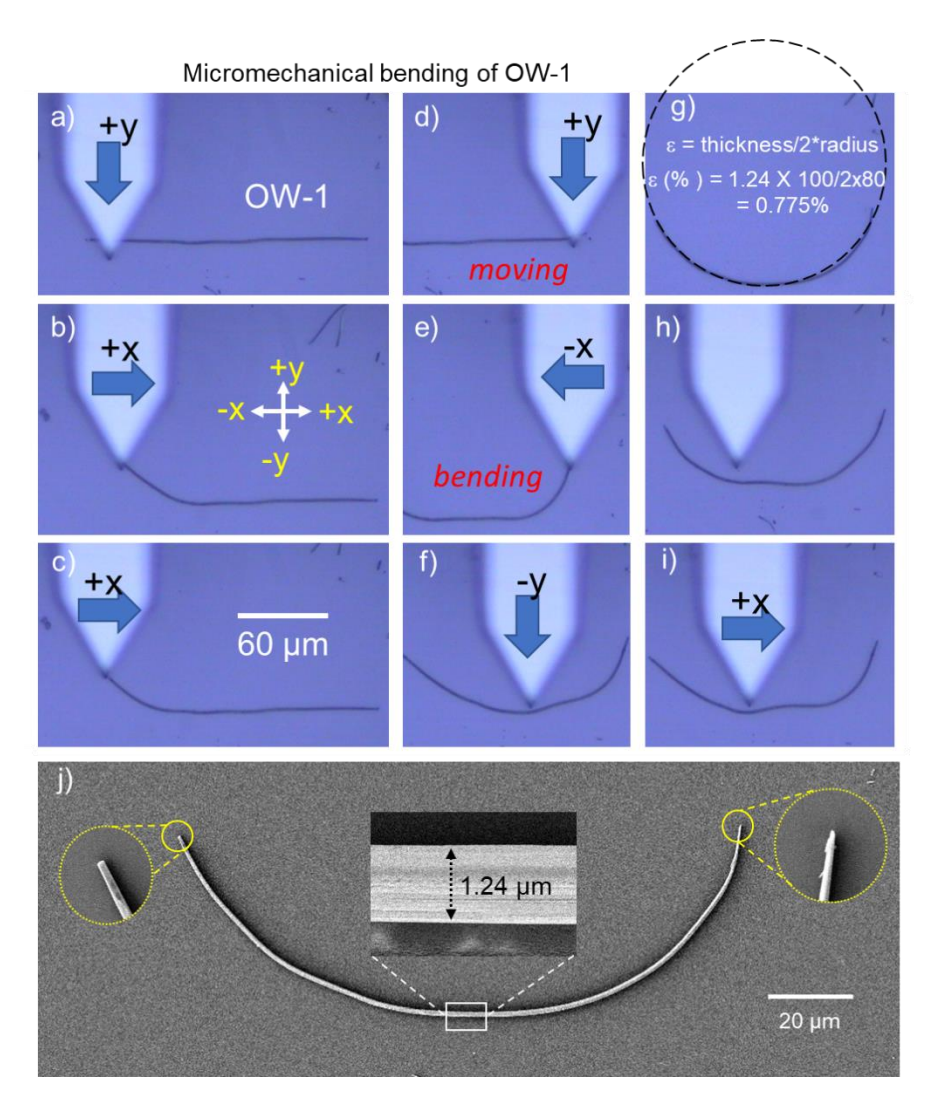


**Figure 2.8.** a-i) Confocal optical images depicting the micromechanical bending of BPyIN microcrystal with AFM cantilever tip. Inset in g shows the mechanical bending-induced strain calculation. j) FESEM image of the pseudo-plastic, bent BPyIN microcrystal. Insets show the close-up view of microcrystal and its respective ends.

The confocal image of the bent crystal with a tip-to-tip separation of 145  $\mu$ m is shown in Figure 2.9a. The FL microscopy image of bent OW1 comprised of radiant microcrystal termini, suggesting the intact optical properties in strained geometry (Figure 2.9b). Optical excitation of the bent crystal in the middle with focused laser beam exhibited a bright green FL output at both tips, corroborating the crystal's waveguiding nature even in the strained state (Figure 2.9c). The light-reflective surface of the bent waveguide supports FP-type optical modes in the FL spectrum (Figure 2.9g,h). The  $\alpha$ ' of the bent waveguide estimated using the excitation position-dependent emission spectra was 0.1288 dB  $\mu$ m<sup>-1</sup> (Figure 2.9d,e). Noticeably, the optical modes obtained for the strained waveguide cavity were different from

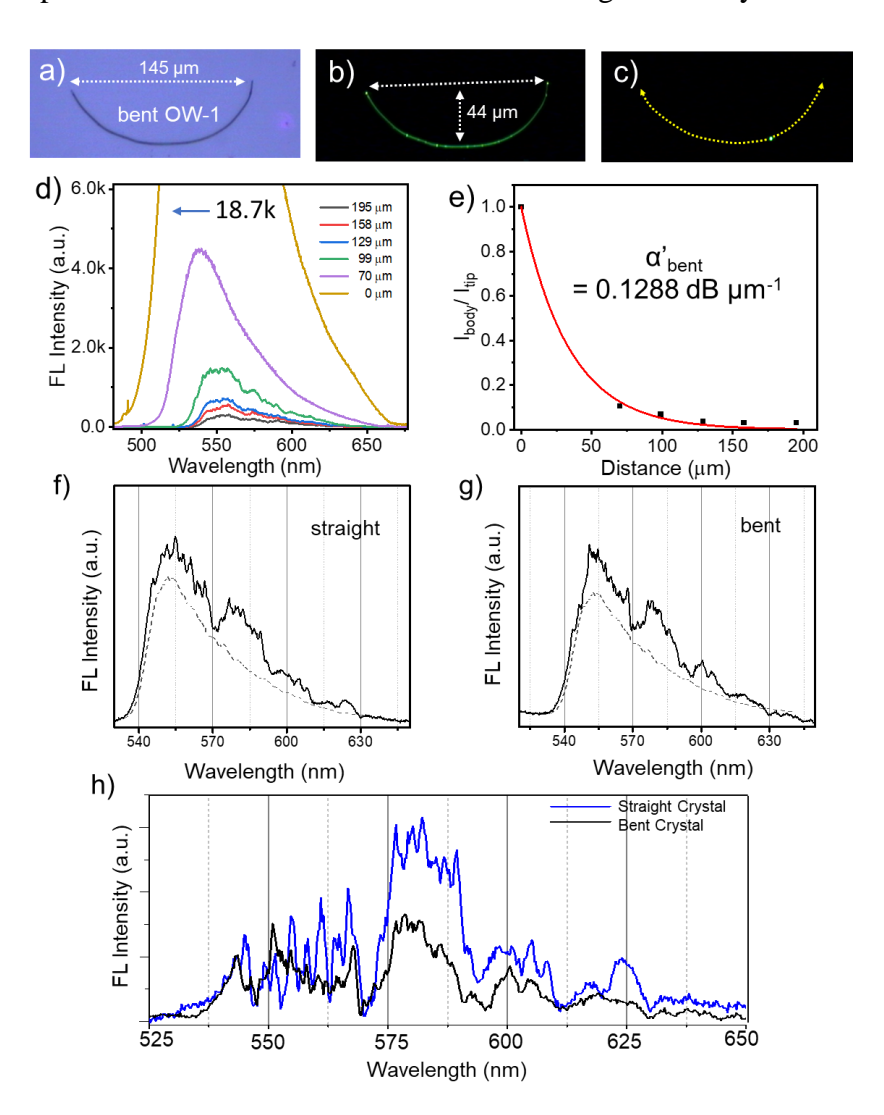


**Figure 2.9.** a-c) Confocal, FL microscope and laser FL microscope images of bent BPyIN microcrystal (bent OW-1), respectively. (Yellow dotted lines in c, represent the light propagation direction for 405 nm laser light input on the bent microcrystal). d,e) Emission spectra collected for various excitation points along the body of the bent microcrystal and plot of  $I_{tip}/I_{body}$  vs distance (red fit) used for optical loss calculation, respectively. f,g) FL spectra recorded in straight and bent BPyIN microcrystals for excitation on the left tip and collection on the right tip. (Dotted line represents the spectra used for background subtraction to obtain optical modes). h) Comparison of optical modes in BPyIN microcrystal (OW-1) before and after micromechanical bending.

the unstrained waveguide (Figure 2.9f-h). This vital observation revealed the influence of cavity geometry on the optical modes. The critical analysis of the spectra suggests the appearance and disappearance of modes before and after the crystal's mechanical bending (Figure 2.9h). Further, spectral broadening due to mode overlap is observed in the region 570 - 590 nm. These optical mode modulations indicate variation in the optical interference caused by the change in the crystal geometry. The bending-induced expansion and contraction of crystal's convex and concave areas, respectively, along with the corresponding expansion and compression of molecular packing can be understood from the following equation, <sup>204</sup>

$$\frac{d\lambda}{\lambda} = \frac{da}{a} + \frac{dn}{n} \tag{26}$$

Therefore, the change in the cavity's size (a) or the refractive index n, which leads to the resonant wavelength shifts, could also be a possible reason for observed changes in optical modes.

#### 2.3.5 Fabrication of compact organic IM

To fabricate a compact FLM-like geometry, a BPyIN microcrystal of  $L\approx123~\mu m$  and thickness ≈384 nm was selected (Figure 2.10a i,ii). With the help of the AFM tip, the crystal's first left tip was pushed forward, followed by the same on the right tip employing bending micromechanical operation (Figure 2.10a, iii-v). Later, the microcrystal was carefully manipulated in x,y plane using the same procedure (Figure 2.10a, vi). After a series of complex manoeuvres, the straight microcrystal was made into a pre-FLM with both necks separated by 2 µm without contact (Figure 2.10a, vi-xvi). Then, the necks were brought into physical contact by mechanically moving them towards each other to create a closed-loop, and to realize a compact organic FLM-like geometry (Figure 2.10b, i-iii). The close-up FESEM view clearly shows the evanescent contact between both necks (Figure 2.10d, left inset). Later, to create an IM, another straight microcrystal waveguide of  $L\approx147~\mu m$  was bent in two regions,  $\approx 35 \, \mu \text{m}$  from the left tip, and  $\approx 28 \, \mu \text{m}$  from the right tip (Figure 2.10c, i-v). The bending-induced strain at both the curved places was calculated to be approximately ≈4.7%. The fabricated doubly bent waveguide was integrated with FLM-like geometry to fabricate an IM (Figure 2.10c, vi-viii). The FESEM images of the waveguide-cavity with a FLM-like geometry exhibited that the horizontal diameter of a near-circular loop is ≈21 µm, and the thickness of the neck-region is ≈512 nm (Figure 2.10d). The strain stored in the loop is estimated to be 10.3%.

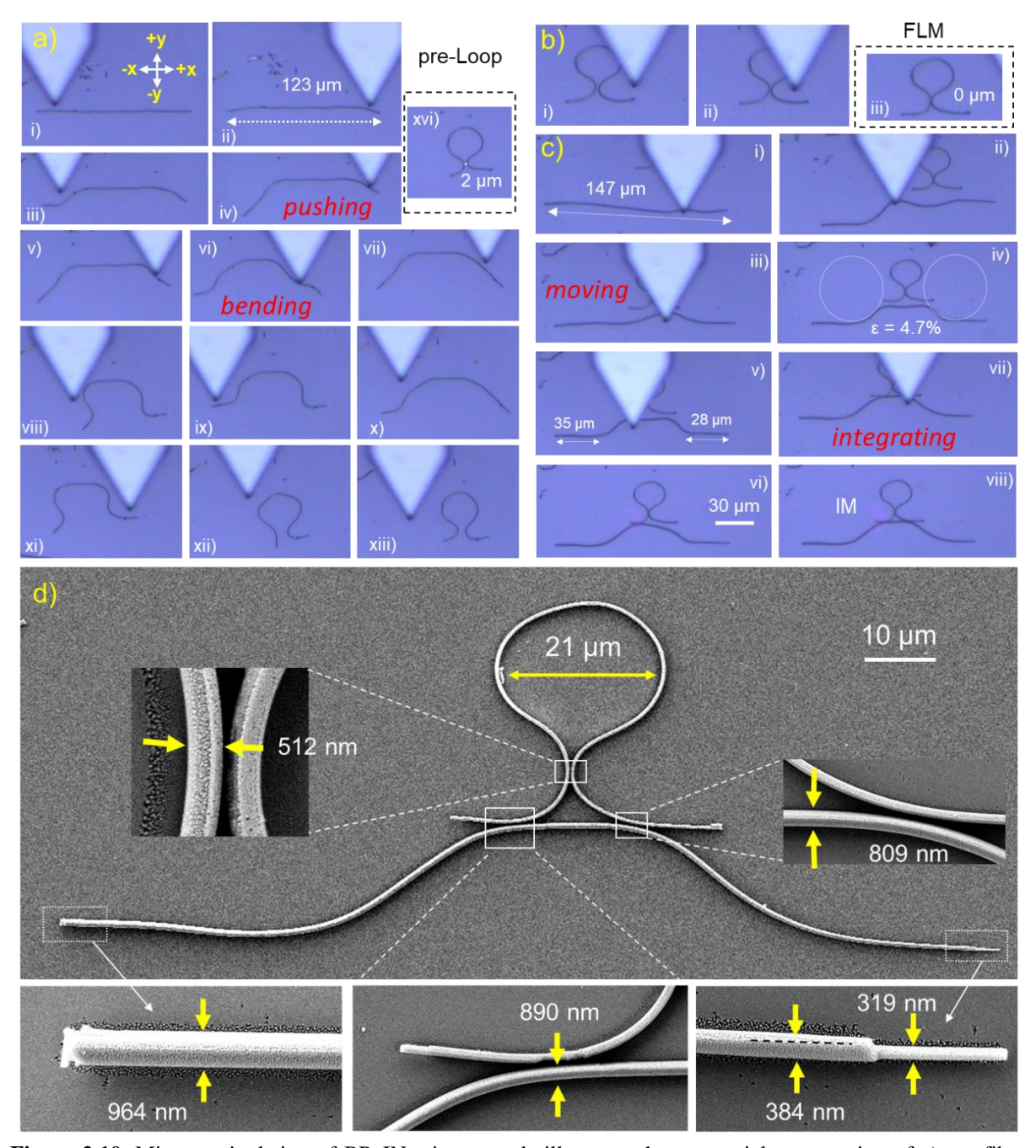


**Figure 2.10.** Micromanipulation of BPyIN microcrystals illustrates the sequential construction of a) pre-fibre loop mirror (pre-FLM) like geometry, b) organic FLM, and c) integrating FLM with a doubly bent waveguide to realize an FLM-based interferometer, IM using AFM tip aided mechanophotonics technique. d) FESEM image of the fabricated organic IM. Insets show a close-up view of the coupling junctions and the tips of the bottom waveguide.

The photonic properties of the organic IM were investigated sequentially. Firstly, the waveguiding property of straight microcrystal (L=123  $\mu$ m) before mechanical manipulation was studied by exciting the left tip (I) with 405 nm diode laser and collecting the corresponding emission spectrum at the right tip (I) (Figure 2.11a, FL image). The extracted optical modes are presented in Figure 2.11h with a label I (which means excitation at tip-I and spectral collection at tip-I). Secondly, the bending-induced FL changes after

construction of pre-FLM were studied (Figure 2.11b) and presented with and labelled as b) 1-2 in Figure 2.10i). The optical spectrum of extremely strained geometry, such as pre-FLM, possessed most of the optical modes as observed in the case of an unperturbed waveguidecavity; however, with a slight intensity alteration (Figure 2.11i). Thirdly, the fabricated FLMlike crystal's (Figure 2.11c) spectrum was recorded and presented as c) 1-2 in Figure 2.11j. Later, the photonic properties of IM were also studied by exciting it at tip 4 (Figure 2.11d,e) and the corresponding spectra are shown in Figure 2.10k,l. In Figure 2.10f, the IM was excited in a such way that the laser beam irradiates both tip I and convex contact area of the doubly-bent waveguide-cavity to facilitate light travelling through FLM and convex part. The observed changes in optical modes at the output point(s) (2 or 3) for the same excitation points (1 or 4) were compared for the straight waveguide-cavity, pre-FLM, FLM and IM. Significant changes observed in the spectra are as follows. The peak at 548.9 nm in a) 1-2 disappeared in b) 1-2, and a strong mode appeared at 555.2 nm (see Figure 2.11h and i). Additionally, the peak intensities at 550.8, 573.1, 576.6, and 587.2 nm were enhanced in the pre-FLM compared to the straight waveguide (indicated by green arrows facing upwards). The FWHM (indicated by red double-headed arrows) of highly intense mode at ≈564 nm reduced from 11.7 nm in a 1-2 to 6.8 nm in pre-FLM.

When the two neck regions of the extremely bent waveguide cavity were brought into physical contact to realize a loop (Figure 2.11c), the light signal-transducing in the waveguide could take two circular paths at the evanescent coupling region. The signal can propagate clockwise, and part of the light travels in the anticlockwise direction due to the signal splitting at the coupling region. When two different optical signals (one travelling in the clockwise direction and the other in the anticlockwise direction) meet in the waveguide, it causes optical interference and modulates the output signal. The optical spectrum obtained in the FLM (Figure 2.11j) produced different optical modes compared to pre-FLM shown in Figure 2.11i. The intensity of 587.2 nm mode has increased in FLM compared to pre-FLM. The mode intensity at 573.1 nm reduced dramatically in FLM compared to pre-FLM. The modes at 571.8 nm and 593.7 nm possessed higher signal intensities compared to that in pre-FLM. Further, the FWHM of the mode at ≈564 nm in FLM has reduced to 6 nm from 6.8 nm in pre-FLM.

In the IM, the output signals are distinct due to intricate optical paths when excited at tip 4 or 1 and the convex contact area of the doubly-bent waveguide-cavity (Figure 2.11e). Alteration of spectral intensities of the multiple peaks could be noted (Figure 2.111 and m).

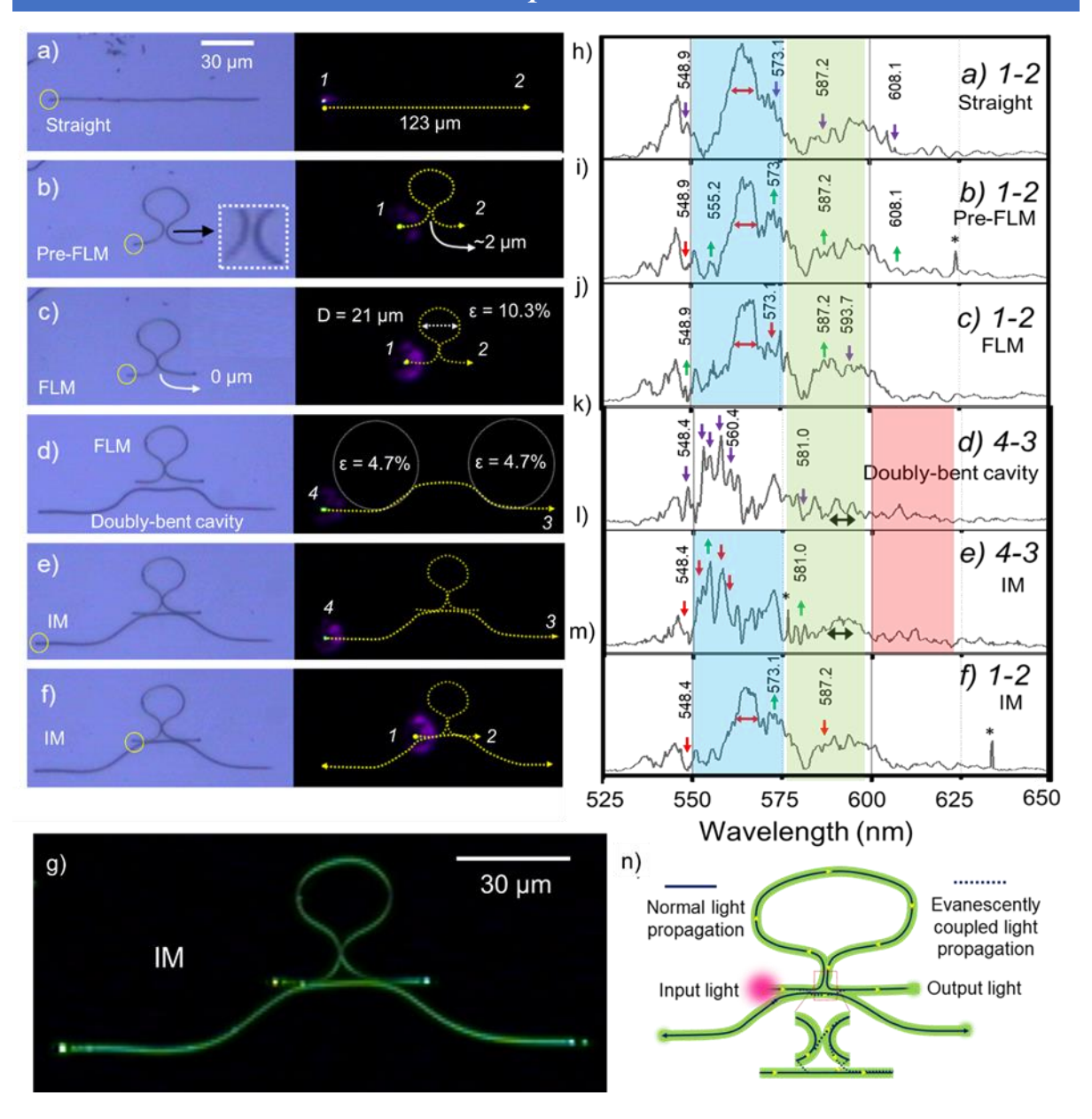


**Figure 2.11.** a-f) Stepwise fabrication of the organic interferometer, IM. The yellow circles show the excitation area. g) FL microscope image of the fabricated FLM-based IM. h-m) Optical modes extracted from the FL spectrum obtained for a-f, when left tip was excited and emission was collected at right tip (\*indicates noise). n) Schematic representation of light propagation path inside the IM when excited at tip *1* shown in f. The inset shows the possibility of evanescent light propagation in different directions.

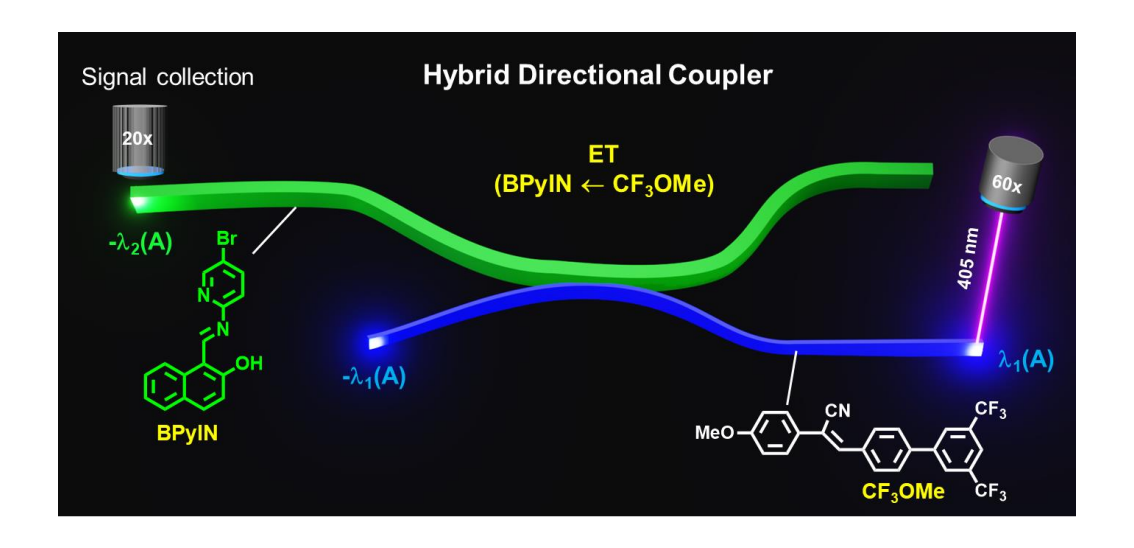
The modes at 548.4 nm and 587.2 nm in FLM were suppressed in IM (Figure 2.11k and 1). The peak at 573.1 nm suppressed in FLM became well pronounced in FLM-IM (Figure 2.11j and m). The FWHM of the mode at  $\approx$ 564 nm increased to 7.4 nm in FLM-IM from 6.8 nm in FLM. On the same line, the optical properties of a doubly bent waveguide, before (represented as d) d-d in Figure 2.11d and k) and after integrating to the FLM (represented as d) d-d in Figure 2.11e and l) displayed distinct optical response. The interference effect in the doubly bent waveguide before and after coupling to the FLM is reflected in its optical response to the input light. A sharp 545.7 nm peak has appeared in coupled FLM-IM (Figure

2.11l) compared to the physically uncoupled FLM-IM (Figure 2.11k). The peak at 548.4 nm was suppressed, and 560.4 nm peak disappeared in *e*) 4-3 relative to the uncoupled waveguide *d*) 4-3. Further, noticeable alterations in the intensities of modes in the region 550-575 nm can be observed. A strong peak at 581.0 nm has appeared in the fabricated FLM-IM compared to uncoupled FLM-IM. The mode overlapping/merging in the region 589.5 nm to 597.5 nm was observed due to interference.

#### 2.4 Summary

This chapter successfully illustrated the fabrication of an organic crystal-based optical IM using a mechanophotonics approach. For this, extremely flexible BPyIN crystals were designed and synthesized. The excellent mechanical flexibility of BPyIN crystals was supported by the specific supramolecular interactions and resultant molecular packing. The extreme flexibile microcrystals act as waveguide-cavities and exhibits subtle bending-induced optical mode alteration. This understanding was carefully exploited to fabricate a tailor-made compact FLM-like single-crystal geometry. The compact FLM-like crystal acting as a waveguide-cavity was integrated with a doubly bent waveguide-cavity to achieve a novel IM. The plausible optical trajectories responsible for the mode changes in the constructed IM via optical interferences were clearly established. The novel design strategies employed to realize organic single-crystal-based IM open new dimensions to develop advanced IMs for diverse applications.

Mechanophotonics: Fabrication of a 2×2 hybrid directional coupler from flexible organic crystals



3.1 Abstract: Microcrystalline organic optical components with multi-tasking capabilities are crucial to constructing miniature photonic devices. This chapter presents the design and fabrication of an organic directional coupler with multifunctional capabilities. Herein, the synthesis of mechanically flexible blue-emissive (Z)-3-(3',5'-bis(trifluoromethyl)-[1,1'-biphenyl]-4-yl)-2-(4-methoxyphenyl)acrylonitrile (CF3OMe) crystal waveguide is reported. The exceptional mechanophtonic properties exhibited by CF3OMe crystals manifest their suitability for photonic circuits. The integration of CF3OMe microcrystal waveguide with a green-emissive BPyIN microcrystal waveguide via mechanophotonics technique allows the creation of an innovative hybrid 2×2 directional coupler (HDC) with four terminals. The HDC functions as an optical signal splitter and signal chromaticity modulator when CF3OMe crystal receives the input signal. The same device becomes only a signal splitter for light input at the BPyIN crystal. Thereby, a novel HDC performing multiple functions, viz., splitting, chromaticity modulation, and directed delivery of an optical signal, was realized. The demonstration of such innovative circuits corroborates the versatility of organic crystal photonics for devising technologically relevant organic photonic integrated circuits.

#### 3.2 Introduction

The growing technological needs demand the development of multifunctional PICs. 4,53 One such multifunctional photonic component is a 2×2 hybrid DC (HDC) with four termini or ports. The monolithic nature of previously reported DCs allowed only signal splitting at the forward terminal, limiting their performance specificity to a single task. 174,207 However, a HDC can split the light signal, and also modulate the output signal's color and direction depending on the port receiving the input signal but this is not known yet. The challenging aspect regarding HDC's construction is the requirement of mechanical microintegration of two chemically and optically different organic microcrystals with suitable mechanical attributes.

The present chapter discusses the design and synthesis of efficient blue-emissive CF<sub>3</sub>OMe flexible crystals. The molecular origin of (Z)-3-(3',5'-bis(trifluoromethyl)-[1,1'-biphenyl]-4-yl)-2-(4-methoxyphenyl)acrylonitrile (CF<sub>3</sub>OMe) crystal's flexibility is established from a supramolecular perspective. The micromechanical and photonic properties are explored to utilize CF<sub>3</sub>OMe crystals for the construction of HDC. CF<sub>3</sub>OMe and BPyIN were integrated on a single borosilicate chip (coverslip) by transferring BPyIN crystal to the substrate containing CF<sub>3</sub>OMe crystal via a *mechanophotonics* approach. The constructed HDC implements multiple functions: (i) acting as an optical beam splitter ( $\lambda_2$ ; only green).

(ii) direction- and (iii) color-modulator ( $\lambda_1$  and  $\lambda_2$ ; blue and green) depending on whether CF<sub>3</sub>OMe or BPyIN crystals receive the same input light.

#### 3.3 Results and Discussion

## $3.3.1 \quad Synthesis \quad of \quad (Z)-3-(3',5'-bis(trifluoromethyl)-[1,1'-biphenyl]-4-yl)-2-(4-methoxyphenyl) acrylonitrile (CF_3OMe)$

Synthesis of 3',5'-bis(trifluoromethyl)-[1,1'-biphenyl]-4-carbaldehyde (CF<sub>3</sub>CHO): Compound CF<sub>3</sub>CHO was synthesized using the procedure previously reported by Jyoti *et al.*<sup>206</sup> A mixture of 1-bromo-3,5-bis(trifluoromethyl)benzene (5 mmol), (4-formylphenyl) boronic acid (5.5 mmol) and tetrakis(triphenylphosphine) palladium(0) ( 0.04 mmol) was dissolved in tetrahydrofuran (45 mL) and purged with N<sub>2</sub> gas for 2 h. After the addition of aqueous 2 N potassium carbonate solution (12 mL), the reaction mixture was stirred and heated to reflux overnight. The crude mixture was cooled to room temperature and poured into 200 mL of water. Later, the aqueous solution was extracted with ethyl acetate (150 mL), and dried over anhydrous sodium sulfate. Finally, silica gel column chromatography (n-hexane:EtOAc, 3:1) gave the product as a white powder with 80% yield. <sup>1</sup>H NMR (400 MHz, CDCl<sub>3</sub>) δ (ppm) 10.08 (s, 1H), 8.05-8.00 (m, 4H), 7.79 (s, 1H), 7.77 (d, 2H, <sup>3</sup>J<sub>H.H</sub>= 8 Hz).

F<sub>3</sub>C 
$$CHO$$
 +  $OMe$   $MeOH$ ,  $OMe$   $OMe$ 

**Scheme 3.1.** Scheme for the synthesis of CF<sub>3</sub>OMe.

**Synthesis of CF<sub>3</sub>OMe:** For the synthesis of CF<sub>3</sub>OMe, 3,5bis(trifluoromethyl)phenylacetonitrile (1.1 mmol, 1.1 eq) was taken in 20 mL methanol and added with sodium methoxide (2 mmol, 2 eq). To this solution, CF<sub>3</sub>CHO (1 mmol, 1 eq in 5 mL of methanol) was slowly added at rt. The reaction mixture was heated at 60 °C for 4 h. Then the white fibre-like compound was filtered and purified by recrystallization in (1:1) dichloromethane:hexane solution to obtain pure CF<sub>3</sub>OMe in 65% yield. <sup>1</sup>H NMR (500 MHz, CDCl<sub>3</sub>)  $\delta$  (ppm) 8.06 (s, 2H), 8.00 (d, 2H,  ${}^{3}J_{H,H} = 4$  Hz), 7.89 (s, 1H), 7.72 (d, 2H,  $J_{H,H}$ = 4 Hz), 7.63 (d, 2H,  $J_{H,H}$  = 4 Hz), 7.48 (s, 1H), 6.98 (d, 2H,  $J_{H,H}$  = 4 Hz), 3.91 (s, 3H). <sup>13</sup>C **NMR** (100 MHz, CDCl<sub>3</sub>):  $\delta$  (ppm) 160.93, 142.42, 139.64, 138.83, 134.80, 132.73, 132.40, 130.12, 127.87, 127.66, 127.36, 126.89, 122.15, 121.65, 118.17, 114.76, 112.68, 55.69;

**FTIR** ( $\bar{v}$  cm<sup>-1</sup>): 2217, 1606, 1510, 1245, 1118, 820, 741; **HR-MS**: m/z Calculated: 447.38, Found: 448.32; **UV-Vis** (Solid-state):  $\lambda_{abs-max}$  425 nm and  $\lambda_{FL-max} \approx 475$  nm (blue emission); **Melting point**  $\approx 187-191$  °C.

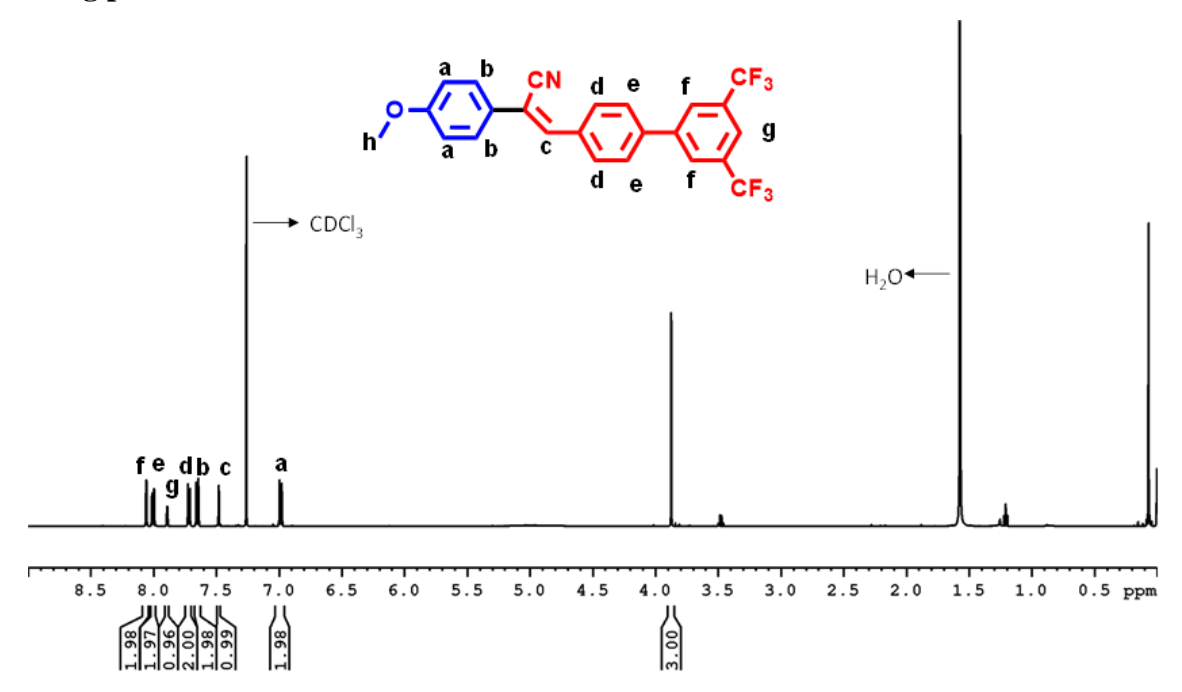
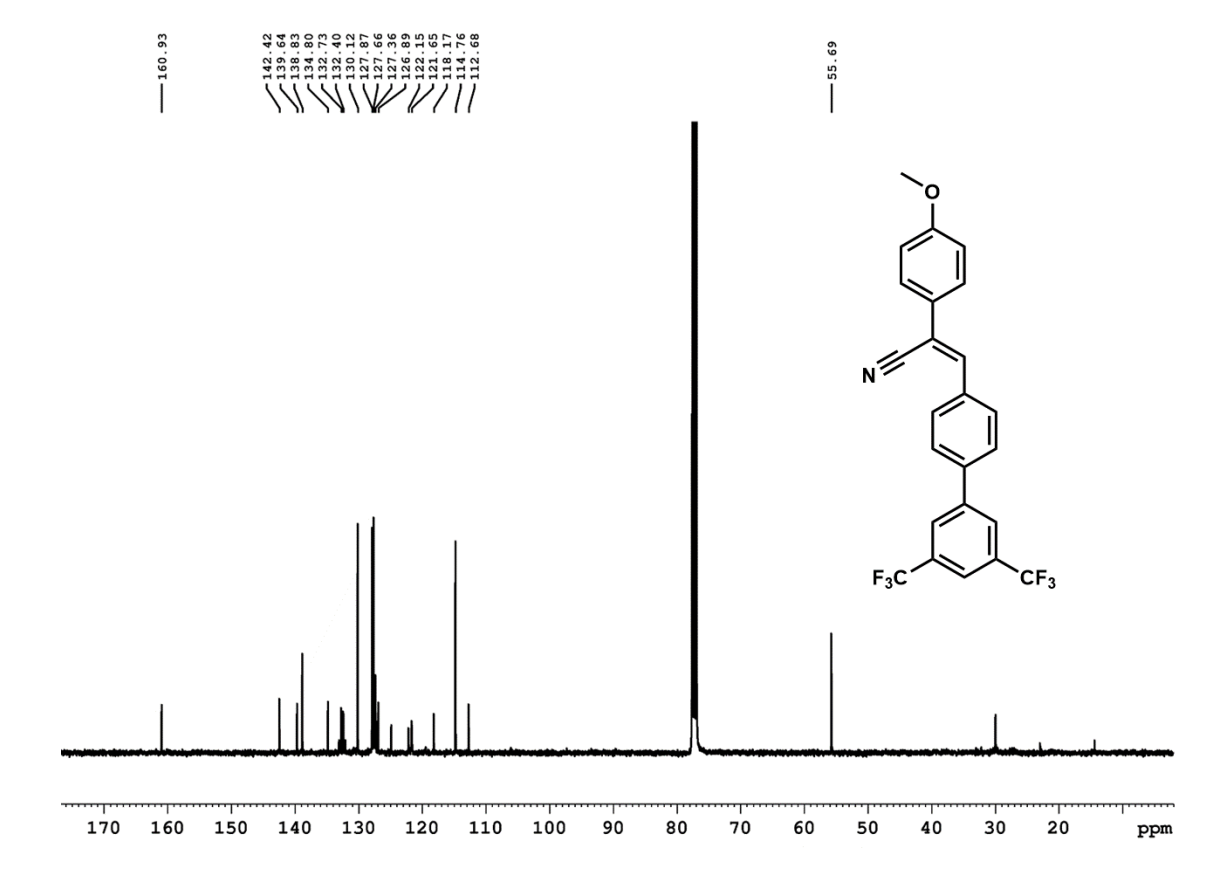


Figure 3.1. <sup>1</sup>H-NMR (400 MHz; CDCl<sub>3</sub>) spectrum of CF<sub>3</sub>OMe.



**Figure 3.2.** <sup>13</sup>C-NMR (100 MHz; CDCl<sub>3</sub>) spectrum of CF<sub>3</sub>OMe.

#### 3.3.2 Solid-state optical characteristics CF<sub>3</sub>OMe and BPyIN

The optical absorption spectrum of CF<sub>3</sub>OMe consisted of absorption maximum at  $\lambda_{max}$  ≈425 nm with tail extending up to ≈475 nm. The optical emission of BPyIN extended till 560 nm with  $\lambda_{max}$  at 525 nm (Figure 3.3a). The fluorescence (FL) spectrum of CF<sub>3</sub>OMe covered 420–660 nm region with a maximum centered at 475 nm (Figure 3.3b). The FL of CF<sub>3</sub>OMe has maximum overlap with the absorption region of BPyIN covering the 422–562 nm spectral bandwidth, suggesting substantial radiative ET from CF<sub>3</sub>OMe to BPyIN. However, there is no significant overlap between the absorption of CF<sub>3</sub>OMe and the emission of BPyIN. Hence, the chance of ET from BPyIN to CF<sub>3</sub>OMe is minimal. The brilliant FL ( $\tau_{FL}$  = 2.95 ns) of CF<sub>3</sub>OMe corroborated well with the solid-state PLQY of 36%, measured using integrated sphere setup. The PLQY of BPyIN crystal was 16.7% as mentioned in section 2.3.2.

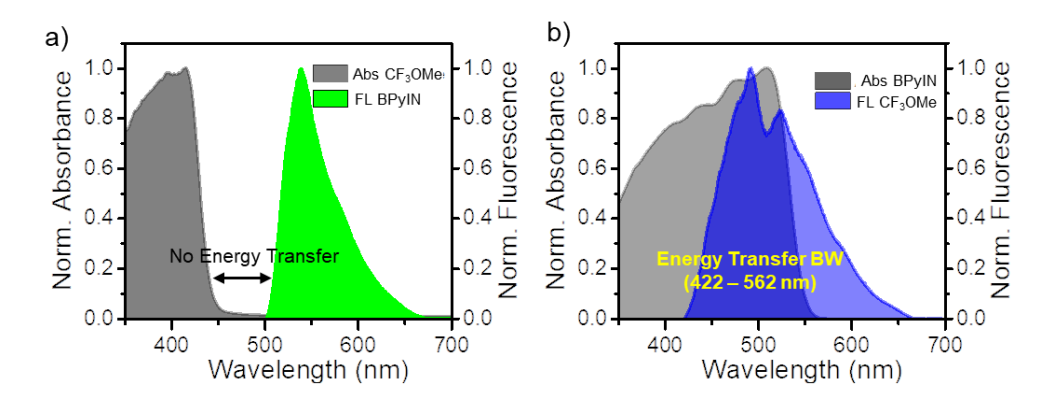


**Figure 3.3.** a,b) Solid-state photophysical properties of  $CF_3OMe$  and BPyIN molecules showing the possibility of ET from earlier to latter (BPyIN  $\leftarrow$   $CF_3OMe$ ).

#### 3.3.3 Structural basis for mechanical flexibility in CF<sub>3</sub>OMe crystals

The fiber-like crystals of CF<sub>3</sub>OMe were grown from dichloromethane:methanol (1:1) solution at room temperature by a slow evaporation method. The molecule crystallized in a triclinic system with P1̄ space group (CCDC number: 2222211). The torsional angle of the phenyls with donor (OMe) and acceptor (CF<sub>3</sub>) moieties with respect to the  $\pi$  spacer is 33.7°and 25.6° respectively (Figure 3.4a). The rich non-covalent interactions like halogen interactions between fluorine atoms, hydrogen bonding between electronegative fluorine and hydrogen atom (C-F···H:  $\approx$ 2.653 Å),  $\pi$ ··· $\pi$  ( $\approx$ 3.985 Å) interactions<sup>205</sup> among stacked layers and possible C-H··· $\pi$  ( $\approx$ 3.063 Å) interactions enable molecular packing in CF<sub>3</sub>OMe crystals (Figure 3.4b). These diverse weak and dispersive molecular interactions allow the crystal to possess strain-withstanding capabilities without developing fatigue. The field emission scanning electron micrograph (FESEM) shows a naturally bent CF<sub>3</sub>OMe crystal

accumulating a strain of 11% at the curved portion (Figure 3.4c). This illustrates strain holding capacity of the CF<sub>3</sub>OMe crystal supported by abundant non-covalent interactions. A closer view suggests the rectangular feature of the bent crystal (Figure 3.4d). The face-indexing and growth morphology predictions confirmed that the wider and thinner faces correspond to (001) and (010) planes, respectively (Figure 3.4e,f).

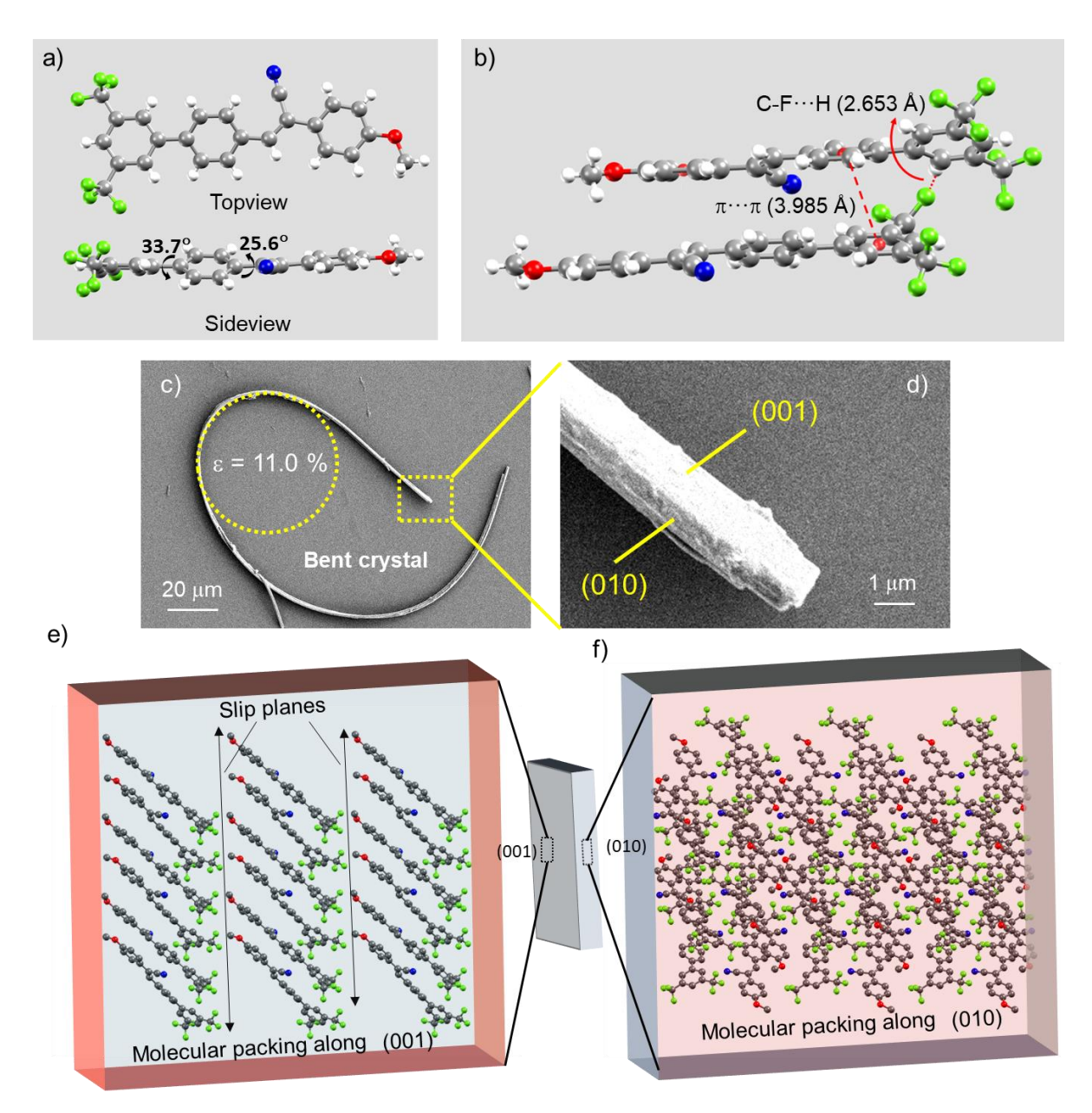


**Figure 3.4.** a) Top and sideview of CF<sub>3</sub>OMe molecule in the crystal. b) Molecular interactions present in CF<sub>3</sub>OMe crystal. c) FESEM image of a representative bent CF<sub>3</sub>OMe crystal. ε represents mechanical bending strain on the crystal. d) Closeup view of end facets of the crystal shown in c. e,f) Molecular packing along (001) and (010) planes in the crystal packing of CF<sub>3</sub>OMe.

To validate the mechanical flexibility of CF<sub>3</sub>OMe crystals, a three-point bending test was performed with the help of a needle and forceps (Figure 3.5a-e). The long crystals of

CF<sub>3</sub>OMe could be reversibly bent multiple times without any observable damage (Figure 3.5f). Interestingly, the crystals exhibited enhanced flexibility with water as a lubricant. The molecular origin of the mechanical flexibility can be understood from robust supramolecular interactions in the crystal packing. The molecular packing along the (001) plane shows a periodic layered arrangement of CF<sub>3</sub>OMe molecules giving rise to slip planes along [010] direction (Figure 3.4e). These slip planes possibly assist the gentle to-and-fro motion of atoms or minute reversible sliding to support stress disbursal. Therefore, when the crystal experiences mechanical force perpendicular to the (001) plane, it performs reversible elastic deformation. However, due to the absence of stress disbursal mechanisms along other thinner faces like (010) plane, the crystal breaks when stress is applied perpendicular to this plane, explaining the anisotropic nature of molecular packing in the CF<sub>3</sub>OMe crystals (Figure 3.4f). Topical developments in the field of mechanophotonics unraveled the peculiar behavior of elastic crystals in the micro-regime. 44,174,193 The demonstration of pseudo-plasticity of (flexible) microcrystals reiterates the influence of the crystal's aspect ratio and their adhesive interaction with the substrate (borosilicate). This pseudo-plasticity observed in CF<sub>3</sub>OMe and BPyIN was ingeniously utilized to fabricate miniature organic-crystal-based HDC.

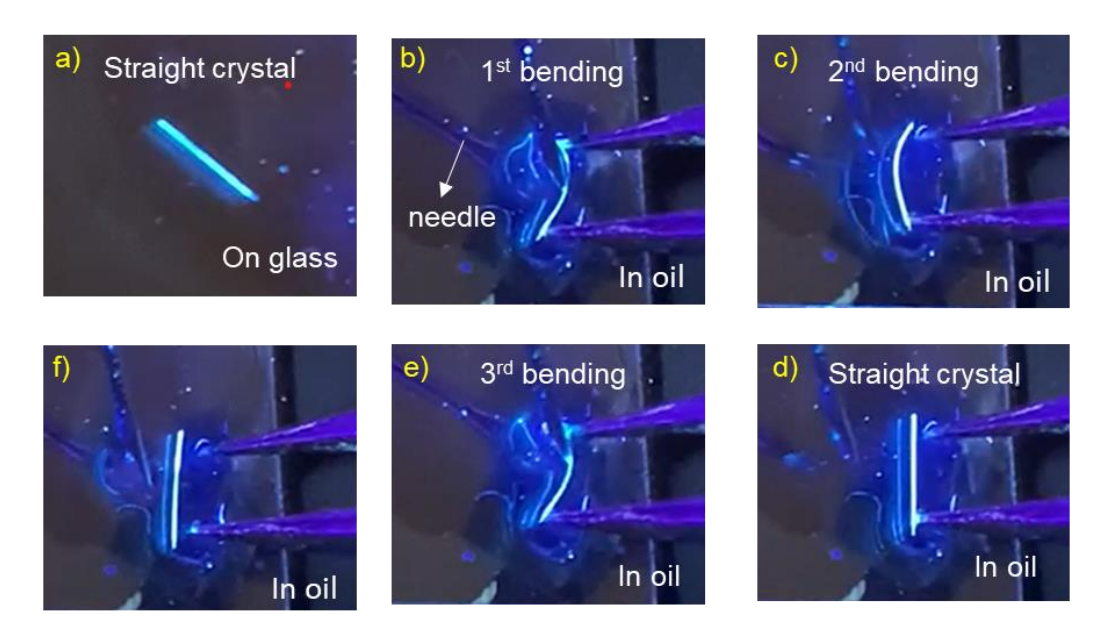


**Figure 3.5.** a-f) Three-point bending performed on a CF<sub>3</sub>OMe millimeter-sized crystal using tweezers and a sharp needle in oil under UV torch illumination.

#### 3.3.4 Self-assembly of CF<sub>3</sub>OMe

For the preparation of CF<sub>3</sub>OMe microcrystals, 1 mg of the compound was dissolved in methanol and left undisturbed for 12 h. Later, a 20  $\mu$ L solution was drop-casted onto a clean borosilicate coverslip. Complete evaporation of the solvent under ambient conditions

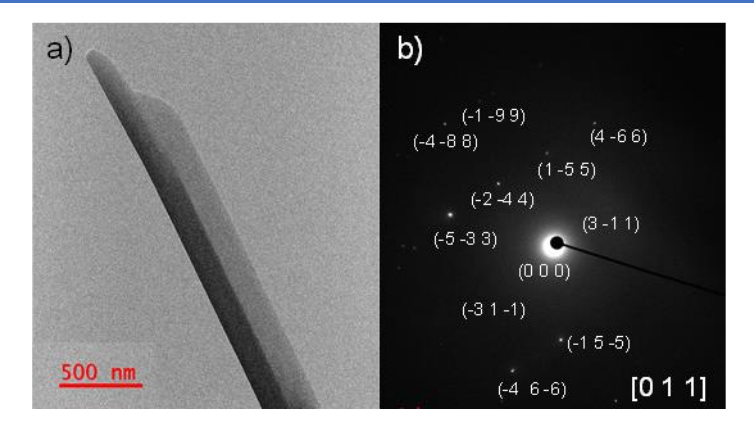


**Figure 3.6.** a) Transmission electron microscope image and b) selected area electron diffraction from the corresponding microcrystal shown in a.

yielded rod-like microstructures. The crystallinity of the CF<sub>3</sub>OMe microstructures was confirmed by the TEM studies performed on the self-assembled structures (Figure 3.6a). The bright spots on the selected area electron diffraction micrographs correspond to planes (-5 -3 3), (-3 1 -1), (-1 5 5), etc. along the [0 1 1] zone axis and confirm the crystalline nature of these self-assembled microstructures (Figure 3.6b). Self-assembly of BPyIN was described previously in section 2.3.4.1.

#### 3.3.5 Mechanophotonic studies of CF<sub>3</sub>OMe and BPyIN

The micromechanical manipulation and photonic studies were performed on a confocal optical microscope attached to an atomic force microscopy cantilever tip. For optical excitation of the crystal terminal, a 60× objective was used, whereas for recording the spectrum and images 20× objective was utilized. The photonic properties of CF<sub>3</sub>OMe microcrystal (OW1) of length,  $L\approx168$  µm were studied by illuminating the left terminal with a 405 nm continuous wave laser (Figure 3.7a,b). At the point of excitation, blue FL of CF<sub>3</sub>OMe with a bandwidth  $\lambda_1 \approx 420-670$  nm was produced. As the generated light propagates towards the crystal's opposite terminal, because of reabsorption, the resultant emission spectrum corresponds to a narrow band signal,  $-\lambda_1 \approx 440-670$  nm (Figure 3.7c). Notably, the FL spectrum at the terminal of OW1 is comprised of sharp peaks called optical modes. The optical modes in CF<sub>3</sub>OMe arise because of the back-and-forth reflection of the confined FL within the crystal cavity. The typical FSR, the spacing between two consecutive modes, was calculated to be  $\approx 11$  nm at  $\lambda_{max}$  475 nm. The light-guiding efficiency of the CF<sub>3</sub>OMe waveguide can be understood from its optical loss. The FL spectrum collected at a fixed end for varied excitation positions along the longitudinal axis of the microcrystal waveguide can be used to calculate the  $\alpha'$  for CF<sub>3</sub>OMe's OW1 of  $L\approx168~\mu m$  to be 0.0979 dB  $\mu m^{-1}$  (Figure

3.7d). Similarly, photonic investigations were carried out on a BPyIN crystal ( $L\approx260~\mu m$ , OW2, Figure 3.7e). Laser light irradiation on OW2's left terminal produced a green FL with a bandwidth  $\lambda_2\approx482-700~nm$  (Figure 3.7f). The reabsorption in BPyIN microcrystal resulted in a narrow bandwidth spectrum ( $-\lambda_2\approx532-700~nm$ ) at the right terminal (Figure 3.5g). The  $\alpha'$  of OW2 was estimated to be 0.0890 dB  $\mu m^{-1}$  (Figure 3.7g,h). The FL spectrum collected at the terminal of OW2 also consisted of optical modes akin to CF<sub>3</sub>OMe crystal due to its smooth light-reflecting crystal facets.

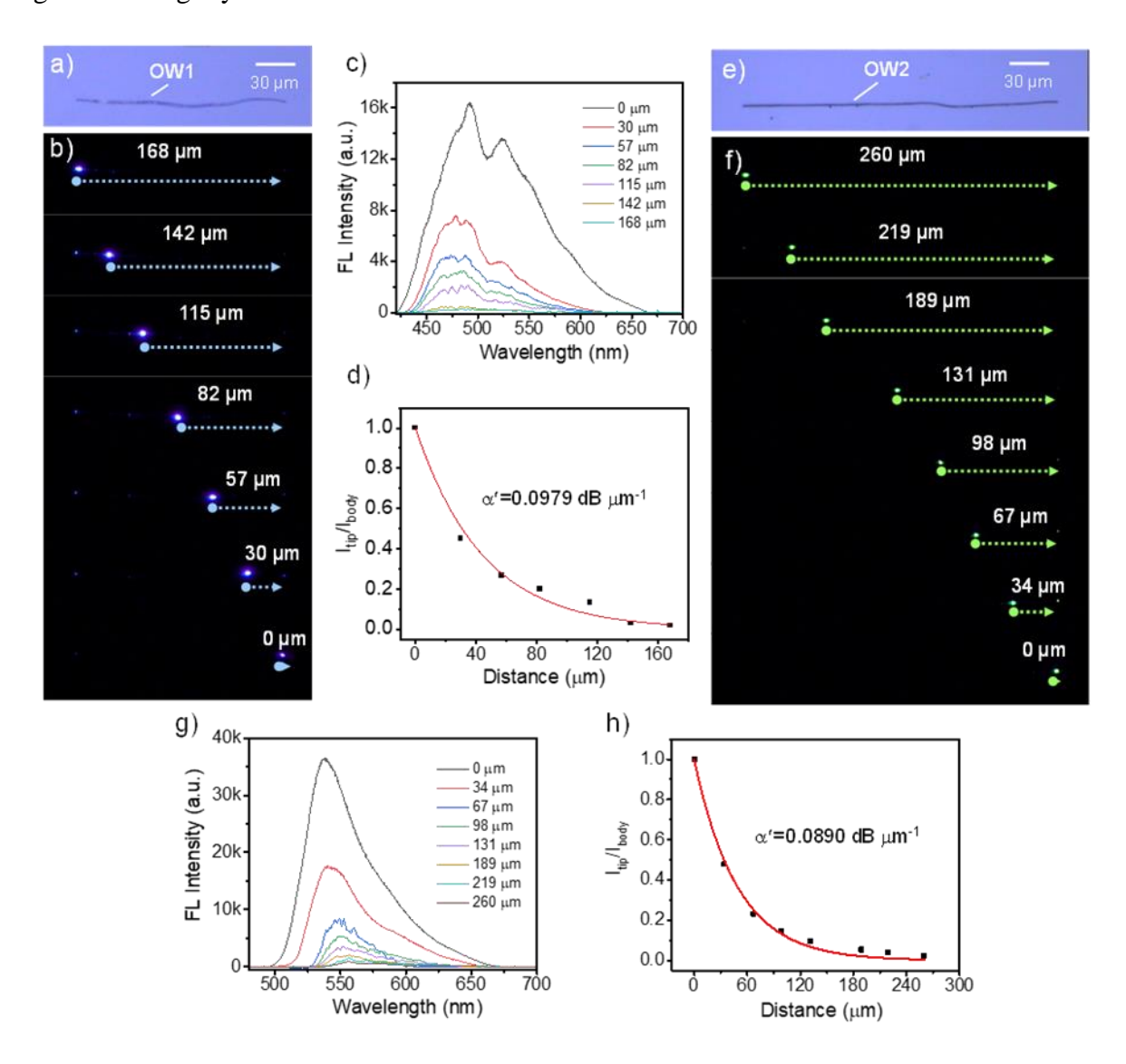


**Figure 3.7.** a,b) Confocal optical image and FL images of  $CF_3OMe$  microcrystal labelled as OW1.c) FL spectra at right tip of OW1 for different distances between excitation and collection points shown in b. d) The plot of  $I_{tip}$  / $I_{body}$  vs Distance to calculate optical loss of OW1.e,f) Confocal optical image and FL images of BPyIN microcrystal labelled as OW2.e g) FL spectra collected at right tip of OW2 for different distances between excitation and collection points shown in f. h) The plot of  $I_{tip}$  / $I_{body}$  vs Distance to calculate optical loss of OW2.e

The previously reported organic directional couplers comprised uniformly strained structures.<sup>174,207</sup> Here, we intended to construct a non-uniformly strained HDC, structurally

close to the conventional silicon-type DC but with two chromatically different FL crystals. For that, a BPyIN microcrystal must be lifted from one substrate and released near the CF<sub>3</sub>OMe microcrystal in another substrate using an AFM cantilever tip to the circuit construction site in another substrate. The BPyIN microcrystal was transferred to the substrate containing CF<sub>3</sub>OMe's OW1 using the *lifting* micromechanical operation described in section 1.6.2.

#### 3.3.6 Fabrication of hybrid directional coupler

The construction of non-uniformly strained HDC requires a bent waveguide. The same was achieved by pushing the BPyIN microcrystal at 135 µm in the forward direction with an AFM tip (Figure 3.8 a-f). Later, a similar strategy was used to create a bend at 186 µm from the left terminal of the microcrystal (Figure 3.8g-h). The strain created at these bent regions reached 1.3% and 3.4%, respectively (Figure 3.8i). Apart from geometrical change, because of the change in the molecular arrangement at the periphery of the strained microcrystal, a slight variation in refractive index (*n*) at convex and concave parts of the crystal is also possible. As a result, the light-confining nature of the cavity is perturbed in the bent microcrystal and leads to changes in optical modes relative to the unstrained waveguide as discussed in section 1.6.2. <sup>197,200</sup>

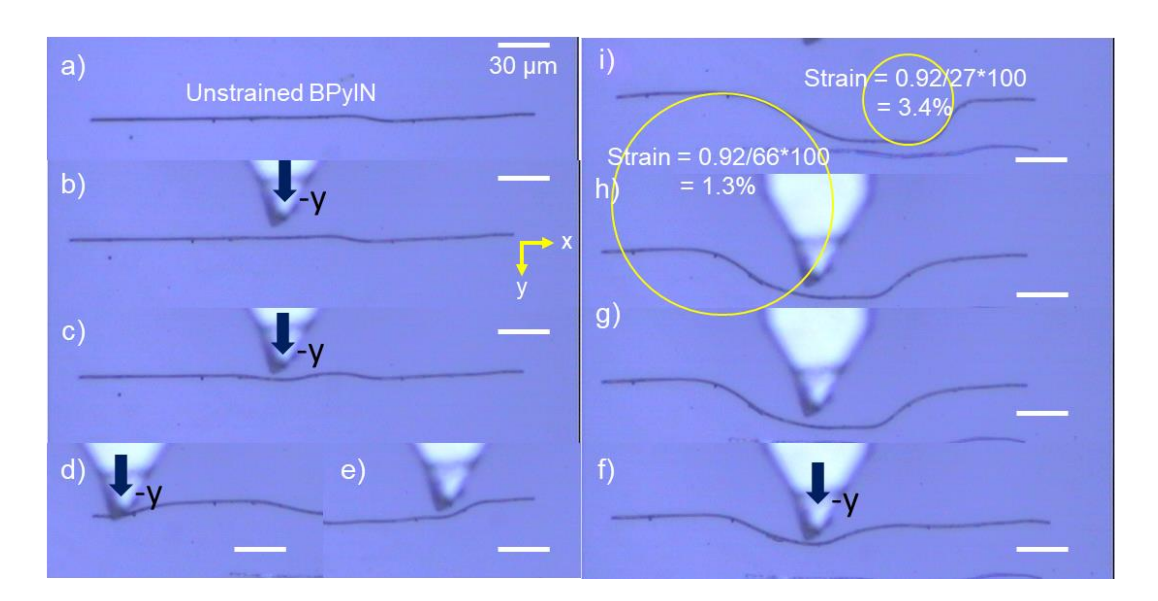


**Figure 3.8.** Confocal optical image of a) unstrained BPyIN waveguide. b-g) Confocal optical images depicting the sequential bending of BPyIN waveguide into a strained waveguide using AFM-tip. and FL images of CF<sub>3</sub>OMe microcrystal labelled as OW1. h, i) Strain developed at the bent regions of the BPyIN waveguide.

The bent BPyIN microcrystal was slowly pushed forward with an AFM tip towards CF<sub>3</sub>OMe microcrystal by moving the piezo stage (Figure 3.9a-d). Later, the CF<sub>3</sub>OMe microcrystal was pushed in x and y directions to bring them into evanescent contact with

BPyIN microcrystal (Figure 3.9e,f). Then, the nearly straight CF<sub>3</sub>OMe crystal was slowly moved in the forward direction on the right side, followed by the same on left side to bend it further away from BPyIN crystal to achieve a non-uniformly strained HDC (Figure 3.9g-l). The FL image (wide-field illumination) of HDC shows four bright termini ascertaining light guiding tendency of both crystals in contact (Figure 3.9m). The color-coded FESEM image illustrates the bent geometries of both waveguides with a T of  $\approx 0.92$  and  $\approx 1.87$   $\mu$ m for BPyIN and CF<sub>3</sub>OMe crystals, respectively are in evanescent contact (Figure 3.9n). The zoom-view of the coupling region depicts close contact between microcrystals (Figure 3.9n, Inset). Hence, effective optical communication can be expected from one crystal to another.

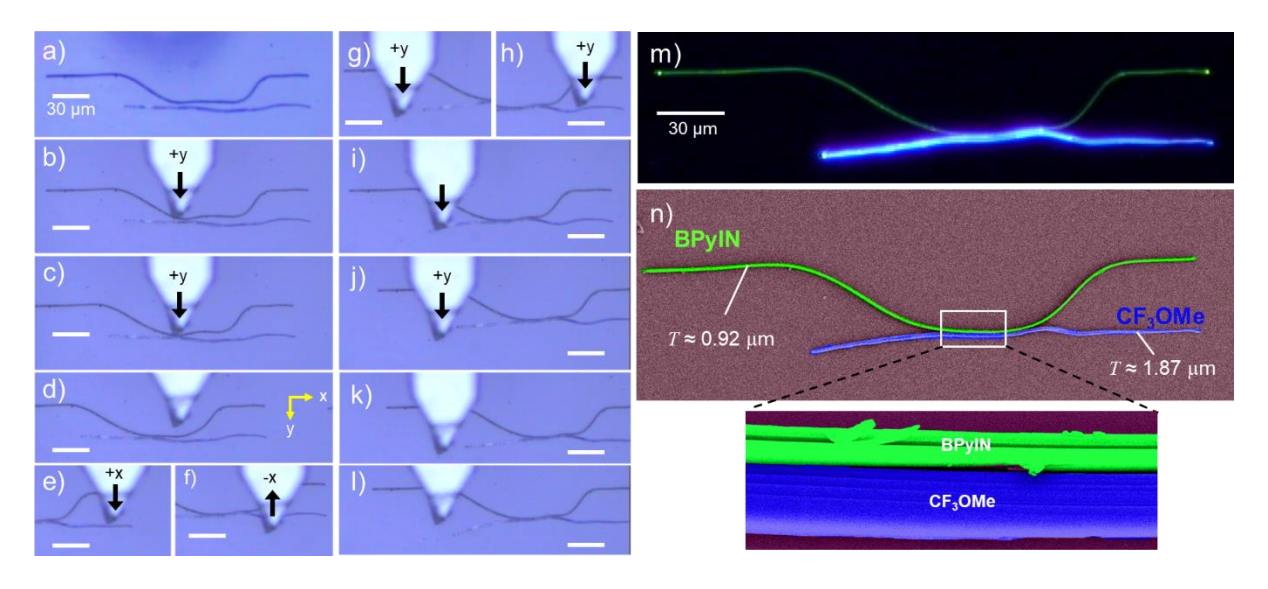


**Figure 3.9.** a-1) Micromechanical integration of bent BPyIN with  $CF_3OMe$  microcrystal to fabricate hybrid directional coupler (HDC). m,n) Confocal FL microscope image and false color-coded FESEM image of the fabricated HDC, respectively. Inset shows a magnified view of the junction between two microcrystals, and T is the microcrystal thickness.

#### 3.3.7 Optical performance of hybrid directional coupler

The optical signal processing and subsequent light routing capabilities of the constructed HDC were investigated by introducing a 405 nm light input at any one of the crystal terminals or ports (abbreviated as P) and recording the FL signal response at the other three ports (Figure 3.10a). For example, when the input was given at P1, it produced an active (A) blue FL signal ( $\lambda_1(A)$ ;  $\approx$ 420-670 nm) corresponding to CF<sub>3</sub>OMe (Figure 3.10b,g). As the produced active signal propagates towards P2, due to the optical reabsorption, a narrow bandwidth signal ( $-\lambda_1(A)$ ;  $\approx$ 440-670 nm) outcoupled at P2 (Figure 3.10g,l). Additionally, when  $\lambda_1(A)$  signal moves towards P2, its evanescent field excites the BPyIN microcrystal via ET in the coupling region. Thus, the active green FL signal ( $-\lambda_2(A)$ ;  $\approx$ 482-700 nm) generated in the BPyIN waveguide near the coupling region propagates to P3 (Figure 3.10k,l). No light

output, 0, signal was recorded at P3 due to the circuit's directional coupling geometry (Figure 3.101). Similarly, for light input at P2, signals  $-\lambda_1(A)$ ,  $-\lambda_2(A)$  and 0 were spectroscopically recorded at P1, P4 and P3, respectively (Figure 3.10c,h). The graphics presented in Figure 3.10f clearly depicts the light splitting and outcoupling of two chromatically different active signals ( $\lambda_2$  and  $\lambda_1$ ) in the forward direction by the HDC.

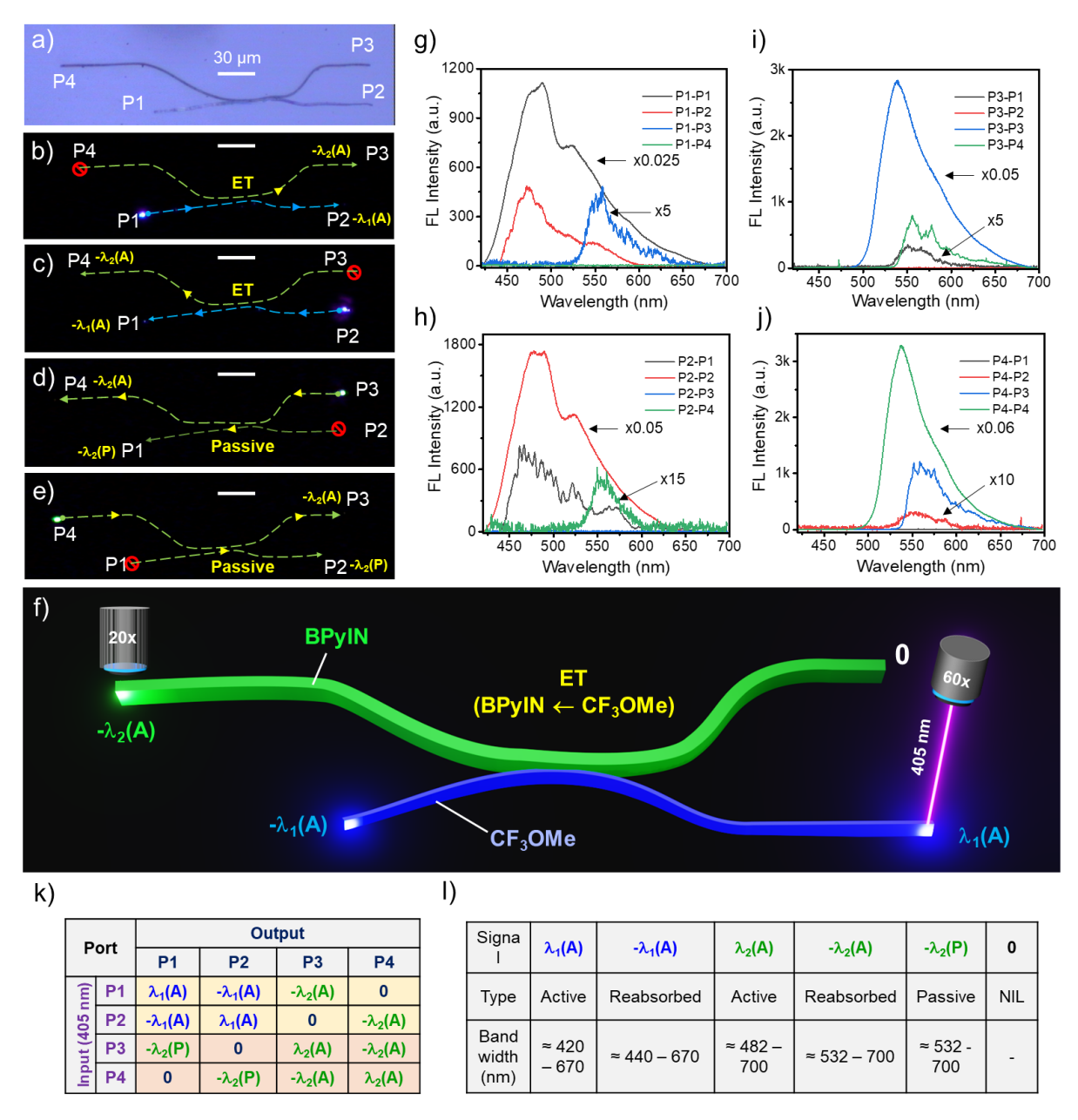


**Figure 3.10.** a) Confocal optical image of hybrid directional coupler (HDC). b-e) Laser FL microscope images of HDC for 405 nm input light given at ends P1-P4, respectively. f) Graphics portraying the functioning of simultaneous functioning of HDC as signal modulator and beam splitter. g-j) Corresponding FL spectra obtained as optical output response at various ends of HDC for respective light input at ends P1-P4, respectively. k) Optical performance of the HDC tabulated according to the signal observed at various ports against given input. (Yellow color highlights signal modulation and red color highlights signal splitting) l) Different optical signal types and bandwidths operational in HDC.

Further, when light input is given to BPyIN (OW2) at P3, a bright green FL signal  $(\lambda_2; \approx 482-700 \text{ nm})$  is produced at the point of excitation (Figure 3.10d,i). The FL signal is reabsorbed and a narrow band active signal ( $-\lambda_2$ ;  $\approx 532-700$  nm) was outcoupled at P4 (Figure 3.10l). The same signal is split at the coupling region due to evanescent coupling with OW1 and passively (P) propagated as  $-\lambda_2$ (P) signal towards P1 as there is no ET possibility from BPyIN to CF<sub>3</sub>OMe. While no signal output is detected at P2 due to the circuit's directionality. Similarly, for input signal at P4,  $-\lambda_2(A)$ ,  $-\lambda_2(P)$  and 0 signals were outcoupled at P3, P2 and P1, respectively (Figure 3.10e,j). Therefore, providing laser input to any one of the ports of CF<sub>3</sub>OMe crystal waveguide in HDC results in chromaticity modulation-andsplitting of the signal in the same circuit. While for same laser input given at any of the ports of BPyIN waveguide results only in splitting the signal (λ<sub>2</sub>) without any chromaticity modulation. Hence, the fabricated HDC acts as an input-selective optical signal splitter/color modulator, demonstrating the multi-tasking capabilities within the same circuit. Interestingly, the optical modes observed in individual (straight and bent) waveguides were distinctly modified in the HDC at respective ports relative to the uncoupled waveguides. This is due to the interference of optical signals at the evanescent coupling region (Figure 3.11).

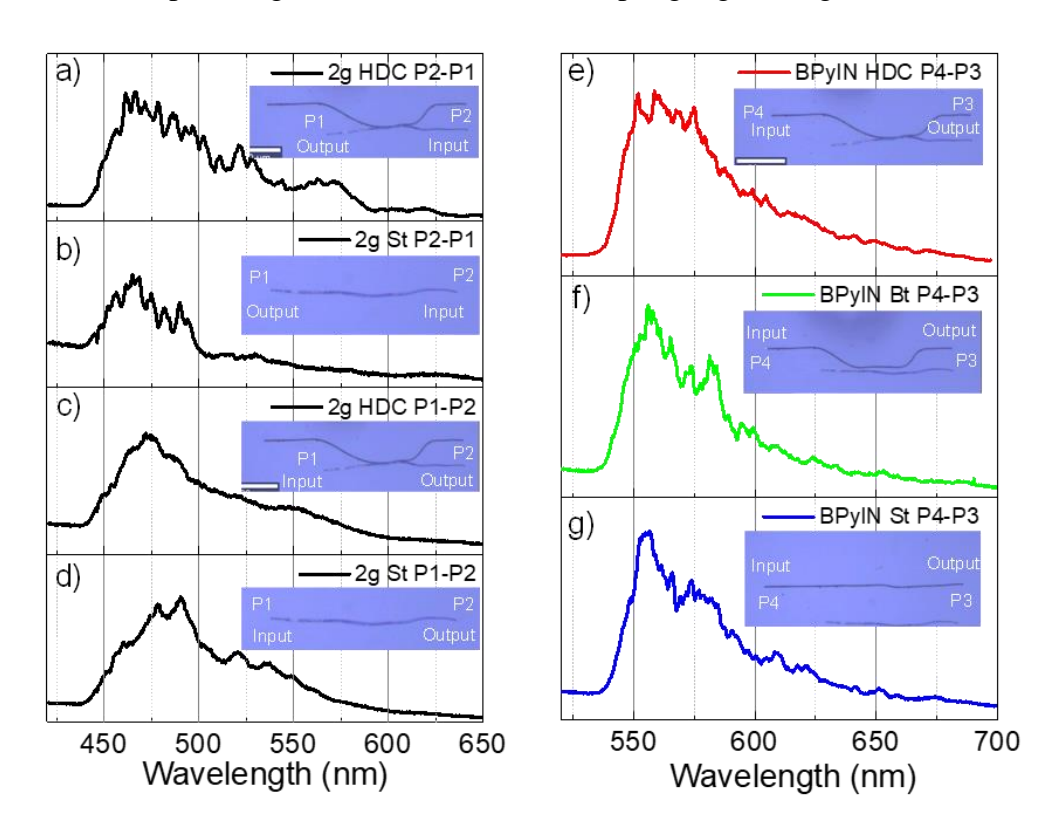


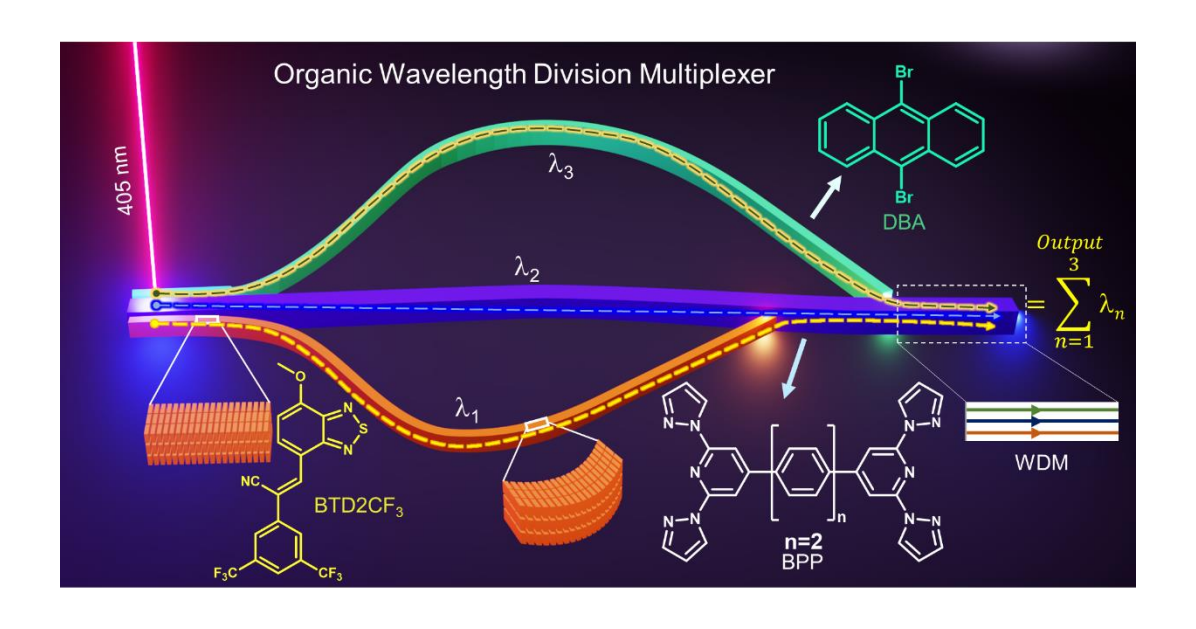
**Figure 3.11.** a-d) Comparison of optical modes in pristine CF<sub>3</sub>OMe and after coupling with BPyIN to realize hybrid directional coupler (HDC). Inset shows the optical images depicting 405 nm light input position and FL output collection point e-g) FL spectra obtained in straight, bent and HDC at the right end of BPyIN waveguide for input at left end. Insets present the optical image with input and output labels.

#### 3.4 Summary

In this chapter, for the first time, a hybrid  $2\times2$  directional coupler (HDC) was fabricated using the blue-emitting CF<sub>3</sub>OMe crystal in combination with a green-emitting elastic crystal. For this, the microcrystals of CF<sub>3</sub>OMe and BPyIN were integrated on a single substrate by transferring the BPyIN crystals from one substrate to another close to the circuit fabrication site using the mechanophotonics approach. The photonic studies demonstrated the signal input-terminal dependent diverse optical functioning of HDC. The HDC acted as signal chromaticity modulator-and-splitter ( $\lambda 1$  and  $\lambda 2$ ; blue and green) in one case and as a simple beam splitter in another case ( $\lambda 2$ ; green). Therefore, HDC exhibited multi-tasking capabilities with single geometry because of the innovative inclusion of two different FL flexible crystals. Developing such pioneering optical components has broader implications for the advancement of flexible photonic device applications, in particular organic neural networks and neuromorphic photonic technologies.

# 4

# A Broadband, Multiplexed-Visible-Light-Transport in Composite Flexible-Organic-Crystal Waveguide



**4.1 Abstract:** This chapter reports the construction of an organic crystal multiplexer using three chemically and optically different acicular, flexible organic crystals for broadband, visible light signal transportation. The mechanical integration of a highly flexible crystal waveguide of (Z)-2-(3,5-bis(trifluoromethyl)phenyl)-3-(7-methoxybenzo[c][1,2,5] thiadiazol-4-yl)acrylonitrile (BTD2CF<sub>3</sub>) displaying bright yellow ( $\lambda_1$ ) fluorescence with blue-emitting ( $\lambda_2$ ) BPP and cyan emitting ( $\lambda_3$ ) DBA crystals using AFM-tip provide a composite organic crystal multiplexer. The constructed hybrid single-crystal multiplexer effectively transduces three optical signals ( $\lambda_1+\lambda_2+\lambda_3$ ) covering the 420-750 nm region as a composite output signal. The presented proof-of-principle experiment demonstrates the real potential of organic flexible crystal waveguides for visible light communication technologies.

#### 4.2 Introduction

Visible light communication (VLC) has emerged as a promising short-range wireless technology for day-to-day applications.<sup>208</sup> VLC combines visible light (400-750 nm) and data communication for ubiquitous computing in light-emitting-diode-based devices such as indoor/outdoor lamps, televisions, car lamps, traffic signals, etc. In VLC technologies, different light signals are combined and transmitted through a wavelength division multiplexer (WDM).<sup>44,193,208</sup> Basically, a WDM transmits multiple light signals (wavelengths) as a composite *multiplexed signal* for processing. In the late 20<sup>th</sup> century, *multiplexing technology* significantly improved how information data was sent and received on radios, telephone lines, and televisions.<sup>126</sup> Mostly, WDM uses inorganic optical waveguides or optical fibers for signal transportation.<sup>128</sup>

Recently, organic crystals effectively transducing near-infrared light signals acting as optical waveguides have been reported. Studies exploring core-shell organic heterostructure crystals for multiple color signal transport are also known. However, constructing an organic crystal waveguide (WDM) transporting a broadband signal covering the VLC region is a non-trivial task. It entails precise design and mechanical integration of at least three opto-electronically different FOC waveguides emitting different colours ( $\lambda_1$ ,  $\lambda_2$  and  $\lambda_3$ ). Further, WDM requires active 66-64 and passive 31-55 waveguides, classified based on the waveguide's ability to generate photoluminescence and self-guide, or merely guide light of any given input colour, respectively. Importantly, one of these waveguides ( $\lambda_1$ ), namely the WDM, should allow passive transmission of various light colours ( $\lambda_2$  and  $\lambda_3$ ) channeled into it by other waveguides. This enables multiplexing transport of all three different

broadband signals ( $\lambda_1+\lambda_2+\lambda_3$ ) through WDM to demultiplex later. To widen the bandwidth for VLC, we envisioned the construction of an organic WDM with blue, cyan, and yellow FL crystals. We selected blue-emitting FOC derived from a back-to-back coupled 2,6-bis(pyrazolyl) pyridine units connected to a biphenyl molecule (BPP) as a WDM waveguide,<sup>55</sup> and cyan FL DBA,<sup>197</sup> and yellow FL (Z)-2-(3,5-bis(trifluoromethyl)phenyl)-3-(7-methoxybenzo[c][1,2,5]thiadiazol-4-yl)acrylonitrile (BTD2CF<sub>3</sub>) flexible crystals as light channeling adjacent waveguides.

Here, this chapter reports the first construction of wide bandwidth organic WDM for VLC by integrating optically and mechanically different BPP, DBA and BTD2CF3 crystal waveguides via a mechanophotonics approach. The optical emission bandwidths of BPP, DBA and BTD2CF3 crystals are  $\approx$ 420-700 nm ( $\lambda_1$  – blue), 445-705 nm ( $\lambda_2$  – cyan), 480-755 nm ( $\lambda_3$  – yellow), respectively. The weak molecular interactions like hydrogen bonding and C-H··· $\pi$  assist in exhibiting reversible crystal deformation in response to the applied external mechanical stress. Mechanical micromanipulation of BPP, DBA and BTD2CF3 single crystals provide organic WDM, wherein the BPP waveguide acts as a multiplexer. The FL of BPP waveguide falls very much within DBA and BTD2CF3 waveguide's absorbance, thereby efficiently facilitating ET-triggered optical excitation and emission of latter crystals. The constructed WDM could successfully transduce three optical signals arising from (i) active self-waveguiding BPP ( $\lambda_1$ ), (ii) active DBA ( $\lambda_2$ ) and BTD2CF3 ( $\lambda_3$ ) waveguides excited directly and through ET from BPP, and (iii) passive/active transmission of a mixed wide bandwidth ( $\lambda_1$ + $\lambda_2$ + $\lambda_3$  = 420-750 nm) signals by the BPP waveguide, proving the multiplexing ability.

#### 4.3 Results and Discussion

4.3.1 Synthesis of (Z)-2-(3,5-bis(trifluoromethyl)phenyl)-3-(7-methoxybenzo[c][1,2,5] thiadiazol-4-yl)acrylonitrile (BTD2CF3): The synthesis of BTD2CF3 was accomplished by base-assisted substitution of bromine with methoxy moiety and condensation of an aldehyde with phenyl acetonitrile derivative in 7-Bromobenzo[c][1,2,5]thiadiazole-4-carbaldehyde, BTDCHO (Scheme 4.1). Sodium methoxide (10 mmol, 2 eq) and bis(3,5-trifluoromethyl)phenyl acetonitrile (5 mmol, 1eq) were dissolved in methanol (15 mL) and added to a two-necked RB flask. BTDCHO (5 mmol, 1eq) was slowly added to the RB flask drop-by-drop for 10 minutes. The mixture was heated at 70 °C for 4 h. After completion of the reaction, monitored by thin layer chromatography, the reaction

mixture was allowed to reach room temperature and the precipitate was filtered off and recrystallized in methanol to obtain BTD2CF<sub>3</sub> crystals. The crystals were used to obtain  $^{1}$ H NMR (Figure 4.1). Yield 65%.  $^{1}$ H NMR (400 MHz, CDCl<sub>3</sub>):  $\delta$  8.75 (d, 1H,  $^{3}J_{H,H}$  = 8.25 Hz), 8.55 (s, 1H), 8.18 (s, 2H), 7.92 (s, 1H), 7.01 (d, 1H,  $^{3}J_{H,H}$  = 8.25 Hz), 4.15 (s, 3H). FTIR ( $\bar{v}$  cm<sup>-1</sup>): 2359, 2033, 1536, 1373, 1277, 1169, 1121, 890, 684, 640; HR-MS: m/z Calculated: 429.08, Found: 430.04; UV-Vis (Solid-state):  $\lambda_{abs-max}$  500 nm and  $\lambda_{FL-max}$  ≈576 nm (orange emission); Melting point: ≈199-203 °C.

Scheme 4.1. Synthesis of BTD2CF<sub>3</sub>.

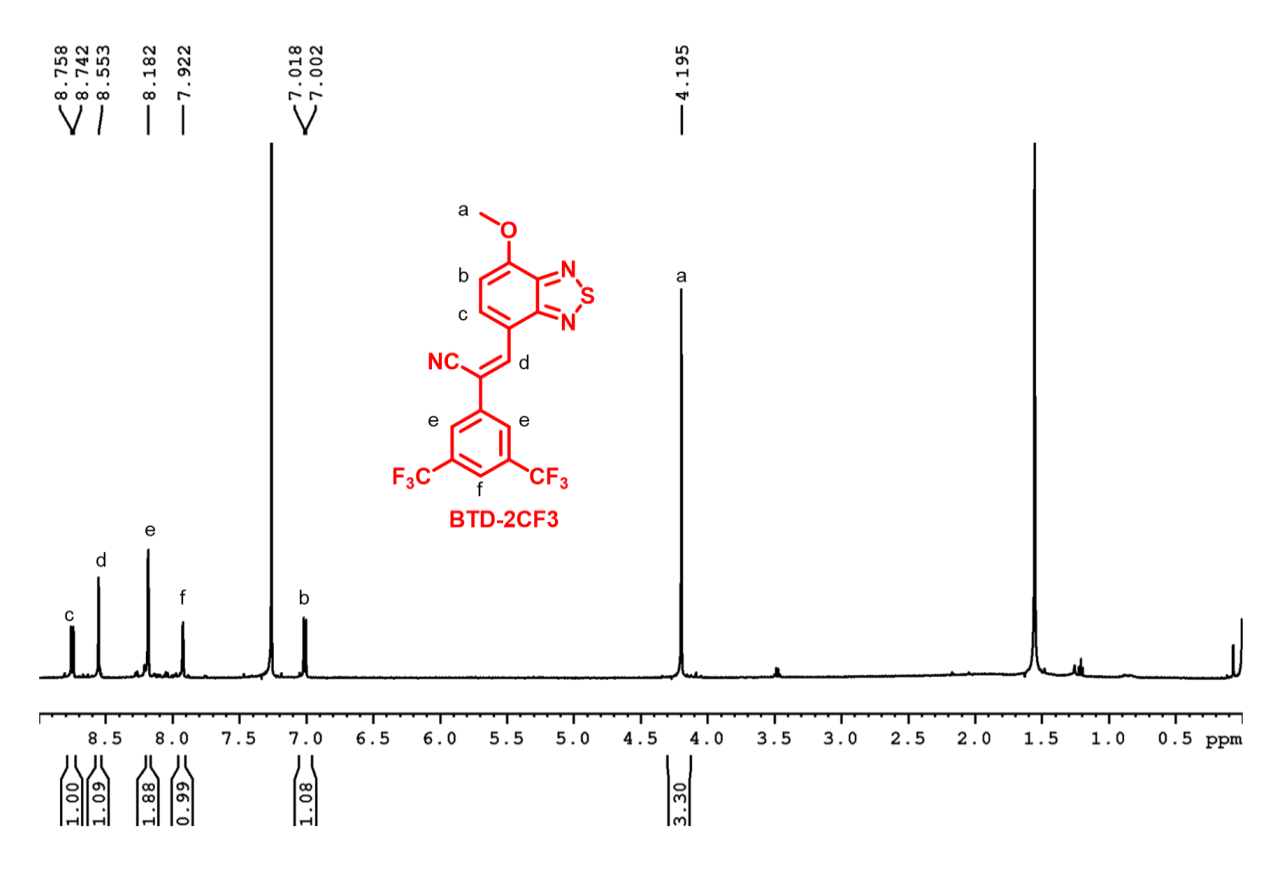


**Figure 4.1.** <sup>1</sup>H NMR (400 MHz) spectrum of BTD2CF<sub>3</sub> in CDCl<sub>3</sub> ( $C \approx 0.01$  M).

**4.3.2 Synthesis of BPP**: The synthesis of 4-iodo-2,6-di-pyrazol-1-ylpyridine, 1 was accomplished following our earlier reported procedure.<sup>55</sup> The synthesis of BPP was accomplished by the Suzuki coupling reaction of 1 with 4,4'-biphenyldiboronic acid. For this, a solution of 1,4-dioxane (25 ml) containing 1 and 2 M Na<sub>2</sub>CO<sub>3</sub> (8 ml) was taken in a clean 250 mL flask and N2 gas was bubbled into the solution for 10 min. Later, 4,4'biphenyldiboronic acid (50 mg, 0.206 mmol) and Pd(PPh<sub>3</sub>)<sub>4</sub> (35 mg, 5 mol %) were added and heated at 70 °C until complete consumption of reactants (monitored by TLC (1: 19 ratio of MeOH: CH<sub>2</sub>Cl<sub>2</sub>)). The crude solid was extracted with a water-CH<sub>2</sub>Cl<sub>2</sub> mixture several times and the organic layers were dried over MgSO<sub>4</sub>. The organic layer was evaporated to obtain a crude light yellow solid product. The yellow solid residue was washed several times with cold CH<sub>2</sub>Cl<sub>2</sub> and methanol to afford analytically pure white color powder of BPP. Yield 0.118 mg (48%). <sup>1</sup>H NMR (400 MHz, CDCl<sub>3</sub>, 25 °C)  $\delta$ /ppm: 8.65 (d, 4H,  $J_{H,H} = 2.36$  Hz), 8.20 (s, 4H), 7.97(d, 4H,  $J_{H,H} = 8.2 \text{ Hz}$ ), 7.83-7.81 (m, 8H,), 6.6-6.5 (m, 4H). <sup>13</sup>C NMR (100 MHz, CDCl<sub>3</sub>, 25 °C) δ/ppm: 150.7, 142.4, 141.5, 136.8, 127.8, 127.3, 108.1, 107.1. **FTIR** (KBr) v in cm<sup>-1</sup>: 3439, 3148, 2932, 2856, 1613, 1572, 1539, 1510, 1460, 1394, 1207, 1157, 1119, 1067, 1036, 953, 936, 914, 872, 824, 787, 768, 690, 627, 606, 507.

Scheme 4.2. Synthesis of BPP.

#### 4.3.3 Solid-state optical characteristics of materials employed for WDM

Solid-state UV-visible and FL spectroscopy were employed to study the optical characteristics of different crystals needed for assessing the suitability for WDM's construction. The Jablonski diagram shows the ET process involving BPP, DBA and BTD2CF<sub>3</sub> crystals (Figure 4.2a). The solid-state absorption of BPP showed a maximum at  $\lambda_1 \approx 330$  nm, and its FL covered the  $\approx 420\text{-}700$  nm region (Figure 4.2b). DBA absorbed from 250 to 650 nm, and its FL maximum appeared at  $\lambda_2 \approx 525$  nm with a bandwidth covering  $\approx 445\text{-}705$  nm region. The absorption of BTD2CF<sub>3</sub> appeared in the 250-600 nm region, and its FL maximum centered at  $\lambda_3 \approx 576$  nm with a bandwidth of  $\approx 482\text{-}760$  nm. The absolute PLQY of BPP, DBA and BTD2CF<sub>3</sub> crystals was estimated to be <1%, 7.4% and 49.1%, respectively. The FL region of BPP falls within the maximum absorption region of DBA and

BTD2CF<sub>3</sub>, facilitating effective ET from BPP to DBA and BTD2CF<sub>3</sub> crystals (Figure 4.2c). The ET triggers FL signals ( $\lambda_2$  and  $\lambda_3$ ) from DBA and BTD2CF<sub>3</sub> crystals, respectively.

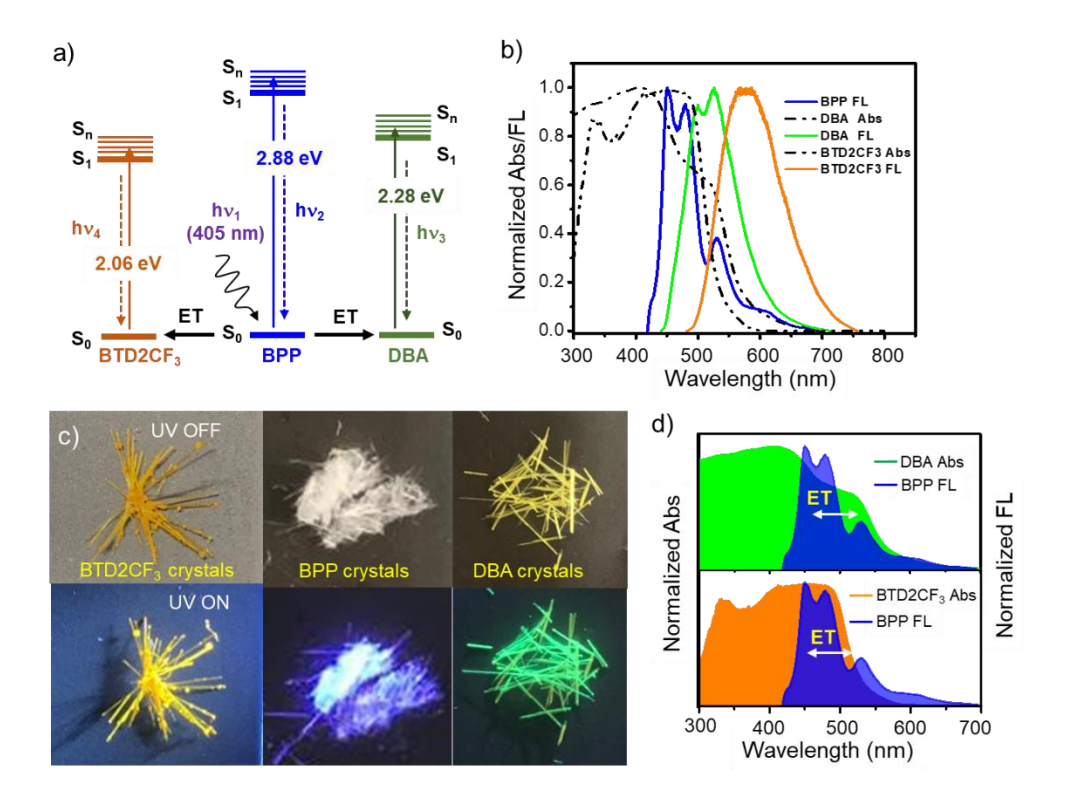


**Figure 4.2.** a) Jablonski diagram depicting the mechanism of ET between different crystals. b) Solid-state absorption and emission spectra of BPP, DBA and BTD2CF $_3$  molecules. c) The photographs of crystals under normal and UV light illumination. d) The spectra showing region of overlap of absorption of DBA (top) and BTD2CF $_3$  (bottom) with the emission of BPP molecules suggesting ET from BPP to DBA/BTD2CF $_3$ .

#### 4.3.4 Single crystal X-Ray and mechanical studies of BTD2CF3 crystals

Molecule BTD2CF<sub>3</sub> crystallizes as thin needles in a mixture of dichloromethane and acetonitrile (1:1) with a P  $\bar{1}$  space group (triclinic system; CCDC number is 2202503). The unit cell is comprised of two BTD2CF<sub>3</sub> molecules. The nitrogen group of the benzothiadiazole (BTD) moiety interacts with adjacent vinylic-hydrogen through intramolecular hydrogen bonding (C-N···H: 2.425 Å, Figure 4.3a). The dihedral angle between BTD and phenyl rings is 57° (Figure 4.3b). The rich presence of hetero atoms like N, O, F and S enhances extensive hydrogen bonding between the molecules. The various noncovalent interactions give rise to a rigid molecular framework with minimal vibrational dissipations; thus, providing high FL efficiency (Figure 4.3c). The molecular packing along (110) and (001) planes are shown in Figure 4.3d,e, respectively.

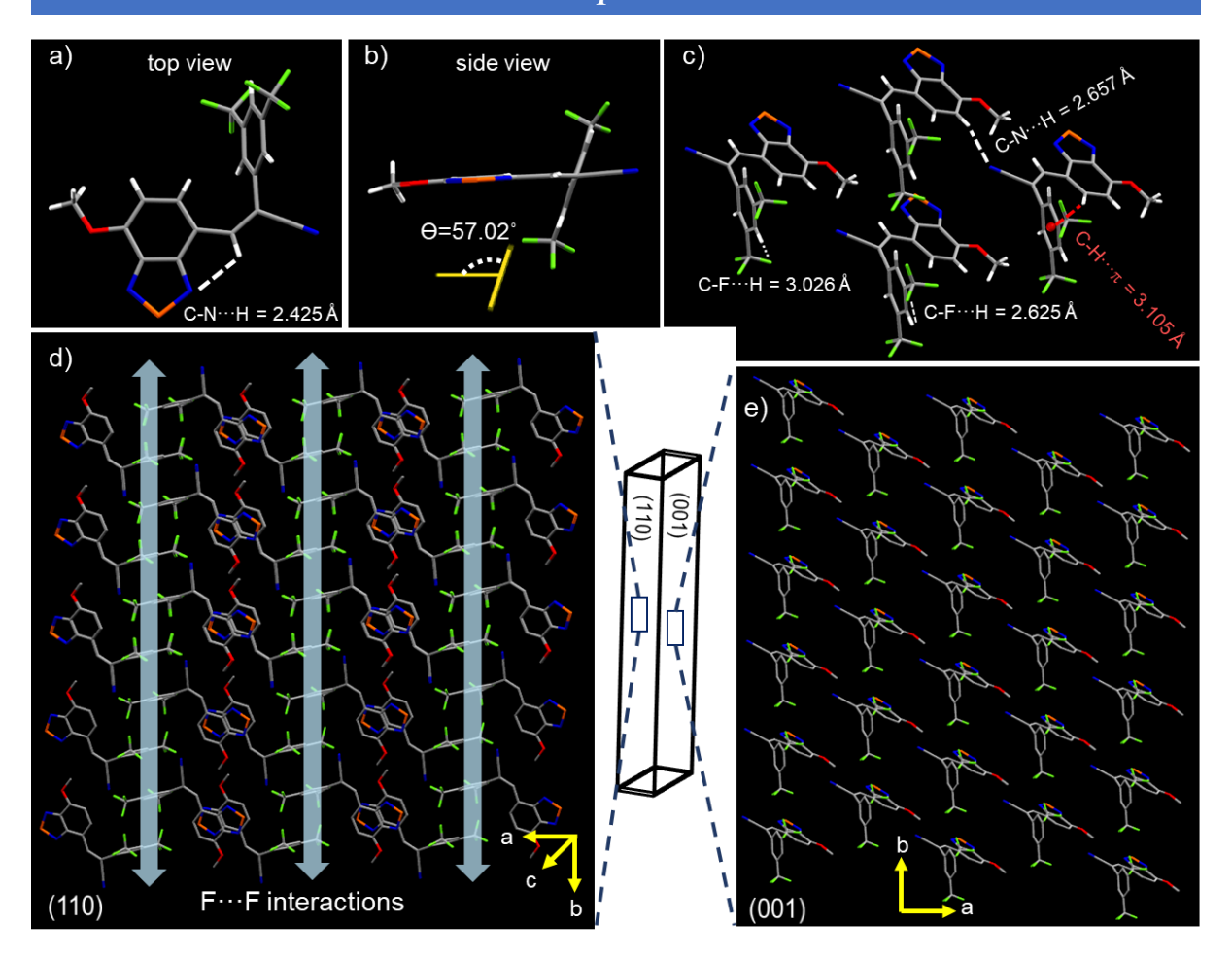


**Figure 4.3**. Crystal structure of BTD2CF<sub>3</sub> presenting a) top view and b) side view. c) different noncovalent interactions. d,e) Molecular packing along (110) and (001) planes in BTD2CF<sub>3</sub> crystal, respectively. The double headed arrows in d, represent the intermolecular F-F interactions along [110] direction.

The mechanical properties of BTD2CF<sub>3</sub> crystals were investigated using a conventional three-point bending technique. The crystal was held with the help of tweezers and applied a mechanical force using a sharp metallic needle (Figure 4.4a,b). The elastically bendable characteristics were evident when BTD2CF<sub>3</sub> crystals were subjected to mechanical force perpendicular to (110) plane. The crystal can be bent multiple times without any fracture (Figure 4.4c-f). The intermolecular halogen interactions running along the crystallographic *b*-axis act as stress-relieving channels (Figure 4.3d). The periodic arrangement of hydrogen bonding chains allows slight movement of atoms involved in these interactions from the equilibrium position during mechanical bending. They possibly act as an ensemble contributing towards resisting the large external force through small contributions, each from a molecular level weak interaction. When the crystal experiences mechanical force in other directions, it does not support elasticity. The mechanical flexibility in DBA crystals was ascribed to the presence of slip planes.<sup>197</sup>

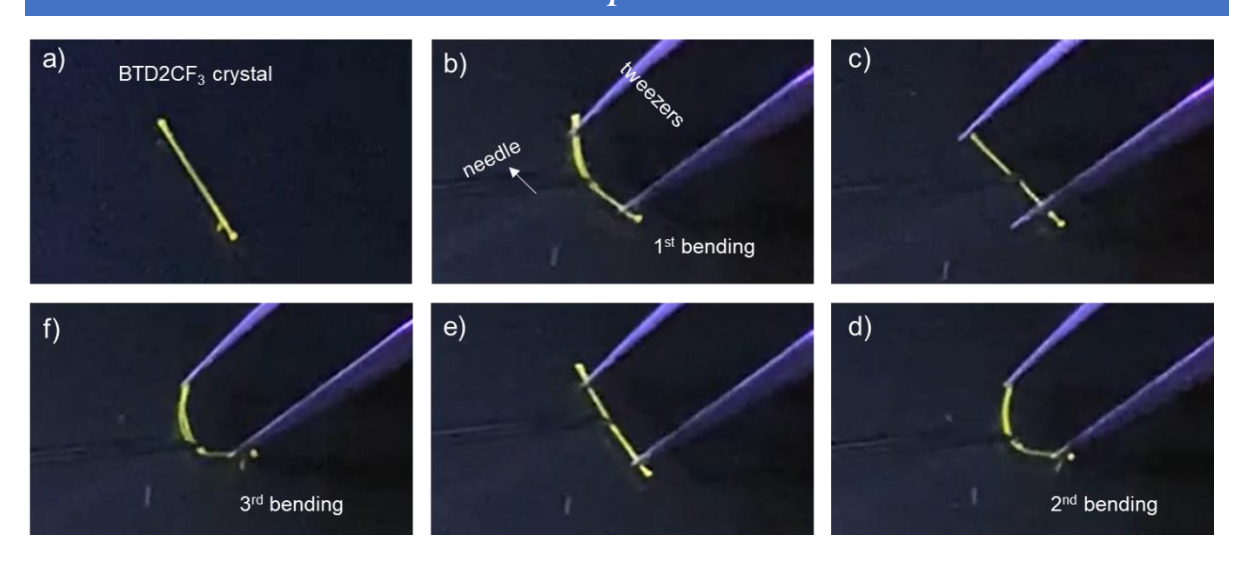


Figure 4.4. a-f) Three-point bending test performed for BTD2CF<sub>3</sub> crystals under UV light.

#### 4.3.5 Mechanophotonic studies

#### 4.3.5.1 Preparation of microcrystals

- i) Preparation of BTD2CF<sub>3</sub>: In a clean vial, BTD2CF<sub>3</sub> (1 mg) was dissolved in hexane (1 mL), and the solution was left undisturbed for 2-3 days and the resulting solution (30  $\mu$ L) was drop casted onto a clean glass coverslip to observe microrods under the confocal microscope.
- ii) Preparation of BPP microrods: Similarly, BPP (1 mg) was dissolved in dichloromethane (1 mL) and left undisturbed at rt for 12 h, under slow evaporation conditions rod-like crystals were formed. The obtained BPP crystals were dispersed in hexane and drop casted onto a clean glass coverslip for microscopic studies.
- iii) Preparation of DBA microcrystals: A similar self-assembly process was applied for obtaining DBA microcrystals as followed for BTD2CF<sub>3</sub> microcrystals. Typically, 2 mg of DBA was dissolved in 2 mL of hexane in a vial and heated at 60  $^{\circ}$ C for 15 minutes. The solution was allowed to cool at rt and left undisturbed for 6 h. Later, 25  $\mu$ L of the solution was drop casted onto a clean coverslip and the solvent was slowly evaporated at ambient conditions. The thin needle-like micro rods were observed under the confocal microscope.

#### 4.3.5.2 Optical waveguiding studies of microcrystals

The mechanophotonic aspects of organic microcrystals were studied using a confocal optical microscope attached to an atomic force microscopy (AFM). Interestingly, when the microcrystals experience AFM cantilever tip-induced mechanical stress, they display *pseudo-plasticity* due to strong CSSI. This *pseudo-plasticity* was used to fabricate micro-photonic circuits on the substrate.<sup>44</sup> To understand the optical signal transducing properties, a

BTD2CF<sub>3</sub> microcrystal of length,  $L\approx130~\mu m$  was selected, and its left terminal was illuminated with a 405 nm (continuous wave) diode laser (Figure 4.5a,b). At the excitation region, the microcrystal generated a bright yellow FL (482-755 nm), which propagated to the opposite terminal of the microcrystal, manifesting crystal's waveguiding tendency. As FL propagated through the waveguide, part of the shorter wavelength band was reabsorbed due to the overlap of absorption and emission regions of BTD2CF<sub>3</sub>. As a result, a long pass filtered signal (525-755 nm) was received at the output terminus relative to the input terminus. Later, the BTD2CF<sub>3</sub> waveguide was excited at different points along its axis, and the output signal was collected at its right terminal (Figure 4.5b,c). The waveguide's  $\alpha$ ' was estimated, from the plot of  $I_{tip}/I_{body}$  versus distance, to be 0.1597 dB  $\mu$ m<sup>-1</sup> (Figure 4.5d).

To study the optical waveguiding properties of DBA crystals, a microcrystal of  $L\approx177$  µm was chosen (Figure 4.5e). The confocal optical and FL images displayed a bright cyan light output when excited with a 405 nm laser at various positions of the microcrystal, confirming the crystal's active light transducing ability (Figure 4.5f). From the corresponding FL spectra collected at the output (Figure 4.5g), the value of  $\alpha'$  was estimated to be 0.0752 dB  $\mu$ m<sup>-1</sup> (Figure 4.5h).

The self-assembled BPP microcrystals were investigated for their optical waveguiding characteristics (Figure 4.6a,b). Previously, the passive waveguiding characteristics of flexible BPP waveguides were discussed in section 1.6.3 using a 488 nm laser source. Here, the 405 nm excitation source is used to confirm the active type waveguiding characteristics of BPP as

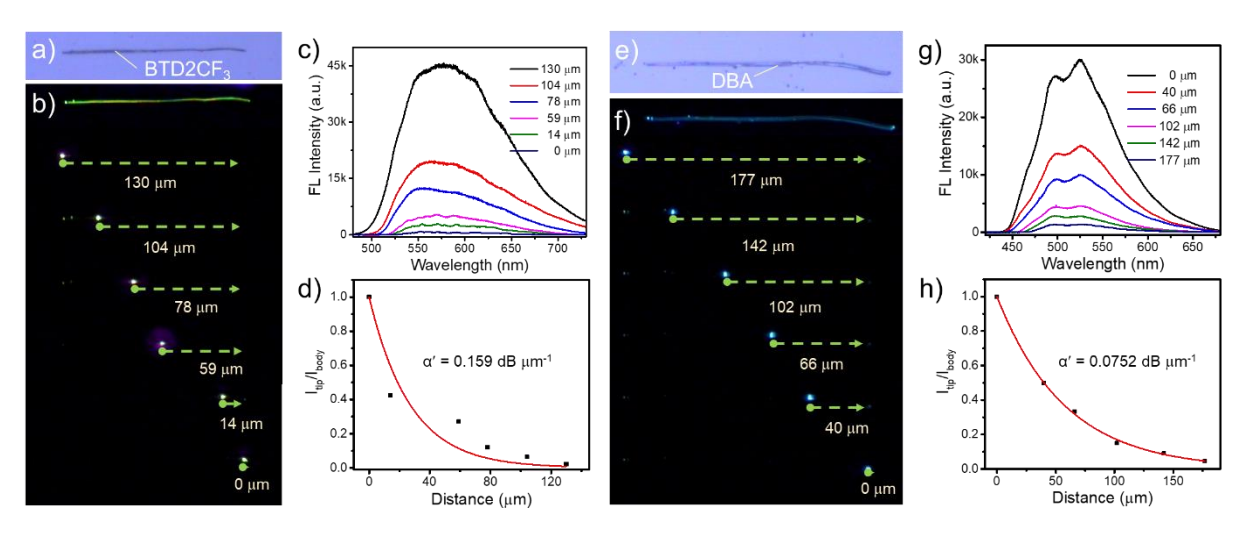


**Figure 4.5.** Confocal optical and FL microscopy images of a,b) BTD2CF<sub>3</sub> and e,f) DBA microcrystals. The light output recorded at the right terminal of c) BTD2CF<sub>3</sub> and g) DBA microcrystals for excitation at various positions on the crystal's body. The plot of  $I_{tip}/I_{body}$  versus distance used for the calculation of optical loss in d) BTD2CF<sub>3</sub> and h) DBA microcrystal waveguides.

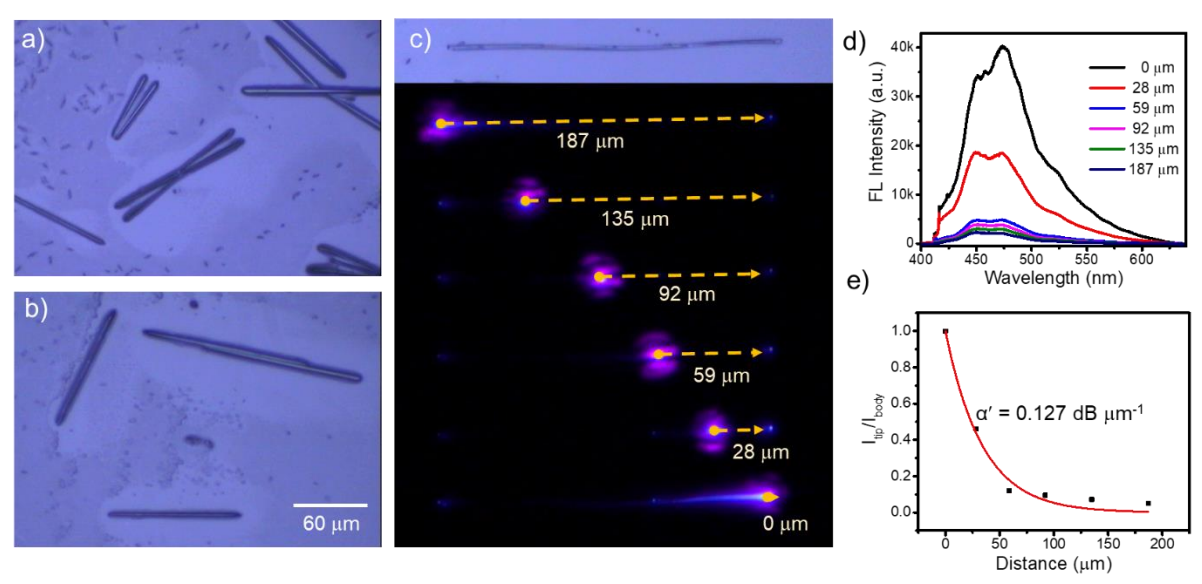


**Figure 4.6.** a,b) Confocal optical microscope images of self-assembled BPP microcrystals. c) Confocal optical and laser FL microscope images of BPP waveguide. d) FL spectra collected at a fixed terminal of BPP waveguide while exciting at different positions on the waveguide with 405 nm laser. e) Estimation of optical loss coefficient of BPP waveguide,  $\alpha'$ , from the plot of  $I_{tip}/I_{body}$  vs distance.

the absorption tail of BPP extended up to 425 nm (Figure 4.6c). The blue FL produced at the left terminal of the BPP waveguide was transported to the other terminal via the TIR mechanism to illustrate the active waveguiding in the BPP waveguide (Figure 4.6d). The excitation position-dependent emission spectra collected at the right tip of BPP microcrystal were used to calculate the  $\alpha'$  of 0.1270 dB  $\mu m^{-1}$  (Figure 4.6e).

#### 4.3.6 Fabrication of organic photonic component (PC-1)

The micromechanical integration of DBA and BPP microcrystals was achieved by lifting DBA microcrystal from one substrate and dropping them at the required construction site in another substrate using an AFM cantilever tip and dropping it close to a BPP crystal in substrate-2 (Figure 4.7a-e). Later, the DBA crystal was slowly moved in the forward direction at the left end using a force, f, with an AFM tip. A similar force was applied to move the right terminal of DBA microcrystal towards the BPP microcrystal (Figure 4.7f-j). The microcrystal was gently adjusted in the x, y plane through a series of micromechanical operations and was brought into evanescent contact after integrating the DBA microcrystal's terminals with BPP microcrystal to yield a bow-shaped photonic component, PC-1 (Figure 4.7k-p).

The right terminals of the DBA and BPP crystals are 27 µm apart (Figure 4.8a). The FL image of PC-1 displayed bright blue and cyan emissive BPP and DBA crystals, respectively. The optical response of PC-1 was investigated by simultaneously exciting the

left termini of BPP/DBA crystals with 405 nm laser (Figure 4.8c). When light input was given at the left terminal of the BPP crystal, a blue emission ( $\lambda_1 \approx 420-570$  nm;  $\lambda_{max} \approx 460$  nm) was observed at the excitation point (Figure 4.8b,d). The FL output collected at the DBA crystal's right terminal comprised of its typical cyan emission ( $\lambda_2 \approx 450$  nm – 705 nm;  $\lambda_{max} \approx 500/525$  nm) due to ET from BPP to DBA (Figure 4.8b,e). As expected, the emission collected at the BPP output terminal differed from the customarily observed BPP spectrum (Figure 4.9d-f). A deeper analysis suggested the coexistence of both BPP and DBA spectra with a bandwidth of 420–650 nm at the right terminal of the BPP waveguide (Figure 4.9f). Additionally, the overlap of BPP emission and DBA absorption facilitates ET from BPP to DBA microcrystal. Hence, the active light transmission ( $\lambda_2$  (A)) in DBA towards its output

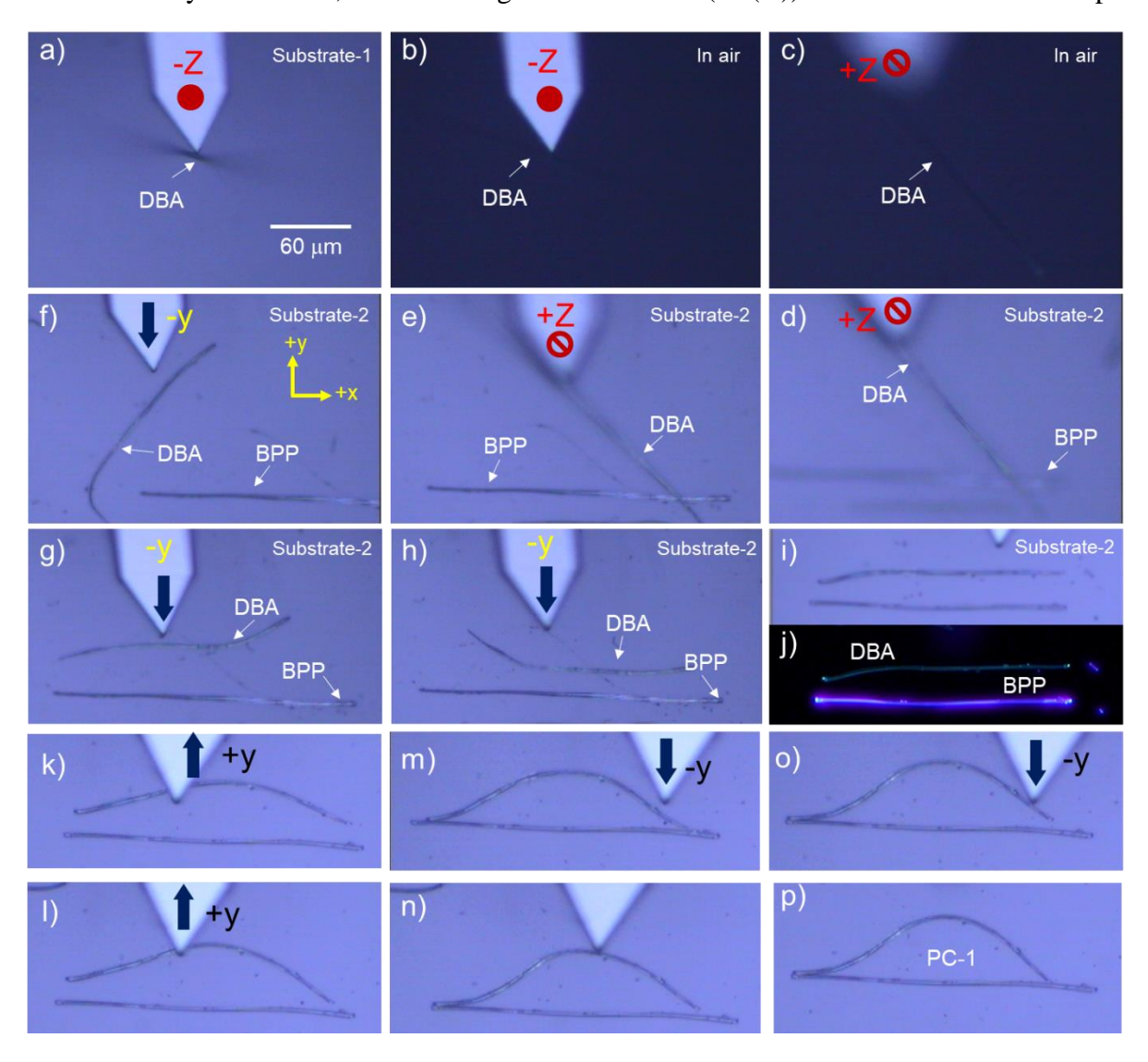


**Figure 4.7.** a-e) Transferring DBA microcrystal from one substrate to another near the desired construction site. f-i) Positioning of DBA and BPP microcrystals. j) FL microscope image of the positioned BPP and DBA microcrystals. k-p) Micromechanical manipulation of BPP and DBA microcrystals towards construction of photonic component, PC-1.

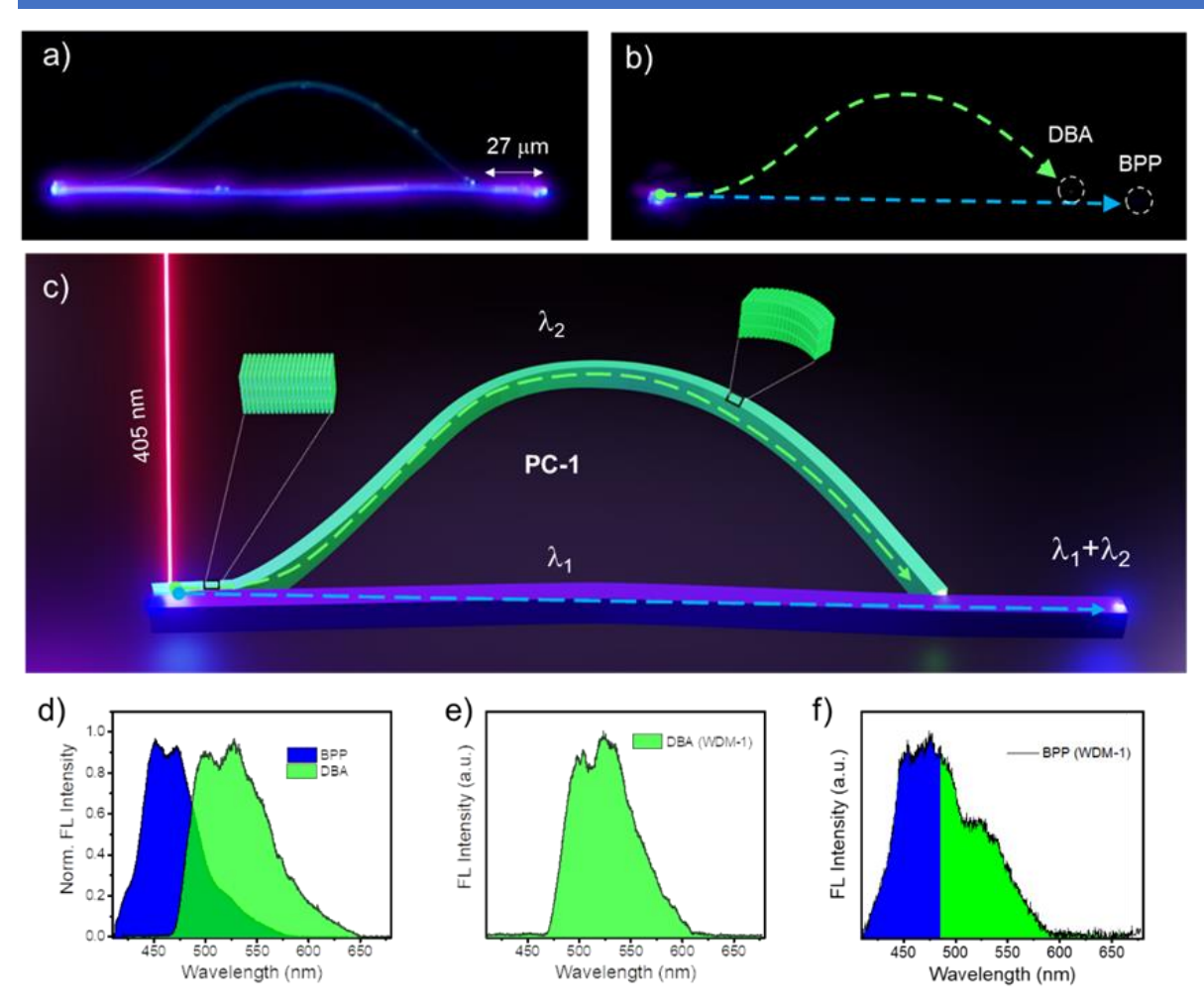


**Figure 4.8.** a) FL microscope image of fabricated PC-1. b) Laser FL microscope image of PC-1 when 405 nm laser beam input was provided at the left end. The dotted circles represent FL collection points on DBA and BPP microcrystal ends. c) Graphics representing the optical functioning of PC-1. Inset shows molecular arrangement of DBA molecules in straight and bent portion of DBA crystals. The two light transducing trajectories in PC-1 are shown in dotted arrows. d) comparison of normalized FL spectra recorded at the ends of DBA and BTD waveguides in respective waveguides. The FL spectra obtained at the right terminals of e) DBA, and f) BPP microcrystal tips in PC-1, respectively.

termini can be observed ( $\approx$ 450–650 nm). While the same signal passively couples into BPP waveguide through the evanescent field and travels together with the BPP emission ( $\lambda_1(A)$ ), delivering a dual  $\lambda_1(A) + \lambda_2(P)$  signal (420-650 nm) at the right terminal of BPP waveguide (Figure 4.8f).

#### 4.3.7 Micromechanical fabrication of organic WDM

The typical WDM applications require multiple spectral bandwidths to be merged for transmission along the multiplexer. Therefore, the PC-1 geometry was further extended with a differently emissive crystal to construct a custom-made WDM by micromechanically integrating a third crystal, i.e., BTD2CF<sub>3</sub> waveguide. The BTD2CF<sub>3</sub> was lifted from one substrate and carefully dropped near the PC-1 site (Figure 4.9a-c). The BTD2CF<sub>3</sub> crystal

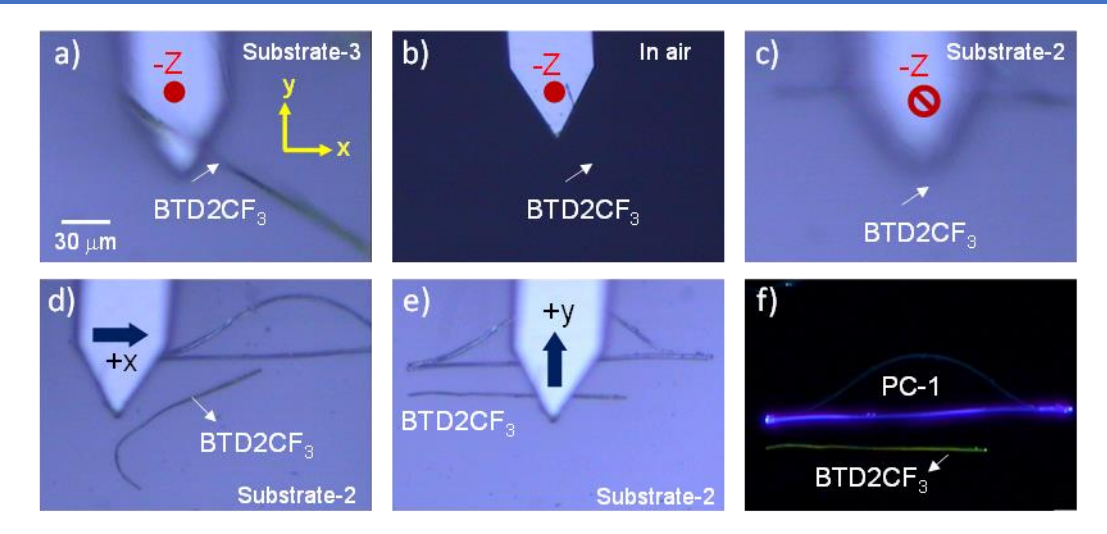


**Figure 4.9.** a-e) Confocal optical images of BTD2CF<sub>3</sub> crystal being lifted from substrate-3 and transferred to the circuit construction site in substrate-2. f) Fluorescence image of PC-1 and BTD2CF<sub>3</sub> before integration at the construction site.

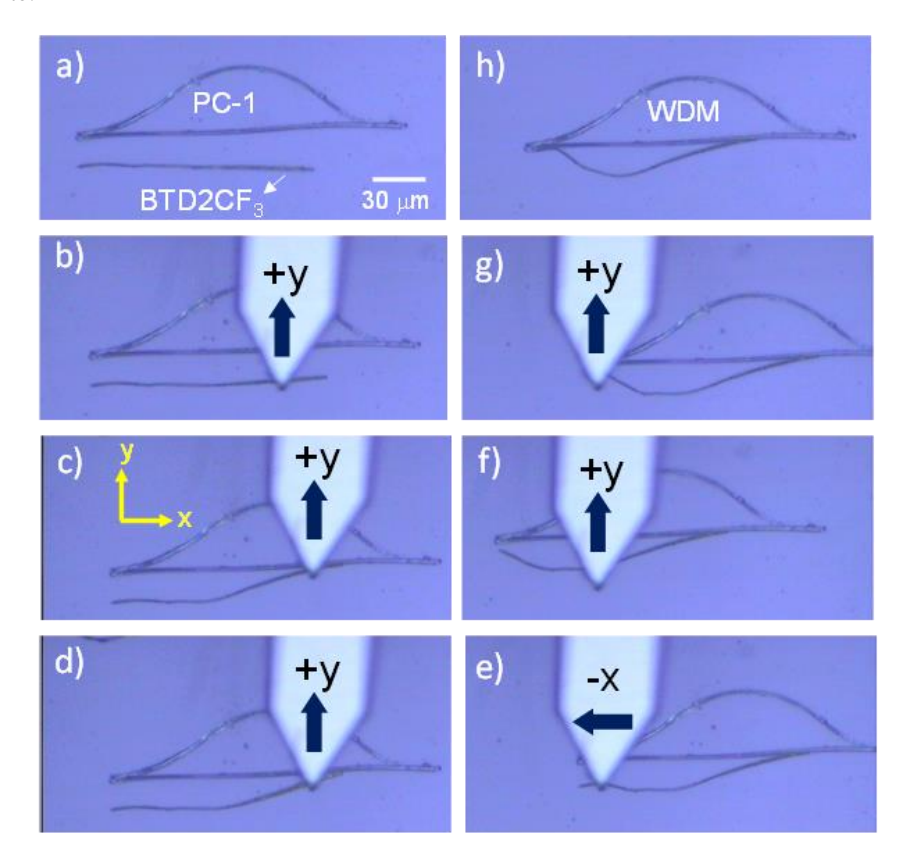


Figure 4.10. a-h) Micromechanical integration of BTD2CF<sub>3</sub> with PC-1 to fabricate WDM.

was carefully moved towards the PC-1 (Figure 4.9d,e). The FL microscope image of the construction site displayed three different emissions from three respective crystals with vibrant tips of BPP, DBA, and BTD2CF<sub>3</sub>, respectively. Later, the BTD2CF<sub>3</sub> microcrystal was meticulously integrated with PC-1 as both ends of the BTD2CF<sub>3</sub> microcrystal were brought into optical contact with the BPP crystal in PC-1 (Figure 4.10a-h). The tailor-made WDM is

#### Chapter 4 b) c) DBA tip BTD2CF<sub>3</sub> tip d) $\lambda_2(A)$ DBA, *T* ≈ 1.8 μm BPP, *T* ≈ 2.9 μm $\lambda_1(A)$ D ≈28 μm $\lambda_3(A)$ $\lambda_1(A) + \lambda_3(P)$ $\lambda_1(A) + \lambda_2(P) + \lambda_3(P)$ BTD2CF<sub>3</sub>, *T* ≈ 0.6 μm e) BPP 650 nm 420 nm DBA 705 nm 445 nm BTD2CF<sub>3</sub> 480 nm 755 nm -WDM FL Intensity (a.u.)

Figure 4.11. a,b ) Confocal optical and FL microscope images of WDM. c) Confocal laser FL microscope image of WDM when left end was excited with 405 nm laser light. d) False colour-coded FESEM image of WDM. Insets show the closeup view of the BTD2CF<sub>3</sub> and DBA junctions with BPP. e) Optical signal detected at the BPP right tip possessing multiplexed signal for collective excitation of the left side of WDM. The spectral bandwidths of BPP, DBA and BTD2CF3 are represented as double-headed arrows (blue, green and orange, respectively) above the multiplexed spectrum.

Wavelength (nm)

600

650

700

550

100

50

450

500

shown in Figure 4.11a. On the right side of WDM, the distance between the termini of BTD2CF<sub>3</sub> and BPP crystals is ≈55 µm (Figure 4.11a). The FL image of the fabricated WDM showed bright FL from BPP, DBA and BTD2CF3 terminals (Figure 4.11b). The WDM's structural stability allowed us to perform field emission scanning electron microscopy (FESEM) to unveil surface morphology and the extent of crystal contacts. The false colorcoded FESEM image revealed both left terminals of DBA and BTD2CF3 crystals are in direct

contact with BPP crystal (Figure 4.11d). The thickness of BPP, DBA and BTD2CF<sub>3</sub> microcrystals are about 2.9, 1.8 and 0.6 µm, respectively (Figure 4.11d).

#### 4.3.8 Optical functioning of organic WDM

To study the photonic performance of the constructed WDM, the left end of the WDM, i.e., the three waveguide terminals were simultaneously illuminated with a 405 nm laser (Figure 4.12c). The FL spectrum obtained at DBA terminal resembled the isolated DBA crystal's FL spectrum  $\lambda_2(A)$  (Figure 4.12a,b). Similarly, the FL range recorded at the BTD2CF<sub>3</sub> crystal output comprised of its conventional spectrum,  $\lambda_3(A)$  (Figure 4.12c.d). Remarkably, the output signal collected at the BPP crystal's right terminal possessed the multiplexed FL signals  $(\lambda_1 + \lambda_2 + \lambda_3)$  of three waveguides (Figure 4.11e). This multiplexing occurs via passive coupling of signals  $\lambda_2$  and  $\lambda_3$  of DBA and BTD2CF<sub>3</sub>, respectively into BPP waveguide. Here, the BPP waveguide transduces a mixed  $\lambda_1(A) + \lambda_3(P)$  signals covering 420–650 nm regions for ≈28 µm distance, followed by simultaneous transmission of three multiplexed  $\lambda_1(A) + \lambda_2(P) + \lambda_3(P)$  signals with a total bandwidth of 420-700 nm, for 27 µm distance. This result demonstrates the stepwise bandwidth increase from 420-570 nm to 420-700 nm through the multiplexing BPP crystal waveguide supported by the crystal's WDM geometry. The CIE chromatography coordinates for different crystals and WDM are compared in Figure 4.12e. Interestingly, the multiplexed output signal also retains the optical modes observed in the waveguide before their integration. These outcoupled optical modes are advantageous for multichannel visible light data communication.

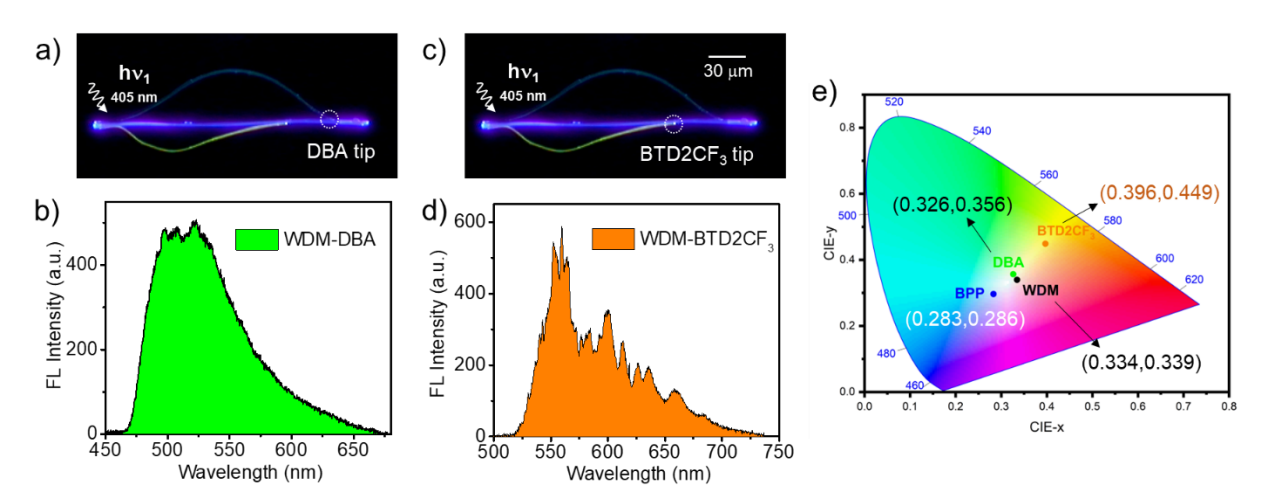


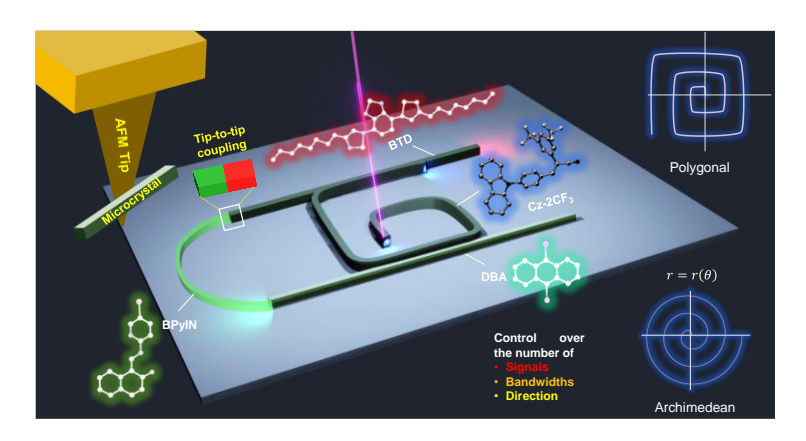
**Figure 4.12.** Fluorescence microscopy images showing the FL output collection point at a) DBA and c) BTD2CF<sub>3</sub> terminals in WDM. Corresponding FL spectra recorded at b) DBA and d) BTD2CF<sub>3</sub> terminals are shown in a,c respectively. e) The CIE diagram depicting the color coordinates for BPP, DBA, BTD2CF<sub>3</sub> and WDM.

#### 4.4 Summary

This chapter, for the first time, successfully demonstrated the fabrication of an organic crystal-based wavelength division multiplexer (WDM) using tailor-made BTD2CF<sub>3</sub>, BPP and DBA crystals. The construction of WDM required a crafty choice of crystals from blue, cyan to yellow emissive crystals, all with increasing PLQY. The micromechanical integration of these crystals using the mechanophotonics approach produced the required WDM. The optical functions of the constructed organic WDM established its efficient broadband visible light multiplexing capability. The mimicking of such photonic components recapitulates the abilities of organic crystals as promising photonic materials platforms for flexible device applications and visible light communication technologies.



A Pick-and-Place Technology Enabled,
Mechanically Programmable, Spiral
Optical Waveguides Integrated Hybrid
Circuits from Four Extremely PseudoPlastic Organic Crystals for Visible
Spectral Band Tunability



5.1 Abstract: This chapter reports the advantages of SWs for photonic circuit applications from a custom-designed extremely flexible novel blue-emitting organic crystal, namely, Cz-2CF3. The micromechanical compliance was channelized to fabricate organic spiral waveguides (SWs) such as cornu type, elliptical, Archimedean, and four-sided polygonal SWs using mechanophotonics technique (an atomic force microscope, tip-based microwaveguide manipulation). Further, a rectangular SW of Cz-2CF3 was integrated with cyan emissive DBA and red emissive 4,7-bis(4-octylthiophen-2-yl)benzo[c][1,2,5]thiadiazole, BTD crystals to achieve a spiral photonic circuit (SC), SC-1 and SC-2 with four and six ports, respectively. The programmability of the fabricated spiral circuits was demonstrated by mechanically detaching DBA crystal and integrating it with green emissive BPyIN crystal. The total number of ports was altered and adjusted by placing BPyIN and BTD tips in an end-to-end fashion to facilitate effective optical signal transmission in the circuit. These circuits displayed input port-dependent output signals. Therefore, a mechanically programmable multi-component OPIC with multi-tasking capabilities and full visible spectral bandwidth coverage was achieved.

#### **5.2 Introduction**

The realization of SWs from organic crystals is a highly challenging endeavour, primarily because it requires an exceedingly flexible crystal with unaltered optical properties in highly strained geometries. 193 The construction of miniature optical elements is not possible with conventional practices. Nevertheless, a microcrystal processing technique like mechanophotonics approach becomes handy for fabricating organic SWs (OSWs). Importantly, different mechanically flexible organic crystals (MFOCs) can be easily integrated onto a single chip for hybrid OPIC production. MFOC-based active/passive waveguides in linear, bent, ring configurations and organic PICs (OPICs) have been successfully made.44 However, these materials' accessible optical bandwidth (BW) covers only part of the visible region. Organic materials emitting the entire visible region (400-750 nm) are still hard to accomplish. An approach to expand the accessible spectral BW to the full visible range is to employ different blue-to-red FL flexible crystals as elements in OPICs. Therefore, the design of MFOCs (carrying electron donor, D, and acceptor, A groups) with compact packing governed by various supramolecular interactions is a potential solution. The tight molecular packing reduces non-dissipative radiation and enhances the optical emission, while the supramolecular interactions contribute to superior mechanical compliance.

This chapter reports the first micromechanical fabrication of different compact OSWs like Archimedean, Cornu, elliptical, and three- and four-sided polygonal SWs from a diligently designed, extremely flexible, blue-emitting, organic crystal, namely (Z)-3-(4-(9Hcarbazol-9-yl)phenyl)-2-(3,5-bis(trifluoromethyl)phenyl)acrylonitrile  $(Cz-2CF_3)$ using mechanophotonics enabled pick-and-place technology. The molecular design of blueemissive Cz-2CF<sub>3</sub> comprised of electron-rich carbazole (Cz), acts as donor (D) and bis(trifluoromethyl)phenyl derivative as an acceptor (A). The electronegative atoms (N, O and F) provide ample opportunity for enriched supramolecular interactions like hydrogen and halogen bonding contributing towards the mechanical flexibility of Cz-2CF<sub>3</sub> crystals. Mechanical integration of four-sided polygonal OSW of Cz-2CF<sub>3</sub> with two chemically and optically different crystal waveguides, namely, DBA, and 4,7-bis(4-octylthiophen-2yl)benzo[c][1,2,5]thiadiazole (BTD), provides first of its kind hybrid, OSW driven OPCs with mechanical reconfigurability (Figure 1.38b). The advantages displayed by these OSWs and circuits in terms of supramolecular interactions-assisted high mechanical compliance, compactly packed highly-dense circuits, and full-visible spectral coverage are unprecedented. The circuits operate using optical excitation of the input crystal terminal (port), reabsorption during guided FL propagation, and optical ET from one crystal to another via evanescent coupling. The optical BW of the fabricated spiral circuit expands to a full visible range (blue to red region including cyan; 410-750 nm). Finally, replacing the DBA crystal waveguide with BPyIN waveguide via the pick-and-place technology demonstrates the first organic spiral crystal-based programmable photonic circuit.

#### 5.3 Results and discussion

5.3.1 Syntheses of (Z)-3-(4-(9H-carbazol-9-yl)phenyl)-2-(3,5-bis(trifluoromethyl)phenyl)acrylonitrile (Cz-2CF<sub>3</sub>)

**Synthesis of 4-(9H-carbazol-9-yl)benzaldehyde (Cz-CHO):** Cz (18 mmol) was completely dissolved in dry DMF (20 mL) and the solution was degassed with nitrogen for 10 min before adding NaH (19.8 mmol). After stirring the solution for 30 min, 4-fluoro benzaldehyde (18 mmol) was added dropwise. The reaction progress was monitored by thin layer chromatography (TLC). Once the reaction was complete, water was added and the solid was filtered and washed thoroughly with water. The organic solid was recrystallized from THF: hexane to yield pale yellowish crystals. (Yield, 60%) <sup>1</sup>**H NMR** (400 MHz, CDCl<sub>3</sub>): δ (ppm) 10.12 (s, 1H), 8.16-8.13 (m, 4H), 7.80 (d, 2H,  $^3J_{H,H} = 8.0$  Hz,), 7.51 (d, 2H,  $^3J_{H,H} = 8.5$  Hz,), 7.44 (td, 2H,  $^3J_{H,H} = 6.8$ ,  $^4J_{H,H} = 1.2$  Hz,), 7.33 (td, 2H,  $^3J_{H,H} = 7.2$ ,  $^4J_{H,H} = 1.2$  Hz,).

**Synthesis of Cz-2CF3:** Cz-CHO (0.734 mmol), (3,5 bis trifluoromethyl)phenyl acetonitrile (0.667 mmol) and NaOMe (0.667 mmol) were dissolved in methanol (15 mL). The reaction mixture was heated at 60 °C for 4 h. Later, the solution was left undisturbed at RT for 12 h to obtain a greenish precipitate. The crude product was purified by column chromatography (2% ethylacetate:hexane) to attain a greenish crystalline compound. The resulting solid was further purified by recrystallization using a dichloromethane:hexane solvent system. (Yield, 68%) <sup>1</sup>H NMR (500 MHz, CDCl<sub>3</sub>): δ (ppm) 8.20 (d, 2H,  $^3J_{H,H}$  = 8.5 Hz), 8.16-8.14 (m, 4H), 7.94 (s, 1H), 7.77 (d, 2H,  $^3J_{H,H}$  = 10.0 Hz,), 7.73 (s, 1H), 7.52 (d, 2H,  $^3J_{H,H}$  = 8.0 Hz), 7.45 (td, 2H,  $^3J_{H,H}$  = 8.5,  $^4J_{H,H}$  = 1.0 Hz,), 7.33 (td, 2H,  $^3J_{H,H}$  = 7.5,  $^4J_{H,H}$  = 0.5 Hz,). <sup>13</sup>C NMR (125 MHz, CDCl<sub>3</sub>) δ (ppm): 144.06, 140.88, 140.17, 136.68, 133.28, 1333.01, 132.74, 132.47, 131.36, 127.03, 126.28, 126.05, 123.94, 122.88, 122.85, 122.82, 120.76, 120.51, 119.71, 116.8, 109.81, 109.55, 109.09. FTIR ( $v\bar{v}$  cm<sup>-1</sup>): 2958, 2921, 2846, 2204, 2191, 2158, 1995, 1946, 1733, 1591, 1450, 1274, 1125, 964, 755; HR-MS: m/z Calculated: 506.12, 507.13, Found: 507.13, 508.13; UV-Vis (Solid-state):  $\lambda_{abs-max}$  400 nm and  $\lambda_{FL-max}$  ≈498 nm (blue emission); Melting point ≈234-236 °C

Scheme 5.1. Synthetic route towards Cz-2CF<sub>3</sub>.

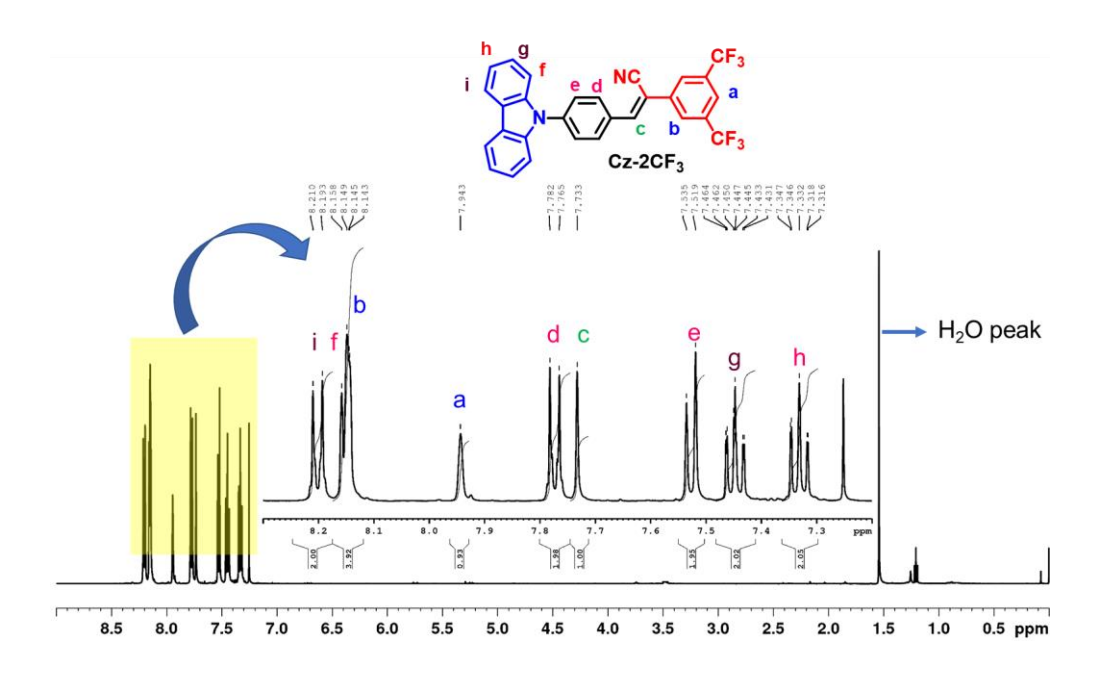


**Figure 5.1.** <sup>1</sup>H NMR (500 MHz) spectrum of Cz-2CF<sub>3</sub> in CDCl<sub>3</sub>.

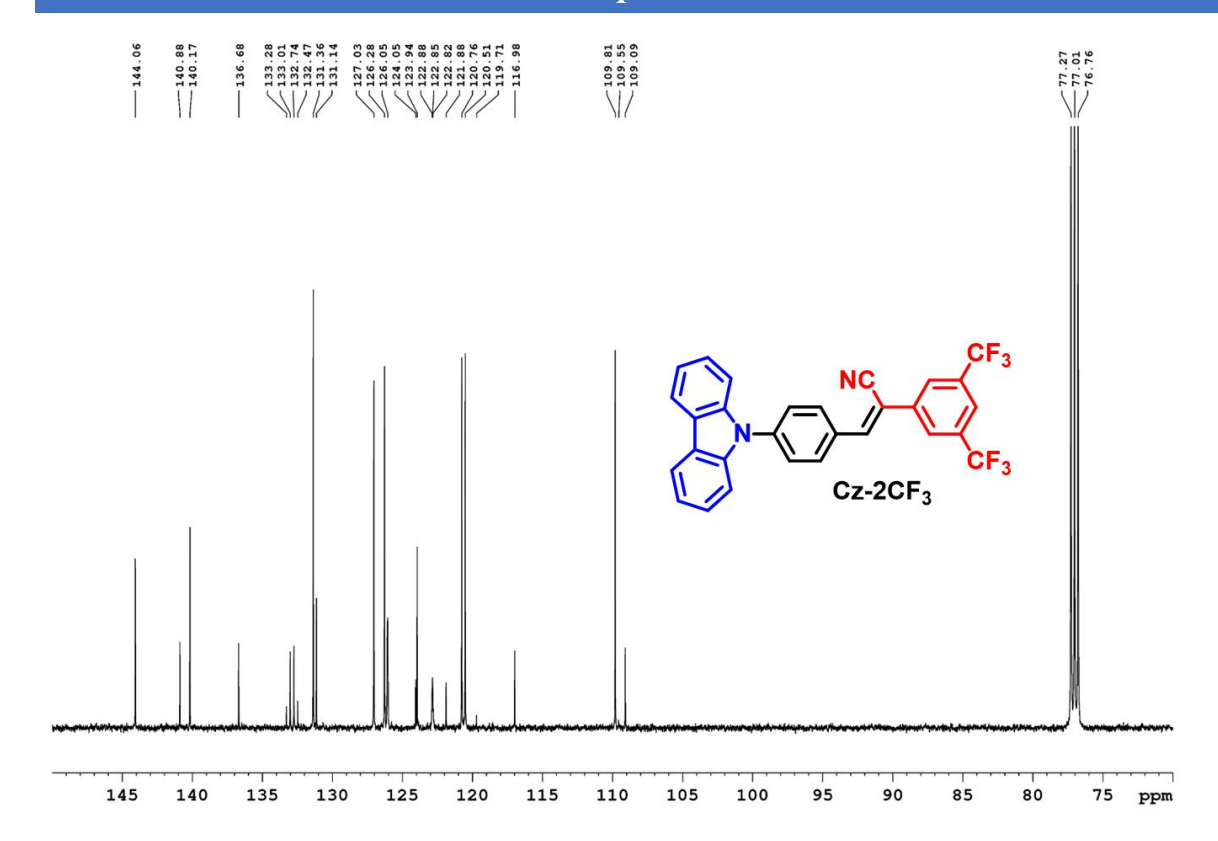


Figure 5.2. <sup>13</sup>C NMR (125 MHz) spectrum of Cz-2CF<sub>3</sub> in CDCl<sub>3</sub>.

#### 5.3.2 Synthesis of 4,7-bis(4-octylthiophen-2-yl)benzo[c][1,2,5]thiadiazole (BTD):

BTD is prepared according to the previously developed procedure.<sup>211</sup> A mixture of 4,7-Dibromobenzo[c] [1,2,5]thiadiazole (4.0 mmol), Pd(PPh<sub>3</sub>)<sub>2</sub>Cl<sub>2</sub> (281 mg, 0.4 mmol) and tributyl(4-octylthiophen-2-yl)stannane (12 mmol) in dry THF (20 mL) was stirred and refluxed at 70 °C for 48 h. After completion of the reaction, the THF solvent was evaporated under vacuum and the crude product was purified by column chromatography to afford compound BTD as an orange solid (Yield, 65%). <sup>1</sup>**H-NMR** (500 MHz, CDCl<sub>3</sub>, ppm):  $\delta$  7.96 (s, 2H), 7.80 (dd, 2H,  $J_{H,H}$  = 4.0 Hz,  $J_{H,H}$  = 1.6 Hz,), 7.02 (s, 2H), 2.68 (t, 4H,  $^3J_{H,H}$  = 7.8 Hz,), 1.70 (t, 4H,  $^3J_{H,H}$  = 7.2 Hz,), 1.28-1.39 (m, 20H), 0.88 (s, 6H).

The synthesis of BPyIN was described in section 2.3 earlier.

#### **5.3.3 Optical characteristics**

The UV-Visible absorption and FL spectroscopy investigations were carried out in the solid-state to evaluate the optical properties of Cz-2CF<sub>3</sub>, DBA, BPyIN and BTD (Figure 5.3a). The absorption tail of Cz-2CF<sub>3</sub> ends at  $\approx$ 500 nm, while its blue FL appears at  $\approx$ 410-650 nm with a maximum of 482 nm (Figure 5.3b). The material exhibits reabsorption of shorter wavelength (410-490 nm) FL due to overlap of the absorption tail with part of its FL. The brilliant blue emissive property is related to Cz-2CF<sub>3</sub>'s high PLQY,

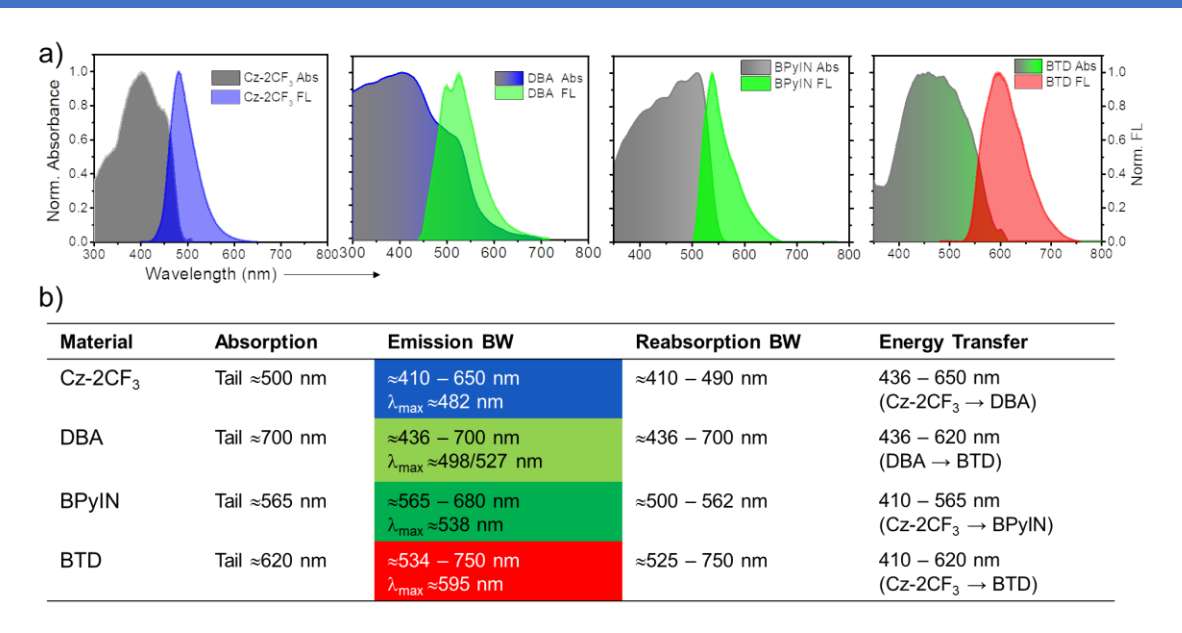


**Figure 5.3.** a) The solid-state optical absorption and emission spectra of Cz-2CF<sub>3</sub>, DBA, BPyIN and BTD, respectively. b) Table demonstrating absorption maxima and tail, emission bandwidth, reabsorbance band width, and intermolecular radiative energy transfer, ET.

36.7% with a typical FL lifetime of 2.6 ns (Figure 5.4a). The PLQY of DBA and BPyIN are reported to be 7.4% and 16.7%, respectively.

The solvatochromic studies performed in different organic solvents (like hexane, dichloromethane, chloroform, tetrahydrofuran, ethyl acetate, acetonitrile and methanol) corroborate the charge-transfer characteristics in Cz-2CF<sub>3</sub> (Figure 5.4b). The significant red shift in the emission of Cz-2CF<sub>3</sub> in polar solvent compared to non-polar solvent clearly indicates the charge transfer from D (Cz) to A (3,5-bistrifluoromethylphenyl moiety). The absorption tail of DBA, BPyIN, and BTD appear at≈700, 565, and 620 nm, respectively. For the corresponding molecules, the FL maxima sequentially shifted to ≈498/727, 538 and 595 with the FL tail reaching ≈750 nm for BTD. The ET from Cz-2CF<sub>3</sub> to DBA, 436-650 nm takes place as the emission of Cz-2CF<sub>3</sub> falls in the absorption region of DBA. On the same line, ET from Cz-2CF<sub>3</sub> to BPyIN and BTD, and DBA to BTD is also possible (Figure 5.3b).

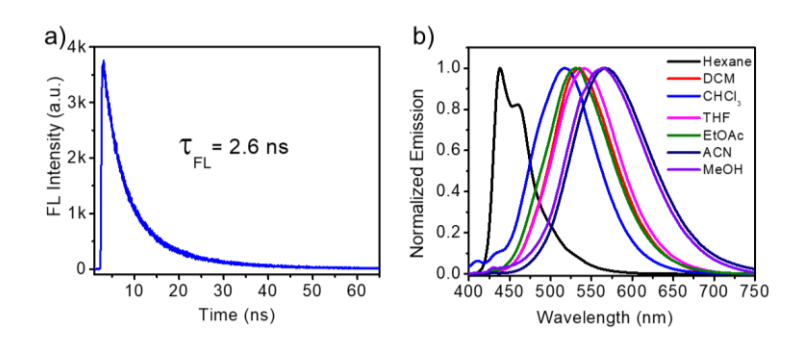


**Figure 5.4**. a) Prompt FL decay profile used for calcaulating the lFL lifetime of Cz-2CF<sub>3</sub>. b) Solvatochromism exhibited by Cz-2CF<sub>3</sub> in different polar solvents.

#### 5.3.4 Structural basis for mechanical flexibility in CF<sub>3</sub>OMe crystals

Single crystal X-ray diffraction studies were performed to ascertain the molecular structure and packing of Cz-2CF<sub>3</sub>. The Cz-2CF<sub>3</sub> molecule crystallizes in a monoclinic system. A  $\pi$ -spacer phenyl group separates the D (Cz) and A (3,5-bis(trifluoromethyl)phenyl moiety) units. The twist angle between Cz and phenyl ring is about 50° and the same between A and phenyl is about 32° (Figure 5.5a,b). The various non-covalent interactions stabilizing the molecule are type II halogen bonding interaction (F···F = 2.88 Å), hydrogen bonding (C-F···H = 2.83 Å) and inter layer stacking distance of  $\approx$ 4.3Å (Figure 5.5c). The molecular packing follows a head-to-head packing as observed for several Cz-based compounds. Such packing reduces thermal deactivations and other motions (rotational or vibrational), thereby promoting efficient radiative emission. The packing of molecules along (010) and (00-1) is shown in Figure 5.5d,e. The infinitely long layered molecular arrangement along the

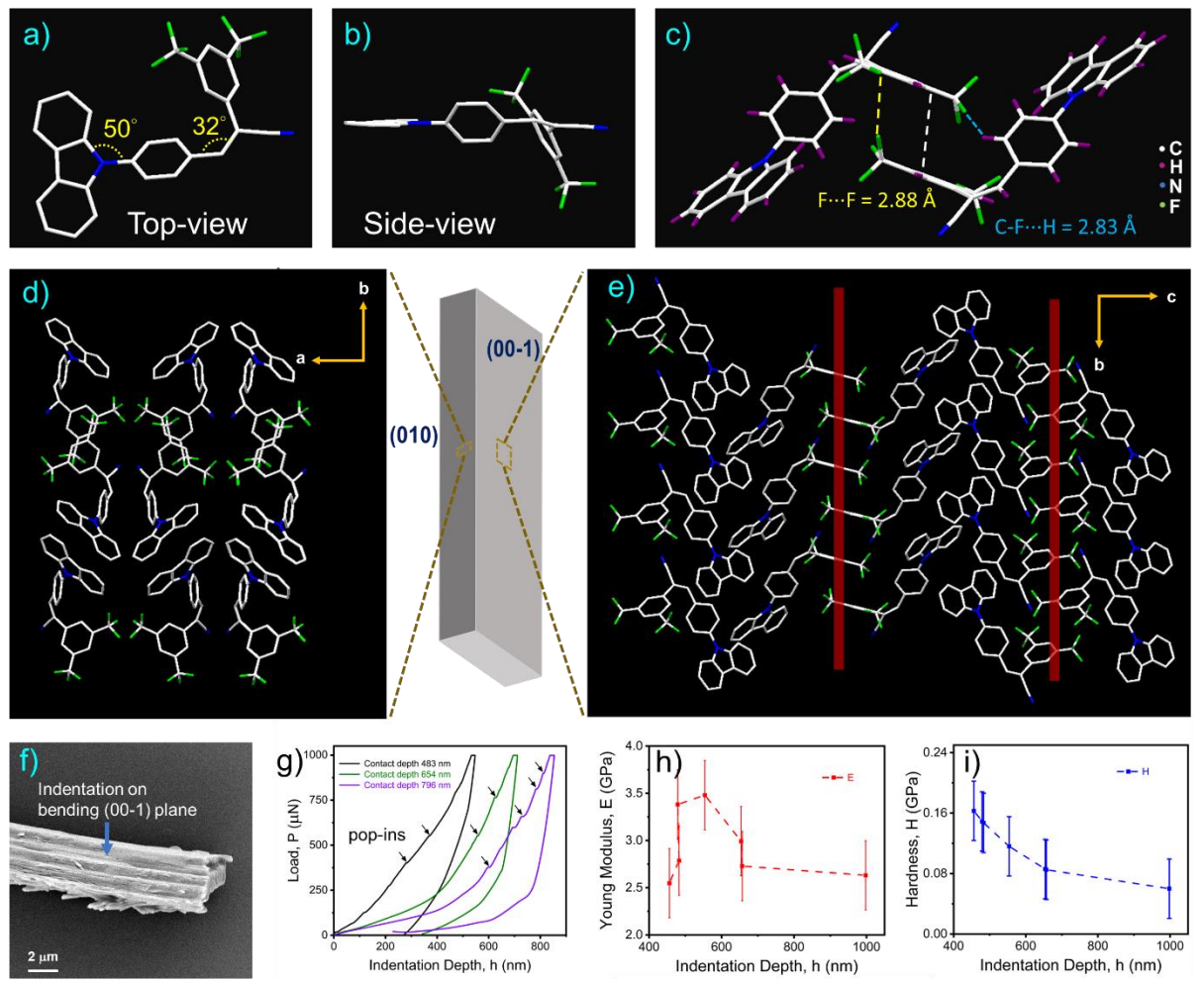


**Figure 5.5.** a) Top view and b) Side view of Cz-2CF<sub>3</sub> in the crystal. c) Various non-covalent interactions stabilizing the Cz-2CF<sub>3</sub> crystal. d) Molecular stacking along the (010) plane. e) Molecular arrangement along (00-1). The red lines indicate the presence of fluorine interactions in Cz-2CF<sub>3</sub> crystal. f) A representative FESEM image of Cz-2CF<sub>3</sub> crystal portraying the nanoindentation direction. g) Load vs displacement curve. h) Young's modulus and i) hardness curves obtained for indentation on (00-1) plane.

crystallographic 'b' axis is supported by halogen bonding (Figure 5.5e). When mechanical stress is experienced perpendicular to this plane, the weak interactions act as stress absorbers and sustain the applied force. Later, the absorbed stress is dissipated to regain the original shape of the crystal.

To appraise the mechanical flexibility of the Cz-2CF<sub>3</sub> crystals (millimetres in length) a familiar three-point bending was probed. When the crystal was pushed in the middle with the help of a thin needle, it could be reversibly bent multiple times into a semi-circle without any observable physical damage (Figure 5.6). The nanoindentation performed on the bending (00-1) plane is shown in Figure 5.5f with a representative FESEM image showing stacked layers. The load-displacement curve presented large residual depths upon unloading, suggesting that the crystal undergoes elastic deformation during indentation (Figure 5.5g). There were several displacement bursts (called pop-ins) on the load-displacement curve when the load was applied. Such a phenomenon is observed for crystals with mechanical anisotropic characteristics and arises due to the disruption of molecular layers occurring at the indented position. The estimated average Young's modulus is 2.94±0.366 GPa (Figure 5.5h). The average hardness value is calculated to be 0.115±0.039 GPa (Figure 5.5i). Based on previously reported literature values, the smaller hardness and Young's modulus suggest the super-soft and super-complaint nature of Cz-2CF<sub>3</sub> crystals. The mechanical flexibility of BPyIN crystal was discussed in section 2.3.3.

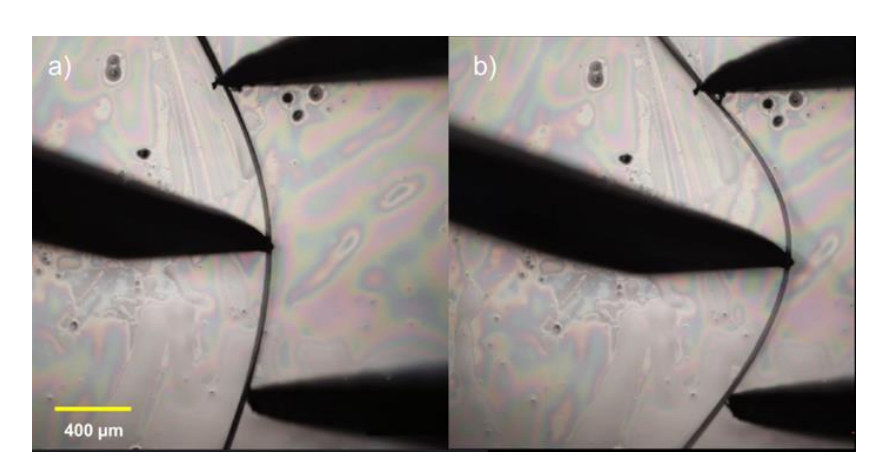


Figure 5.6. a,b) Three-point bending test performed on a millimeter sized Cz-2CF<sub>3</sub> crystal.

#### **5.3.5** Preparation of microcrystals

i) Preparation of Cz-2CF<sub>3</sub>: In a clean vial, Cz-2CF<sub>3</sub> (1 mg) was dissolved in hexane (1 mL) and the solution was left undisturbed for 24 h and the solution (30  $\mu$ L) was drop casted onto a clean glass coverslip to observe microrods under the confocal microscope.

- ii) Preparation of BPyIN and DBA microcrystals was discussed in chapter 2 and 4, respectively.
- iii) Preparation of BTD microcrystals: BTD (1 mg) was dissolved in methanol and the solution was heated at 60 °C for 15 minutes. The solution was allowed to cool at room temperature, followed by drop casting the solution (30  $\mu$ L) on a coverslip. The confocal images revealed microrods of BTD.

#### **5.3.6** Fabrication of strained spiral architectures

The capability of a material to be employed for reconfigurable PICs can be tested by its ability to withstand different architectures with large strain. Importantly, the materials must be scalable down to the nano level without compromising their mechanical and photonic properties. The mechanophotonic aspects of Cz-2CF<sub>3</sub> were tested on a naturally bent microcrystal (Figure 5.7a). The optical excitation (using 405 nm continuous wave laser) of a naturally bent Cz-2CF<sub>3</sub> microcrystal self-assembled on a silica substrate produced a bright blue FL ( $\lambda_1 \approx 410$ -650) at the contact point (Figure 5.7b). The generated blue light transduced to the other end of microcrystal demonstrating the active type waveguiding in Cz-2CF<sub>3</sub> microcrystal (Figure 5.7i). As it propagated along the long axis of the waveguide some

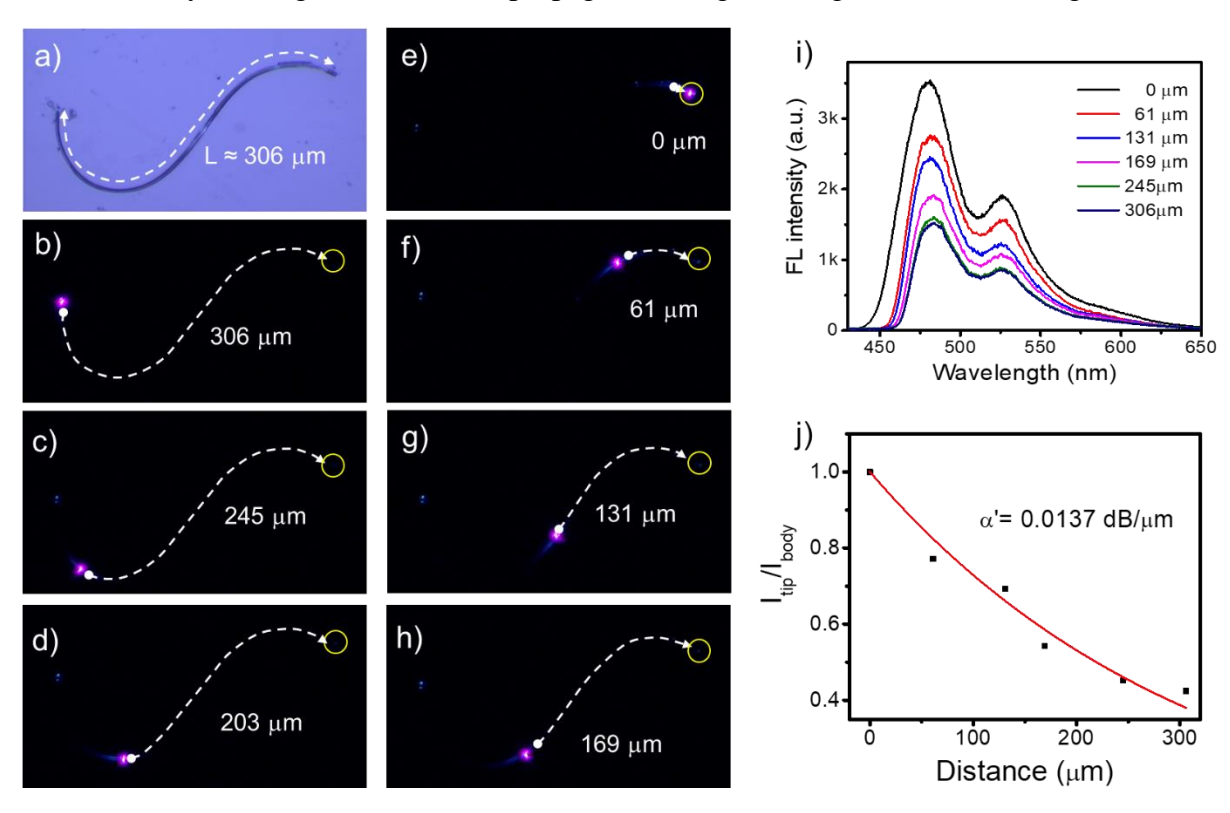


**Figure 5.7.** a) Confocal optical microscope image, b-h) confocal laser FL microscope images of bent  $Cz-2CF_3$  crystal. i) FL spectra recorded at various excitation positions shown in b-h. j) The plot of  $I_{tip}/I_{body}$  used for the calculating optical loss (red fit) of  $Cz-2CF_3$  microcrystal.

portion of higher energy region from FL bandwidth (410-490 nm) was absorbed by themicrocrystal producing a long-pass filtered signal  $-\lambda_1\approx$ 490-650 nm at the other end (Figure 5.7i). The microcrystal was excited at different positions along the long axis of the microcrystal and recorded the light output at the opposite end to calculate the optical loss of microcrystal to be 0.0137 dB  $\mu$ m<sup>-1</sup> (Figure 5.7b-h,j).

The construction of various μ-spiral architectures (μ-SAs) was accomplished using mechanophotonics approach using a confocal optical microscope attached with AFM tip. In line with our previous studies, the elastic Cz-2CF<sub>3</sub> microcrystals on silica substrate exhibited 'pseudo-plasticity' (irreversible, permanent deformation) due to CSSI. This hypothesis was validated when microcrystals grown on one substrate were physically lifted and transferred onto another via AFM cantilever tip. These transferred microcrystals were used to fabricate different micro µ-spiral architectures (µ-SAs). For the fabrication of a Cornu type SW, a 306 um long naturally bent microcrystal was chosen (Figure 5.8a). To achieve spiral shape, the right end of the microcrystal was pushed initially in the (+y) direction, with a force (F), using AFM cantilever tip for 29 mm in the forward direction (Figure 5.8b). Then, minor micromechanical adjustments on the right side of the microcrystal in  $(\pm x)$  and  $(\pm y)$  directions resulted in a doubly bent waveguide (Figure 5.8c-f). The left end of the doubly bent waveguide was slowly moved in the +x direction by 34 µm by applying force (Figure 5.8g,h). Later, the same end was pushed in the +y direction for 16 µm resulting in a near circular shape at the left end (Figure 5.8i,j). Similarly, the right end of doubly bent waveguide was pushed in the (-y) direction for 50 µm followed by careful crafting on the right end in both  $(\pm x)$  and  $(\pm y)$  directions resulting in the desired Cornu type SW (Figure 5.8k-n). The typical radius of the near-circular shapes on the left and right side of Cornu type SW are 20 and 18 µm, respectively and the subsequent strain induced by them on the microcrystal amounts to 12.1 and 11.6% respectively (Figure 5.8o).

The uniqueness of Cornu type SW is the ability to transduce light by changing the input signal's direction over 360° as it delivers the optical signal at the opposite end. The FL image of Cornu type SW comprises of two radiant tips suggesting intact optical waveguiding properties in the extremely strained structure (Figure 5.8r). The smooth homogenous surface morphology of the fabricated Cornu type SW was evident from the FESEM image (Figure 5.8t). The circular regions of the SW were 176 µm apart from each other. The focused light illumination at the body of the Cornu type SW conducts optical signal in two opposite

directions, where the signal in one direction propagates via clockwise pathway while in the other direction it travels in the counterclockwise direction. Hence, they are important for systems that require simultaneous light transport in opposite directions. To establish the light-guiding efficiency of the Cornu-type SW, excitation position-dependent emission spectra were collected at the right tip as the SW was excited at different positions (Figure 5.8s,p). The FL intensity at the right tip gradually increased as the distance between the collection and excitation points decreased. The optical loss coefficient ( $\alpha'$ ) was estimated to be 0.169 dB  $\mu m^{-1}$  (Figure 5.8q).

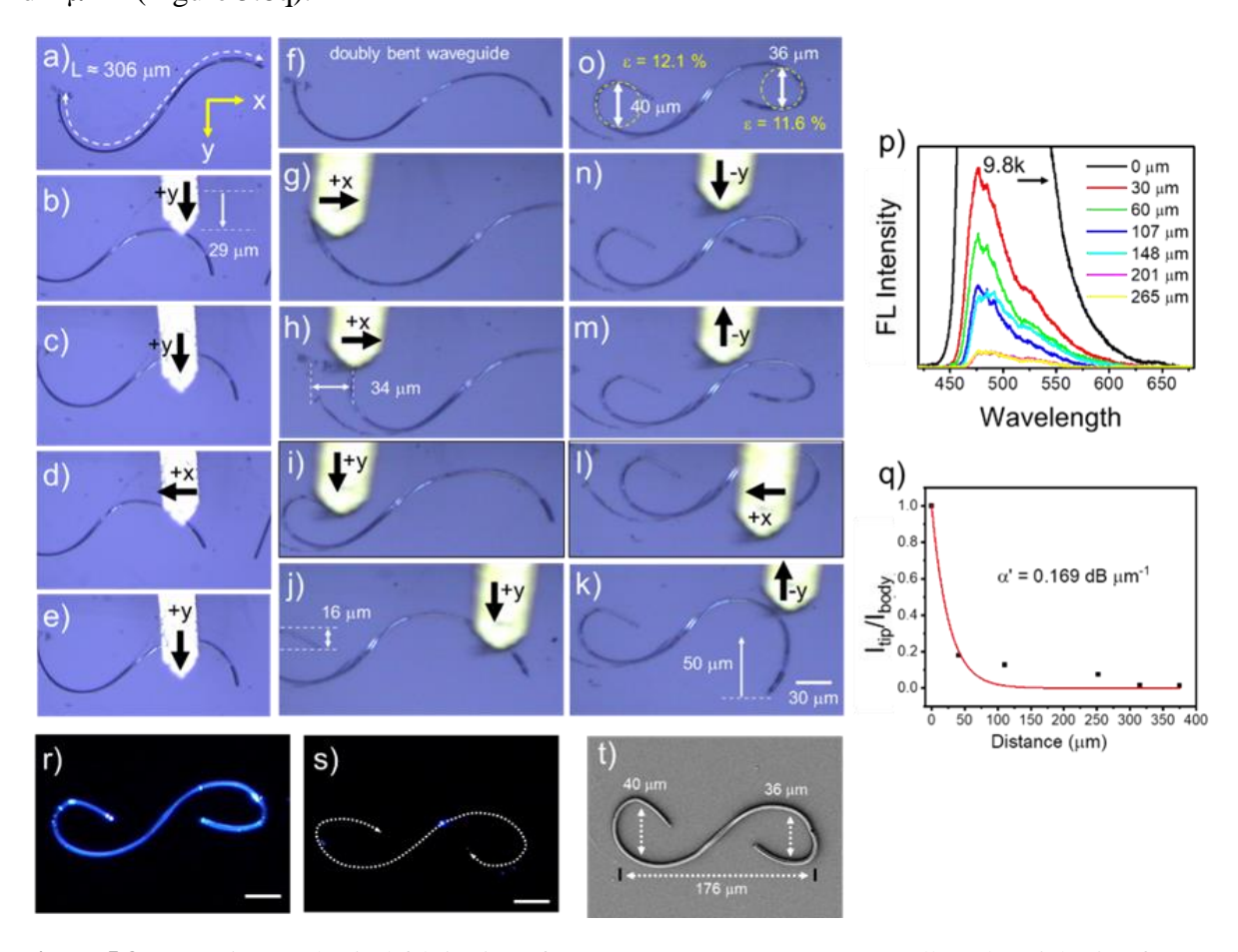


**Figure 5.8.** a-o) Micromechanical fabrication of Cornu type SW. p) FL spectra collected at right tip of Cornu type SW for excitation at various positions on the microcrystal. Insets in o shows the strain accumulated at the circular regions. p) FL spectra recorded at different positions on the Cornu type SW. q) The plot of  $I_{tip}/I_{body}$  used for the calculation of optical loss in Cornu type SW. r) FL microscope, s) laser confocal FL microscope and t) FESEM image of the fabricated Cornu type SW.

The fabrication of an elliptical SW was achieved from the Cz- $2CF_3$  microcrystal of length 479  $\mu$ m. The selected microcrystal's one end was in the air relative to the remaining portion of the crystal (Figure 5.9a). The microcrystal was subjected to careful micromanipulation with the help of an AFM tip to create the elliptical SW. Initially, the right tip of the microcrystal was pushed towards the centre (Figure 5.9b-h). Later, the microcrystal

was meticulously spun around the centre (Figure 5.9i-k). Finally, out of the plane tip was brought into the plane consisting of the microcrystal to realize a 2D elliptical SW (Figure 5.9l). The FESEM image shows increasing longitudinal dimensions per every turn from 47 to 85 and 121  $\mu$ m, respectively (Figure 5.9m). The FL microscope image reveals optical waveguiding properties which were confirmed when 405 nm light illumination at the centre resulted in the FL output at the other ends of the elliptical SW (Figure 5.9n,o). The  $\alpha'$ , of elliptical SW was estimated to be 0.151 dB  $\mu$ m<sup>-1</sup> from excitation position-dependent emission (EPDES, FL output collected at one fixed end, for laser excitation at different positions on waveguide) experiments (Figure 5.9p,q).

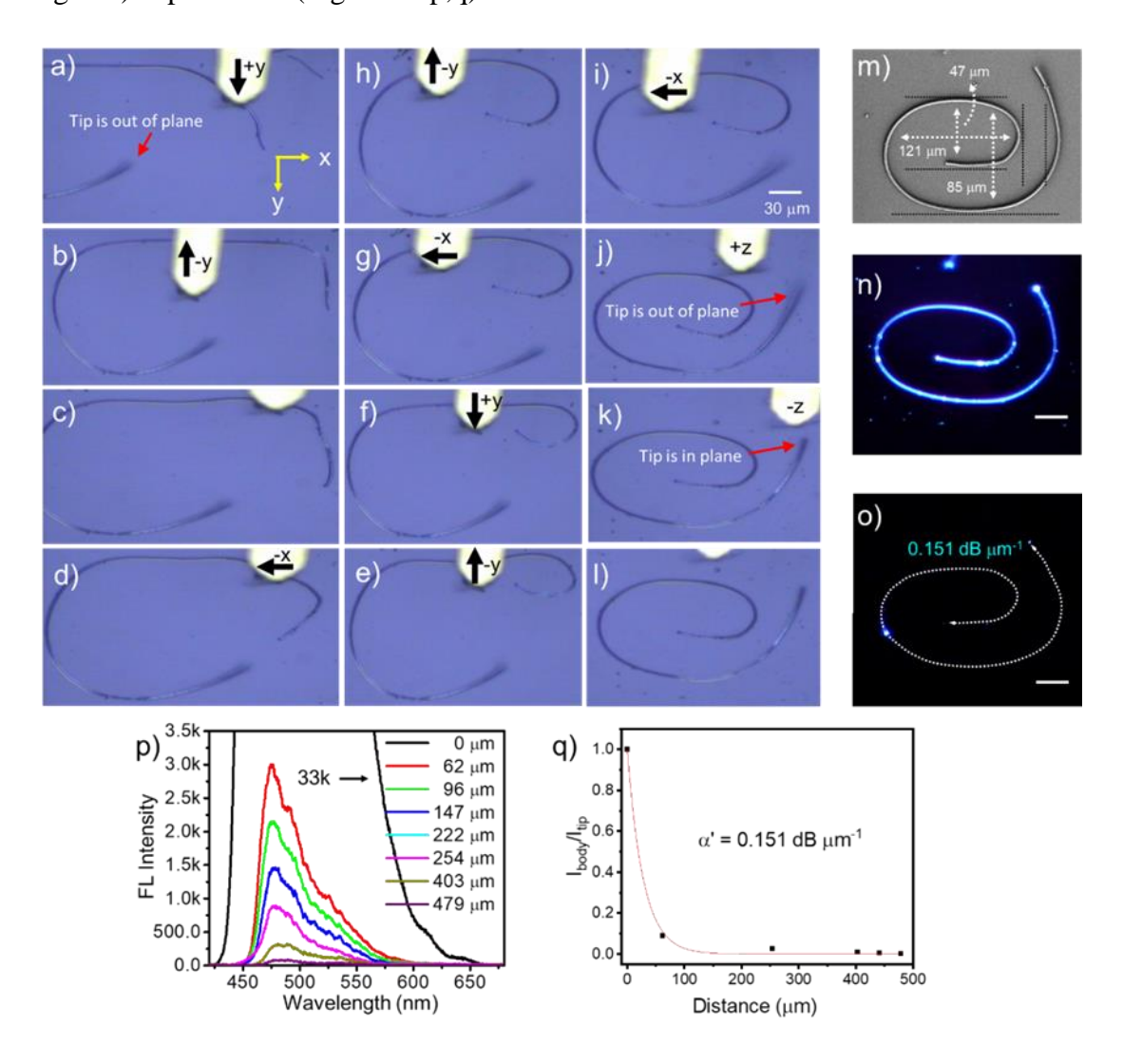


**Figure 5.9.** a-i) Micromechanical fabrication of an elliptical SW. m) FESEM n) FL microscope, and o) laser confocal FL microscope images of the fabricated elliptical SW, respectively. p) FL spectra collected at right tip of elliptical SW for excitation at various positions on the microcrystal. q) The plot of  $I_{tip}/I_{body}$  used for the calculation of optical loss of elliptical SW.

An Archimedean spiral is a spiral named after the renowned Greek mathematician Archimedes. In an Archimedean SW the new points move away from the locus at a constant

distance with a fixed angle. The construction of such micro-SAs in organic crystals was not envisaged earlier. The Archimedean SW was fabricated from a 377 μm long Cz-2CF<sub>3</sub> microcrystal (Figure 5.10a). The careful mechanical manoeuvring using the AFM tip resulted in the near-circular geometry (Figure 5.10b-i). Later, the same was meticulously positioned such that the Archimedean-type geometry was resembled (Figure 5.10j-m). The FESEM image shows increasing longitudinal dimensions per every turn away from the centre from 35 to 67 and 102 μm, respectively (Figure 5.10p). It also confirms the smooth surface morphology of the fabricated structure The FL microscope image of the fabricated Archimedean SW displayed bright crystal ends, suggesting the waveguiding attributes (Figure 5.10q). The same was reiterated from the laser excitation experiment when a focused laser beam directed at the body of the SW, produced FL output at both the crystal tips (Figure 5.10r). The EPDES experiment was used to calculate the optical loss of Archimedean type SW to be 0.0339 dB μm<sup>-1</sup> (Figure 5.10n,o).

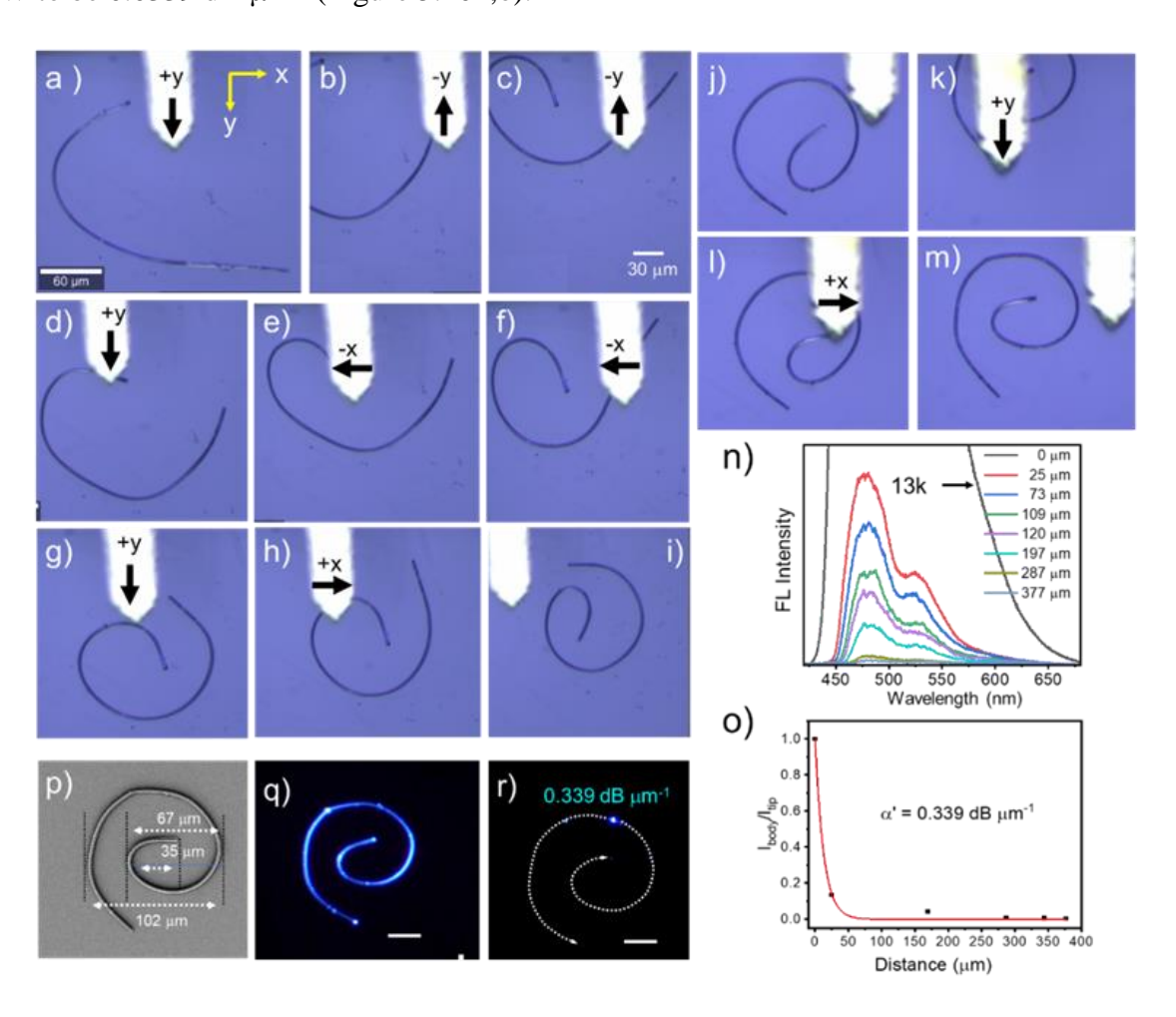


**Figure 5.10.** a-m) Micromechanical fabrication of an Archimedean SW. n) FL spectra collected at right tip of Archimedean SW for excitation at various positions on the microcrystal. o) The plot of  $I_{tip}/I_{body}$  used for the calculation of optical loss in Archimedean SW. p) FESEM q) FL microscope, and r) laser confocal FL microscope images of Archimedean SW, respectively.

#### 5.3.7 Fabrication of spiral waveguide-based reconfigurable OPICs

The unique characteristics of SW rely on their capability to route light in either directions, clockwise or anticlockwise. Generally, guiding the optical signal in orthogonal pathways is challenging. In this regard, we envisioned the design and fabrication of a four-sided polygonal SW (PSW) with five right-angles at 34, 79, 143, 219 and 299  $\mu$ m on a 389  $\mu$ m long waveguide (Figure 5.11a). The ease of fabricating such SWs using the the mechanophotonics technique is demonstrated in the earlier section. The FL image of the PSW possesses two bright FL spots at both ends of the PSW suggesting decent optical guiding ability (Figure 5.11m). When the PSW was irradiated with 405 nm light in the middle, it generated blue FL at the point of excitation which transduced to the crystal ends corroborating the optical waveguiding properties (Figure 5.11n). The optical loss of the constructed PSW was calculated to be 0.0763 dB  $\mu$ m<sup>-1</sup> (Figure 5.11o,p). This PSW was used to construct a hybrid two or three component reconfigurable OPIC, which required the integration of different optical components/materials at the same site.

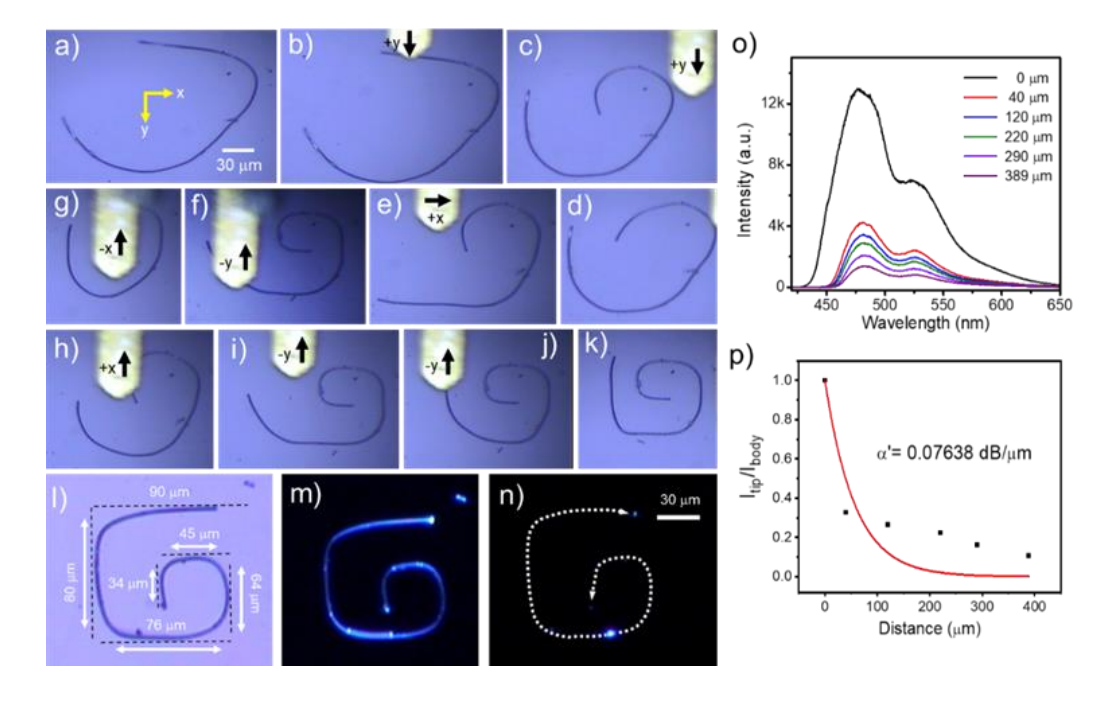


**Figure 5.11.** a-k) Micromechanical manipulation of four-sided polygonal spiral waveguide (PSW) from Cz-2CF<sub>3</sub> microcrystal. l) Confocal, m) FL microscope, and n) laser FL microscope images of PSW, respectively. o) Excitation-position dependent emission spectra collected at the top end of PSW. p)  $I_{tip}/I_{body}$  vs distance plot used to (red line) calculate the optical loss coefficient of PSW. A representative scale is provided in a.

The conventional microcrystal growth process does not allow self-assembly of structurally and chemically different materials in the same substrate with desired morphological requirements. Hence, two different microcrystals, achieved via individual self-

assembly process, must be transferred from one substrate to another by lifting one of the microcrystals to the desired OPIC site. This complex task can be accomplished with *mechanophotonics* technique by air-lifting a microcrystal from one substrate and dropping it at a required site in another substrate (known as *integration* discussed in section 1.6.2). Therefore, to construct a hybrid two-component circuit, a DBA ( $L \approx 312 \mu m$ ;  $\alpha' \approx 0.0558 \text{ dB} \mu m^{-1}$ ) microcrystal was transferred to the PSW's site and brought into optical contact by *integrating* micromechanical operation resulting in spiral circuit-1 (SC-1, Figure 5.12a,b).

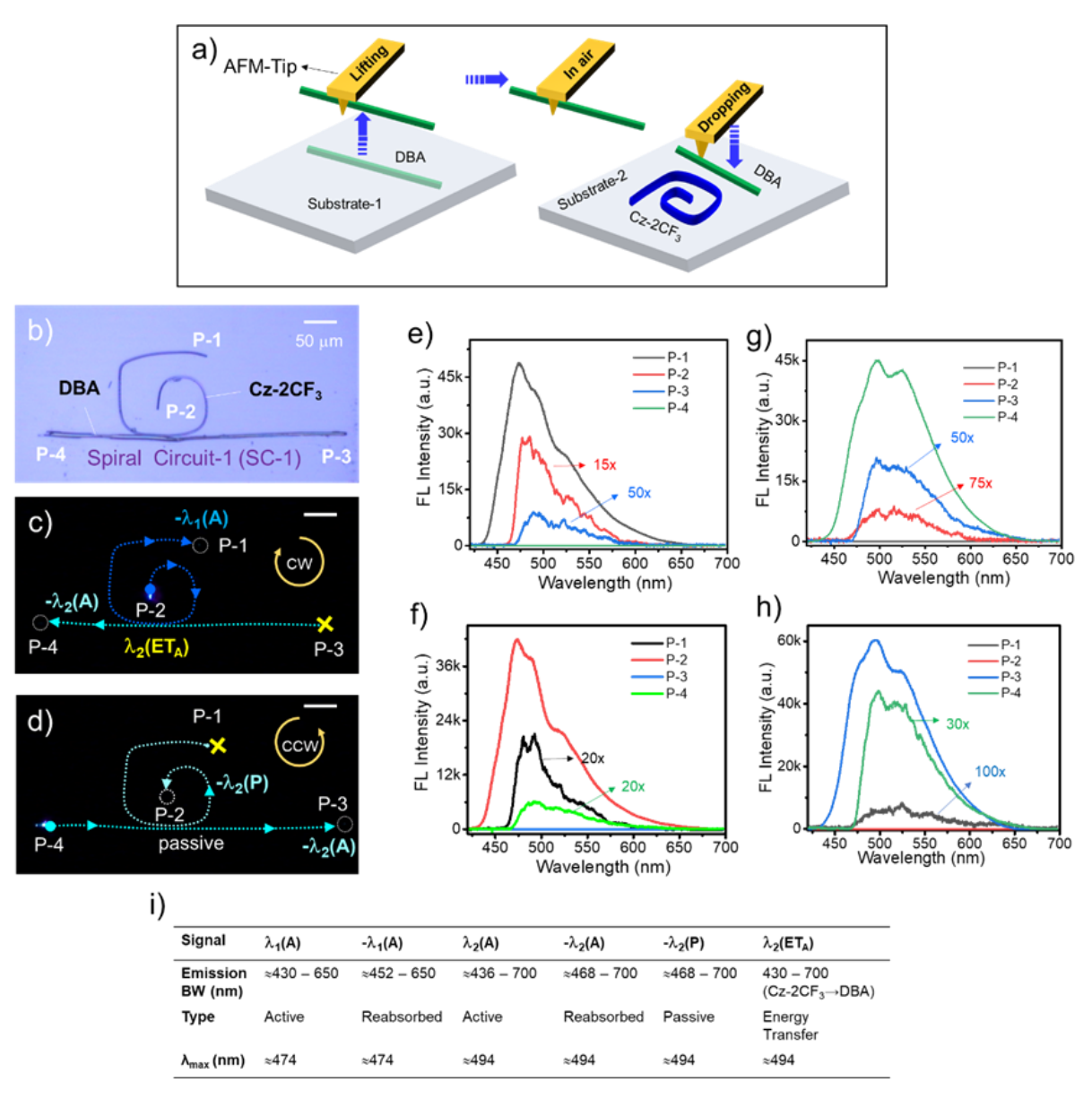


**Figure 5.12.** a) Graphical representation of transferring crystals from one substrate to another for the fabrication of spiral circuit -1 (SC-1). b) Confocal microscope image of SC-1. c,d) FL images of SC-1 for a 405 nm input at P-1 and P-4, respectively. e-h) Optical response of SC-1 for a 405 nm input at P-1 to P-4, respectively. (CW/CCW indicate clockwise or counterclockwise optical signal routing in SC-1; White circles represent FL output collection points). i) Table depicting the optical mechanism and bandwidth of signals involved in functioning of SC-1.

Various types of signals and optical functions operating in circuits are provided in Figure 5.12i. When 405 nm light is introduced at P-2, it generated FL signal  $\lambda_1(A)$  at P-2 and long pass filtered output,  $-\lambda_1(A)$  (here, minus and A denote reabsorption and active signals, respectively), was delivered at P-1 (Figure 5.12c,f). While a signal of  $-\lambda_2$  (ET<sub>A</sub>; ET from Cz-2CF<sub>3</sub> $\rightarrow$ DBA), at P-4 was recorded due to ET mechanism (Figure 5.12g). As expected, no optical signal (0), is observed at P-3 because of CW optical trajectory of spiral geometry. However, when light input was changed to P-1,  $-\lambda_1(A)$  signal at P-2 due to reabsorption,  $-\lambda_2$ (ET<sub>A</sub>) signal at P-3 owing to ET mechanism, and a null signal (0) at P-4 as a result of CCW light routing of SW were observed (Figure 5.12e). Interestingly, when light input is provided at P-3 (or P-4), only  $\lambda_2$  type signal was observed in SC-1 (Figure 5.12g,h). For light input directed at P-4,  $-\lambda_2$ (A) at P-3 and  $-\lambda_2$ (P) (here P denotes passive signal, because there is no ET from DBA $\rightarrow$ Cz-2CF<sub>3</sub>) at P-2 was evident (Figure 5.12d,h). No optical signal was observed at P-1 due to CCW light propagation in the circuit. Thereby, port specific optical performance from circuit was evident because of CW/CCW directional light routing (in PSW) and ET mechanism making them good candidates for multi-tasking optical circuitry.

The complex operations involved in a circuit and the number of optical operations performable by a single circuit make it desirable for diverse applications. Also, the accessible bandwidths in SC-1 are limited to the blue and cyan regions of the visible spectrum. Therefore, to increase the number of optical signals, operational bandwidths and functions, and to demonstrate the capability of the mechanophotonics approach to build multifaceted OPICs with broad operational spectral regions (from 430–700 nm), required the integration of red emissive BTD microcrystals with SC-1. Initially, a BTD microcrystal ( $L \approx 200 \, \mu m$ ) was illuminated with 405 nm laser light source at the left end (Figure 5.13a). The photoexcitation produced red FL corresponding to  $\lambda_3 \approx 534-750$  nm and the same signal transduced to the other end as reabsorbed signal  $-\lambda_3 \approx 571-750$  nm (Figure 5.13b,c). The optical loss of the waveguide was estimated to be 0.1064 dB  $\mu m^{-1}$  (Figure 5.13d). The BTD crystal was transported to the circuit construction site carefully by lifting it from substrate-3 (Figure 5.13e). The air-lifted crystal was carefully dropped near the SC-1's circuit construction site (Figure 5.13f-1).

Precise positioning of BTD waveguide at the top portion of SC-1 resulted in the broad bandwidth operatable spiral circuit-2 (SC-2). The number of output ports in SC-2 increased to six from four in SC-1 (Figure 5.14a). The FL microscope image of SC-2 clearly depicts three

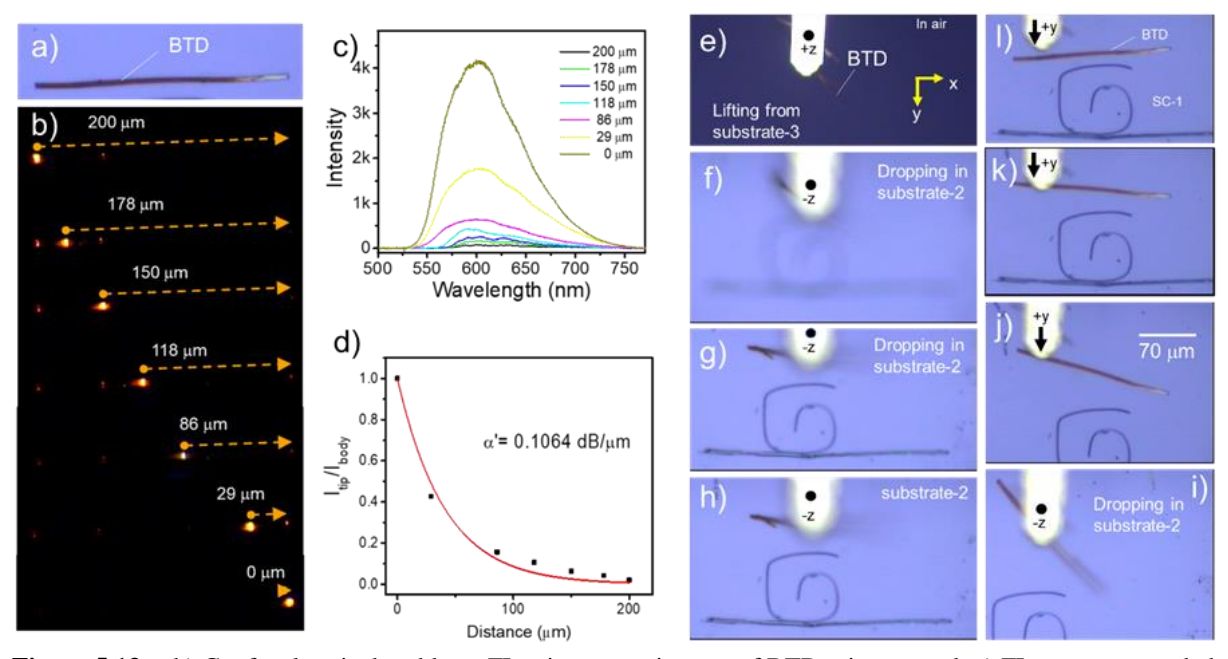


**Figure 5.13.** a,b) Confocal optical and laser FL microscope images of BTD microcrystal. c) FL spectra recorded at various lengths between excitation and collection points. d) The plot of  $I_{tip}/I_{body}$  used for the calculation of optical loss of BTD. e-l) Confocal microscope images showing the micromechanical transfer of BTD waveguide near the circuit construction site. Representative scale bar is provided in j.

functional colors blue, green and red emissions with six outputs labelled as ports P-1 to P-6 (Figure 5.14b). To validate the optical performance of fabricated hybrid SC-2, input light was given at one port and processed light output at remaining ports was recorded (Figure 5.14i). When input light is offered at P-2, we see three different emission bands (blue  $-\lambda_1(A)$ , cyan - $\lambda_2(ET_A)$ , red  $-\lambda_3(ET_B)$ ) spanning from 430 nm to 750 nm at P-1, P-4 and P-6, respectively (Figure 5.14c). Initially at the excitation port P-2, a radiative blue signal is generated due to optical excitation and the same signal travels to the other end of the SW taking a CCW pathway to reflect blue output at P-1 (Figure 5.14e). As the blue signal passes along the bottom portion of SW, which is in contact with DBA waveguide, it leads to radiative ET from Cz-2CF<sub>3</sub> to DBA, and irradiates DBA waveguide (Figure 5.14i). The ET produced cyan emission travels in the DBA waveguide to yield a cyan output at P-4. Similarly, the ET from Cz-2CF<sub>3</sub> to BTD at the top portion of SW results in red emission at BTD waveguide, subsequently producing a red signal at P-6 (Figure 5.14g). While input light triggered at P-4 produces only signal type  $\lambda_2$  at P-3 and P-2 in orthogonal directions (Figure 5.14g). For a light input at P-3, two different optical signals, cyan (at P4) and red at P-6 are observed (Figure 5.14d,f). Interestingly, in this pathway Cz-2CF<sub>3</sub> SW acts as a passive only signal transducer (Figure 5.14h). However, when light input was changed to P-6 (or P-5), only passive  $-\lambda_3(P)$  signal travelled to ports P-2 and P-3, due to lack of ET (from BTD to DBA or

Cz-CF<sub>3</sub>) and CCW-directed signal propagation, apart from long-pass filtered  $-\lambda_3(A)$  at P-5 in BTD waveguide (Figure. 5.14g).

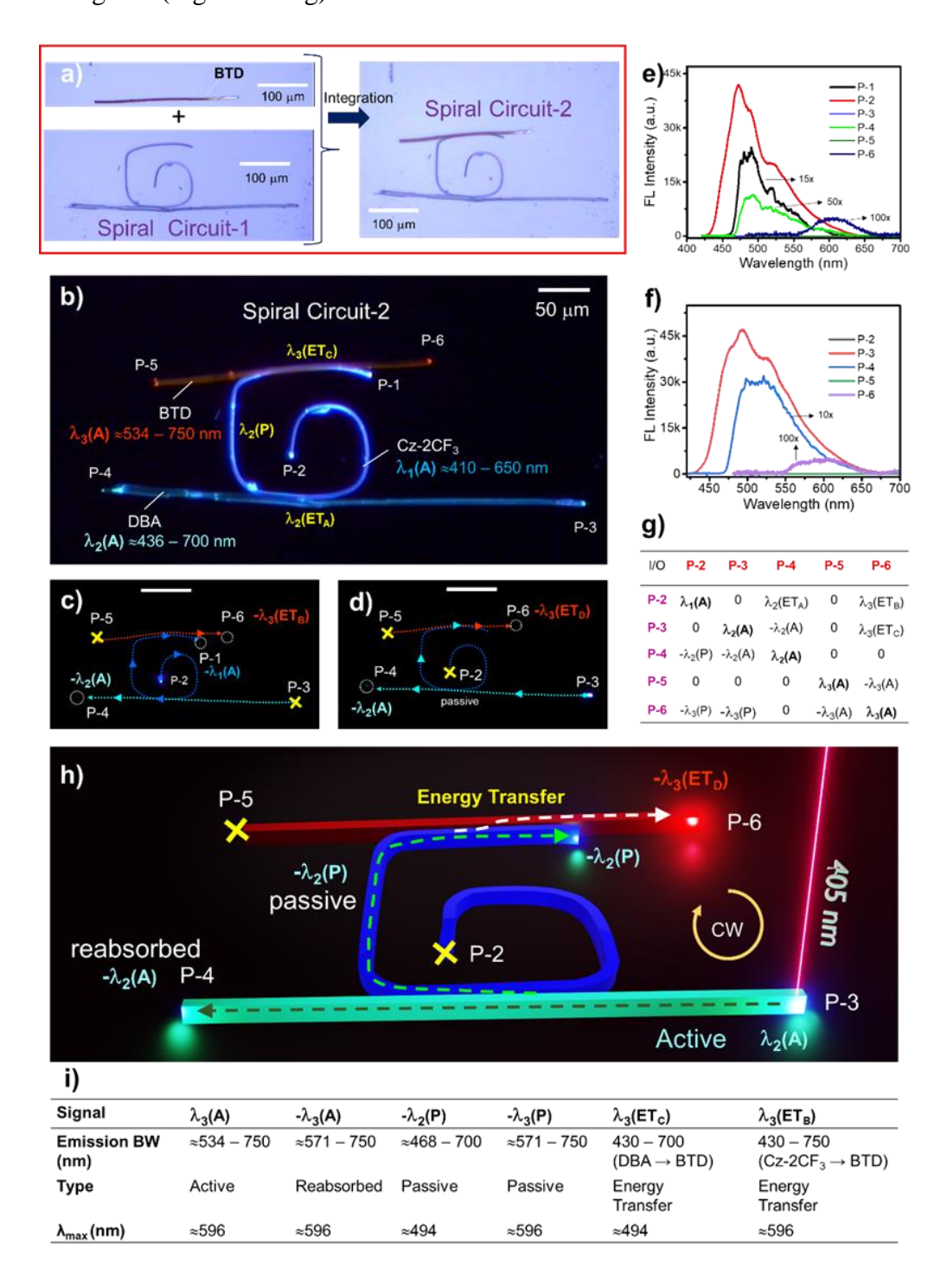


**Figure 5.14.** a) Micromechanical fabrication of spiral circuit-2 (SC-2). b) FL microscope image of SC-2 showing six ports namely P-1 to P-6 and bandwidths of various materials. c,d) Confocal FL image of SC-2 depicting light propagation in SC-2 for 405 nm optical signal input at P-2 and P-3, respectively. Scale bar corresponds to  $100 \ \mu m$ . e,f) Optical response of SC-2 for light input at P-2 and P-6, respectively. g) Compilation displaying the optical signals produced at various ports for light input at different ports P2-P6. h) Graphics illustrating the type, direction and number of optical signals operating in SC-2 for 405 nm laser light illuminated at port P-3. i) Table depicting the optical mechanisms and bandwidth of the signals responsible for functioning of SC-2. The scale bars provided in c,d correspond to  $100 \ \mu m$ .

In programmable circuits, the number of ports or signals can be modulated externally. The programmable attributes of the fabricated SC-2 were shown by detaching the DBA crystal and integrating it with a highly flexible green emissive BPyIN ( $L \approx 200 \mu m$ ;  $\alpha'$  $\approx 0.0669 \text{ dB } \mu\text{m}^{-1}$ ) to achieve reconfigured SC-2 (Figure 5.15a,b). Further, the tips of BPyIN and BTD were attached in an end-to-end fashion to facilitate efficient optical signal propagation directly into the BTD waveguide, unlike the evanescent coupling mode (Figure 5.15c). The reconfigured circuit effectively reduced the number of outputs and behaved according to the input-specific output response, as observed in the previous case (Figure 5.15e). As the light input is given at P-2, the blue FL was transduced to the other end of PSW (Figure 5.15e,g,). The FL light propagating inside PSW excites BPyIN crystal via ET to yield a signal green signal -λ<sub>4</sub>(ET<sub>D</sub>) due to energy transfer from Cz-2CF<sub>3</sub> to BPyIN. The BPyIN spontaneously excites BTD through ET producing a red signal -λ<sub>3</sub>(ET<sub>E</sub>) along with a green signal at J1 (Figure 5.15d). Thereby, we see two operational ET mechanisms spontaneously for one light input. This results in a  $-\lambda_3(A)$  red signal at P-6. However, at P-3 no optical output could be observed due to the circuit geometry (Figure 5.15d,f). Interestingly, when light input was given at P-3, it produced a green signal  $\lambda_4(A)$  at the excitation port, which traveled to J1 and excited BTD crystal to result in a red signal  $-\lambda_3(A)$  signal at P-6. When excitation was changed to P-6, as there is no ET from BTD to BPyIN or Cz-2CF<sub>3</sub>, only red signal,  $\lambda_3(A)$  produced at the point of excitation passively coupled into BPyIN and SW to be observed as  $-\lambda_3(P)$  signal at both P-3 and P-2 corroborating the input port dependent optical signal response (Figure 5.15d,h). The development of such complex OPICs with state-of-theart mechanophotonics technique opens new dimensions in organic photonics for flexible photonic device technologies.

#### **5.4 Summary**

In this chapter, mechanically flexible blue-emissive Cz-2CF<sub>3</sub> was designed and synthesized. perform The extreme flexibility of Cz-2CF<sub>3</sub> is attributed to various supramolecular interactions stabilizing the crystal. The unusual mechanical flexibility at micro-regime due to CSSI was exploited to fabricate different μ-SA like Cornu type, elliptical, Archimedean, rectangular, square-shaped, and triangular spiral waveguides. The rectangular SW was integrated with cyan emissive DBA crystal to construct a hybrid two-component OPIC with four ports. The fabricated circuit operates via diverse optical mechanisms like active and passive waveguiding along with reabsorption and ET mechanisms to facilitate input-dependent signal output at different ports. Later, the two-

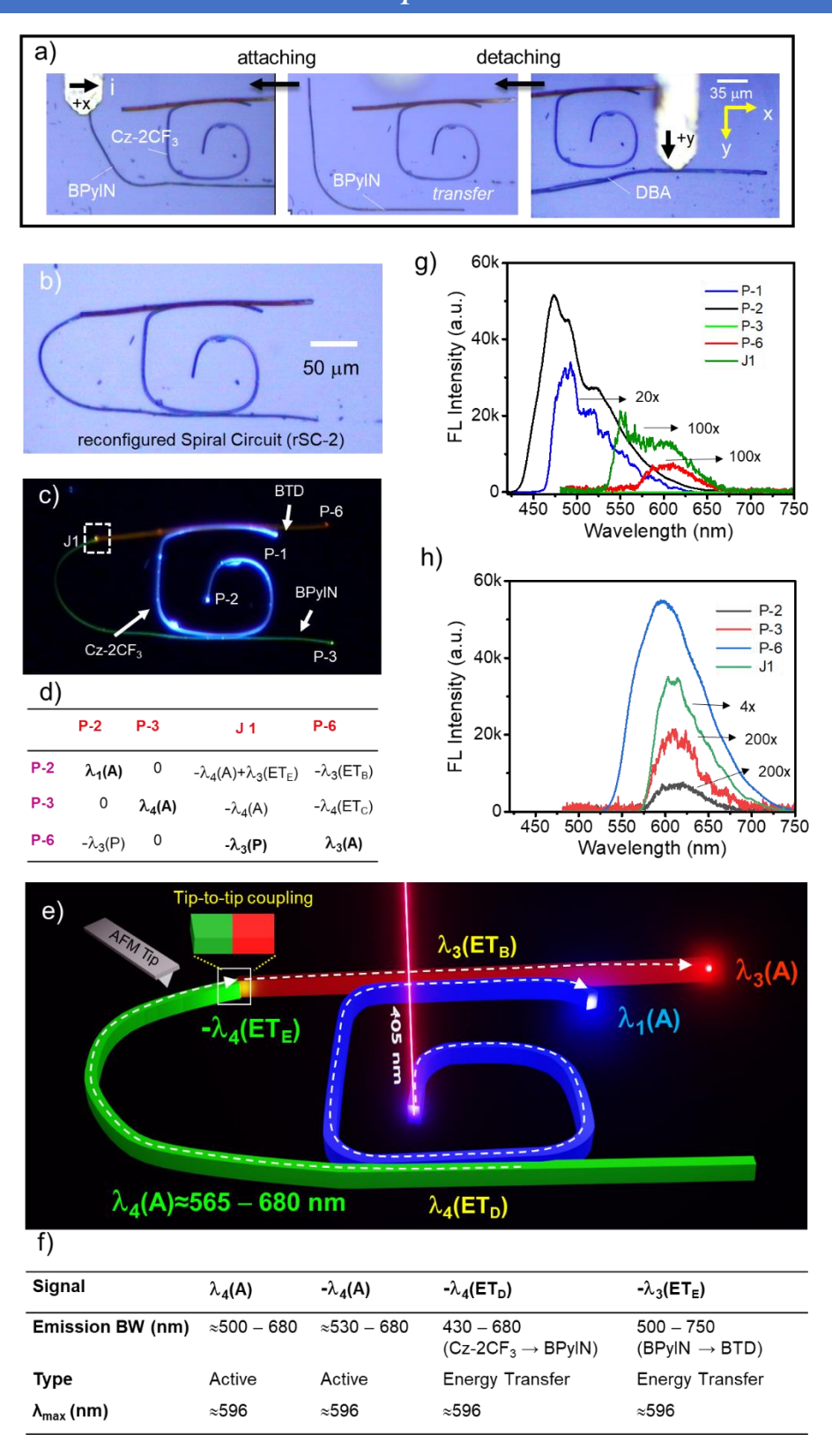


**Figure 5.15.** a) Micromechanical replacement of DBA with BPyIN microcrystal. b) confocal **o**ptical microscope image of reconfigured spiral circuit-2 (rSC-2). c) FL microscope image of rSC-2 with ports P-2, P-3 and P-6. d) Port-specific optical signals processed by the rSC-2 depending on port receiving the input light signal. (The violet label reflects light input, and the red label indicates the output signal. e) Graphics illustrating the functioning of rSC-2 for 405 nm light input at port P-2. f) Table depicting the optical mechanism and bandwidth of the signal. g, h) Optical performance of rSC-2 for light input at P-2 and P-6, respectively.

component OPIC was integrated with red emissive BTD crystal to obtain a first-of-its-kind hybrid three-component OPIC with six ports. The operational and directional specific optical signal output strictly depended on the port receiving input signal. The high input-selective optical performance of the circuit strongly supports their multi-tasking capabilities. To prove the reconfigurability and tune the operational bandwidth, OPIC's ports were reconfigured by detaching DBA and attaching BPyIN crystal. The number of ports was reduced to three by inducing a tip-to-tip coupling (between BPyIN and BTD crystal) and facilitating effective optical signal transmission in the circuit. Therefore, a mechanically programmable OPIC with a broad operational bandwidth range covering entire visible region was achieved. The unprecedented control offered by the mechanophotonics approach in combination with flexible organic crystals to configure the number of ports and to modulate the signal output direction paves the path to realize functional programmable OPIC devices in the future when used in tandem with micro-electromechanical systems technology.

# **Conclusions and Future Scope**

#### **6.1 Conclusions**

This thesis entitled "Mechanophotonics: Pseudo-Plastic Organic Crystal-based Photonic Components and Circuits" described the burgeoning utility of flexible organic crystalline microwaveguides for photonic circuit applications. The advantages of organic materials in terms of exceptional mechanical properties, tuneable optical bandwidth, clever usage of reabsorption, and energy transfer (ET) processes for photonic circuit technologies resonate with the superior qualities of organic materials.

Chapter-1 provided a brief introduction to the importance of photonic integrated circuits (PICs) for science and technology and their pivotal role in transforming next-generation data transfer and processing technologies. Initially, the important photophysics governing light generation and modulation in organic and inorganic materials were discussed. Followed by the principles governing the light propagation and confinement in microstructures were presented. Various photonic components like directional couplers (DCs), interferometers (IMs), wavelength division multiplexers (WDMs), add-drop filters, and spiral waveguides (SWs) necessary for the fabrication of photonic integrated circuits (PICs) were elaborately discussed. A similar analogy of the Si optical components with organic crystals emphasizing their advantages in terms of active, passive, reabsorption and ET mechanisms was summarized. The pseudo-plastic mechanical behaviour of elastic

microcrystals and the importance of substrate-crystal surface adhesive interactions to exhibit pseudo-plasticity were clearly described. The availability of microcrystal processing techniques like mechanophotonics and various micromechanical tools (like bending, lifting, cutting, integrating, rolling, etc.) needed for organic PIC fabrication were presented.

The fabrication of miniature optical IMs with organic crystals remained an unfathomable endeavor because of the lack of a suitable microcrystal and its microprocessing technique. Accomplishing such burgeoning tasks requires resilient organic materials with an intelligent approach. Hence, *Chapter-2* demonstrated the fabrication of an organic crystal-based optical IM constructed using flexible organic crystals and mechanophotonics technique. In the strained microcrystal cavity, there is a change in optical modes compared to the unstrained cavity, attributed to the minute changes in the refractive index of the cavity due to the strain induced by mechanical bending. These studies enabled the detailed investigation of mechanical strain on optical modes which was further utilized for clearly understanding the optical pathways involved in the constructed IM. Therefore, a novel organic IM was fabricated, and the optical mode change due to bending and interference was clearly established. The optical pathways responsible for the functioning of the interferometer were uncovered.

Ever-increasing global data traffic and the necessity to miniaturize the photonic devices and modules mandate the construction of optical components and circuits with multifunctional capabilities. The fabrication of such multi-functional components is feasible by employing two or more optically different materials on a chip. In *Chapter-3*, a hybrid directional coupler capable of modulating the direction, chromaticity, and split ratio of the input signal was illustrated successfully. Micromechanical integration of a blue-emitting CF<sub>3</sub>OMe microcrystal with a green-emitting BPyIN microcrystal resulted in the HDC. The HDC performed signal and chromaticity modulation for light input at the CF<sub>3</sub>OMe microcrystal while it functioned as only a signal splitter when BPyIN received the light input. Thereby, the HDC performed multiple functions without altering the circuit geometry. These HDCs are needed to study artificial neural networks.

A vast majority of PICs reported to date operate in the mid-IR region. The optical non-transparency of Si-based PICs in the visible region restricts their usage for visible light technologies. The visible bandwidth region is crucial for LiFi and related technologies. In this aspect, WDMs operating in the visible region are essential. *Chapter-4* demonstrated the construction and functioning of organic WDM. Typically, a blue-emissive BPP microcrystal

capable of acting as an active and passive waveguide was sequentially integrated with a cyanemissive DBA microcrystal followed by custom-synthesized BTD-2CF<sub>3</sub> microcrystal using micromanipulation tools. The propagation of blue, cyan, and orange emissions along the BPP waveguide proves the multiplexing ability of organic microcrystals. In the process, WDM utilized active, passive, reabsorption and energy transfer mechanisms to illustrate the desired function. The demonstration of such optical components is critical for the advancement of technologies intended to use ambient light.

The ability to draw long waveguides into smaller compact regions on the photonic chips is essential to construct delay lines needed for spectrometers, sensors, and related photonic applications. One way to achieve the delay lines is by inducing a spiral structure with many turns. Such spiral waveguides (SWs) are well-known in Si-based materials. While analogous organic spiral waveguides have not been reported yet. Chapter-5 showcased the elegant manufacturing of organic spiral waveguides (OSWs) using extremely flexible Cz-CF<sub>3</sub> microcrystals. The exceptional mechanical properties studied by nanoindentation experiments illustrate the role of supramolecular interactions for mechanical flexibility. The constructed OSWs include Cornu-type, Archimedean, elliptical, three-sided, and four-sided polygonal OSWs. A blue-emissive four-sided polygonal OSW fabricated from Cz-2CF<sub>3</sub> was integrated with cyan-emissive DBA and red-emissive BTD microcrystals to realize an organic circuit operating in the entire visible region with six ports. This reconfigurable circuit was programmed by replacing DBA microcrystal with BPyIN microcrystal in a tip-to-tip fashion and demonstrated mechanical control over the number of output ports. Therefore, suggesting the programmable nature of spiral circuits. Interestingly, the number and direction of output signals depend on the clever choice of input port, which is determined by the operational mechanisms (passive and energy transfer) involved in the functioning of the circuit.

#### **6.2 Future Scope of the Work**

This thesis illustrated an innovative and cost-effective approach to constructing organic photonic components and circuits. The choice-based selection of organic crystals (available from the vast library of organic crystals) depending on their mechanical, optical, and optoelectronic properties provide a strong materials platform to surpass the demerits of Si-based PICs. The observation of mechanical bending influence on a microcrystal cavity's optical modes is crucial to constructing interferometers. The exceptional material properties in combination with a cost-effective, hassle-free manipulation technique allow steady-fast

fabrication of hybrid photonic circuits. The ease with which multiple crystals can be integrated (or replace with other crystals) onto a chip with the help of mechanophotonics microcrystal processing technology, manifests the creation of desired hybrid photonic components and circuits operating in the custom-controllable optical bandwidths from visible to NIR region. The mechanical reconfigurable nature of these circuits allows the mechanical control over the number of signals and induces programmable attributes to these circuits.

Despite the progress made so far with organic PICs, realizing functional all-organic PIC performing a real-time function necessitates tremendous improvements to the prototype organic circuits demonstrated till now. Firstly, the difficulty of attaining identical microcrystals with the same aspect ratio, crystal ends, or similar intrinsic defects in organic crystals is challenging. Second, the minute mechanical damage (depending on the level of micromechanical manipulation needed for circuit fabrication) induced onto the crystal surface can cause light leakage and can interfere with the device's photonic performance if the damage is significant. Thirdly, the scalable OPIC production with mechanophotonics technique can be amplified by switching to automatic manipulation methods. However, engineering high-quality microcrystal growth remains unclear. Moreover, most of the OPICs deployed 1D microcrystals for circuit fabrication, while the use of disk resonators mandates the precise geometrical shaping of 2D microcrystals, which is hard to achieve with the AFMtip-aided mechanophotonics technique. In this aspect, exploring the possibility of different fabrication processes like focused ion beam milling, and micropatterning techniques or a combination of multiple techniques could be a solution. Leaving aside the fabrication part, the issues about powering these microphotonic devices must be addressed appropriately to meet the end-user's needs.

Finally, to accomplishing a functional OPIC addressing real-time problems is a distant dream as this study uncovered a plethora of opportunities and improvements possible with organic crystal-based OPICs.

- 1. R. E. Hummel, Electronic Properties of Materials, Springer, Berlin Heidelberg, 1985.
- 2. J. D. Meindl, Comput. Sci. Eng. 2003, 5, 20.
- 3. K. E. Hamilton, C. D. Schuman, S. R. Young, R. S. Bennink, N. Imam, T. S. Humble, *ACM Trans. Parallel Comput.* **2020**, *7*, 1.
- 4. W. Bogaerts, D. Pérez, J. Capmany, D. A. B. Miller, J. Poon, D. Englund, F. Morichetti, A. Melloni, *Nature* **2020**, *586*, 207.
- 5. Y. Liu, A. Houck, Nat. Phys. 2016, 13, 48.
- H.-S. Zhong, H. Wang, Y.-H. Deng, M.-C. Chen, L.-C. Peng, Y.-H. Luo, J. Qin, D. Wu, X. Ding, Y. Hu, P. Hu, Y. Xiao-Yan, W. Zhang, H. Li, Y. Li, X. Jiang, L. Gan, G. Yang, L. You, Z. Wang, L. Li, N.-L. Liu, C. Lu, J.-W. Pan, *Science* 2020, 370, 1460.
- 7. J. D. Franson, B. C. Jacobs, T. B. Pittman, *Phys. Rev. A* **2004**, *70*, 062302.
- 8. K. Lee, C. Ji, H. Iizuka, D. Banerjee, J. App. Phys. 2021, 129, 048846.
- 9. H. Chen, B. Zheng, L. Shen, H. Wang, X. Zhang, N. I. Zheludev, B. Zhang, *Nat. Commun.* **2013**, *4*, 3652.
- 10. S. Saha, O. Segal, C. Fruhling, E. Lustig, M. Segev, A. Boltasseva, V. M. Shalaev, *Opt. Express* **2023**, 31, 8267
- 11. T. Liu, J. Ou, K. F. MacDonald, N. I. Zheludev, Nat. Phys. 2023, 19, 986.
- 12. R. Nagarajan, C. H. Joyner, R. Schneider, J. Bostak, T. Butrie, A. G. Dentai, V. Dominic, P. Evans, M. Kato, M. Kauffman, D. Lambert, S. K. Mathis, A. Mathur, R. H. Miles, M. Mitchell, M. Missey, S. Murthy, A. Nilsson, F. Peters, S. C. Pennypacker, J. L. Pleumeekers, R. A. Salvatore, R. Schlenker, R. B. Taylor, H.-S. Tsai, M. F. Van Leeuwen, J. Webjörn, M. Ziari, D. Perkins, J. Singh, S. G. Grubb, M. Reffle, D. Mehuys, F. Kish, D. Welch, *IEEE J. Sel. Top. Quantum Electron.* 2005, 11, 50.
- 13. https://www.shutterstock.com/search/electronic+circuit
- 14. Photonic Integrated Circuit: The Future of High-Speed Data Processing HIGH-END FPGA Distributor (ebics.net)
- 15. https://www.servethehome.com/intel-silicon-photonics-update-at-interconnect-day-2019/
- 16. R. Corneliu, Proc. of SPIE, 2019, 11143, DOI:10.1117/12.2523863
- 17. I. R. Ruiz, T. N. Ackermann, X. M. Berbel, A. Llobera, Anal. Chem. 2016, 88, 1345.
- 18. R. Chandrasekar, Z. J. Lapin, A. S. Nichols, R. M. Braun, A. W. Fountain, Opt. Eng. 2019, 58, 020901.
- 19. Q. Cheng, M. Bahadori, M. Glick, S. Rumley, K. Bergman, Optica 2018, 5, 1354.
- 20. https://www.minacned.nl/blog/2020/07/15/how-integrated-photonics-accelerate-the-roll-out-of-point-of-care-diagnostics-for-covid-19-cancer-and-other-diseases/
- 21. A. Grosman, T. Duanis-Assaf, N. Mazurski, R. Zektzer, C. Frydendahl, L. Stern, M. Reches, U. Levy, *Nanophotonics* **2023**, *12*, 2831.
- 22. A. Hänsel, M. J. R. Heck, J. Phys. Photonics 2020, 2, 012002.
- 23. E. D. Palik, Handbook of Optical Constants of Solids, Academic, New York 1998.
- 24. X. Chen, M. M. Milosevic, S. Stanković, S. Reynolds, T. D. Bucio, K. Li, D. J. Thomson, F. Gardes, G. T. Reed, *Proc. IEEE*, **2018**, *106*, 2101.
- 25. S. Lourdodoss, R. T. Chen and C. Jagadish, Semiconductors and Semimetals Book Series, Academic Press, Cambridge, **2018**.
- 26. P. Dong, Y. K. Chen, G. H. Duan, D. T. Neilson, *Nanophotonics*, **2014**, *3*, 215.
- 27. J. Bowers, Proc. Cust. Integ. Circuits Conf. 2013, 1-89
- 28. T. Hu, B. Dong, X. Luo, T. Y. Liow, J. Song, C. Lee, G. Q. Lo, *Photonics Res.* 2017, 5, 417.
- 29. W. Bogaerts, L. Chrostowski, Laser & Photonics Rev. 2018, 12, 1700237.
- 30. a) T. Poon, T.-G. Kim, Engineering Optics with MATLAB, World Scientific Publishing, Singapore, **2006**; b) https://www.wired.com/2013/07/is-light-a-wave-or-a-particle/
- 31. https://tipteh.com/sensors/industrial-interferometer-for-accurate-non-contact-measurements/#:~:text=An%20interferometer%20can%20be%20used,stability%20of%20the%20performed%20measurements.
- 32. N. Rivera, I. Kaminer, Nat. Rev. Phys. 2020, 2, 538.

- 33. T. Byrnes, N. Y. Kim and Y. Yamamoto, Nat. Phys. 2014, 10, 803.
- 34. V. V. Zalamai, N. N. Syrbu, I. G. Stamov, S. I. Beril, J. Opt. 2020, 22, 085402.
- 35. P. E. Barclay, K. Srinivasan O. Painter, Opt. Express 2005, 13, 801.
- 36. A. Arbabi and L. L. Goddard, Opt. Lett. 2013, 38, 3878.
- 37. T. Miya, IEEE J. Sel. Top. Quantum Electron. 2000, 6, 38.
- 38. N. M. Margalit, C. Xiang, S. M. Bowers, A. Bjorlin, R. Blum, J. E. Bowers, *Appl. Phys. Lett.* **2021**, *118*, 50117.
- 39. A. Kaneko, T. Goh, H. Yamada, T. Tanaka and L. Ogawa, J. Sel. Top. Quantum Electron. 1999, 5, 1227.
- 40. T. D. Bucio, C. Lacava, M. Clementi, J. Faneca, I. Skandalos, A. Baldycheva, M. Galli, K. Debnath, P. Petropoulos, F. Gardes, *IEEE J. Sel. Top. Quantum Electron.* **2020**, *26*, 1.
- 41. D. J. Moss, R. Morandotti, A. L. Gaeta, M. Lipson, Nat. Photonics, 2013, 7, 597.
- 42. J. Frenkel, Phys. Rev. 1931, 37, 17.
- 43. C. Zhang, C. Zou, Y. Zhao, C. Dong, W. Cong, H. Wang, Y. Liu, G. Guo, J. Yao, Y. S. Zhao, *Sci. Adv.* **2015**, *1*, e1500257.
- 44. R. Chandrasekar, Small 2021, 17, 2100277.
- a) R. Chandrasekar, *Phys. Chem. Chem. Phys.* 2014, 16, 7173; b) D. Venkatakrishnarao, E. A. Mamonov, T. V. Murzina, R. Chandrasekar, *Adv. Opt. Mater.* 2018, 6, 1800343; c) Y. Chen, Y. Yin, L. Ma, O. G. Schmidt, *Adv. Opt. Mater.* 2021, 9, 2100143.
- 46. S. Chen, M. P. Zhou, X. D Wang, G. Q. Wei, L. S. Liao. *Photonix.* 2021, 2, 2.
- 47. Y. Zhao, J. Xü, A. Peng, H. Fu, Y. Ma, L. Jiang, J. Yao, Angew. Chem. Int. Ed. 2008, 47, 7301.
- 48. Y. Zhao, A. Peng, H. Fu, Y. Ma, J. Yao, Adv. Mater. 2008, 20, 1661.
- 49. C. Tardío, V. V. Pradeep, R.l Martín, A. M. Rodríguez, A. D. L. Hoz, J. Ravi, M. Annadhasan, P. Prieto, R. Chandrasekar, *Chem. Asian J.* **2021**, *16*, 3476.
- 50. S. Ramachandran, D. Cohen, A. P. Quist, R. Lal, Sci. Rep. 2013, 3, 2133.
- 51. H. Toba, K. Oda, K. Nakanishi, N. Shibata, K. Nosu, N. Takato, and M. Fukuda, *J. Lightwave Technol.* **1990**, *8*, 1396.
- 52. K. Iwatsuku, J. Kani, J. Opt. Commun. Netw. 2009, 1, 17.
- 53. M. Lipson, Nat. Mater. 2022, 21, 974.
- 54. X. Xu, G. Ren, T. Feleppa, X. Liu, A. Boes, A. Mitchell, A. J. Lowery, Nat. Photon. 2022, 16, 595.
- 55. N. Chandrasekhar, M. A. Mohiddon, R. Chandrasekar, Adv. Opt. Mater. 2013, 1, 305.
- 56. K. Takazawa, Y. Kitahama, Y. Kimura, G. Kido, Nano Lett. 2005, 5, 1293.
- 57. K. Takazawa, Chem. Mater. 2007, 19, 5293.
- 58. H. Liu, Z. Lu, Z. Zhang, Y. Wang, H. Zhang, Angew. Chem. Int. Ed. 2018, 57, 8448.
- 59. M. Annadhasan, S. Basak, N. Chandrasekhar, R. Chandrasekar, Adv. Opt. Mater. 2020, 8, 200959.
- 60. H. Liu, Z. Bian, Q. Cheng, L. Lan, Y. Wang, H. Zhang, Chem. Sci. 2019, 10, 227.
- 61. A. V. Kumar, M. Rohullah, J. Ravi, M. Godumala, M. Annadhasan, R. Chandrasekar, *CrystEngComm* **2021**, *23*, 5774.
- 62. J. Ravi, D. Venkatakrishnarao, C. Sahoo, S. R. G. Naraharisetty, N. V. Mitetelo, A. A. Ezhov, E. A. Mamonov, T. V. Murzina, R. Chandrasekar, *Chem. Nano. Mat.* **2018**, *4*, 764.
- 63. A. D. Nidhankar, Goudappagouda, D. S. M. Kumari, S. K. Chaubey, R. Nayak, R. G. Gonnade, G. V. P. Kumar, R. Krishnan, S. S. Babu, *Angew. Chem. Int. Ed.* **2020**, *59*, 13079.
- 64. J. Roux, J. Coutaz, P. L. Barny, E. Chastaing, J. Opt. Soc. Am. B 1995, 12, 428.
- 65. B. E. A. Saleh and M. C. Teich, Fundamentals of Photonics, John Wiley & Sons, Inc., Hoboken, NJ, 1991.
- 66. R. S. Quimby, Photonics and Lasers—An Introduction, John Wiley & Sons, Inc, Hoboken, NJ, 2006.
- 67. W. Yao, Y. Yan, L. Xue, C. Zhang, G. Li, Q. Zheng, Y. S. Zhao, H. Jiang, J. Yao, *Angew. Chem. Int. Ed.* **2013**, *52*, 8713.
- 68. R. Chen, V. D. Ta, H. D. Sun, ACS Photonics 2014, 1, 11.
- 69. S. G. Lipson, H. Lipson, and D. S. Tannhauser, Optical Physics (3rd ed.). London: Cambridge U.P. 1995.

- 70. W. Weng, J. D. Anstie, T. M. Stace, G. Campbell, F. N. Baynes, and A. N. Luiten, *Phys. Rev. Lett.* **2014**, *112*, 160801.
- 71. M. G. Scullion, T. F. Krauss and A. D. Falco, Sensors 2013, 13, 3675.
- 72. F. Vollmer, S. Arnold, and D. Keng, *Proc. Natl. Acad. Sci.* **2008**, *105*, 20701.
- 73. D. V. Strekalov, C. Marquardt, A. B. Matsko, H. G. L. Schwefel, G. Leuchs, J. Opt. 2016, 18, 123002.
- 74. A. Kiraz, A. Kurt, M. Dündar, A. Demirel, Appl. Phys. Lett. 2006, 89, 081118.
- 75. F. Albert, T. Braun, T. Heindel, C. Schneider, S. Reitzenstein, S. Höfling, L. Worschech, A. Forchel, *Appl. Phys. Lett.* **2010**, *97*, 101108.
- 76. V. S. Ilchenko, A. B. Matsko, IEEE J. Sel. Top. Quant. Electron. 2006, 12, 15.
- 77. A. Yalcin, K. C. Popat, J. C. Aldridge, T. A. Desai, J. Hryniewicz, N. Chbouki, B. E. Little, O. King, V. Van, S. Chu, *IEEE J. Sel. Top. Quant. Electron.* **2006**, *12*, 148.
- 78. S. T. Chu, B. E. Little, W. Pan, T. Kaneko, S. Sato, Y. Kokubun, Photon. Technol. Lett. 1999, 11, 691.
- 79. C. Fabry, A. Perot, Ann. Chim. Phys. 1889, 16, 7.
- 80. M. S. Nawrocka, T. Liu, X. Wang, R. R. Panepucci, Appl. Phys. Lett. 2006, 89, 071110.
- 81. Q. Zheng, W. Zhou, Y. Peng, Y. Yin, M. Zhong, Z. Zhao, Q. Zhang, D. Tang, R. Zeng, B. S. Zou, *Nanotechnology* **2018**, *29*, 465709.
- 82. M. L. Gorodetsky, A. A. Savchenkov, V. S. Ilchenko, Opt. Lett. 1996, 21, 453.
- 83. G. C. Righini, Y. Dumeige, P. Féron, M. Ferrari, G. N. Conti, D. Ristic, S. Soria, *Riv. Nuovo Cimento*. **2011**, *34*, 435.
- 84. C. Wang, I. Gonin, A. Grassellino, S. Kazakov, A. Romanenko, V. Yakovlev, S. Zorzetti, *Npj Quantum Inf.* **2022**, *8*, 664.
- 85. Y.-D. Yang, H.-Z. Weng, Y.-Z. Hao, J.-L. Xiao, Y. Huang, Chin. Phys. B 2018, 27, 114212.
- 86. https://phys.libretexts.org/Bookshelves/University\_Physics/Book%3A\_Introductory\_Physics\_-\_Building\_Models\_to\_Describe\_Our\_World\_(Martin\_Neary\_Rinaldo\_and\_Woodman)/14%3A\_Wave s/14.07%3A\_Standing\_waves
- 87. S. Yang, Y. Wang, H. Sun, Adv. Opt. Mater. 2015, 3, 1136.
- 88. Y.-D. Yang, Y.-Z. Huang, Q. Chen, Phys. Rev. A 2007, 75, 013817.
- 89. I. Kandas, B. Zhang, C. Daengngam, I. Ashry, C.-Y. Jao, B. Peng, S. K. Ozdemir, H. D. Robinson, J. R. Heflin, L. Yang, Y. Xu, *Opt. Express* **2013**, *21*, 18.
- 90. V. B. Braginsky, M. L. Gorodetsky, and V. S. Ilchenko, Phys. Lett. A 1989, 137, 393.
- 91. G. C. Righini, Y. Dumeige, P. Féron, M. Ferrari, G. N. Conti, D. Ristic, S. Soria, *Riv. Nuovo Cimento*. **2011**, *34*, 435.
- 92. S. M. Spillane, PhD Thesis, California Institute of Technology, May, 2004.
- 93. A. V. Kumar, E. Mamonov, T. Murzina, R. Chandrasekar, Adv. Opt. Mater. 2023, 11, 202201507.
- 94. R. Vattikunta, D. Venkatakrishnarao, Md. A. Mohiddon, R. Chandrasekar, *Chem. Phys. Chem.* **2016**, 17, 3435.
- 95. K. Vahala, Nature, 2003, 424, 839.
- 96. L. Rayleigh, Lond. Edinb. Dubl. Phil. Mag. 1910, 20, 1001.
- 97. L. Rayleigh, Proc. R. Soc. London A 1912, 86, 207
- 98. X. Zhang, L. Liu, L. Xu, Appl. Phys. Lett. 2014, 104, 033703.
- 99. S. Berneschi, D. Farnesi, F. Cosi, G. N. Conti, S. Pelli, G. Righini, S. Soria, Opt. Lett. 2011, 36, 3521.
- 100. V. D. Ta, R. Chen, H. D. Sun, Adv. Mater. 2012, 24, 60.
- 101.J. Haase, S. Shinohara, P. Mundra, G. Risse, V. Lyssenko, H. Fröb, M. Hentschel, A. Eychmüller, K. Leo, *Appl. Phys. Lett.* **2010**, *97*, 211101.
- 102. G. Zhu, J. Li, N. Zhang, X. Li, J. Dai, Q. Cui, Q. Song, C. Xu, Y. Wang, Sci. Rep. 2020, 10, 253.
- 103.G. Schunk, J. U. Furst, M. Fortsch, D. V. Strekalov, U. Vogl, F. Sedlmeir, H. G. L. Schwefel, G. Leuchs, C. Marquardt. *Opt. Express* **2014**, 22, 30795.
- 104.A. N. Oraevsky, Quantum Electron. 2002, 32, 377.
- 105.P. N. Prasad, B. A. Reinhardt, Chem. Mater. 1990, 2, 660.
- 106.Z. Fang, S. Haque, S. Farajollahi, H. Luo, J. Lin, R. Wu, J. Zhang, Z. Wang, M. Wang, Y. Cheng, T. Lü, Phys. Rev. Lett. 2020, 125, 173901.

- 107.N. Mitetelo, D. Venkatakrishnarao, J. Ravi, M. Popov, E. Mamonov, T. Murzina, R. Chandrasekar, *Adv. Opt. Mater.* **2019**, *7*, 1801775.
- 108.M. Göppert-Mayer, Ann. Phys. 1931, 401, 273.
- 109.H. Huang, Z. Yu, D. Zhou, S. Li, L. Fu, Y. Wu, C. Gu, Q. Liao, H. Fu, ACS Photonics 2019, 6, 3208.
- 110.K. K. Lee, D. R. Lim, H.-C. Luan, A. Agarwal, J. Foresi, L. C. Kimerling, *Appl. Phys. Lett.* **2000**, 77, 1617.
- 111.T. J. Davis, D. E. Gómez, A. Roberts, *Nanophotonics* **2016**, *6*, 543.
- 112.S. Khan, S. L. Calvé, D. Newport. Sensors and Actuators A: Physical, 2020, 302,111.
- 113.M. Hofmann, Y. Xiao, S. Sherman, U. Gleißner, T. L. Schmidt, H. Zappe, App. Opt. 2016, 55, 1124.
- 114.Q. Bao, W. Li, P. Xu, M. Zhang, D. Dai, P. Wang, X. Guo, L. Tong, Light Sci. App. 2020, 9, 42.
- 115.R. S. E. Shamy, A. E. Afifi, M. M. Badr, M. A. Swillam, Sci. Rep. 2022, 12, 3598.
- 116.L. Jiang, J.-Y. Wu, Q. Li, G. Deng, X. Zhang, Z. Li, K. Chen, K. S. Chiang, *J. Mater. Chem. C* **2019**, 7, 6257.
- 117.https://www.menlosystems.com/products/femtosecond-lasers-and-amplifiers/
- 118.G. P. Agrawal, Applications of Nonlinear Fiber Optics, 2nd ed., Elsevier, Amsterdam 2008.
- 119.X. P. Dong, S. Li, K. S. Chiang, M. N. Ng, B. C. B. Chu, Electron. Lett. 2000, 36, 1609.
- 120.W. Hänsel, H. Hoogland, M. Giunta, S. Schmid, T. Steinmetz, R. Doubek, P. Mayer, S. Dobner, C. Cleff, M. Fischer, R. Holzwarth, *Appl. Phys. B* **2017**, *123*, 41.
- 121.A. M. R. Pinto, M. Lopez-Amo, Nanophotonics 2013, 2, 355
- 122.M. Katzman, Y. Piasetzky, E. Rubin, B. Barenboim, M. Priel, M. Erew, A. Zadok, H. Suchowski, *J. Lightwave. Technol.* **2022**, *40*, 7634.
- 123.G. M. Nikolopoulos, Phys. Rev. Lett. 2008, 101, 200502.
- 124.A. Politi, M. J. Cryan, J. Rarity, S. Yu, J. L. O'Brien, Science 2008, 320, 646.
- 125. Y. Akihama, K. Hane, Light Sci. App. 2012, 1, e16.
- 126.D. J. Richardson, J. M. Fini, L. E. Nelson, Nat. Photon. 2013, 7, 354.
- 127.A. D. Ellis, J. Zhao, D. Cotter, J. Lightwave Technol. 2010, 28, 423.
- 128.N. K. Fontaine, C. R. Doerr, M. A. Mestre, R. Ryf, P. Winzer, L. Buhl, Y. Sun, X. Jiang, R. Lingle, Optical Fiber Communication Conference (Optical Society of America, **2012**).
- 129.Z. A. Shikha, S. K. D. Nath, N. Sikder, I.-B. Sohn, H.-K. Choi, Md. S. Ahsan, *Int. Conf. Commun. Inf. Technol.* **2021**, 9641183.
- 130.D. Melati, A. Alippi, A. Annoni, N. Peserico, A. Melloni, Opt. Lett. 2017, 42, 342.
- 131.C. A. Pickover, Leonardo 1998, 21, 173.
- 132.R. Hayes, D. Yap, J. Light. Tech. 1993, 11, 523.
- 133.H. Lee, T. Chen, J. Li, O. Painter, K. J. Vahala, Nat. Commun. 2012, 3, 867.
- 134.B. Redding, S. F. Liew, Y. Bromberg, R. Sarma, H. Cao, Optica, 2016, 3, 956.
- 135.A. D. Simard, Y. Painchaud, S. LaRochelle, Opt. Express 2013, 21, 8953.
- 136.S. Tang, S. Liu, X. Yu, Q. Song, Q. Gong, Y. Xiao, Adv. Mater. 2018, 30, 1800262.
- 137.D. X. Xu, A. Densmore, A. Delage, P. Waldron, S. Janz, J. Lapointe, G. Lopinski, T. Mischki, R. McKinnon, P. Cheben, J. H. Schmid, *Opt. Express* **2008**, *16*, 15137.
- 138.N. Chauhan, A. Isichenko, K. Liu, J. Wang, Q. Zhao, R. O. Behunin, P. T. Rakich, A. M. Jayich, C. Fertig, C. Hoyt, D. J. Blumenthal, *Nat. Commun.* **2021**, *12*, 24926.
- 139.Z. Ye, P. Zhao, K. Twayana, M. Karlsson, V. Torres-Company, P.A. Andrekson, Sci. Adv. 2021, 7, eabi8150.
- 140.B. Lee, X. Chen, A. Biberman, X. Liu, I.-W. Hsieh, C.-Y. Chou, J. Dadap, F. Xia, W. Green, L. Sekaric, Y. Vlasov, R. Osgood, Jr., K. Bergman, *IEEE Photon. Technol. Lett.* **2008**, *20*, 398.
- 141.W. Bogaerts, S. K. Selvaraja, P. Dumon, J. Brouckaert, K. De Vos, D. Van Thourhout, R. Baets, *IEEE J. Sel. Top. Quantum Electron.* **2010**, *16*, 33.
- 142.M. Gnan, S. Thoms, D. Macintyre, R. De La Rue, M. Sorel, Electron. Lett. 2008, 44, 115.
- 143. Y. A. Vlasov, S. McNab, Opt. Express 2004, 12, 1622.
- 144.D. Xu, A. Delâge, R. McKinnon, M. Vachon, R. Ma, J. Lapointe, A. Densmore, P. Cheben, S. Janz, J. H. Schmid, *Opt. Express* **2010**, *18*, 1937.
- 145.Z. Xu, B. Z. Tang, Y. Wang, D. Ma, J. Mater. Chem. C 2020, 8, 2614.

- 146.D. Venkatakrishnarao, M. A. Mohiddon, N. Chandrasekhar, R. Chandrasekar, *Adv. Opt. Mater.* **2015**, *3*, 1035.
- 147.F. Y. Gardes, D. J. Thomson, N. G. Emerson, G. T. Reed, Opt. Express 2011, 19, 11804.
- 148.D. Venkatakrishnarao, Y. S. L. V. Narayana, M. A. Mohaiddon, E. A. Mamonov, N. V. Mitetelo, I. A. Kolmychek, A. I. Maydykovskiy, V. B. Novikov, T. V. Murzina, R. Chandrasekar, *Adv. Mater.* 2017, 29, 1605260.
- 149.Y. S. Zhao, Organic Nanophotonics: Fundamentals and Applications, Springer Berlin Heidelberg, 2014.
- 150.W. Zhang, J. Yao, Y. S. Zhao, Acc. Chem. Res. 2016, 49, 1691.
- 151.S. Yang, B. Wu, S. Chen, J. Sun, Y. Yu, M. Zhuo, Z. Wang, X. Wang, *Angew. Chem. Int. Ed.* **2022**, *61*, e2117857.
- 152.S. Yang, B. Xu, X. Feng, R. Lin, Y. Xu, S. Chen, Z. Wang, X. Wang, X. Meng, Z. Gao, *Chem. Mater.* **2023**, *35*, 01362.
- 153.Q. Lv, X. Wang, Y. Yu, M. Zhuo, M. Zheng, L. Liao, Nat. Commun. 2022, 13, 30870.
- 154.M. Zhuo, J. Wu, X. Wang, Y. Tao, Y. Yuan, L. Liao, Nat. Commun. 2019, 10, 11731.
- 155.M. Zhuo, G.-P. He, X. Wang, L. Liao, Nat. Commun. 2021, 12, 22513.
- 156.U. Venkataramudu, C. Sahoo, S. Leelashree, M. Venkatesh, D. S. Ganesh, S. R. G. Naraharisetty, A. K. Chaudhary, S. Srinath, R. Chandrasekar, *J. Mater. Chem. C* **2018**, *6*, 9330.
- 157.S. Guerin, S. a. M. Tofail, D. Thompson, NPG Asia Mater. 2019, 11, 01901105.
- 158.M. Owczarek, K. A. Hujsak, D. P. Ferris, A. Prokofjevs, I. Majerz, P. Szklarz, H. Zhang, A. A. Sarjeant, C. L. Stern, R. Jakubas, S. Hong, V. P. Dravid, J. F. Stoddart, *Nat. Commun.* **2016**, *7*, 13108.
- 159.A. V. Kumar, M. Annadhasan, V. V. Pradeep, M. Jyothi, K. V. J. Jose, R. Chandrasekar, *J. Phy. Chem. C* **2021**, *125*, 4909.
- 160.M. Annadhasan, A. Vinod Kumar, S. Nandy, P. Giri, M. K. Panda, K. V. J. Jose, R. Chandrasekar, *Angew. Chem. Int. Ed.* **2023**, *62*, e202302929.
- 161.T. Fukaminato, J. Photochem. Photobiology. C: Photochem. Rev. 2011, 12, 177.
- 162.M. Irie, T. Fukaminato, K. Matsuda, S. Kobatake, Chem. Rev. 2014, 114, 12174.
- 163.S. Saha, M. K. Mishra, C. M. Reddy, G. R. Desiraju, Acc. Chem. Res. 2018, 51, 2957.
- 164.P. Naumov, C. A. Chizik, M. K. Panda, N. Nath, E. B. Boldyreva, Chem. Rev. 2015, 115, 12440.
- 165.G. R. Krishna, R. Devarapalli, G. Lal, C. M. Reddy, J. Am. Chem. Soc. 2016, 138, 13561.
- 166.F. Zhang, Q. Li, C. Wang, D. Wang, M. Song, Z. Li, X. Xue, G. Zhang, G. Qing, *Adv. Funct. Mater.* **2022**, *32*, 2204487.
- 167.A. V. Kumar, M. Rohullah, M. Chosenyah, J. Ravi, U. Venkataramudu, R. Chandrasekar, *Angew. Chem. Int. Ed.* **2023**, *62*, e2300046.
- 168.S. Yousuf, J. M. Halabi, I. Tahir, E. Ahmed, R. Rezgui, L. Li, P. Laws, M. F. Daqaq, P. Naumov, *Angew. Chem. Int. Ed.* **2023**, 62, e2217329.
- 169.H. Wang, Q. Tang, X. Zhao, Y. Tong, Y. Liu, ACS Appl. Mater. Interfaces. 2018, 10, 2785.
- 170.D. Qi, L. Li, X. Miao, L. Lan, X. Yu, B. Liu, Y. Yi, P. Naumov, H. Zhang, *Nat. Commun.* **2022**, *13*, 32894.
- 171.A. Hasija, A. J. Thompson, L. Singh, S. N. Megha, M. S. R. N. Kiran, J. C. McMurtrie, M. Bhattacharjee, J. K. Clegg, D. Chopra, *Small* **2023**, *19*, 2206169.
- 172.X. Yang, L. Lan, L. Li, X. Liu, P. Naumov, H. Zhang, Nat. Commun. 2022, 13, 29959.
- 173. W. Wu, K. Chen, T. Wang, N. Wang, X. Huang, L. Zhou, Z. Wang, H. Hao, *J. Mater. Chem. C* **2023**, *11*, 2026.
- 174.M. Annadhasan, A. R. Agrawal, S. Bhunia, V. V. Pradeep, S. S. Zade, C. M. Reddy, R. Chandrasekar, *Angew. Chem. Int. Ed.* **2020**, *59*, 13852.
- 175.M. Annadhasan, D. P. Karothu, R. Chinnasamy, L. Catalano, E. Ahmed, S. Ghosh, P. Naumov, R. Chandrasekar, *Angew. Chem. Int. Ed.* **2020**, *59*, 13821.
- 176.J. Ravi, M. Annadhasan, A. V. Kumar, R. Chandrasekar, Adv. Funct. Mater. 2021, 31, 2100642.
- 177.J. Ravi, A. V. Kumar, D. P. Karothu, M. Annadhasan, P. Naumov, R. Chandrasekar, *Adv. Funct. Mater.* **2021**, *31*, 2105415.
- 178.J. Ravi, A. V. Kumar, M. Annadhasan, R. Chandrasekar, Adv. Opt. Mater. 2022, 10, 2102545.
- 179.P. Commins, D. P. Karothu, P. Naumov, Angew. Chem. Int. Ed. 2019, 58, 10052.

- 180.B. P. A. Gabriele, C. J. Williams, M. E. Lauer, B. Derby, A. J. Cruz-Cabeza, *Cryst. Growth Des.* **2020**, 20, 5956.
- 181.S. Varughese, M. S. R. N. Kiran, U. Ramamurty, G. R. Desiraju, Angew. Chem. Int. Ed. 2013, 52, 2701.
- 182.J. S. Haggerty, D. W. Lee, J. Am. Cermac. Soc. 1971, 54, 572.
- 183.C. M. Reddy, K. A. Padmanabhan, G. R. Desiraju, Cryst. Growth Des. 2006, 6, 2720.
- 184.S. Ghosh, C. M. Reddy, Angew. Chem. Int. Ed. 2012, 51, 103191.
- 185.R. Huang, C. Wang, Y. Wang and H. Zhang, Adv. Mater. 2018, 30, 1800814.
- 186.A. Worthy, A. Grosjean, M. C. Pfrunder, Y. Xu, C. Yan, G. Edwards, J. K. Clegg, J. C. Mc. Murtrie, *Nat. Chem.* **2018**, *10*, 65.
- 187.S. Basak, P. Hui, R. Chandrasekar, Chem. Mater. 2013, 25, 3408.
- 188.N. Chandrasekhar, R. Chandrasekar, Chem. Commun. 2010, 46, 2915.
- 189. V. V. Pradeep, R. Chandrasekar, Adv. Opt. Mater. 2022, 10, 2201150.
- 190. V. V. Pradeep, M. Chosenyah, E. Mamonov, R. Chandrasekar, Nanoscale, 2023, 15, 12220.
- 191. V. V. Pradeep, G. Ummethala, S. R. K. Malladi, R. Chandrasekar, Cryst. Growth Des. 2023, 23, 5414.
- 192. W. Li, J. Van Baren, A. J. Berges, E. Bekyarova, C. H. Lui, C. J. Bardeen, *Cryst. Growth Des.* **2020**, 20, 1583.
- 193.R. Chandrasekar, Chem. Commun. 2022, 58, 3415.
- 194.S. Basak and R. Chandrasekar. J. Mater. Chem. C 2014, 2, 1404.
- 195.D. Venkatakrishnarao and R. Chandrasekar, Adv. Opt. Mater. 2015, 4, 112.
- 196.M. Rohullah, V. V. Pradeep, J. Ravi, A. V. Kumar, R. Chandrasekar, *Angew. Chem. Int. Ed.* **2022**, *61*, e2202114.
- 197.S. Hayashi, F. Ishiwari, T. Fukushima, S. Mikage, Y. Imamura, M. Tashiro, M. Katouda, *Angew. Chem. Int. Ed.* **2020**, *59*, 16195.
- 198.B. Bhattachary, D. Roy, S. Dey, A. Puthuv akkal, S. Bhunia, S. Mondal, R. Chowdhury, Dr. M. Bhattachary a, M. Mandal, Dr. K. Manoj, P. K. Mandal, C. M. Reddy, *Angew. Chem. Int. Ed.* **2020**, *59*, 19878.
- 199. Y. Wang, Y. Yang, C. Wei, P. Yu, X. Cheng, J. Li, J. Zhao, J. Lin, L. Xie, *Cryst. Growth Des.* **2023**, 23, 5651.
- 200.S. Zhao, H. Yamagishi, O. Oki, Y. Ihara, N. Ichiji, A. Kubo, S. Hayashi, Y. Yamamoto, *Adv. Opt. Mater.* **2021**, *10*, 2101808.
- 201.K. Takazawa, J. Inoue, K. Mitsuishi, T. Kuroda, Adv. Funct. Mater. 2013, 23, 839.
- 202. K. Takazawa, J. Inoue, K. Mitsuishi, ACS Appl. Mater. Interfaces 2013, 5, 6182.
- 203. J. Ravi, R. Chandrasekar, Adv. Opt. Mater. 2021, 09, 2100550.
- 204. T. Ippolo, U. Ayaz, M. V. Ötügen, Proc. SPIE, 2010, DOI: 10.1117/12.841033.
- 205.K. Avasthi, L. Shukla, R. Kant, K. Ravikumar, Acta Crystallogr. Sec. C Str. Chem. 2014, 70, 555.
- 206.M. Jyothi, M. Annadhasan, V. V. Pradeep, R. Chandrasekar, Soft Matter 2020, 16, 2664.
- 207.M. Annadhasan, V. Vinay Pradeep, A. V. Kumar, J. Ravi, R. Chandrasekar, *Small Struct.* **2021**, *3*, 2100163.
- 208.S. N. Ismail, M. H. Salih, AIP Conf. Proc. 2020, 2213, 020289.
- 209.D. P. Karothu, G. Dushaq, E. Ahmed, L. Catalano, S. Polavaram, R. Ferreira, L. Li, S. Mohamed, M. Rasras, P. Naumov, *Nat. Commun.* **2021**, *12*, 1326.
- 210.M. -P. Zhuo, J. -J. Wu, X. -D. Wang, Y. -C. Tao, Y. Yuan, L. -S. Liao, Nat. Commun. 2019, 10, 3839
- 211.L. Wang, L. Yin, C. Ji, Y. Li, Dyes Pigm. 2015, 118, 37.

# Appendix

# Appendix-A

# Materials

2-hydroxy 1-napthaldehyde	Sigma-Aldrich, 98%
2-amino-5-bromo pyridine	Sigma-Aldrich, 98%
1-bromo-3,5-bis(trifluoromethyl)benzene	TCI, 99%
(4-formylphenyl)boronic acid	Avra ,99%
Tetrakis(triphenylphosphine) palladium(0)	Sigma-Aldrich, 97%
Potassium carbonate	Sigma-Aldrich, 98%
Anhydrous sodium sulfate	Sigma-Aldrich, 98%
3,5-bis(trifluoromethyl)phenylacetonitrile	Sigma-Aldrich, 98%
Sodium methoxide	Sigma-Aldrich, 98%
7-Bromobenzo[c][1,2,5]thiadiazole-4-	BLD Pharma LTD,
carbaldehyde	98%
4,4'-biphenyldiboronic acid	Sigma-Aldrich, 98%
Sodium carbonate	Sigma-Aldrich, 98%
Carbazole	Alfa Aesar, 98%
4-fluoro benzaldehyde	Sigma-Aldrich, 98%
4,7-Dibromobenzo[c][1,2,5]thiadiazole	Sigma-Aldrich, 95%
Bis(triphenylphosphine)palladium(II)	Sigma-Aldrich
dichloride	
Ethyl acetate	Merck, HPLC grade
Tetrahydrofuran	Merck, HPLC grade
Ethanol	Merck, HPLC grade
Methanol	Merck, HPLC grade

# Appendix

#### Appendix-B

#### Instrumentation

#### Nuclear Magnetic Resonance (NMR) Spectroscopy

<sup>1</sup>H and <sup>13</sup>C NMR spectra were recorded on a Bruker DPX 400 and 500 MHz spectrometer with a solvent proton as internal standard (CDCl<sub>3</sub>: <sup>1</sup>H: 7.26 ppm, <sup>13</sup>C: 77.16 ppm). Commercially available deuterated CDCl<sub>3</sub> was used. Chemical shifts (δ) are given in parts per million (ppm). Spectra were processed using topspin 4. 1. 1. software.

#### Optical Absorption Spectroscopy

The solution-state and solid-state absorption spectra were collected using Jasco V-750 spectrophotometer in a diffuse reflectance UV-visible (DR-UV-vis) mode. The reflectance spectra were converted to absorbance using the Kubelka-Munk function.

#### Fluorescence Spectroscopy

The solution-state and solid emission spectra were recorded using an FP-8500 fluorescence spectrometer. Excitation and emission bandwidth are 2.5 nm, sensitivity= medium, data interval=0.5 nm, response=1 sec, and scan speed 500 nm/min. The absolute photoluminescence quantum yield is measured using the integrated sphere setup in fluorescence spectroscopy.

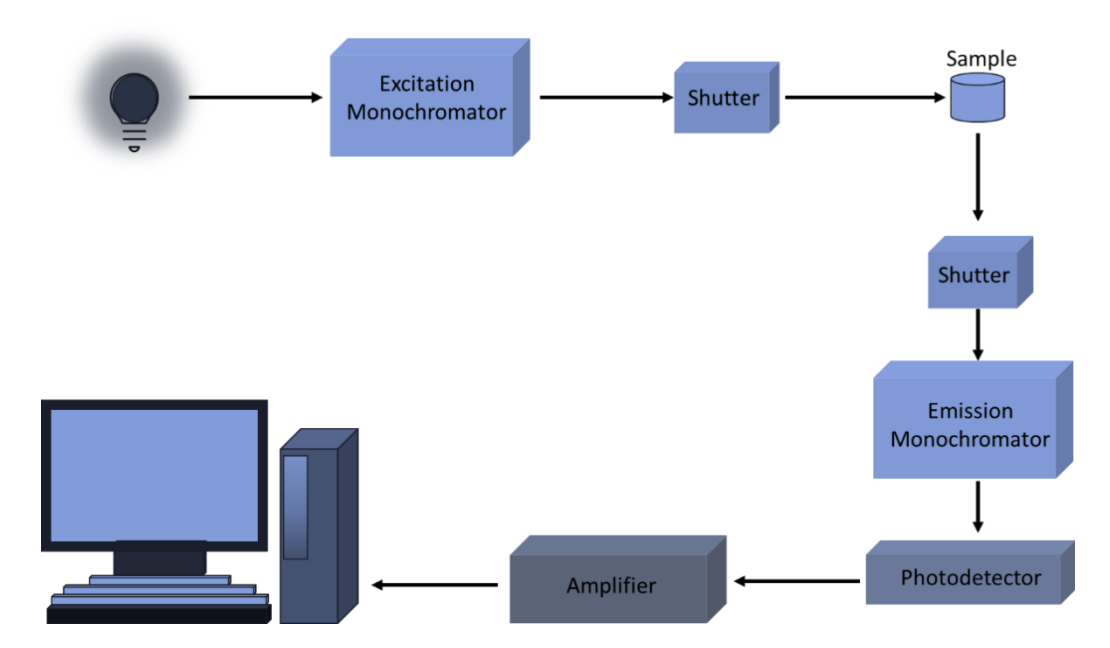


Figure I: Schematic representation of fluorescence spectroscopy.

## Polarized light microscopy

The optical images of microcrystals and the fabricated circuit were captured using a NIKON eclipse LV100N POL polarizing microscope. It was equipped with an epiilluminator (NIKON 12V 50W), DS-Fi3 camera having a 5.9-megapixel CMOS sensor, which enables superior color reproduction and NIKON TU plan fluor EPI P series objectives  $(4\times, 10\times, 20\times$  and  $50\times)$  for pin-sharp aberration-free images regardless of magnification.

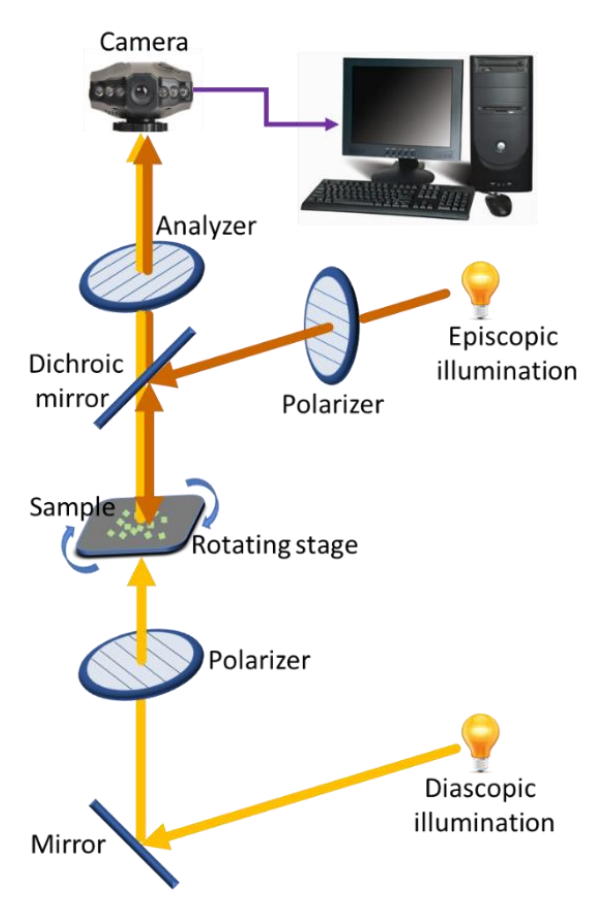
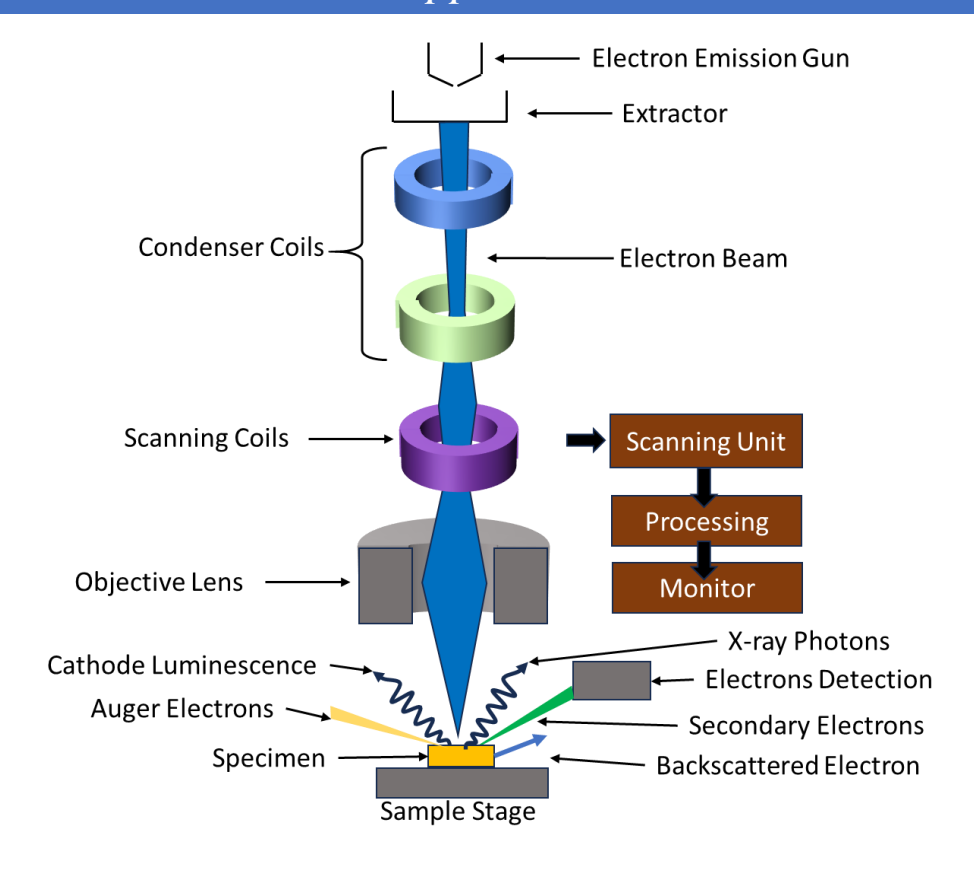


Figure II: Schematic representation of various components and the light path in polarized light microscopy.

## Field Emission Scanning Electron Microscopy (FESEM)

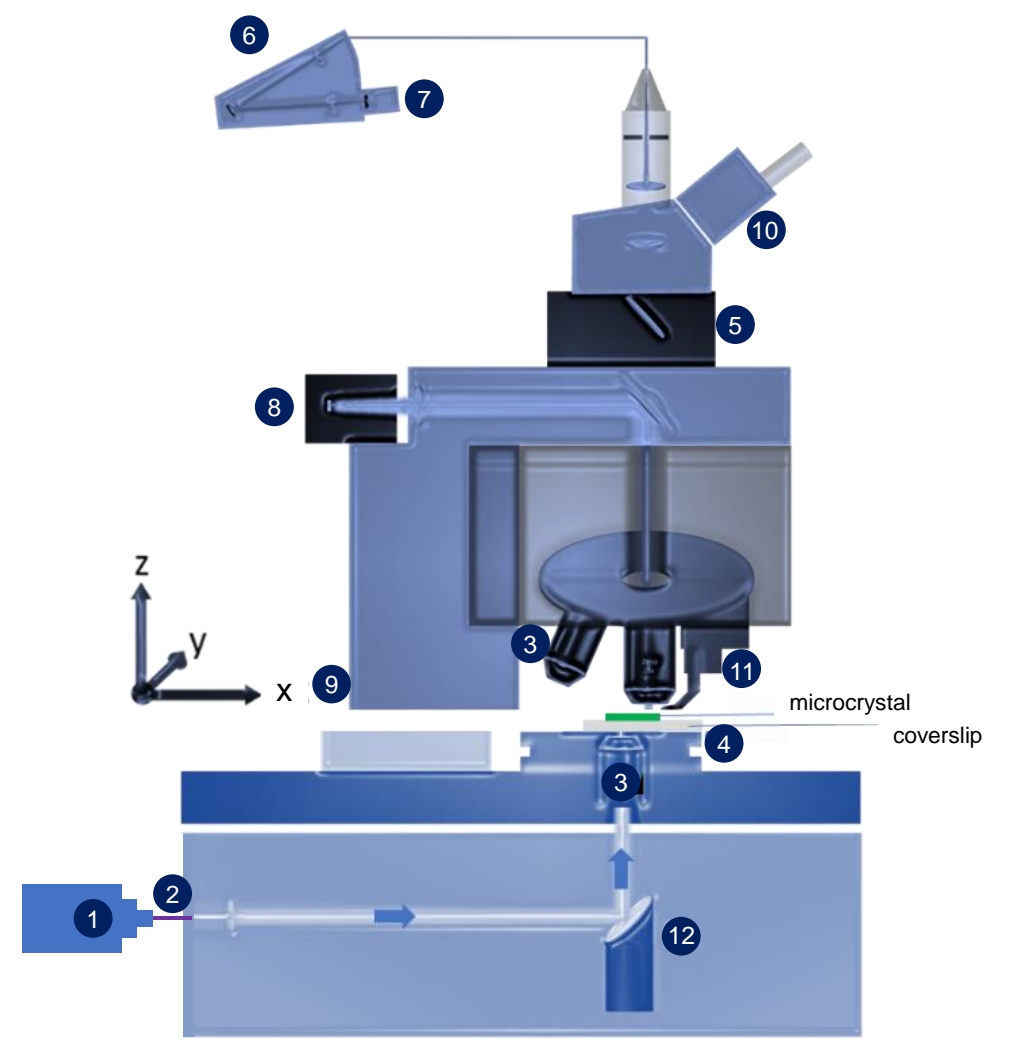
A thin layer of gold was coated on the substrate using a 15  $\mu A$  current for 80 sec. The size and morphology of the microcrystals and the circuit were examined by using a Zeiss FESEM operating at an accelerating voltage of 5 kV. The schematic of the instrument is given below.



**Figure IV:** Schematic representation of FESEM setup.

## Confocal micro-spectroscopy

Fluorescence spectra of the microcrystals were recorded on a WI-Tec confocal spectrometer equipped with a Peltier-cooled CCD detector. Using 300 grooves/mm grating BLZ = 750 nm. All measurements were performed in transmission mode geometry. A solid state 405 nm laser was used as an excitation source. To collect the output signals from the specific area of microcrystals, 150x objective (NA.: 0.95) was used. For acquiring a single spectrum before FIB milling, the laser power, integration time and accumulations were optimized to 0.05 mW, 2 s and 5, respectively. Whereas, after FIB milling, it is 4 mW power, 1 s integration time and 20 accumulations for acquiring a single spectrum. To capture the dark field images higher laser powers were used (before milling: 0.1 mW, after milling: 15 mW). The images were processed by using WI-Tec 5.2 software.



1. Laser, 2. Optical fiber, 3. Objectives (20x and 60x), 4. Piezo stage, 5. Coupler, 6. Lens-based spectroscopy, 7. CCD detector, 8. Light illumination source, 9. Z-stage focus, 10. Camera, 11. AFM cantilever-tip holder, 12. Mirror.

**Figure V:** Schematic representation of confocal micro-spectroscopy setup in transmission and reflection geometry.

## Micromanipulation (Mechanophotonics)

Mechanical micromanipulation approach was inherited to attain desired OPIC. In order to do this, an atomic force microscope (AFM)-equipped WITec alpha-300 confocal optical microscope was used. The holder was loaded with the AFM cantilever (TipsNano: NSG10, Force constant 3.1-37.6 N/m), and is attached to the 20x objective. The typical radius of curvature of AFM cantilever tip is about 10 nm. The sample holder stage was moved in x-, y-, and cantilever tip was moved in z-directions for carrying out various micromechanical operations like transferring (lifting and dropping), moving, and aligning/integrating.

## Fluorescence Lifetime Imaging (FLIM)

FL decay and FL lifetime images were recorded on a time-resolved (Micro-Time 200, Pico Quant) confocal FLIM setup, which was equipped with an inverted microscope (Olympus IX 71). Measurements were performed at room temperature, on a microcrystals deposited cover-slip. The samples were excited by a 405 nm ps diode pulse laser (power  $\approx 5~\mu W$ ) with a stable repetition rate of 20 MHz (FWHM: 176 ps) through a water immersion objective (Olympus UPlans Apo; 60 ×; NA 1.2). Signal from the samples was collected by the same objective and passed through the dichroic mirror, filtered by using a 430 nm long-pass filter to cut off any exciting light. The signal was then focused onto a 50  $\mu m$  diameter pinhole to remove the out-of-focus signal, recollimated, and directed onto a (50/50) beam splitter prior to entering two single-photon avalanche photodiodes. The data acquisition was carried out with a SymPhoTime software-controlled PicoHarp 300 time-correlated single-photon counting module in a time-tagged time-resolved mode. The overall resolution of the setup was 4 ps.

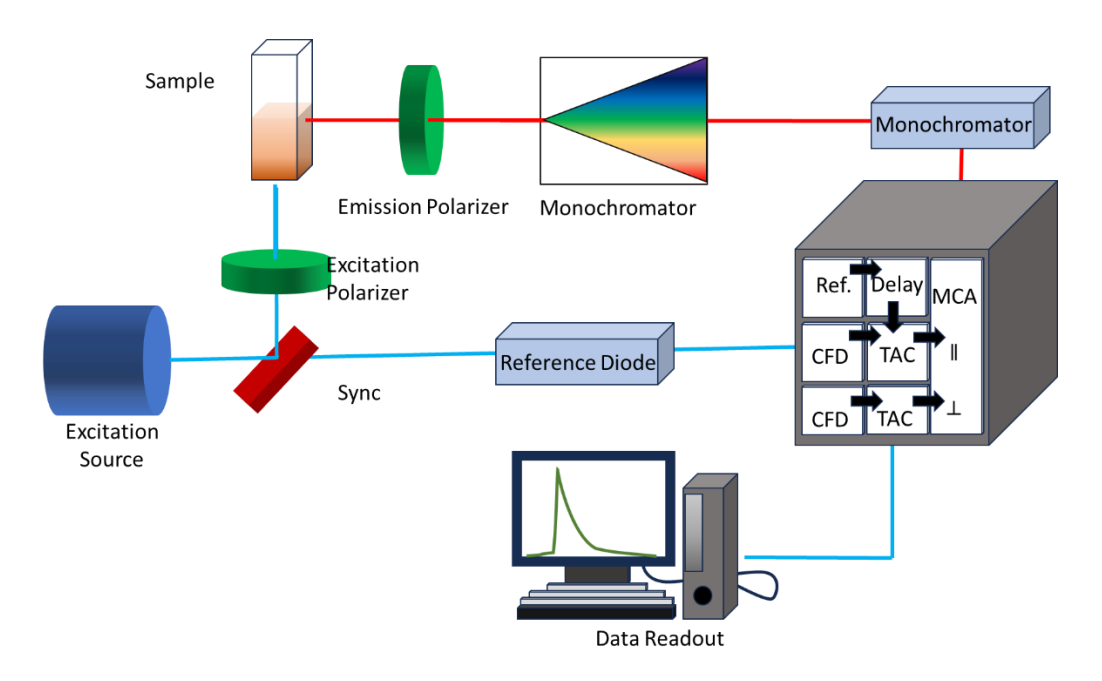


Figure VI: Schematic representation of FLIM setup.

## **Publications**

## **Complete List of Publications**

#### 2023

20. A Pick-and-Place Technology Enabled, Mechanically Programmable, Spiral Optical Waveguides Integrated Hybrid Circuits from Four Extremely Pseudo-Plastic Organic Crystals for Visible Spectral Band Tunability.

**A. Vinod Kumar**, M. Godumala, J. Ravi, R. Chandrasekar *Adv. Opt. Mater.* **2023**, doi.org/10.1002/adom.202302807.

19. Highly-Strained, Pseudo-plastic, Cu-pyridyl Coordination Polymer Crystal based Optical Waveguide-Cavity.

P. Shiva, A. Khapre, M. Chosenyah, A. Vinod Kumar, R. Chandrasekar *Chem. Mater.* **2023**, *35*, 10169-10177.

18. A Tandem Approach to Fabricating a Hybrid, Organic-Add-Drop Filter Using Single-Crystal Disk-Resonators and Pseudo-Plastic Crystal Waveguides

**A. Vinod Kumar**, V. V. Pradeep, R. Chandrasekar. *Laser Photonics Rev.* **2023**, *17*, 2300552. (\secondarrow-Contributed equally)

17. Dimension Engineering of Light-Stimulus-Responsive 1D Molecular Crystals into Unusual 2D and 3D Zigzag Waveguides

**A. Vinod Kumar**, M. Annadhasan, P. Giri, S. Nandy, M. K. Panda, K. V. Jovan Jose, R. Chandrasekar.

Angew. Chem. Int. Ed. 2023, 62, e202302929. (\strace{\strace}\)-Contributed equally).

16. Amphibian-like Flexible Organic Crystal Optical Fibres for Underwater/Air Micro-Precision Lighting and Sensing

**A. Vinod Kumar**, M. Rohullah, M. Chosenyah, J. Ravi, U. Venkataramudu, R. Chandrasekar.

*Angew. Chem. Int. Ed.* **2023**, *62*, e2300046. (§-Contributed equally ).

15. Mechanophotonics: Fabrication of a 2x2 hybrid directional coupler from flexible organic crystals.

**A. Vinod Kumar**, R. Chandrasekar. *J. Mater. Chem. C* **2023**, *11*, 7885-8001.

2022

14. A Broadband, Multiplexed-Visible-Light-Transport in Composite Flexible-Organic-Crystal Waveguide.

**A. Vinod Kumar**, M. Godumala, J. Ravi, R. Chandrasekar. *Angew. Chem. Int. Ed.* **2022**, *61*, e2212382.

13. Race-Track type Resonator Integrated Active Add-Drop Filter from Flexible Organic Crystals: Experiments and Numerical Calculations.

A. Vinod Kumar, E. Mamonov, T. Murzina, R. Chandrasekar.

Adv. Opt. Mater. 2023, 11, 202201507.

## **Publications**

12. A Mechanophotonic Approach towards an Organic, Flexible Crystals Optical Interferometer.

A. Vinod Kumar, R. Chandrasekar.

Adv. Opt. Mater. 2023, 11, 202201009.

Micromechanically-Powered Rolling Locomotion of Twisted-Crystal Optical-Waveguide-Cavity as a Mobile Light Polarization Rotor.
 M. Rohullah, V. V. Pradeep, J. Ravi, A. Vinod Kumar, R. Chandrasekar.

Angew. Chem. Int. Ed. 2022, 61, e202202114.

10. Realization of Mechanically Maneuverable Circuit Ports in Organic Hybrid Photonic Chip for 360° Steering of Bandwidth Engineered Signals.

J. Ravi, A. Vinod Kumar, M. Annadhasan, R. Chandrasekar.

Adv. Opt. Mater. 2022, 10, 2102545.

#### 2021

9. Integrating Triply- and Singly-Bent Highly Flexible Crystal Optical Waveguides for Organic Photonic Circuit with a Long-Pass-Filter Effect.

M. Annadhasan, V. V. Pradeep, A. Vinod Kumar, J. Ravi, R. Chandrasekar.

Small Struct. 2021, 3, 2100163.

8. Room temperature phosphorescent organic materials for optical waveguides

**A. Vinod Kumar**§, M. Godumala§, R. Chandrasekar.

*J. Mater. Chem. C* **2021**, *9*, 14115-14132. (§-Contributed equally)

7. Geometrically-Reconfigurable, Two Dimensional, All-Organic Photonic Integrated Circuits Made from Two Mechanically and Optically Dissimilar Crystals.

J. Ravi, A. Vinod Kumar, D. Prasad Karothu, M. Annadhasan, P. Naumov, R. Chandrasekar.

Adv. Funct. Mater. 2021, 31, 2105415.

6. Mechanophotonic aspects of a room temperature phosphorescent flexible organic microcrystal.

**A. Vinod Kumar**, M. Rohullah, J. Ravi, M. Godumala, M. Annadhasan, R. Chandrasekar.

Crys. Engg. Comm. 2021, 23, 5774 - 5779.

5. Mechanically Reconfigurable Organic Photonic Integrated Circuits Made from Two Electronically Different Flexible Microcrystals.

J. Ravi, M. Annadhasan, A. Vinod Kumar, R. Chandrasekar.

Adv. Funct. Mater. 2021, 31, 2100642.

4. Spatio-Temporal Growth Anomalies in Photo-Isomerisable Cyanostilbene-Based Crystals Triggered by Light.

**A. Vinod Kumar**<sup>§</sup>, M. Annadhasan<sup>§</sup>, V. V. Pradeep, M. Jyothi, K. V. J. Jose, R. Chandrasekar.

*J. Phys. Chem. C* **2021**, *125*, 4909-4916. (§-Contributed equally)

## **Publications**

- Magnetic Field-Assisted Manipulation of Polymer Optical Microcavities.
   M. Annadhasan, A. Vinod Kumar, E. A. Mamonov, T. Murzina, R. Chandrasekar. *Adv. Photonics Res.* 2021, 2, 2000146.
- 2. Mechanical Processing of Naturally Bent Organic Crystalline Microoptical Waveguides and Junctions.

  V. V. Pradeen, C. Tardío, I. T. Moya, A. M. Podrígue, A. Vined Kumpr, M.

V. V. Pradeep, C. Tardío, I. T. Moya, A. M. Rodrígue, A. Vinod Kumar, M. Annadhasan, A. de la Hoz, P. Prieto, R. Chandrasekar. *Small* **2021**, *17*, 2006795.

## 2020

- 1. Mechanophotonics: Precise-Selection, assembly and disassembly of polymer optical microcavities via mechanical manipulation for spectral engineering.
  - M. Annadhasan, **A. Vinod Kumar**, D. Venkatakrishnarao, E. A. Mamonov, R. Chandrasekar.

Nanoscale Adv. 2020, 2, 5584-5590.

## **Presentations**

## **Presentations in Conferences and Symposia**

- 1. A. Vinod Kumar and R. Chandrasekar
  - "Dimension Engineering of Stimuli-Responsive 1D Organic Molecular Crystals into 2D and 3D Optical Waveguides". Oral presentation at ICOBIN-2023, IIT-Roorkee, Roorkee. (ACS Applied Nanomaterials Best Poster Award)
  - 2. A. Vinod Kumar and R. Chandrasekar
    - "A Broadband, Multiplexed-Visible-Light-Transport in Composite Flexible-Organic-Crystal Waveguide". Oral presentation at Dr. K. V. Rao Scientific Society, Hyderabad. (Winner of Rasayanam Research Award)
  - 3. A. Vinod Kumar and R. Chandrasekar
    - "Flexible Organic Crystal-based Visible Light-Multiplexer for Visible Light Communication Technologies". Poster presentation, CHEMFEST-2023 at SoC, UoH, Hyderabad, India. (Best poster award)
  - 4. A. Vinod Kumar and R. Chandrasekar
    - "Broadband Visible Light-Multiplexer from Flexible Organic Crystals". Poster presentation, BSCI MEETING-2022 at Banaras Hindu University, Varanasi. (National conference, (Best poster award)
  - 5. A. Vinod Kumar and R. Chandrasekar
    - "An Organic Wavelength Division Multiplexer from Flexible-Crystal Waveguides". Oral presentation, COLLOQIUM-2022, School of Physics, University of Hyderabad, Hyderabad, India.
  - 6. A. Vinod Kumar and R. Chandrasekar
    - "Organic Spiral waveguides for Photonic Circuit Applications". Poster presentation, ICFAST-2022, at University of Hyderabd, Hyderabad, India.
  - 7. Vinod Kumar and R. Chandrasekar
    - "Organic Spiral waveguides for Photonic Circuit Applications". Oral presentation, CHEMFEST-2022 at SoC, UoH, Hyderabad, India. (Best Question award)

## Curriculun Vitae

## **Curriculum Vitae**

#### **Research Scholar**

Advanced Organic Photonic Materials and Technology Laboratory School of Chemistry University of Hyderabad Hyderabad, India

Mobile: +91 8801534577

Email: vinod.avulu@gmail.com



Research Scholar (**Organic photonics**), Advanced Organic Photonic Materials and Technologies Laboratory, University of Hyderabad, India.

#### **Fields of Interest**

- Design and fabrication of organic photonic (linear and non-linear) components and circuits
- Design, synthesis, and characterization of small organic and inorganic molecules for developing fluorescence-based sensors

## **Education**

January 2018-	Doctoral Research Fellow
present	Supervisor: Prof. Rajadurai Chandrasekar
	School of Chemistry, University of Hyderabad, India
July 2012 – May	M. Sc. in Chemical Sciences, First Class, 7.2/10.0 (CGPA)
2017	B. Sc. [Major-Chemistry, Minors-Physics, Mathematics & Biology],
[5-yr Int. M. Sc	First Class (among top 5%), <b>7.2/10.0</b> (CGPA)
program]	University of Hyderabad, India
May 2012	Higher secondary school, First class with Distinction, 77%
v	Conducted by Central Board of Secondary Education
	Kendriya Vidhyalaya, Gachibowli, Hyderabad
May 2010	Secondary school examination, First Class with Distinction, 9.0/10.0
1714y 2010	(CGPA) 3 <sup>rd</sup> Rank holder at school-level
	Conducted by Central Board of Secondary Education
	University of Hyderabad Campus School, Hyderabad

## **Research Experience**

## **Device Physics**

• More than 3 years of experience in the design, fabrication, and testing of organic flexible crystal-based photonic integrated circuits on a confocal Raman microscope attached with atomic force microscopy cantilever-tip.

## **Self-assembly**

• Self-assembly of organic small molecules and polymers to obtain microstructures acting as optical cavities (Fabry–Pérot or Whispering Gallery Mode resonators).



## Curriculun Vitae

- Expertise in achieving high-quality flexible micro waveguides from flexible organic crystals.
- Doping organic/inorganic molecules or particles into polymer microcavities to modify their optical and physical properties.

#### **Synthesis**

More than 5 years of experience in the synthesis of inorganic complexes, organic
molecules such as mechanically flexible crystals, core-shell polymer
microparticles, photoresponsive molecular crystals, and
fluorescent/phosphorescent molecules.

#### Skills

- Micromanipulation (to fabricate organic photonic components and circuits)
- Investigating the performance of organic photonic circuits
- Proficient verbal and written communication skills
- Fab management and leadership skills
- Data Analysis and Interpretation

- XRD, SEM, TEM, AFM, Raman, and UV-vis spectroscopy
- Well-versed with Origin, Mercury, Top Spin, and Chem Draw software
- Guided M. Sc students and monitored junior Ph. D students
- Self-assembly of organic molecules
- Project Design and Management

#### **Honors and awards**

- 1. December-2023: ACS Nano Materials Best Poster Award at ICOBIN-2023, Roorkee, India.
- 2. August-2023: Winner of Dr. K. V. Rao Scientific Society's Rasayanam (Chemistry) Research Award, Hyderabad, India.
- 3. May-2023: Admitted as a Member of the *Royal Society of Chemistry*, Cambridge, UK.
- 4. March-2023: Best Poster Award at ChemFest-2023, Hyderabad, India.
- 5. December-2022: Best Poster Award at BSCI-2022, Varanasi, India.
- 6. April-2022: Best Question Award at ChemFest-2022, Hyderabad, India.
- 7. March-2019: Qualified GATE, conducted by IIT Madras, Rank 2095.
- 8. July-2018: Qualified TSSET, conducted by Osmania University, Telangana, India.
- 9. December-2016: Represented the University of Hyderabad Cricket Team at "Inter-University Cricket Tournament", Hindustan Technological University, Chennai, India.
- 10. November-2013: Selected for "Young Achievers Summit" organized by Karnataka Pradesh Congress Committee, Bangalore, India.
- 11. April-2013: Selected for Indian Academy of Sciences Summer Internship Program and worked under the guidance of Dr. Manish Naja, on a project titled "Tropospheric ozone variability in rural and cleaner sites" at Aryabhata Research Institute for Observational Sciences, Nainital, India.
- 12. September-2012: Elected as "School Board Member (student representative)" of College for Integrated Studies University of Hyderabad.

# Mechanophotonics: Pseudo-Plastic Organic Crystal-based Photonic Components and Circuits

by Vinod Kumar

Indira Gandhi Memorial Library Central University P.O.

HYDERABAD-500 046.

Submission date: 29-Dec-2023 03:26PM (UTC+0530)

**Submission ID: 2265463116** 

File name: AVULU VINOD KUMAR.pdf (744.34K)

Word count: 28688

Character count: 157020

# Mechanophotonics: Pseudo-Plastic Organic Crystal-based Photonic Components and Circuits

**ORIGINALITY REPORT** 

35% SIMILARITY INDEX

5%
INTERNET SOURCES

29%
PUBLICATIONS

8%

STUDENT PAPERS

**PRIMARY SOURCES** 

Avulu Vinod Kumar, Rajadurai Chandrasekar.

"A Mechanophotonic Approach toward an
Organic, Flexible Crystal Optical
Interferometer", Advanced Optical Materials,
2022

Publication

Avulu Vinod Kumar, Mallesham Godumala, Jada Ravi, Rajadurai Chandrasekar. "A Broadband, Multiplexed-Visible-Light-Transport in Composite Flexible-Organic-Crystal Waveguide", Angewandte Chemie International Edition, 2022

Publication

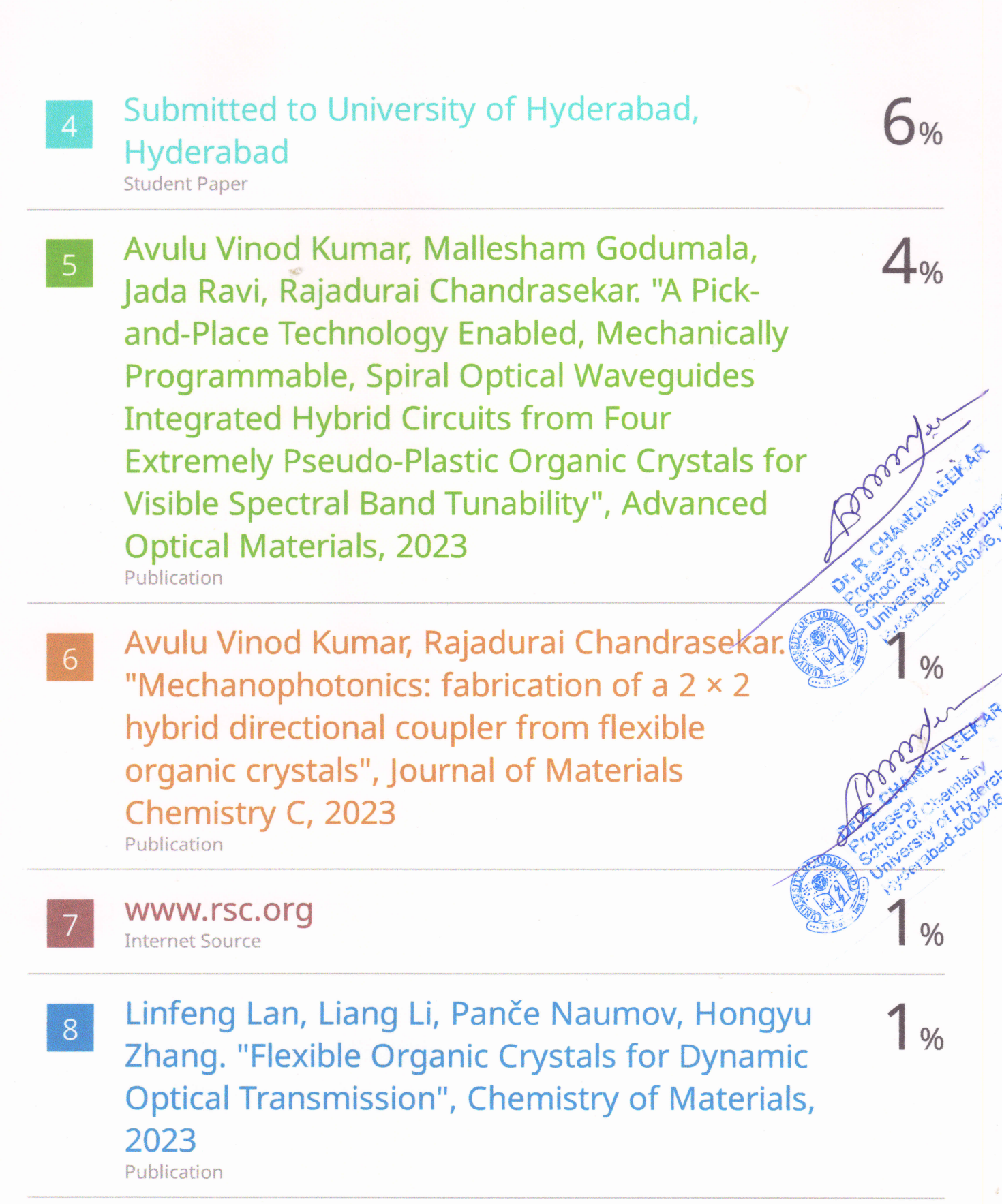
Avulu Vinod Kumar, Rajadurai Chandrasekar. "Mechanophotonics: Fabrication of a 2x2 hybrid directional coupler from flexible organic crystals", Journal of Materials Chemistry C, 2023

Publication

A Contraction of the state of t

Cranoc grad door e

The Superior of the Superior



9 www.menlosystems.com
Internet Source

<1%

10	Submitted to University of Liverpool  Student Paper	<1%
11	www.freepatentsonline.com Internet Source	<1%
12	Shiva Panbarasu, Ankur Khapre, Melchi Chosenyah, Avulu Vinod Kumar, Rajadurai Chandrasekar. "Highly Strained, Pseudoplastic, Cu-Pyridyl Coordination Polymer Crystal-Based Optical Waveguide Cavity", Chemistry of Materials, 2023 Publication	<1%
13	onlinelibrary.wiley.com Internet Source	<1%
14	Submitted to Middle East Technical University  Student Paper	<1%
15	Han Huang, Zhenyi Yu, Dandan Zhou, Shuai Li, Liyuan Fu, Yishi Wu, Chunling Gu, Qing Liao, Hongbing Fu. "Wavelength-Turnable Organic Microring Laser Arrays from Thermally Activated Delayed Fluorescent Emitters", ACS Photonics, 2019	<1%
16	Huapeng Liu, Zhuoqun Lu, Zuolun Zhang, Yue Wang, Hongyu Zhang. "Highly Elastic Organic Crystals for Flexible Optical Waveguides",	<1%

# Angewandte Chemie International Edition, 2018

**Publication** 

Felix Sunjoo Kim, Guoqiang Ren, Samson A. <1% 17 Jenekhe. "One-Dimensional Nanostructures of π-Conjugated Molecular Systems: Assembly, Properties, and Applications from Photovoltaics, Sensors, and Nanophotonics to Nanoelectronics ", Chemistry of Materials, 2011 Publication core.ac.uk 18 Internet Source Avulu Vinod Kumar, mehdi Rohullah, Melchi 19 Chosenyah, Jada ravi, uppari Venkataramudu, Rajadurai Chandrasekar. "Amphibian-like Flexible Organic Crystal Optical Fibers for Underwater/Air Micro-Precision Lighting and Sensing", Angewandte Chemie, 2023 Publication patents.glgoo.top <1% 20 Internet Source dspace.uohyd.ac.in Internet Source Submitted to University of Sheffield 22 Student Paper

pubs.rsc.org

23	Internet Source	<1%
24	smartech.gatech.edu Internet Source	<1%
25	Wenbo Wu, Kui Chen, Ting Wang, Na Wang, Xin Huang, Lina Zhou, Zhao Wang, Hongxun Hao. "Stimuli-Responsive Flexible Organic Crystals", Journal of Materials Chemistry C, 2023 Publication	<1%
26	www.schematicsforfree.com Internet Source	<1%
27	Chun-Liu Zhao, Xinyong Dong, H. Y., H. Y "Chapter 2 Photonics Crystal Fiber Loop Mirrors and Their Applications'", IntechOpen, 2012 Publication	<1 %
28	pubmed.ncbi.nlm.nih.gov Internet Source	<1%
29	thesis.library.caltech.edu Internet Source	<1%
30	"Functional Organic Materials", Wiley, 2006 Publication	<1%
31	Submitted to Icon College of Technology and Management Student Paper	<1%



# Submitted to Indian Institute of Technology, Madras

<1%

Student Paper

33

Mehdi Rohullah, Vuppu Vinay Pradeep, Jada Ravi, Avulu Vinod Kumar, Rajadurai Chandrasekar. "Micromechanically-Powered Rolling Locomotion of a Twisted-Crystal Optical-Waveguide Cavity as a Mobile Light Polarization Rotor", Angewandte Chemie International Edition, 2022 <1%

\_\_\_\_

Cai, T.. "Low bandgap polymers synthesized by FeCl"3 oxidative polymerization", Solar Energy Materials and Solar Cells, 201007

<1%

- Publication
- 35

assets.researchsquare.com

Internet Source

Publication

<1<sub>0</sub>

Exclude quotes

On

Exclude matches

< 14 words

Exclude bibliography